

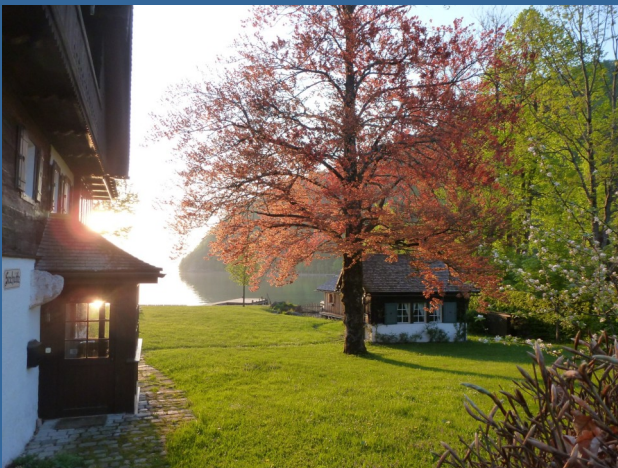


11th INTERNATIONAL CONFERENCE ON SCIENTIFIC COMPUTING IN ELECTRICAL ENGINEERING

hosted by **ÖAW RICAM**



October 3—7, 2016 in St. Wolfgang, Austria
www.ricam.oeaw.ac.at/events/conferences/scee2016/



TOPICS

- COMPUTATIONAL ELECTROMAGNETICS
- CIRCUIT AND DEVICE MODELLING & SIMULATION
- COUPLED PROBLEMS AND MULTI-SCALE APPROACHES IN SPACE AND TIME
- MATHEMATICAL AND COMPUTATIONAL METHODS INCLUDING UNCERTAINTY QUANTIFICATION
- MODEL ORDER REDUCTION
- INDUSTRIAL APPLICATIONS

IMPORTANT DATES

May 31, 2016:

Deadline for submission

June 15, 2016:

Notification of Acceptance

June 30, 2016:

Deadline for early-bird registration

August 15, 2016:

Deadline for registration

The scientific program includes invited and contributed talks, poster sessions and an industrial day.

The conference proceedings will be published by Springer. Selected Papers will be published in a special issue of the Springer Journal of Mathematics in Industry.

INVITED SPEAKER

Regular Program...

Ram Achar, Canada
Hans-Georg Brachtendorf, Austria
Carlo de Falco, Italy
Victorita Dolean, UK
Lihong Feng, Germany
Eric Keiter, USA
Roland Pulch, Germany
Joachim Schöberl, Austria

....Industrial Day

Massimiliano Cremonesi, Polimi, Italy
Lars Kielhorn, TailSiT GmbH, Austria
Stefan Reitzinger, CST, Germany
Ehrenfried Seebacher, austriamicrosystems, Austria
Siegfried Silber, LCM GmBH, Austria

SCIENTIFIC COMMITTEE

Gabriela Ciuprina, Bucharest, Romania
Herbert De Gersem, Darmstadt, Germany
Georg Denk, Munich, Germany
Michael Günther, Wuppertal, Germany
Ulrich Langer, Linz, Austria
Jan ter Maten, Wuppertal, Germany
Jörg Ostrowski, Baden-Dättwil, Switzerland
Ursula van Rienen, Rostock, Germany
Vittorio Romano, Catania, Italy
Ruth Sabariego, Leuven, Belgium
Wil Schilders, Eindhoven, The Netherlands
Caren Tischendorf, Berlin, Germany



Scientific Committee

Gabriela Ciuprina, Bucharest, Romania
Herbert De Gersem, Darmstadt, Germany
Georg Denk, Munich, Germany
Michael Günther, Wuppertal, Germany
Ulrich Langer, Linz, Austria
Jan ter Maten, Wuppertal, Germany
Jörg Ostrowski, Baden-Dättwil, Switzerland
Ursula van Rienen, Rostock, Germany
Vittorio Romano, Catania, Italy
Ruth Sabariego, Leuven, Belgium
Wil Schilders, Eindhoven, The Netherlands
Caren Tischendorf, Berlin, Germany

Local Organizing Committee

Wolfgang Amrhein, JKU & LCM, Austria
Gerd Bramerdorfer, JKU, Linz, Austria (Co-Chair)
Armin Fohler, LCM, Linz, Austria
Wolfgang Forsthuber, RICAM, Linz, Austria (Technical Service)
Peter Gangl, JKU & LCM, Linz, Austria
Christoph Hofer, RICAM, Linz, Austria
Ulrich Langer, JKU & RICAM, Linz, Austria (Chair)
Ewald Lindner, JKU, Linz, Austria
Svetlana Matculevich, RICAM, Linz, Austria
Martin Neumüller, JKU, Linz, Austria
Stefan Takacs, RICAM, Linz, Austria
Annette Weihs, RICAM, Linz, Austria (Conference Secretary)
Thomas Wick, RICAM, Linz, Austria
Walter Zulehner, JKU, Linz, Austria (Co-Chair)

Conference Desk

Annette Weihs, RICAM, Linz, Austria
Wolfgang Forsthuber, RICAM, Austria

Contents

I Program	1
II Abstracts of Invited Talks	9
III Abstracts of Invited Talks - Industrial Day	27
IV Abstracts of Contributed Talks	39
V Abstracts of Poster Session 1	79
VI Abstracts of Poster Session 2	109
VII List of Participants	137

Part I
Program

Monday, October 3

16:00 – 20:00 Registration (Bürglhaus)

Tuesday, October 4

08:30 – 09:15 Registration (Bürglhaus)

09:15 – 09:25 Opening by Ulrich Langer (chair) and Meinhard Lukas (Rector of the JKU)

Session 01: Chair: Ursula van Rienen

09:25 – 10:15 **IT 1:** Victorita Dolean

Microwave Tomographic Imaging of Cerebrovascular Accidents by Using High-Performance Computing

10:15 – 10:40 **CT 1:** Sebastian A. Schuhmacher

Sensitivity of Lumped Parameters to Geometry Changes in Finite Element Models

10:40 – 11:10 Coffee Break

Session 02: Chair: Jörg Ostrowski

11:10 – 11:35 **CT 2:** Raffael Casagrande

A Trefftz Method for the time-harmonic Eddy Current Equation

11:35 – 12:00 **CT 3:** Yun Ouédraogo

Modelling and simulation of electrically controlled droplet dynamics

12:00 – 12:25 **CT 4:** Jennifer Dutiné

Survey on Semi-Explicit Time Integration of Eddy Current Problems

12:30 – 13:30 Lunch

Session 03: Chair: Michael Guenther

14:00 – 14:25 **CT 5:** Neil V. Budko

On the spatial variations of the electric network frequency

14:25 – 14:50 **CT 6:** Wim Schoenmaker

Stability Analysis of Electromagnetic Transient Simulations

14:50 – 15:15 **CT 7:** Christoph Winkelmann

Electro-Thermal Simulations with Skin-Layers and Contacts

Poster Session 1: Chair: Gerd Bramerdorfer

15:15 – 15:50 **PS 1:** Posters fast-forward presentation (2 minutes presentations)

15:50 – 16:40 **PS 1:** Presentation of Posters & Coffee Break

Session 04: Chair: Herbert De Gerssem

16:40 – 17:30 **IT 2:** Joachim Schöberl

Mapped Tent-pitching methods for Maxwell Equations

17:30 – 17:55 **CT 8:** Scott Bagwell

Finite Elements for the Simulation of Coupled Acousto-Magneto-Mechanical Systems with Application to MRI Scanner Design

17:55 – 18:20 **CT 9:** Idoia Cortes Garcia

Structural and Implementation Aspects of Field/Circuit Coupling in A-V and T- Ω Based Formulations

18:30 – 19:30 Dinner / Get-together

Wednesday, October 5 - Industrial Day

Session 05: Chair: Wolfgang Amrhein

09:00 – 09:35 **IT ID 1:** Stefan Reitzinger
Broadband Solution Methods for Maxwell's Equations in Laplace Domain

09:35 – 10:10 **IT ID 2:** Lars Kielhorn
A Symmetric FEM-BEM Formulation for Magnetostatics

10:10 – 10:45 **IT ID 3:** Siegfried Silber
Optimization of mechatronic components with MagOpt

10:45 – 11:15 Coffee Break

Session 06: Chair: Georg Denk

11:15 – 11:50 **IT ID 4:** Massimiliano Cremonesi
A Lagrangian approach to the simulation of a vacuum arcs in a transverse magnetic field

11:50 – 12:25 **IT ID 5:** Ehrenfried Seebacher
Compact Modeling for HV CMOS Technologies

12:30 – 13:30 Lunch

13:30 – 19:00 Excursion

19:00 – 20:00 Dinner

Thursday, October 6

Session 07: Chair: Caren Tischendorf

09:00 – 09:50 **IT 3:** Peter Benner
Parametric model order reduction for ET simulation in nanoelectronics

09:50 – 10:40 **IT 4:** Roland Pulch
Global sensitivity analysis for parameter variations in electric circuits

10:40 – 11:10 Coffee Break

Session 08: Chair: Ruth Sabariego

11:10 – 11:35 **CT 10:** Andrea Böhme
An Atlas Model for Simulating Deep Brain Stimulation in the Rat Model for Parkinson's Disease

11:35 – 12:00 **CT 11:** Giovanni De Luca
Fast and Accurate Time-Domain Simulations of Industrial PLLs

12:00 – 12:25 **CT 12:** Thorben Casper
Equivalent Netlist Extraction for Electrothermal and Electromagnetic Problems Discretized by the Finite Integration Technique

12:30 – 13:30 Lunch

Session 09: Chair: Michael Günther

14:00 – 14:50 **IT 5:** Carlo de Falco
Numerical Modeling of Organic Electronic and Photovoltaic Devices

14:50 – 15:15 **CT 13:** Andreas Pels
Multirate Partial Differential Equations for Pulsed Excitations

Poster Session 2: Chair: Walter Zulehner

15:15 – 15:50 **PS 2:** Posters fast-forward presentation (2 minutes presentations)

15:50 – 16:40 **PS 2:** Presentation of Posters & Coffee Break

Session 10: Chair: Jan ter Maten

16:40 – 17:05 **CT 14:** Piotr Putek
Robust optimization of a RFIC isolation problem under uncertainties

17:05 – 17:30 **CT 15:** Kai Gausling
Density Estimation in Cosimulation using Spectral- and Kernel Methods

Session 11: Chair: Gabriela Ciuprina

17:30 – 17:55 **CT 16:** Rokibul Hasan
POD-based reduced-order model of an eddy-current levitation problem

17:55 – 18:20 **CT 17:** Christoph Hachtel
Multirate DAE/ODE-Simulation and Model Order Reduction for Coupled Circuit-Field Systems

19:00 – 22:00 Conference Dinner

Friday, October 7

Session 12: Chair: Vittorio Romano

09:00 – 09:50 **IT 6:** Ram Achar

Challenges and Opportunities: Modeling and Simulation for the Emerging High-Speed Multi-Function Designs

09:50 – 10:15 **CT 18:** Stefan Takacs

Fast multigrid solvers for isogeometric discretizations

10:15 – 10:40 **CT 19:** Gerhard Unger

Convergence analysis of a boundary element method for Maxwell's time-harmonic interior and exterior eigenvalue problem

10:40 – 10:50 Coffee Break

Session 13: Chair: Wil Schilders

10:50 – 11:40 **IT 7:** Eric Keiter

Gradient-Enhanced Polynomial Chaos Methods for Circuit Simulation

11:40 – 12:30 **IT 8:** Hans-Georg Brachtendorf

Coupled Multirate Simulation by the MPDE technique for Radio Frequency Circuits

12:30 – 12:35 Closing

12:35 – 13:30 Lunch

Poster Session 1: Applications

P 1:	Muhamet Alija A New Charge Simulation Approach for Dielectric Design of High Voltage Switchgear
P 2:	Kai Bittner Coupled circuit device simulation
P 3:	Andreas Blaszczyk Virtual High Voltage Lab
P 4:	Gerd Bramerdorfer Topology optimization of synchronous reluctance motors for achieving maximum torque capability
P 5:	Gabriela Ciuprina Compact Reduced Order Multiphysics Models for Electrostatic Actuated MEMS Switches
P 6:	Nhung T.K Dang Solution of linear systems for electronic circuits with large numbers of parasitics capacitances
P 7:	Viktoria O. Gaidar Automatic epilepsy seizure detection using wavelet transform
P 8:	Tomas Gotthans Different DC fusing scenarios of encapsulated bonding wires
P 9:	Jonas Pade Convergence of a Waveform Relaxation Method for Index-2 DAEs of Electromagnetic Field/Circuit Simulation
P 10:	Theresa Roland Simulation of the EMG for evaluation of capacitive sensors
P 11:	Christian Strohm Holistic Transient Coupled Field and Circuit Simulation
P 12:	Duy T. Truong The cell contractility model and the cell adhesion model: Reducing the complexity and preparing the coupling to electrical forces
P 13:	Ursula van Rienen Preliminary numerical study on electrical stimulation at alloplastic reconstruction plates of the mandible
P 14:	Wei Wu Thermal modeling of liquid-filled transformer radiators using network approach

Poster Session 2: Methods

-
- P 15:** Nicodemus Banagaaya
Modified Block-Diagonal Structured Model Order Reduction for Electro-Thermal Problems in Industrial Electronics Simulations
-
- P 16:** E. Jan W. ter Maten
Fitting Generalized Gaussian Distributions for Process Capability Index
-
- P 17:** Marco Coco
Heat effects in graphene due to charge transport
-
- P 18:** Ana Drandić
Computation of electric field in transformers by boundary element method and fast multipole method
-
- P 19:** Armin Fohler
Adaptive Meshrefinement for Rotating Electrical Machines taking Boundary Approximation Errors into Account
-
- P 20:** Peter Gangl
An Efficient Optimization Tool for the Design of Electric Motors
-
- P 21:** Qingzhe Liu
Numerical methods for derivative based global sensitivity measures in high dimensions
-
- P 22:** Sangye Lungten
Fill-reducing reordering of saddle-point matrices for block $LD^{-1}L^T$ factorization
-
- P 23:** Jan Philipp Pade
The dynamical impact of structural perturbations in electrical circuits
-
- P 24:** Marta Piñeiro
Numerical Simulation of Magnetization and Demagnetization Processes
-
- P 25:** Vittorio Romano
Deterministic and stochastic solutions of the Boltzmann equation for charge transport in graphene on substrates
-
- P 26:** Ruth V. Sabariego
Time-domain reduced-order modelling of linear finite-element eddy-current problems via RL-ladder circuits
-
- P 27:** Markus Schöbinger
Error Estimation for MSFEM for elliptic problems in 2D
-

Part II

Abstracts of Invited Talks

Microwave Tomographic Imaging of Cerebrovascular Accidents by Using High-Performance Computing

P.-H. Tournier^{1,2}, I. Aliferis³, M. Bonazzoli⁴, M. de Buhan⁵, M. Darbas⁶, V. Dolean^{4,7}, F. Hecht^{1,2}, P. Jolivet⁸, I. El Kanfoud³, C. Migliaccio³, F. Nataf^{1,2}, C. Pichot³, and S. Semenov⁹

¹ Laboratoire Jacques-Louis Lions, UMR CNRS 7598, Sorbonne Universités, UPMC, Paris, France

² INRIA-Paris, EPC Alpines, Paris, France

³ Université Côte d'Azur, CNRS, LEAT, France

⁴ Université Côte d'Azur, CNRS, LJAD, France

⁵ MAP5, UMR CNRS 8145, Université Paris-Descartes, Sorbonne Paris Cité, France

⁶ LAMFA, UMR CNRS 7352, Université de Picardie Jules Verne, Amiens, France

⁷ Dept of Maths and Stats, University of Strathclyde, Glasgow, UK

⁸ IRIT, UMR CNRS 5505, Toulouse, France

⁹ EMTensor GmbH, TechGate, 1220 Vienna, Austria

Summary. The motivation of this work is the detection of cerebrovascular accidents by microwave tomographic imaging. This requires the solution of an inverse problem relying on a minimization algorithm (for example, gradient-based), where successive iterations consist in repeated solutions of a direct problem. The reconstruction algorithm is extremely computationally intensive and makes use of efficient parallel algorithms and high-performance computing. From the mathematical and numerical point of view, this means solving Maxwell's equations in time-harmonic regime by appropriate domain decomposition methods, which are naturally adapted to parallel architectures.

Cerebrovascular accidents (CVA) or strokes are caused by a perturbation in the blood supply of the brain leading to a quick loss of cerebral functions, that is very often lethal. There are two categories of CVA: ischemic (80% cases) resulting from the occlusion of a cerebral artery and hemorrhagic (20% cases) provoked by a bleeding vessel. From a medical point of view, the detection and characterization of a CVA are crucial for patient survival. Moreover, a continuous monitoring requires an image of the brain every fifteen minutes. Nowadays physicians use two imaging systems of the brain: Magnetic resonance imaging (MRI) and CT (cerebral tomogram) scan. Even if these techniques are very precise their use is not well adapted to a prompt medical care. They can be also harmful in the case of a continuous monitoring with CT scan that measure the absorption of X rays by the tissues. Our research team, has carried out its work in collaboration with EMTensor¹, an Austrian innovative SME, dedicated to biomedical imaging. For the first time in the world, we have demonstrated on synthetic data the feasibility of a new imaging technique based on microwave, allowing both the characterization of the CVA from the very first patient care in an ambulance and throughout his con-

tinuous monitoring during hospitalization. How does it work? Electric properties of biological tissues are a great indicator of their functional and pathological conditions. Microwaves can image them, on the basis of differences in their dielectric properties. In such a system, the patients head is equipped with a helmet consisting of electromagnetic antennas, that transmit data to a high-performance computing center which is sending back images of the brain to doctors at the hospital where the patient will be treated. This type of imaging requires a reduced data acquisition phase with a satisfying spatial resolution and it is less harming than a mobile phone. These characteristics make microwave imaging very attractive. From a computational point of view, this implies the solving of an inverse problem and subsequently a fast solution of Maxwell equations. To prove the feasibility of such a technique, we have developed a high-performance computing approach which generates brain images in less than 15 minutes.

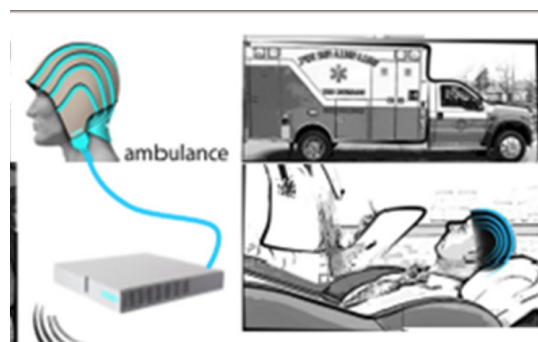


Fig. 1. Principle of microwave imaging—courtesy of EMTensor

¹ <http://entensor.com/>

In order to develop a robust and precise methodology for microwave imaging, a few distinct research fields must be mastered: optimization, inverse problems, approximation and solution methods for the simulation of the direct problem modeled by Maxwell equations. The precise simulation of a direct problem for a complex and highly heterogeneous medium is a challenge in itself. A few tools already developed by the researchers of the team were used: the HPDDM² library for domain decomposition and its interface with the FreeFem++³ software (finite elements).

EMTensors experimental system to be simulated consists in an electromagnetic reverberating chamber surrounded by five layers of 32 antennas each, able to work alternately as an emitter or a receptor. The object to be reconstructed is introduced in the chamber. Alternately, each of the 160 antennas emits a signal at a fix frequency, typically 1 GHz. The electromagnetic field is propagated within the chamber and the object to be imaged regarding its properties. The other 159 antennas record the total field in the form of complex transmission. The inversion algorithm is reconstructing a brain image on the basis of these data. A first step was to successfully compare the measure of data acquisition made with EMTensors system with those numerically performed by the resolution of Maxwell equations on a 3D mesh.

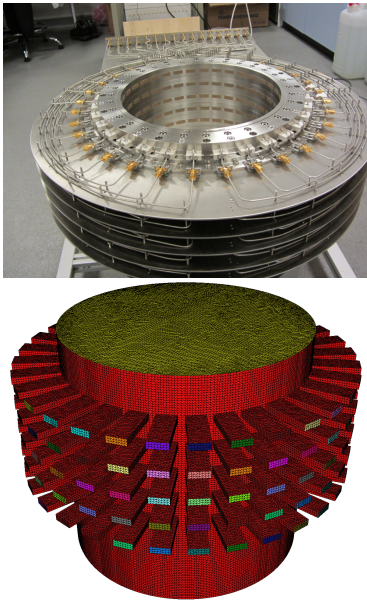


Fig. 2. Measurement chamber (above) and corresponding mesh (below) for numerical simulation (diameter: 28.5 cm). Image courtesy of EMTensor.

² <https://github.com/hpddm/hpddm>

³ <http://www.freefem.org/>

For the second step, we have created synthetic data on a brain model coming from scan sections (362x434x362 voxels) and then simulated a hemorrhagic CVA. At last, we designed and tested an inversion algorithm for monitoring the evolution of the CVA, reconstructed by successive slices. Here, a slice corresponds to one layer of 32 antennas on the five equipping the experimental system. Thanks to the use of parallelism, the reconstruction of each layer can be generated independently. The inversion algorithm helps reconstruct an image in less than 2 minutes (94 seconds) using 4096 computing cores. This restitution time, that can be further refined, already fits the physicians objective to get an image every fifteen minutes for an efficient monitoring of the patient.

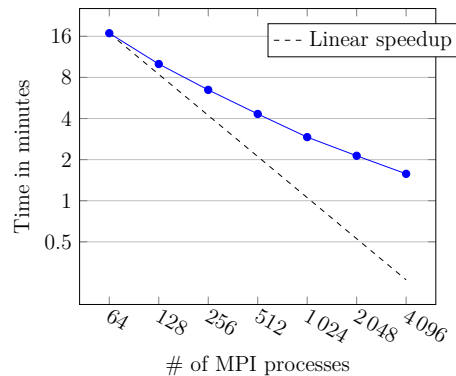


Fig. 3. Reconstruction time of an image regarding the number of computing cores

The medical and industrial challenge of this work is very important. It is the first time that such a realistic study demonstrates the feasibility of microwave imaging with a promising potential for the future.

Acknowledgement. This work has been supported in part by ANR⁴ through the project MEDIMAX (led by C. Pichot from the University of Nice). Large-scale numerical simulations have been possible thanks to the technical support and computing hours on large supercomputers: Curie (CEA, Bull) and Turing (CNRS, IBM) via GENCI⁵ (allocations 2016-067519 and 2016-067730) or PRACE⁶ calls.

More details can be found in the preprint "*Microwave Tomographic Imaging of Cerebrovascular Accidents by Using High-Performance Computing*", P.-H. Tournier, I. Aliferis, M. Bonazzoli, M. de Buhan, M. Darbas, V. Dolean, F. Hecht, P. Jolivet, I. El Kanfoud, C. Migliaccio, F. Nataf, C. Pichot, S. Semenov, <http://arxiv.org/abs/1607.02573>.

⁴ French National Research Agency

⁵ <http://www.genci.fr/en>

⁶ <http://www.prace-ri.eu/>

Mapped Tent-pitching methods for Maxwell Equations

Joachim Schöberl¹, Jay Gopalakrishnan², Christoph Wintersteiger¹, and Matthias Hochsteger¹

¹ Institute for Analysis and Scientific Computing, TU Wien joachim.schoeberl@tuwien.ac.at, christoph.wintersteiger@tuwien.ac.at, matthias.hochsteger@tuwien.ac.at

² Maseeh Department of Mathematics + Statistics, Portland State University gjay@pdx.edu

Summary. We present a new numerical method for solving time dependent Maxwell Equations. It is based on the tent-pitching algorithm, which is a domain decomposition method in space-time. Provided that an approximate solution is available at the tent-bottom, the equation can be locally evolved up to the top of the tent. With mapped tent-pitching, we present a new, completely explicit version of tent-pitching. This leads to an highly parallel algorithm, which utilizes modern computer architectures extremely well.

1 Tent-pitching space time meshes

We are solving time dependent Maxwell equations with the usual initial and boundary conditions. The tent-pitching method is based on a conforming spatial mesh, which can be locally refined for resolving geometric details or singularities. For the initial time t_0 , we are given initial conditions for E and H . Now we erect the first layer of tents by pitching a set of vertices forward in time, see Figure 1. The slope of

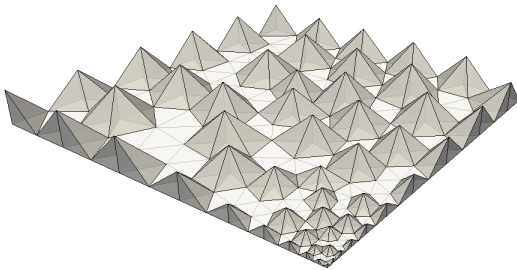


Fig. 1. First layer of tents

the tents are limited by the speed of light. Thus, the solution within one tent only depends on the initial conditions on the tent bottom. We can now apply some numerical method to compute an approximate solution on every tent, independently and parallel on every tent of this layer. This method propagates the solution up to the top boundary. Now, we build the next layer of tents on top of the first one, and solve there, and so on. In every step, we store the solution field for the current front manifold. This requires the same amount of memory as storing the spatial field.

1.1 Mapped tent-pitching (MTP) method

Tent-pitching algorithms from [2, 3] use space-time discontinuous Galerkin discretizations within one tent-domain. In [1] we have proposed an alternative local solution method named mapped tent-pitching: The tent is considered as a deformed space-time cylinder, which allows to pull-back the equation to the cylinder. Here, we can apply conventional space discretization and implicit or explicit time-stepping methods. In this

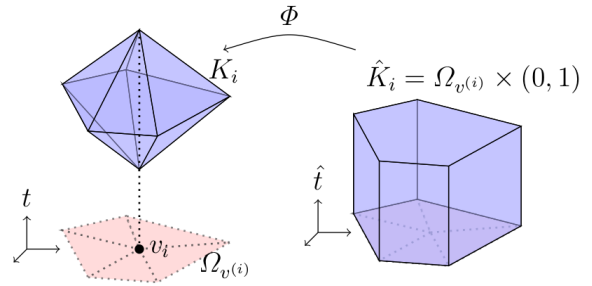


Fig. 2. Mapping from cylinder to tent

work we present new explicit time-stepping methods which lead to optimal order of convergence.

The methods are implemented in an extension module to NGSolve-Python. Numerical results on modern computer architectures are presented.

References

1. J. Gopalakrishnan, J. Schöberl, and C. Wintersteiger. *Mapped tent pitching schemes for hyperbolic systems*. arXiv:1604.01081, 2016.
2. P. Monk and G. R. Richter. *A discontinuous Galerkin method for linear symmetric hyperbolic systems in inhomogeneous media*. *J. Sci. Comput.*, 22/23: 443–477, 2005
3. L. Yin, A. Acharia, N. Sobh, R. B. Haber, and D. A. Tortorelli. *A spacetime discontinuous Galerkin method for elastodynamics analysis* in *Discontinuous Galerkin Methods: Theory, Computation and Applications*, B. Cockburn, G. Karniadakis, and C.W.Shu (eds), 459–464, 2000

Parametric model order reduction for ET simulation in nanoelectronics

Peter Benner and Lihong Feng

Max Planck Institute for Dynamics of Complex Technical Systems, Sandtorstr. 1, 39106 Magdeburg, Germany
benner@mpi-magdeburg.mpg.de, feng@mpi-magdeburg.mpg.de

Summary. Electro-thermal (ET) simulation is essential in today's design of integrated circuits. Numerical simulation of the ET problems results in very large-scale ET coupled systems. Especially, when parameter variations are considered in multi-query tasks, such as optimization, or uncertainty quantification, repeated simulation of large-scale systems causes unaffordable computational load. We discuss using parametric model order reduction to construct small-sized parametric reduced-order models replacing the large-scale systems in the numerical simulations required in the given multi-query context. The reliability and automatic generation of the reduced-order models are guaranteed by a robust a posteriori error bound recently proposed in [5].

1 Introduction

With the scaling down of integrated circuits, thermal issues have attracted increasingly more attention and become a major consideration in design of integrated circuits. Detailed description of ET problems easily leads to very large-scale ET coupled systems with dimension (degrees of freedom) as high as 10^6 , which require a significant amount of memory in computer simulations. Simulation software can often not run the simulation due to memory limitations or since they are too time-demanding. Furthermore, parameter variations have become essential in design of micro- and nano-electronic (-mechanical) systems as well as ET coupled problems, since in many analyses such as optimization and uncertainty quantification, simulation at varying values of the parameters is unavoidable. This implicates that simulations have to be repeatedly implemented due to parameter variations in the corresponding multi-query tasks.

Parametric model order reduction (PMOR) computes a reduced-order model (ROM) of much smaller size, which can replace the large-scale system for device- and chip-level simulation under parameter variations, without large-memory requirements and without loss of accuracy. As a result, simulation using the ROM can be accomplished much faster than using the detailed system, which is especially useful for multi-query tasks. In recent years, numerous model order reduction (MOR) methods for parametrized systems have been developed [1]. Among these methods, only for the reduced basis method, a posteriori error bounds have been derived systematically [4]. These

enable automatic generation of reliable reduced parametric models.

We have recently proposed an a posteriori error bound [5] in frequency domain for linear non-parametric and parametric systems. The error bound is the bound for the difference between the transfer function of the original system and that of the ROM, and is applicable to any MOR or PMOR methods based on approximation/interpolation of the transfer function, including the (multi-)moment-matching methods [2]. Technically, the error bound provides a way of automatically generating reliable ROMs computed by the (multi-)moment-matching methods, which is desired in design automation for integrated circuits.

As an example, we show in the next section automatic PMOR of a nonlinear coupled parametric power-MOS device model shown in Figure 2. Under the guidance of the proposed error estimate, the ROM can be automatically constructed, and is further used for accelerating uncertainty quantification of the ET problem with conductivity variation. To deal with the coupling of the electrical and the thermal fields, the error bound is applied to the electrical subsystem and the thermal subsystem separately, so that projection matrices (reduced subspaces) for the state vectors of the two subsystems are separately constructed. Due to limited space, details of constructing the ROM of the coupled system will not be presented and can be found in [3].

2 Automatic PMOR of a ET coupled power-MOS device model

The power-MOS device model has 6 inputs and 12 outputs. It is an ET system coupling the electrical and the thermal subsystems. The system is parameterized by the conductivity σ of the third metal layer and excited by the inputs:

$$u_i = \begin{cases} 0, & i = 1, 2, \\ 10^7 t, & i = 3, t \in [0, 10^{-6}], \\ 10 & i = 3, t > 10^{-6}, \\ 26.85 & i = 4, 5, 6. \end{cases}$$

The initial condition for all electrical state variables is 0 V, and for all thermal state variables is 26.85 degrees centigrade. The electrical subsystem is a para-

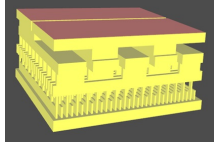


Fig. 1. A power-MOS device (stretched in the vertical direction)

metric system of 1160 algebraic equations, and the thermal subsystem consists of 11556 differential algebraic equations. Using the adaptive pMOR algorithm [5] developed based on the error bound, the electrical subsystem is reduced from order 1160 to order 2, and the thermal subsystem is reduced from order 11556 to order 35. The convergence behavior of the algorithm is shown in Table 1. At the final iteration step, the ROM meeting the accuracy requirement ϵ_{tol} , is derived. In the mid column are the samples of the Laplace variable s , and/or the samples of the parameter σ , which are automatically selected by the PMOR algorithm according to the error bound.

The output of the original model at the output port 7 changing with the parameter and the time, as well as the corresponding relative error of the ROM are shown in Figure 2. In Figure 2(b), the relative error is large at first because the thermal flux is still very close to zero, $O(10^{-14})$ (the circuit is hardly heated up) and the numerical error arising from the discretization of the original model results in numerical noise, which dominates the output of the original model when the true physical dynamics is small. As Figure 2(b) shows, the ROM approximates the thermal flux accurately after the thermal flux dominates the numerical error ($t > 2 \times 10^{-7}$). Therefore, the ROM not only approximates the true dynamics accurately, but also is robust to the numerical error present in the original model due to discretization. Simulating the ROM shows a speedup factor of 65.93 as compared with simulating the original model.

The ROM is again used in uncertainty quantification (UQ) of the ET problem. The means and stan-

Table 1. Convergence behavior of the pMOR method for the electrical and the thermal sub-systems, respectively ($\epsilon_{tol} = 10^{-4}$).

Electrical-subsystem		
Iteration	Selected sample σ	Error bound
1	10^7	7.165399×10^{-24}
Thermal-subsystem		
Iteration	Selected sample (σ, s)	Error bound
1	$(2.736 \times 10^7, 0)$	43.73
2	$(2.537 \times 10^7, 10^6)$	4.225×10^{-4}
3	$(1.694 \times 10^7, 2.632 \times 10^5)$	4.345×10^{-8}

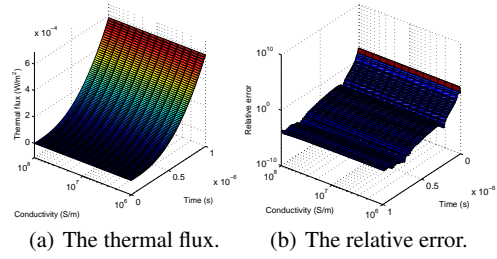


Fig. 2. The thermal flux and its relative error at the drain.

dard deviations of the thermal fluxes on the drain, on the source, as well as on the back contact are computed using both the original model and the ROM. The means computed by the ROM are accurate up to the 4-th digit, and the errors of the standard deviations are also acceptable, though the standard deviations are as small as (10^{-10}) . UQ analysis with stochastic collocation using the ROM has achieved a speedup factor of 20 as compared with that using the original model.

3 Conclusions

In this work, automatic parametric model order reduction for electro-thermal coupled problems is discussed. An a posteriori error bound is successfully applied to PMOR of a power-MOS device model. The efficiency of the ROM is demonstrated by the simulation results and the UQ analysis. With the guidance of the error bound, the ROM computed with the adaptive PMOR algorithm can be generated automatically and reliably.

References

1. P. Benner, S. Gugercin, and K. Willcox. A survey of model reduction methods for parametric systems. *SIAM Review*, 57(4):483-531, 2015.
2. P. Benner and L. Feng. A robust algorithm for parametric model order reduction based on implicit moment matching. In *Springer MS & A series, Vol. 8: Reduced Order Methods for modeling and computational reduction* (A. Quarteroni, G. Rozza, Eds), 159-185, 2014.
3. L. Feng, Y. Yue, N. Banagaaya, P. Meuris, W. Schoemaker, P. Benner. Parametric modeling and model order reduction for (electro-)thermal analysis of nanoelectronic structures. *Submitted to Journal of Mathematics in Industry*, 2016.
4. J. S. Hesthaven, G. Rozza and B. Stamm. Certified Reduced Basis Methods for Parametrized Partial Differential Equations. *Springer Briefs in Mathematics*, Springer, 2016.
5. L. Feng, A. C. Antoulas, and P. Benner. Some a posteriori error bounds for model order reduction of parametrized linear systems. *Preprint MPIMD/15-17, Max Planck Institute Magdeburg, Germany*, 2015.

Global sensitivity analysis for parameter variations in electric circuits

Roland Pulch

Institut für Mathematik und Informatik, Ernst-Moritz-Arndt-Universität Greifswald, Walther-Rathenau-Straße 47, 17489 Greifswald, Germany. roland.pulch@uni-greifswald.de

Summary. The mathematical modelling of electric circuits yields dynamical systems, which include physical parameters. The parameters often vary in some domain due to uncertainties. A global sensitivity analysis decomposes the variations in the output of a circuit and ranks the importance of parameters. We investigate numerical methods for the computation of sensitivity indices. Furthermore, we discuss the determination of sparse expansions into orthogonal basis functions depending on the parameters. Numerical simulations of circuit models are illustrated.

1 Problem Definition

We consider dynamical systems in form of ordinary differential equations (ODEs) or differential algebraic equations (DAEs), which include physical parameters $\mathbf{p} = (p_1, \dots, p_q) \in \Pi$. Without loss of generality, the system is assumed to be single-input-single-output. For the linear case, the dynamical system reads as

$$\begin{aligned} E(\mathbf{p})\dot{\mathbf{x}}(t, \mathbf{p}) &= A(\mathbf{p})\mathbf{x}(t, \mathbf{p}) + B(\mathbf{p})u(t) \\ y(t, \mathbf{p}) &= C(\mathbf{p})\mathbf{x}(t, \mathbf{p}) \end{aligned} \quad (1)$$

with state variables $\mathbf{x} : I \times \Pi \rightarrow \mathbb{R}^n$, an input $u : I \rightarrow \mathbb{R}$ and an output $y : I \times \Pi \rightarrow \mathbb{R}$ as quantity of interest in the time interval $I := [t_0, t_{\text{end}}]$. The mapping from inputs to outputs can be specified by a complex-valued transfer function $H : \mathbb{C} \times \Pi \rightarrow \mathbb{C}$ with

$$H(s, \mathbf{p}) = C(\mathbf{p})(sE(\mathbf{p}) - A(\mathbf{p}))^{-1}B(\mathbf{p}) \quad (2)$$

in the frequency domain. For the nonlinear case, the dynamical system becomes

$$\begin{aligned} M(\mathbf{p})\dot{\mathbf{x}}(t, \mathbf{p}) &= \mathbf{f}(\mathbf{x}(t, \mathbf{p}), \mathbf{p}) + B(\mathbf{p})u(t) \\ y(t, \mathbf{p}) &= C(\mathbf{p})\mathbf{x}(t, \mathbf{p}) \end{aligned} \quad (3)$$

with a nonlinear function \mathbf{f} . The input-output relation cannot be described by a kind of transfer function except for special cases.

Now the aim is to determine global sensitivity measures for the quantity of interest y with respect to the variations of the parameters $\mathbf{p} \in \Pi$. This sensitivity analysis is related to uncertainty quantification, where the exact position of the parameters is unknown within the domain Π . In a stochastic modelling, the parameters are replaced by independent random variables. We assume uniform probability distributions on Π , while generalisations to other probability laws are feasible.

2 Sensitivity analysis

There are both variance based measures and derivative based measures for a global sensitivity analysis, see [5]. In the variance based concept, first order indices and total effect indices can be defined by an ANOVA (analysis of variance) decomposition. We focus on the determination of total effect sensitivity indices. Let $g : \Pi \rightarrow \mathbb{R}$ be a nonlinear function depending on the parameters, for example, $g(\mathbf{p}) := y(t, \mathbf{p})$ for a fixed time $t \in I$ with the output of (1),(3) or $g(\mathbf{p}) := |H(s, \mathbf{p})|$, $g(\mathbf{p}) := \arg H(s, \mathbf{p})$ for a fixed frequency $s \in \mathbb{C}$ with the transfer function (2).

Assuming $\Pi = [0, 1]^q$, the total effect sensitivity indices can be formulated for $j = 1, \dots, q$ as

$$S_j^T = \frac{1}{2D} \int_{\Pi} \int_0^1 (g(\mathbf{p}) - g(\mathbf{p}'))^2 dp'_j d\mathbf{p} \quad (4)$$

with $\mathbf{p}' = (p_1, \dots, p_{j-1}, p'_j, p_{j+1}, \dots, p_q)$ and the total variance $D > 0$ of g . It follows that $0 \leq S_j^T \leq 1$ for each j and $S_1^T + \dots + S_q^T \geq 1$.

In the linear case (1), the sensitivity analysis is applied to the transfer function (2) on the imaginary axis, which allows for conclusions on the quantity of interest y in the time domain for arbitrary input u , see [3]. In the nonlinear case (3), the sensitivity computations require the consideration of the quantity of interest y for each input u separately in the time domain. Moreover, we examine and compare numerical methods for the computation of the sensitivity indices (4).

3 Orthogonal expansions

The quantity of interest from (1) or (3) can be expanded into a series

$$y(t, \mathbf{p}) = \sum_{i=1}^{\infty} w_i(t) \Phi_i(\mathbf{p}) \quad \text{for each } t \in I \quad (5)$$

with a complete system of basis functions $(\Phi_i)_{i \in \mathbb{N}}$, $\Phi_i : \Pi \rightarrow \mathbb{R}$. The basis functions are assumed to be orthogonal with respect to the inner product on the Hilbert space $L^2(\Pi)$. In the standard case $\Pi = [0, 1]^q$, the multivariate Legendre polynomials are typically applied according to the concept of the (generalised)

polynomial chaos, see [7]. The coefficient functions $w_i : I \rightarrow \mathbb{R}$ are unknown a priori. Likewise, orthogonal expansions of the transfer function (2) exist in the frequency domain. Truncated orthogonal expansions of the type (5) can be used to compute approximations of the sensitivity indices (4), cf. [6].

If the number q of parameters is large, then a huge number of basis polynomials appears in a truncation of the expansion (5). Thus we address the determination of a sparse representation

$$\tilde{y}(t, \mathbf{p}) = \sum_{i=1}^s \tilde{w}_i(t) \Psi_i(\mathbf{p}) \quad \text{for each } t \in I \quad (6)$$

with a low number s for an alternative orthogonal basis $\{\Psi_1, \dots, \Psi_s\}$. Yet the difference between (5) and (6) should be small in the norm of $L^2(I)$ for all times. There are several approaches for this task like least angle regression, compressed sensing and ℓ^1 -minimization, see [2]. In [4], a model order reduction (MOR) of the linear dynamical system (1) is applied to construct an alternative basis for (6), where the transfer function (2) yields error estimates. Now we investigate also nonlinear dynamical systems (1) and an associated MOR for the determination of a sparse representation (6).

4 Illustrative Example

We apply a mathematical model from [1] for the electric circuit of a Miller integrator shown in Fig. 1. An input voltage is supplied and an output voltage drops at a specific node. Modified nodal analysis yields a linear system (1) of DAEs with nilpotency index two. Nevertheless, the system is stable as well as strictly proper. Four parameters appear in the system: two capacitances, a conductance and an amplification factor. We arrange independent uniform distributions for each parameter, which vary 10% around the means.

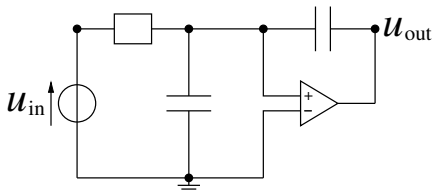


Fig. 1. Electric circuit of a Miller integrator.

Now the transfer function (2) of the linear dynamical system (1) is analysed. The total effect sensitivity indices (4) are computed approximately by a truncated polynomial chaos expansion (5). Figure 2 illustrates the sensitivity coefficients for the magnitude and the phase of the transfer function in a broad frequency window. We recognise that the amplification factor represents the most important parameter.

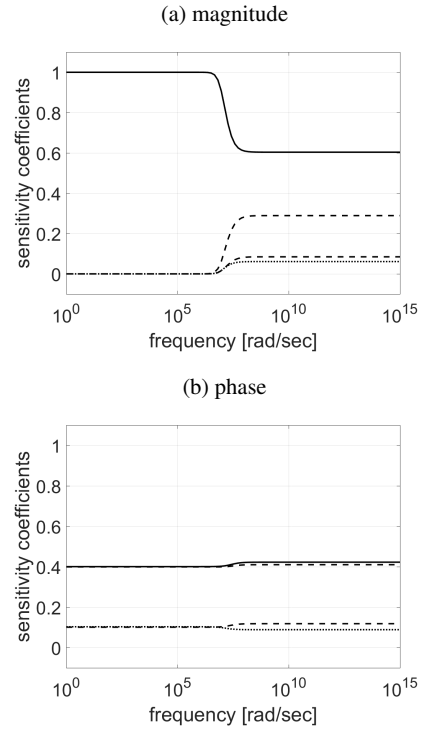


Fig. 2. Sensitivity indices for magnitude (a) and phase (b) of the transfer function with respect to amplification factor (solid line), two capacitances (dashed lines) and conductance (dotted line).

References

1. M. Günther, U. Feldmann, and J. ter Maten. Modelling and discretization of circuit problems. In P.G. Ciarlet, editor, *Handbook of Numerical Analysis*. Vol. 13, pp. 523–659, Elsevier, 2005.
2. J.D. Jakeman, M.S. Eldred, and K. Sargsyan. Enhancing ℓ^1 -minimization estimates of polynomial chaos expansions using basis selection. *J. Comput. Phys.*, 289:18–34, 2015.
3. R. Pulch, J. ter Maten, and F. Augustin. Sensitivity analysis and model order reduction for random linear dynamical systems. *Math. Comput. Simulat.*, 111:80–95, 2015.
4. R. Pulch. Model order reduction and sparse orthogonal expansions for random linear dynamical systems. arXiv:1605.06979v1, May 23, 2016.
5. I.M. Sobol and S. Kucherenko. Derivative based global sensitivity measures and their link with global sensitivity indices. *Math. Comput. Simulat.*, 79:3009–3017, 2009.
6. B. Sudret. Global sensitivity analysis using polynomial chaos expansions. *Rel. Eng. Syst. Saf.*, 93:964–979, 2008.
7. D. Xiu. *Numerical Methods for Stochastic Computations: A Spectral Method Approach*. Princeton University Press, 2010.

Numerical Modeling of Organic Electronic and Photovoltaic Devices

Carlo de Falco¹

MOX Modeling and Scientific Computing, Dipartimento di Matematica, Politecnico di Milano, Piazza L. da Vinci 32, 20133, Milano, Italy carlo.defalco@polimi.it

Summary. The relatively recent discovery of semiconducting properties of a class of organic materials represented a breakthrough opening the way to a plethora of highly innovative products. Organic semiconductors can be exploited in the production of electronic devices because of their many advantages, such as easy and low cost fabrication, high transparency, mechanical flexibility, biocompatibility. While light emitting devices such as Organic Light Emitting Diodes (OLED) are already on the market, other devices (such transistors, organic solar cells and photodetectors) are still subject of intensive research and accurate numerical simulation tools can be a key enabling tool for new developments in this direction. In this communication we give an account of ongoing research in macro- and meso-scale numerical modeling of electronic devices based on Organic Semiconductor materials being carried out in collaboration between the departments of Mathematics and Electronics of Politecnico di Milano and the Center for Nano Science and Technology of the Istituto Italiano di Tecnologia. In doing so we highlight both similarities and remarkable differences of the models being studied with the case of more conventional semiconductor materials.

1 Macro- and Meso-scale Numerical Models for Organic Semiconductors

The discovery of semiconducting properties of a class of organic materials represented a breakthrough opening the way to a plethora of highly innovative products. Organic semiconductors can be exploited in the production of electronic devices because of their many advantages, such as easy and low cost fabrication, high transparency, mechanical flexibility, biocompatibility. While light emitting devices[2] such as Organic Light Emitting Diodes (OLED) are already on the market, other devices (such transistors, organic solar cells and photodetectors) are still subject of intensive research and accurate numerical simulation tools can be a key enabling tool for new developments in this direction.

Development of such numerical tools has been in recent years a topic of an intense dedicated research carried out in collaboration between the departments of Mathematics and Electronics of Politecnico di Milano and the Center for Center for Nano Science and Technology of the Istituto Italiano di Tecnologia which has spawned a number of scientific publications [1–7] as well as Bachelor’s, Master’s and Ph.D. theses [8–12]. In this communication we

present a review of such research effort highlighting both similarities and specific differences in the modeling of Organic Semiconductors with respect to more conventional semiconductor materials.

Physical phenomena governing charge transport in organic materials are inherently different from those occurring in inorganic semiconductors. While the latter have a relatively ordered crystalline structure within which carriers move approximately as free particles, in the former charge transport occurs via a sequence of thermally activated hops between strongly localized sites.

Due to such differences in physical origin of charge transport phenomena between organic and inorganic semiconductors, particle based simulators adopting Monte Carlo approaches are very different in the two cases. On the other hand, the continuum mathematical models which we focus on, are usually based in both cases on the so called Drift–Diffusion (DD) equations; there the peculiarities of the new materials are represented mainly through appropriate constitutive relations for the equation coefficients.

Complex models are available for the mobility coefficients, which represent the ability of the carriers to move in response to an electric field and play a leading role in the continuity equations, together with the net recombination/generation rates due to processes that exchange carriers between the Highest Occupied Molecular Orbital (HOMO) and the Lowest Unoccupied Molecular Orbital (LUMO), often mediated by so-called intermediate charge transfer states whose lifetime and dynamics can be crucial in determining the transient behaviour of (opto-)electronic devices.

In this presentation we will discuss the, on the one hand, the sensitivity of (opto-)electronic device simulation results on the mobility and generation/recombination model parameters and, on the other hand, techniques based on a combination of experiments and numerical simulations for the accurate estimation of such model parameters.

2 Acknowledgment

Topics presented in this communication are subject of past and ongoing research being carried out by the author in very close collaboration with many other researchers. We would like in particular to acknowledge

contributions by Prof. R.Sacco and Prof. M.Verri of the Department of Mathematics of Politecnico di Milano, by Prof. D.A. Natali of the Department of Electronics and Bio-Engineering of Politecnico di Milano, by Dr. M. Caironi and Prof. G. Lanzani of the Center for Nano Science and Technology (CNST) of the Istituto Italiano di Tecnologia (IITPolimi), by Dr. F. Maddalena and Dr. M. Porro both formerly at CNST and by P.C. Africa of MOX.

References

1. P. C. Africa, F. Maddalena, C. de Falco, M. Caironi, and D. Natali. Simultaneous Extraction of Density of States Width and Injection Barriers in Organic Semiconductors *Submitted*, 2016.
2. C. de Falco, R. Sacco, and M. Verri. Analytical and numerical study of photocurrent transients in organic polymer solar cells. *Computer Methods in Applied Mechanics and Engineering*, 199(25):1722–1732, 2010.
3. C. de Falco, M. Porro, R. Sacco, and M. Verri. Multiscale modeling and simulation of organic solar cells. *Computer Methods in Applied Mechanics and Engineering*, 245:102–116, 2012.
4. F. Maddalena, C. de Falco, M. Caironi, and D. Natali. Assessing the width of Gaussian density of states in organic semiconductors. *Organic Electronics*, 17, 304–318, 2015.
5. M. Porro, C. de Falco, M. Verri, G. Lanzani, and R. Sacco. Multiscale simulation of organic heterojunction light harvesting devices. *COMPEL: The International Journal for Computation and Mathematics in Electrical and Electronic Engineering*, 33(4):1107–1122, 2014.
6. C. de Falco, A. Iacchetti, M. Binda, D. Natali, R. Sacco, and M. Verri. Modeling and simulation of organic solar cells. In *Scientific Computing in Electrical Engineering SCEE 2010*, pages 329–337. Springer Berlin Heidelberg, 2012.
7. M. J. Sung, A. Luzio, W. T. Park, R. Kim, E. Gann, F. Maddalena, G. Pace, Y. Xu, D. Natali, C. de Falco, et al. High-mobility naphthalene diimide and selenophene-vinylene-selenophene-based conjugated polymer: n-channel organic field-effect transistors and structure–property relationship. *Advanced Functional Materials*, 2016.
8. M.M. Cogliati, and M. Porro. Third generation solar cells: Modeling and simulation, 2010. Master Thesis, Politecnico di Milano.
9. M. Favino. Mathematical modeling and numerical simulation of third generation solar cells. Master’s thesis, Politecnico di Milano, 2008–2009.
10. G. Abbati. Trasporto di Carica nei Semiconduttori Organici Amorfi Bachelor’s thesis, Politecnico di Milano, 2012–2013.
11. F. Destefano. Stima di parametri per modelli numerici di fotorivelatori organici Bachelor’s thesis, Politecnico di Milano, 2010–2011.
12. P. C. Africa. Numerical Modeling of Organic Thin Film Transistors Master’s thesis, Politecnico di Milano, 2014–2015.

Challenges and Opportunities: Modeling and Simulation for the Emerging High-Speed Multi-Function Designs

Ram Achar

Department of Electronics, Carleton University, Ottawa, Ontario, Canada achar@doe.carleton.ca

Summary. The recent trend towards high-speed and multi-function designs has presented numerous challenges and opportunities for EDA tools focused on circuit simulation and modeling. This paper will focus on these challenges and opportunities with emphasis on signal/power integrity and also on exploiting the emerging multicore computational platforms.

1 Introduction

The massive user demand for higher bandwidth and advanced communication as well as better information management are necessitating newer generations of multi-function electronic circuits and systems that operate with lower-power and sharper excitations. However, with the rapid increase in operating frequencies and the desire for low-power designs, signal/power integrity in VLSI packages, interconnects and ground/power planes becomes a critical factor in determining the overall system performance.

At higher frequencies, electromagnetic interaction on interconnects can lead to severe signal degradation (such as crosstalk, delay and distortion). In such a scenario, distributed models (such as quasi-TEM models based on lossy, multiconductor transmission line (MTL) equations) become necessary. Also, to model current distribution related effects (such as skin, proximity and edge effects), frequency-dependent RLCG parameters become important. In addition, the desire for nanoscale designs is causing significantly reduced noise margins due to the variability issues [1]-[4]. Consequently, managing the intricate nature of modeling and simulation of modern high-frequency and low-power design environments presents the following challenges:

- a) Mixed frequency/time analysis presents significant difficulty for traditional time-domain based simulators due to the frequency-dependent nature of high-speed models.
- b) CPU efficiency during simulation suffers due to the large sizes of interconnect circuits.

However, these high-frequency issues are not handled adequately by the current simulators [1]-[4].

In order to handle these issues, robust interconnect modeling approaches, such as Matrix Rational Approximation (MRA) [5], Delay Extraction based Passive Compact Macromodeling (DEPACT) [6], Waveform Relaxation and Transverse Partitioning (WR-TP) [7] have been proposed.

Also in recent years, model-order reduction (MOR) algorithms have been developed to address the difficulties with interconnect analysis [8], [9]. In addition, approaches based on macromodeling of the tabulated data (such as scattering parameters) have been developed to include high-speed modules as black-box entities in a simulation environment [10]. These methods primarily involved using the vector fitting approach [11] to fit the given data and subsequently applying passivity verification and correction algorithms (based on first order perturbation methods) on the synthesized macromodel [12], [13].

In addition, the traditional analog circuit simulation algorithms are based on time stepping methods and are limited to second order integration formula, in order not to violate the conditions for stability. Recently, high-order integration methods with guaranteed stability for fast circuit simulation were proposed [14], which removed the instability issues when orders above 2 are taken. Further efficiency improvements through their structural characterization and customization to the case of high-speed interconnects were introduced in [15], [16].

Also, with the emergence of affordable computers with large number of cores, if exploited properly, parallel processing can significantly reduce the solution time of VLSI systems by simultaneously solving partitioned blocks on different processors and combining the results at the intermediate/final stages. The major challenges here are to construct efficient partitions, minimizing communication between cores and merging the results. Parallel circuit simulation was traditionally approached via domain decomposition (DD) [17], however, its performance doesn't scale well with the increasing number of processors. Recently, efficient simulation

methodologies such as, Parallel Circuit Simulation Algorithm via Binary Link Formulations (PvB) [18], [19] have been developed.

In this presentation, while outlining the emerging high-speed design issues and the recent developments in the field of modeling and simulation of high-speed interconnects, the challenges and opportunities for the next generation tools and methodologies with emphasis on signal and power integrity will also be described. Particular attention will be paid on macromodel properties, such as causality and passivity. Also, challenges for exploiting the parallel platforms will be discussed.

References

- [1] R. Achar and M. Nakhla, "Simulation of High-Speed Interconnects", *Proceedings of The IEEE*, Vol. 89, pp. 693-728, May 2001.
- [2] E. Bogatin, *Signal Integrity Simplified*, NJ: Prentice-Hall, 2004.
- [3] M. Swaminathan and A. E. Engin, *Power Integrity Modeling and Design for Semiconductors and Systems*, NJ: Prentice-Hall, 2007.
- [4] R. Achar "High-Speed Interconnect Modeling", *IEEE Microwave Magazine*, pp. 61-74, Aug. 2011.
- [5] A. Dounavis, R. Achar and M. Nakhla, "A General Class of Passive Macromodels for Lossy Multiconductor Transmission Lines", *IEEE Transactions on Microwave Theory and Techniques*, Vol. 49, pp. 1686 -1696, October. 2001.
- [6] N. Nakhla, M. Nakhla, and R. Achar, "Simplified Delay-Extraction Based Passive Transmission Line Macromodeling Algorithm," *IEEE Transactions on Advp*, pp. 498-509, May 2010.
- [7] N. Nakhla, A. Ruehli, M. Nakhla, R. Achar and C. Chen, "Waveform Relaxation Techniques for Simulation of Coupled Interconnects with Frequency-Dependent Parameters", *IEEE Transactions on Advanced Packaging*, pp. 257-269, May 2007.
- [8] W. H. A. Schilders, H. A. van der Vorstand, and J. Rommes, Eds. Berlin, Model Order Reduction: Theory, *Research Aspects and Applications*, Germany: Springer, 2008.
- [9] B. Nouri, M. Nakhla, and R. Achar, "Optimum Order Estimation for Reduced Macromodels based on a Geometrical Approach to Model Order Reduction," *IEEE Transactions on Components, Packaging and Manufacturing Technology*, pp. 1218-1227, July 2013.
- [10] S. G. Talocia and B. Gustavsen, *Passive Macromodeling: Theory and Applications*, NJ: Wiley, 2015.
- [11] B. Gustavsen and A. Semlyen, "Rational Approximation of Frequency Domain Responses By Vector Fitting", *IEEE Transactions on Power Delivery*, pp. 1052-1061, July 1999.
- [12] D. Saraswat, R. Achar and M. Nakhla, "GloPassivity Enforcement Algorithm for Macromodels of Interconnects Characterized by Tabulated Data, *IEEE Trans. on VLSI*, pp. 819-832, July 2005.
- [13] A. Chinae and S. Grivet-Talocia, "Perturbation Schemes for Passivity Enforcement of Delay-Based Transmission Line Macromodels", *IEEE Transactions on Advanced Packaging*, pp. 568-578, August, 2008.
- [14] E. Gad, M. Nakhla, R. Achar and Y. Zhou, "A-Stable and L-Stable High-Order Integration Methods for Stiff Differential Equations", *IEEE Trans. on Computer Aided Design*, pp. 1359-1372, Sept. 2009.
- [15] E. Gad, M. Nakhla, R. Achar and Y. Zhou, "Structural Characterization and Efficient Implementation Techniques for A-stable High-Order Integration Methods", *IEEE Trans. on Computer Aided Design*, pp.101-108, Jan. 2012.
- [16] M. Farhan, E. Gad, M. Nakhla and R. Achar, "New Method for Fast Transient Simulation of Large Linear Circuits using High-Order Stable Methods", *IEEE Transactions Components, Packaging and Manufacturing Technology*, pp. 661-669, Apr. 2013.
- [17] N. Frohlich, B. M. Riess, U. A. Wever, and Q. Zheng, "A new approach for parallel simulation of VLSI circuits on a transistor level," *IEEE Trans. Circuits Syst. I, Fundament. Theory Appl.*, vol. 45, no. 6, pp. 601-613, Jun. 1998.
- [18] D. Paul, N. Nakhla, R. Achar and M. Nakhla "Parallel Simulation of Massively Coupled Interconnect Networks", *IEEE Transactions on Advanced Packaging*, pp. 115-127, Feb. 2010.
- [19] D. Paul, M. Nakhla, R. Achar and N. Nakhla, "Parallel Circuit Simulation via Binary Link Formulations (PvB)", *IEEE Transactions on Components, Packaging and Manufacturing Technology*, pp. 768- 782, May 2013.

Gradient-Enhanced Polynomial Chaos Methods for Circuit Simulation

Eric R. Keiter¹, Laura P. Swiler², and Ian Z. Wilcox³

¹ Electrical Models and Simulation, Sandia National Laboratories, MS 1177, Albuquerque, NM, 87185 USA
erkeite@sandia.gov,

² Optimization and Uncertainty Quantification, Sandia National Laboratories, MS 1318, Albuquerque, NM, 87185 USA
lpswiler@sandia.gov,

³ Component and Systems Analysis, Sandia National Laboratories, MS 1177, Albuquerque, NM, 87185 USA
iwilcox@sandia.gov

Summary. Uncertainty Quantification (UQ) is an important topic in electronic design automation (EDA), as parametric uncertainties are a significant integrated circuit design concern. Sampling methods such as Latin Hypercube Sampling (LHS) are popular but expensive. Polynomial Chaos Expansion (PCE) methods are often proposed as an efficient sampling alternative. One PCE variation, regression-based PCE, is convenient because it doesn't require specific quadrature points. However, this comes at the cost of accuracy. In this paper we explore the idea of enhancing regression-based PCE methods with gradient information, provided by a transient direct sensitivity algorithm in the circuit simulator.

1 Introduction

Sensitivity analysis and uncertainty quantification (UQ) are important capabilities for circuit simulation. Sensitivity analysis allows one to determine the most important parameters governing the response of interest, and UQ allows one to understand the probability distribution of the response, given the input probability distributions. In this work, we describe transient direct sensitivity for circuit simulation, and explore the use of these sensitivities in PCE. The implementations of the approaches are in two open-source software frameworks: Xyce [2], a parallel circuit simulator developed at Sandia National Laboratories; and Dakota [1], an optimization and UQ toolkit also developed at Sandia. The approaches presented here are general, but the specific implementations we use to demonstrate these approaches are in Xyce and Dakota.

2 Transient Direct Sensitivities

Many UQ techniques can be enhanced if the application code is able to produce parameteretric sensitivities, with respect to an output of interest. For example:

$$\frac{dO}{dp} = \frac{\partial O}{\partial x} \left(\frac{\partial F}{\partial x} \right)^{-1} \frac{\partial F}{\partial p} + \frac{\partial O}{\partial p} \quad (1)$$

Where O is the scalar objective function, p is a scalar parameter, F is the residual equation vector and x

is the solution vector. dF/dx is the Jacobian matrix. Transient direct sensitivities can be derived starting with the differential algebraic equation (DAE) form, in which the residual F is given by:

$$F = \dot{q}(x) + j(x) - b(t) = 0 \quad (2)$$

In circuit simulation, the q vector contains quantities such as capacitor charge, the j vector contains mostly Ohmic currents and the b vector represents independent sources. To obtain the direct sensitivity equation, equation 2 is differentiated with respect to a parameter, p , and then re-arranged to give a linear system to be solved at each time step after equation 2 has been solved. For Backward Euler integration the sensitivity equation is given by:

$$J \frac{\partial x}{\partial p_n} = -FD + CR \quad (3)$$

Where J is the original Jacobian given by:

$$J = \left[\frac{1}{h} \frac{\partial q}{\partial x} + \frac{\partial j}{\partial x} \right] \quad (4)$$

FD is the ‘‘function derivative’’, given by:

$$FD = \frac{1}{h} \left[\frac{\partial q}{\partial p_n} - \frac{\partial q}{\partial p_{n-1}} \right] + \frac{\partial j}{\partial p} - \frac{\partial b}{\partial p} \quad (5)$$

The vectors j , q and b are the device model contributions, h is the step size, and n is the step index. The remaining term, CR , is referred to as the chain-rule term, given by:

$$CR = \frac{1}{h} \left[\frac{\partial q}{\partial x} \right] \frac{\partial x}{\partial p_{n-1}} \quad (6)$$

3 Polynomial Chaos Expansion Methods

Stochastic expansion UQ methods approximate the functional dependence of the simulation response on uncertain model parameters by expansion in a polynomial basis. A polynomial chaos expansion (PCE) is based on a multidimensional orthogonal polynomial approximation. The output response is modeled

as a function of the input random variables using a carefully chosen set of polynomials. Dakota implements the generalized PCE approach using the Wiener-Askey scheme [3]. To apply PCE, Dakota performs the following steps: (1) input uncertainties are transformed to a set of uncorrelated random variables, (2) a basis such as Hermite polynomials is selected, and (3) the parameters of the functional approximation are determined. The general polynomial chaos expansion for a response g has the form

$$g(x) \approx \sum_{j=0}^P \alpha_j \Psi_j(x) \quad (7)$$

where each multivariate basis polynomial $\Psi_j(x)$ involves products of univariate polynomials that are tailored to the individual random variables. Regression-based PCE involves the solution of the linear system:

$$\Psi \alpha = R \quad (8)$$

for a set of PCE coefficients α that best reproduce a set of response values R . Additional regression equations can be obtained through the use of derivative information from each collocation point:

$$\frac{dg(x)}{dx} = \sum_{j=0}^P \alpha_j \frac{d\Psi_j(x)}{dx} \quad (9)$$

Various methods can be employed to solve (8). Traditionally, the most frequently used method has been least squares regression, but compressed sensing methods have been used when Ψ is under-determined.

4 Results

In this section, we demonstrate gradient-enhanced PCE methods for a CMOS inverter chain given in figure 1. The PMOS and NMOS oxide thicknesses are the uncertain parameters, modeled as normal uncertainties centered around a nominal value with a standard deviation equal to 10% of nominal. A generalized Elmore

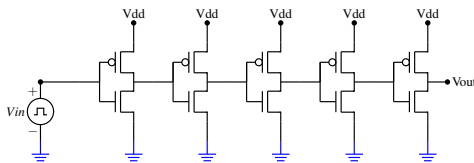


Fig. 1. CMOS inverter chain circuit with five inverters.

delay was used as the objective function, given by:

$$O = \text{Elmore Delay} = \frac{\int_0^T g'_A(t) \cdot t \cdot dt}{\int_0^T g'_A(t) dt} \quad (10)$$

and represents the approximate time for the signal rise or fall. Note that $g_A(t) = V_{out}$.

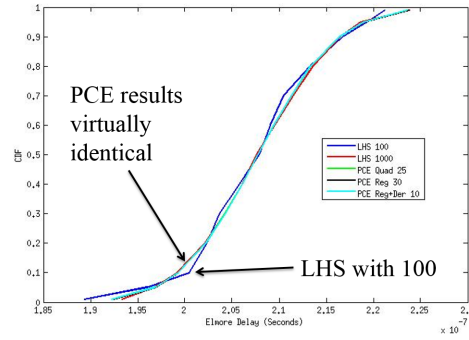


Fig. 2. Cumulative Distribution Function of Elmore Delay using Various UQ Approaches

We performed UQ on the inverter chain with several methods, including LHS with 100 and 1000 samples, PCE with full tensor product quadrature of order 5, and two types of regression-based PCE. The regression-based PCE only used 10 samples. The use of sensitivities in UQ is highlighted in figure 2. Computed cumulative distribution functions (CDFs), giving the probability that the Elmore delay is less than a particular value, are almost the same for an 1000-sample LHS and all the PCE methods, suggesting that a PCE using sensitivities for only 10 samples is comparably accurate to LHS.

Acknowledgement. This work was sponsored by the Laboratory Directed Research and Development (LDRD) Program at Sandia National Laboratories. Sandia National Laboratories is a multi-program laboratory managed and operated by Sandia Corporation, a wholly owned subsidiary of Lockheed Martin Corporation, for the U.S. Department of Energy's National Nuclear Security Administration under contract DE-AC04-94AL85000.

References

1. B. M. Adams, L. E. Bauman, W. J. Bohnhoff, K. R. Dalbey, J. P. Eddy, M. S. Ebeida, M. S. Eldred, P. D. Hough, K. T. Hu, J. D. Jakeman, L. P. Swiler, Stephens J. A., D. M. Vigil, and T. M. Wildey. Dakota, a multilevel parallel object-oriented framework for design optimization, parameter estimation, uncertainty quantification, and sensitivity analysis: Version 6.0 users manual. Technical Report SAND2014-4633, Sandia National Laboratories, Albuquerque, NM, Updated May 2014. Available online from <http://dakota.sandia.gov/documentation.html>.
2. Eric R. Keiter, Ting Mei, Thomas V. Russo, Richard L. Schiek, Peter E. Sholander, Heidi K. Thornquist, Jason C. Verley, and David G. Baur. Xyce Parallel Electronic Simulator: User's Guide, Version 6.4. Technical Report SAND2015-10527, Sandia National Laboratories, Albuquerque, NM, December 2015.
3. D. Xiu and G. M. Karniadakis. The wiener-askey polynomial chaos for stochastic differential equations. *SIAM J. Sci. Comput.*, 24(2):619–644, 2002.

Coupled Multirate Simulation by the MPDE technique for Radio Frequency Circuits

Hans Georg Brachtendorf and Kai Bittner

Embedded Systems Group brachtd@fh-hagenberg.at, Kai.Bittner@fh-hagenberg.at

University of Applied Sciences of Upper Austria, Hagenberg, 4232, Austria

Invited Paper

Summary. In Radio Frequency (RF) circuits one observes on the one hand slowly varying baseband signals and on the other modulated or bandpass signals. The spectra of bandpass signals are centered around a carrier frequency, typically in the GHz range. The baseband are the envelopes of bandpass signals.

Communication engineers are mainly interested in distortions of the baseband signals during transmission. Therefore the method of the Equivalent Complex Baseband (ECB) was developed, which splits the envelope from the carrier waveform. This method circumvents the bottleneck caused by the sampling theorem, what speeds up the run-time significantly.

This technique is however not applicable for nonlinear circuits. Circuits are described by the Modified Nodal Analysis (MNA) and device constitutive equations, resulting in often huge systems of generally nonlinear ordinary differential algebraic equations (DAEs). Standard DAE solvers employing Backward Differentiation Formulas (BDF) are prohibitively slow since the time-steps for numerical integration must be much smaller than the reciprocal of the highest relevant frequency. The Multirate PDE (MPDE) reformulates the system of ordinary DAEs as a system of partial differential equations (PDEs) with mixed boundary/initial value conditions. The baseband and bandpass signals have then appropriate time-steps, circumventing the restriction of the sampling theorem. The solution of the ordinary DAE is obtained along a characteristic curve of the PDE.

The boundary/initial value problem can be solved by standard techniques such as the well known Harmonic Balance (HB) method based on trigonometric basis functions, multistep integration formulas (e.g. BDF methods) etc. On the one hand, trigonometric basis functions are not compact and do not permit local refinements. BDF methods exhibit, on the other hand, a numerical consumption of energy, leading to erroneous results, e.g., for oscillator circuits. In recent research projects spline/wavelet methods with adaptive grids have been developed as an alternative. Due to their compactness B-splines lead to highly sparse systems, making the solution run-time efficient. Moreover Gibb's phenomenon is avoided. Trigonometric B-splines moreover avoid the numerical damping.

In RF circuitry the lumped model assumption is often not valid anymore. Moreover critical devices are to be optimized w.r.t. geometry and even - in the case of semiconductors - doping profile. Therefore, in a current research project

the in-house circuit simulator is coupled with a commercial EM field/device simulator. Critical RF devices are simulated in full 3D, whereas for the remaining circuit lumped device models are employed.

Acknowledgement. This work has been partly supported by the fp7 research project nanoCOPS under grant 619166 and the Austrian FWF under grant P22549.

Part III

Abstracts of Invited Talks Industrial Day

Broadband Solution Methods for Maxwell's Equations in Laplace Domain

M. Eller^{1,2}, S. Reitzinger¹, S. Schöps², and S. Zaglmayr¹

¹ CST AG, Bad Nauheimerstr. 19, 64289 Darmstadt, Germany

{Martin.Eller, Stefan.Reitzinger, Sabine.Zaglmayr}@cst.com,

² Technische Universität Darmstadt, Institut für Theorie Electromagnetischer Felder and Graduate School CE, Dolivostr. 15, 64293 Darmstadt, Germany schoeps@gsc.tu-darmstadt.de

Summary. The robust, efficient and accurate solution of Maxwell's equations in Laplace domain is of great interest for industrial applications. First of all a robust formulation is proposed which is mandatory for an efficient numerical treatment of Maxwell's equations, in the context of variational formulation and finite element discretization. We will discuss the driven- and nonlinear eigenvalue-problem and give appropriate error estimates for the quantities of interest.

1 Problem Formulation

In the following Maxwell's equations in Laplace domain (with Laplace variable $s \in \mathbb{C}$) are considered in a sufficiently smooth and bounded domain $\Omega \subset \mathbb{R}^3$, i.e.,

$$\begin{aligned} s\mu(s)\mathbf{H} + \nabla \times \mathbf{E} &= 0 \\ s\varepsilon(s)\mathbf{E} - \nabla \times \mathbf{H} &= \mathbf{J}_e - \sigma\mathbf{E} \\ \operatorname{div} \varepsilon(s)\mathbf{E} &= \rho \\ \operatorname{div} \mu(s)\mathbf{H} &= 0 \end{aligned}$$

and suitable boundary conditions on $\partial\Omega$. \mathbf{E} , \mathbf{H} are the electric and magnetic fields, respectively. \mathbf{J}_e the impressed current, ρ the impressed charge density. The permeability $\mu(s)$, the permittivity $\varepsilon(s)$ and the conductivity σ are assumed to be scalar valued functions.

The above system of equations can be reduced to the so called **E-field** formulation, where we additionally assume $\mathbf{J}_e = 0$ and $\rho = 0$ for simplicity. By applying the variational formulation in $H_0(\operatorname{curl}, \Omega)$ and appropriate finite elements (see e.g. [1]) the system can be written as

$$T(s)E(s) = 2sF(s) \quad (1)$$

with

$$T(s) = \sum_k \alpha_k(s)T_k + sB(s)B(s)^T \quad (2)$$

$$B(s) = \sum_k \beta_k(s)B_k = F(s). \quad (3)$$

The material functions are represented by $\alpha_k(s) : \mathbb{C} \rightarrow \mathbb{C}$, e.g., $1/\mu(s)$, $T_k \in \mathbb{R}^{N \times N}$ the system matrices from

the finite element discretization, $B_k \in \mathbb{R}^{N \times p}$ the system matrices for given tangential boundary fields (for details see e.g. [2]). In order to setup the source on waveguide ports a generalized eigenvalue problem has to be solved in Laplace domain a priori (see e.g. [3]).

1.1 Stable Formulation

It is known that the **E**-based formulation is not stable as $s \rightarrow 0$, i.e., the condition number of the discretized systems tends to infinity and consequently it is not solveable in a robust way. Therefore the formulation has to be reexpressed since many applications require a broadband solution including $s = 0$. In [4] a low frequency stable formulation was presented which relies on the splitting of $H_0(\operatorname{curl}, \Omega)$, i.e.,

$$H_0(\operatorname{curl}) = U \oplus V \oplus W$$

with, e.g.,

$$\begin{aligned} Y &= \{\mathbf{w} \in H_0(\operatorname{curl}) : \nabla \times \mathbf{w} = 0\} \\ U &= \{\mathbf{u} \in Y : u = 0 \text{ in } \Omega_c\} \\ V &= \{\mathbf{v} \in H_0(\operatorname{curl}) : \langle \mathbf{v}, \mathbf{y} \rangle = 0 \forall \mathbf{y} \in Y\} \\ W &= \{\mathbf{w} \in Y : \langle \mathbf{w}, \mathbf{u} \rangle = 0 \forall \mathbf{u} \in U\} \end{aligned}$$

where U, V, W are closed subspaces, $\Omega_c \subset \Omega$ with $\sigma > 0$, and $Y = \nabla H_0^1(\Omega)$ can be considered. With these prerequisites the electric field is splitted into

$$\mathbf{E} = s\mathbf{E}_V + s^{1/2}\mathbf{E}_W + \mathbf{E}_U$$

which is equivalent to the standard **E**-field formulation, but has bounded condition number for $s \rightarrow 0$ on the discretized system. It is worth noting that

$$\mathbf{H} = -\frac{1}{s\mu(s)}\nabla \times \mathbf{E} = -\frac{1}{\mu(s)}\nabla \times \mathbf{E}_V$$

is evaluated in a robust way if $|\mu(s)| > 0$ for $s \in \mathbb{C}$.

2 Driven Problem

For the driven problem it suffices to consider $s = j\omega$, with $\omega \in [0, \omega_{\max}]$ the angular frequency and

$\omega_{\max} < \infty$. Therefore it is important to use a robust, efficient and accurate broadband solution process, which is achieved by a reduced order model (ROM) method, see e.g., [5]. A ROM method can be applied since (2) and (3) have an affine splitting, which facilitate efficiency for a ROM method. Assume $m \geq 1$ solution snapshots for different ω are performed and collected in the matrix $V \in \mathbb{C}^{N \times pm}$ with $V^H V = I$, then the reduced system reads as

$$\tilde{T}(s)\tilde{E}(s) = 2s\tilde{F}(s) \quad (4)$$

with

$$\begin{aligned} \tilde{T}(s) &= \sum_k \alpha_k(s) V^T T_k V + s\tilde{B}(s)\tilde{B}(s)^T \\ \tilde{B}(s) &= \sum_k \beta_k(s) V^T B_k = \tilde{F}(s) \\ \hat{E}(s) &= V\tilde{E}(s) \end{aligned}$$

Consequently $\hat{E}(s)$ can be evaluated very efficiently on the reduced system (4). An error estimation for $\hat{E}(s)$ is given by

$$\|E(s) - \hat{E}(s)\| \leq \frac{1}{\gamma(s)} \|R(s)\|_*$$

with $\gamma(s)$ the inf-sup constant of $T(s)$, $\|\cdot\|_*$ the dual norm and residual

$$R(s) = F(s) - T(s)\hat{E}(s),$$

see e.g., [6]. A typical quantity of interest is the S-parameter which is defined via

$$S(s) = B(s)^T E(s) - I.$$

The approximated S-parameter $\tilde{S}(s)$ is calculated accordingly with $\hat{E}(s)$. Thus error estimations can be written down with the help of the adjoint problem resulting in

$$\|S(s) - \tilde{S}(s)\| \leq \frac{1}{\gamma(s)} \|R(s)\|_*^2.$$

3 Nonlinear Eigenvalue Problem

If the source of (1) is zero, i.e., $F(s) = 0$, a nonlinear eigenvalue problem is defined. For further discussion we assume $T(s) : \Phi \subset \mathbb{C} \rightarrow \mathbb{C}^{N \times N}$ a holomorphic matrix valued function, which put some additional restrictions on the material functions and $\lambda \in \Phi$ denotes an eigenvalue with corresponding eigenvector $E \in \mathbb{C}^N$. For the Maxwell eigenvalue problem it is well known that there exist a huge eigenspace at $\lambda = 0$. Due to a dedicated low frequency stable formulation (see subsection 1.1) this can be circumvented very elegantly.

For the solution of the nonlinear eigenvalue problem the contour integral method of W. Beyn [7] is

used a building block. The advantage of this method is that all eigenvalues are found in a predefined bounded area $\Phi \subset \mathbb{C}$ with $\partial\Phi = \Gamma$. However, the numerical effort for large systems is very high because of the equidistant sampling along Γ (due to the trapezoidal rule), i.e., the contour integral method requires the solution $E(s)$ along a closed path Γ for some given source of (2). The ROM method is applied and the solution $\hat{E}(s)$ along Γ can be used to form the required integrals. Since the integrand is approximated by the ROM method some error estimations are required. It can be shown that the exact eigenvalue λ_k differs with respect to a calculated eigenvalue $\tilde{\lambda}_k$ by

$$\max_k |\lambda_k - \tilde{\lambda}_k| \leq \sqrt{\left(\int_{\Gamma} \frac{|s|}{\gamma(s)} \|R(s)\|_* ds\right)^2 + c(\Gamma, M)^2}$$

with $c(\Gamma, M)$ a function of the integration path and M the number of integration points used on the reduced system.

4 Outlook

We will show numerical studies for the driven and the eigenvalue problem from industrial applications, especially from the external Q-factor calculation, which show the numerical robustness and efficiency of the proposed methods.

References

1. P. Monk. *Finite Element Methods for Maxwell's Equations*. Numerical Mathematics and Scientific Computation, Clarendon Press, 2003.
2. O. Farle, M. L\"osch, and R. Dyczij-Edlinger. Efficient Fast Frequency Sweep Without Nonphysical Resonances *Electromagnetics*, 30:51–68, 2010.
3. Y. Zhu and A. Cangellaris. *Multigrid Finite Element Methods for Electromagnetic Field Modeling*. IEEE Press Series on Electromagnetic Wave Theory, 2006.
4. M. Eller, S. Reitzinger, S. Sch\"ops and S. Zaglmayr. A Symmetric Low Frequency Stable Broadband Maxwell Formulation for Industrial Applications. *SIAM Journal on Scientific Computing*, submitted, 2016.
5. A. Schultschik, O. Farle, and R. Dyczij-Edlinger. An Adaptive Multi-point Fast Frequency Sweep for Large-Scale Finite Element Models. *IEEE Trans. Magn.*, 44:1394–1397, 2008.
6. M. Hess, S. Grundel and P. Benner. Estimating the inf-sup Constant in Reduced Basis Methods for Time Harmonic Maxwell's Equations. *IEEE Transactions on Microwave Theory and Techniques* 63(11), 3549–3557, 2015.
7. W.J. Beyn. An Integral Method for Solving Nonlinear Eigenvalue Problems. *Linear Algebra and its Applications*, 436(10): 3839–3863, 2012.

A Symmetric FEM-BEM Formulation for Magnetostatics

Lars Kielhorn¹, Thomas R uberg¹, and J urgen Zechner¹

TailSit GmbH, Graz, Austria lars.kielhorn@tailsit.com, thomas.rueberg@tailsit.com, juergen.zechner@tailsit.com

Summary. Electrical machines commonly consist of moving and stationary parts. The electromagnetic simulation of such devices is a challenging task since the changing geometry needs to be incorporated into the numerical scheme. Contrary to Finite Element Methods, FEM-BEM coupling schemes inherently allow for the treatment of moving parts since they don't rely on an artificial discretization of the unbounded air region. While the numerics are certainly more involved, the reward is obvious: The modeling costs decrease and the application engineer is issued with a versatile and accurate simulation tool.

1 Magnetostatic FEM-BEM coupling

We recall the FEM-BEM coupling scheme as it has been proposed in [2]. With $\langle \mathbf{u}, \mathbf{w} \rangle_M := \int_M \mathbf{u} \cdot \mathbf{w} dM$ the variational formulation for magnetostatics reads: Find $\mathbf{A} \in H(\mathbf{curl}, \Omega^-)$ such that

$$\langle \mu^{-1} \mathbf{curl} \mathbf{A}, \mathbf{curl} \mathbf{A}' \rangle_{\Omega^-} - \langle \gamma_N^- \mathbf{A}, \gamma_D^+ \mathbf{A}' \rangle_{\Gamma} = \langle \mathbf{j}, \mathbf{A}' \rangle_{\Omega^-} \quad (1)$$

for all test-functions $\mathbf{A}' \in H(\mathbf{curl}, \Omega^-)$. Above, \mathbf{A} is the non-gauged vector potential and μ is the – possibly non-linear – magnetic permeability. The right hand side is given by a solenoidal excitation current \mathbf{j} . Here, we identify Ω^- with the interior domain and $\Gamma := \partial\Omega^-$ with its boundary. The FEM-BEM coupling is then performed via appropriate transmission conditions. They connect the interior Dirichlet- and Neumann-traces $\gamma_D^+ \mathbf{A}$ and $\gamma_N^- \mathbf{A}$ with their exterior counterparts. The exterior traces fulfill the set of (weak) boundary integral equations

$$\begin{aligned} \langle \gamma_D^+ \mathbf{A}, \zeta \rangle_{\Gamma} &= \langle \mathbf{B}(\gamma_D^+ \mathbf{A}), \zeta \rangle_{\Gamma} - \langle \mathbf{V}(\gamma_N^+ \mathbf{A}), \zeta \rangle_{\Gamma} \\ \langle \gamma_N^+ \mathbf{A}, \mathbf{w} \rangle_{\Gamma} &= \langle \mathbf{N}(\gamma_D^+ \mathbf{A}), \mathbf{w} \rangle_{\Gamma} - \langle \mathbf{B}^*(\gamma_N^+ \mathbf{A}), \mathbf{w} \rangle_{\Gamma} \end{aligned} \quad (2)$$

for $\zeta \in H(\text{div}_{\Gamma}, 0)$ and $\mathbf{w} \in H(\mathbf{curl}_{\Gamma}, \Gamma)$. Here, \mathbf{w} is an element of the trace space of $H(\mathbf{curl}, \Omega^-)$ while ζ is taken from the space of vector fields with vanishing surface divergence. In (2), \mathbf{V} denotes the Maxwell single layer potential, \mathbf{N} is the hypersingular operator, and \mathbf{B}, \mathbf{B}^* are the Maxwell double layer potential and its adjoint, respectively. A conforming discretization of (1) and (2) with N ed elec elements yields the linear system

$$\begin{bmatrix} A + R^{\top}NR & R^{\top}B^{\top} \\ BR & -V \end{bmatrix} \cdot \begin{bmatrix} a_{\text{fem}} \\ a_{\text{bem}} \end{bmatrix} = \begin{bmatrix} f(\mathbf{j}) \\ 0 \end{bmatrix}. \quad (3)$$

$A, N, B,$ and V are matrix representations of the formerly introduced FEM- and BEM-operators. R is a restriction matrix that extracts the boundary degrees of freedom (dofs). Fast Boundary Element Methods are used in order to compress the originally dense BEM matrices. If multiply connected domains are considered, the linear system (3) is augmented by properly chosen surface stream functions [3].

2 Iterative Solver

The linear system (3) is symmetric but not positive definite. We therefore apply a MINRES solver to the preconditioned system. The block preconditioner is given by $P^{-1} = \text{diag}(P_{\text{AMS}}^{-1}, P_V^{-1})$ where P_{AMS}^{-1} is an AMG/AMS preconditioner [1]. The BEM preconditioner P_V^{-1} is based on operator preconditioning techniques [5]. Subspace correction methods are used when higher order schemes are applied [6].

3 Examples

3.1 Magnetized Sphere

First, the FEM-BEM scheme is verified by means of a unit sphere $\Omega := \{\mathbf{x}: |\mathbf{x}| < 1\}$ that features a magnetization $\mathbf{M} = 1\mathbf{e}_z$. In Fig. 2 the results for the FEM-BEM coupling are compared against FEM computations and against the analytic solution [4]. The FEM computations are done for various fictitious air regions $\widehat{\Omega}_R := \Omega \cup \{\mathbf{x}: 1 \leq |\mathbf{x}| < R\}$.

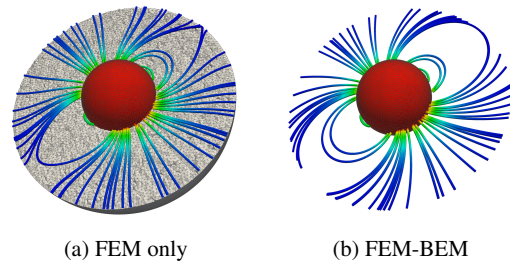


Fig. 1: Comparison between FEM and FEM-BEM

Due to the artificial boundary conditions on $\partial\widehat{\Omega}_R$ (see Fig. 1) the FEM computations cannot converge

towards the exact solution. Contrary, the FEM-BEM scheme reveals accurate results already for the coarsest grid.

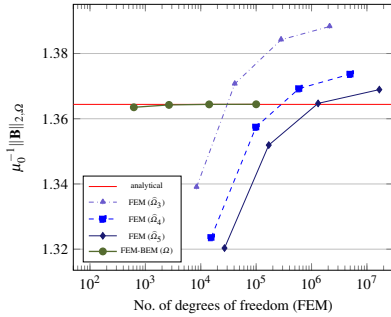


Fig. 2: Verifying the FEM-BEM scheme

3.2 Circular current loop with magnetic core

The efficiency of the preconditioner is investigated for a circular current loop that surrounds a magnetic core (Fig. 3). The model is discretized with three different grids (Tab. 1a).

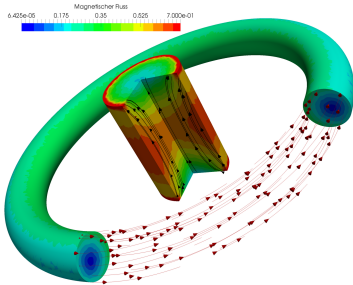


Fig. 3: Magnetic flux \mathbf{B} and excitation current \mathbf{j} .

In Tab. 1b the iteration numbers are given for the three refinement levels L_i as well as for varying permeabilities μ_r . The relative solver tolerance has been fixed at $\epsilon_r = 10^{-8}$. Obviously, the preconditioner is quite efficient since it reveals only a slight dependence on the mesh size and on material jumps.

L_i	Mesh size	N_{FEM}	N_{BEM}	μ_r	L_1	L_2	L_3
1	0.60	5402	706	10^0	47	51	63
2	0.39	27251	2872	10^2	78	88	117
3	0.19	166748	12049	10^5	84	92	119

(a) 3 different grids

(b) Iteration numbers

Table 1: Performance of the preconditioner

3.3 Periodicities

For industrial applications it is important to deal with models that feature geometrical periodicities. Fig. 4 shows a simple motor model that exploits periodicities. Only a sixth of the model has been discretized.

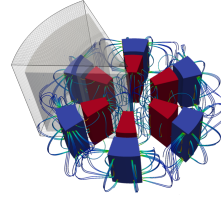


Fig. 4: \mathbf{B} -field. $1.5 \cdot 10^6 / 1.4 \cdot 10^4$ dofs (FEM/BEM)

3.4 Magnetic valve with moving armature

Finally, Fig. 5 shows a magnetic valve that consists of approximately $9 \cdot 10^5$ tetrahedral elements. At its bottom the valve features a moving armature. The excitation is given by a circular current \mathbf{j} .

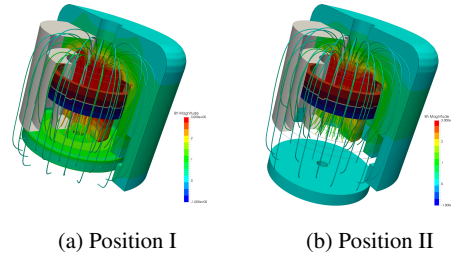


Fig. 5: \mathbf{B} -field. $2.4 \cdot 10^6 / 1.05 \cdot 10^5$ dofs (FEM/BEM)

References

1. R. Falgout and U. Yang. hypre: A library of high performance preconditioners. *Computational Science ICCS 2002*, pages 632–641, 2002.
2. R. Hiptmair. Symmetric coupling for eddy current problems. *SIAM Journal on Numerical Analysis*, 40(1):41–65, 2002.
3. R. Hiptmair and J. Ostrowski. Generators of $H_1(\Gamma_h, \mathbb{Z})$ for Triangulated Surfaces: Construction and Classification. *SIAM Journal on Computing*, 31(5):1405–1423, 2002.
4. J. D. Jackson. *Classical Electrodynamics*. John Wiley & Sons, Inc., 3rd edition, 1999.
5. G. Of. *BETI-Gebietszerlegungsmethoden mit schnellen Randelementverfahren und Anwendungen*. PhD thesis, Institut für Angewandte Analysis und Numerische Simulation, Universität Stuttgart, 2006.
6. Jinchao Xu. Iterative methods by space decomposition and subspace correction. *SIAM review*, 34(4):581–613, 1992.

Optimization of mechatronic components with MagOpt

Siegfried Silber¹, Gerald Jungmayr², Alexander Humer³, Werner Koppelstätter¹, Simon Weitzhofer¹, and Günther Weidenholzer¹

¹ Linz Center of Mechatronics GmbH, Altenbergerstrasse 69, A-4040 Linz, Austria, siegfried.silber@lcm.at, werner.koppelstaetter@lcm.at, simon.weitzhofer@lcm.at, guenther.weidenholzer@lcm.at

² Institute for Electrical Drives and Power Electronics, Johannes Kepler University Linz, Altenbergerstrasse 69, A-4040 Linz, Austria gerald.jungmayr@jku.at

³ Institute of Technical Mechanics, Johannes Kepler University Linz, Altenbergerstrasse 69, A-4040 Linz, Austria alexander.humer@jku.at

Summary. Optimizing mechatronic components is of increasing importance, e.g. to minimize energy consumption and the use of rare and critical materials. To address this issue, the dedicated simulation and optimization tool MagOpt has been developed. MagOpt is a modular tool with a flexible structure for the management and storage of complex simulation data. It features an open and modular interface to existing third party programs like CAD systems, finite element programs and other simulation software. Parametric design optimization can be carried out using various different optimization strategies like gradient-based methods or multi-objective evolutionary or genetic algorithms.

1 Introduction

Designing mechatronic components typically requires experience in different engineering disciplines. Increased requirements in terms of functionality and “smartness” result in higher complexity of such components. For the design process this means that the number of design parameters is continuously increasing. Consequently, optimization by manually tuning the design parameters is hardly feasible anymore.

Model-based simulation and optimization requires the physics of the considered system to be represented by mathematical models with sufficient accuracy. Such models typically incorporate different physical domains with diverse complexity ranging from simple analytical models to complex finite element models. Solving such a complex finite element model may require considerable simulation time especially if numerous simulations have to be carried out as in the case of genetic optimization.

For a systematic simulation and optimization approach the software tool MagOpt (short for **M**agnetic **O**ptimization) has been developed. Although MagOpt was originally designed for magnetic problems it turned out that, due to the very general structure it can also be applied for analyses performed in different physical domains and thus for different mechatronic components. For instance electromagnetic actuators, motors, magnetic bearing systems, hydraulic actuators and many more can be evaluated using MagOpt.

2 Simulation tool MagOpt

Optimization with MagOpt [3, 6] relies on various evolutionary algorithms, which share the characteristic property that a large number of simulations is required to find optima in multidimensional, multi-objective optimization problems. A tree-like, hierarchic structure is used to represent the components of the system to be optimized and to define the design parameters as well as the target functions. During the setup of the model, the dependencies among the various components need to be specified in MagOpt. When varying the design parameters in the actual optimization, MagOpt is aware of the dependencies and only those simulation models and functions affected by a variation are recomputed.

The tree-structure of MagOpt employs the following elements: A `Project` serves as root element when specifying a MagOpt project. Each `Project` may contain `Containers`, `Fields`, `Formulas` and `Functions` as elements.

`Containers` are node elements for branches that are used for structuring and encapsulating data and functionality. `Fields` are elements for data storage offering various data types for numerical values, matrices and signals, for instance. Simple algebraic equations are realized by `Formulas`, which may take `Fields` as input arguments. The central elements in MagOpt are `Functions`, which represent the interface to both internal and external simulation and computation modules. `Functions` are implemented in Java or script languages like JavaScript, Python, Lua or MATLAB. The interface between simulation modules and internal variables of MagOpt is realized by input and output lists of parameters. `Functions` can execute external simulation tools in the optimization process. The external tools typically used in the simulation range from 3D CAD systems to Finite Element Analysis (FEA) software. After an external tool has finished computation, the corresponding output parameters are returned to the MagOpt project and the data is available for further processing. For a number of frequently used mecha-

tronic components, particularly in the context of electric drives, MagOpt offers templates in the form of Components, which already contain the Fields, Formulas and also Functions required for setting up the simulation model.

In MagOpt, well known and widely applied genetic algorithms for multi-objective optimization are implemented. Additionally, we also implemented improved algorithms in terms of simulation speed. Especially for FEA problems, an advanced algorithm was developed that improves convergence of the Pareto-front significantly [8].

3 Examples

In the last few years various mechatronic components have been optimized with MagOpt. For instance, the design of magnetic bearings and the motor of a highly reliable magnetically levitated fan were optimized with MagOpt [4]. The cross section of this fan is shown in Figure 1.

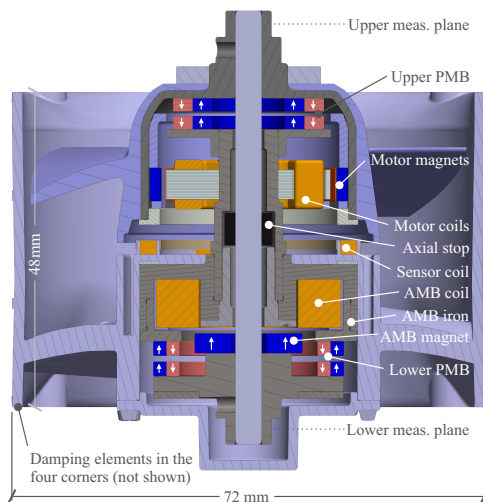


Fig. 1. Cross section of the magnetically levitated fan optimized with MagOpt.

Also the efficiency of industrial motors was increased whereas simultaneously the amount of rare earth magnets could be significantly reduced [1, 7]. MagOpt was also used for hardware in the loop optimization for a fast switching hydraulic valve. In that case the control parameters and the current waveform were optimized by controlling the system. Simulation of a passive permanent magnetic bearing and optimization of its stiffness further demonstrate the versatility of MagOpt [5].

Comparison of different embodiments of mechatronic components by their Pareto-fronts is also supported by MagOpt and was done in [2] for fast switching valves.

Acknowledgement. This work has been carried out at Linz Center of Mechatronics GmbH as part of a K2 project. K2 projects are financed using funding from the Austrian COMET-K2 programme. The COMET K2 projects at Linz Center of Mechatronics GmbH are supported by the Austrian federal government, the federal state of Upper Austria, the Johannes Kepler University and all of the scientific partners which form part of the K2-COMET Consortium.

References

1. G. Bramerdorfer, S. Silber, G. Weidenholzer, and W. Amrhein. Comprehensive cost optimization study of high-efficiency brushless synchronous machines. In *Electric Machines Drives Conference (IEMDC), 2013 IEEE International*, pages 1126–1131, May 2013.
2. P. Foschum, A. Plöckinger, G. Weidenholzer, and R. Scheidl. Triz, design optimization and suh’s 1st axiom - a comparison on the example of fast switching valves. In *Proceedings of the 13th Mechatronics Forum International Conference*, pages 498–505, 2012.
3. A. Humer, G. Jungmayr, W. Koppelstätter, M. Schörghener, S. Silber, and S. Weitzhofer. Multi-objective optimization of complex multibody systems by coupling hotint with magopt. In *Proceedings of the ASME 2016 International Design Engineering Technical Conferences & Computers and Information in Engineering Conference IDETC/CIE*, 2016.
4. G. Jungmayr, J. Loeffler, B. Winter, F. Jeske, and W. Amrhein. Magnetic gear: Radial force, cogging torque, skewing and optimization. In *2015 IEEE Energy Conversion Congress and Exposition (ECCE)*, pages 898–905, Sept 2015.
5. E. Marth, G. Jungmayr, J. Kobleder, M. Panholzer, and W. Amrhein. Realization of a multi-pole permanent magnetic bearing with rotating magnetization. In *Proc. 14th International Symposium on Magnetic Bearings*, pages 599 – 605, 2014.
6. S. Silber, G. Bramerdorfer, A. Doringner, A. Fohler, J. Gerstmayr, W. Koppelstätter, D. Reischl, G. Weidenholzer, and S. Weitzhofer. Coupled optimization in magopt. *Proceedings of the Institution of Mechanical Engineers, Part I: Journal of Systems and Control Engineering*, 2015.
7. G. Weidenholzer, S. Silber, G. Jungmayr, G. Bramerdorfer, H. Grabner, and W. Amrhein. A flux-based PMSM motor model using RBF interpolation for time-stepping simulations. In *Electric Machines Drives Conference (IEMDC), 2013 IEEE International*, pages 1418–1423, May 2013.
8. A.C. Zăvoianu, E. Lughofer, W. Amrhein, and E.P. Klement. Efficient multi-objective optimization using 2-population cooperative coevolution. In *Computer Aided Systems Theory - EUROCAST 2013*, pages 251–258, 2013.

A Lagrangian approach to the simulation of a vacuum arcs in a transverse magnetic field

Massimiliano Cremonesi¹, Attilio Frangi¹, Kai Hencken², Marcelo Buffoni², Markus Abplanalp², and Joerg Ostrowski

¹ Politecnico di Milano massimiliano.cremonesi@polimi.it, attilio.frangi@polimi.it

² ABB Switzerland Ltd., Corporate Research kai.hencken@ch.abb.com, marcelo.buffoni@ch.abb.com, joerg.ostrowski@ch.abb.com, markus.abplanalp@ch.abb.com

Summary. To improve the performance of vacuum interrupters, the numerical simulation of vacuum arc can be very effective. Standard computational fluid dynamics methods based on the Eulerian approach were found to have difficulties in dealing with this kind of problems. So that a new technique, based on a Lagrangian approach, is here proposed. A simplified arc model in a simple geometry is here used to investigate the capability of a Lagrangian approach to vacuum arc simulations. Comparisons with commercial software are also provided to validate the new methodology.

1 Introduction

Vacuum interrupters are electrical protection devices, that are used extensively in the medium voltage range up to 36kV in order to both switch nominal currents of a few kA and interrupt fault currents up to 63kA. They rely on the insulation properties of the vacuum in the gap between the two electrodes for their high voltage withstand capability. When interrupting currents, a vacuum arc is formed for a time of up to a half-wave. A vacuum arc is a metal vapor arc formed by the metal material evaporated by the two electrodes and heated to a high temperature plasma by the ohmic heating of the current. A vacuum arc shows some different appearances depending on current and gap distance [1]. At the relevant conditions the arc is in a constricted mode, which means that it does not cover the full cathode or anode and is in a high density and pressure state. The energy given to the cathode and anode through the exchange of electrons and ions heat them up to such high temperatures that the arc roots are able to provide new metal vapor for the arc to sustain itself. Interruption of large enough currents can only occur at a natural current zero crossing. At this moment the current is low, energy input is small and the gap can be cleared of the plasma and metal vapor. But this can occur only, if the metal vapor density and from this the surface temperature is below a critical level.

To achieve this some arc control is needed. Two main arc control principles have evolved, that try to spread the heating through the arc over a larger area and therefore reducing the temperature and from

this the vapor evaporation at current zero. ABB uses predominantly so-called "transverse magnetic field" principle. In this approach electrode shapes are used, which generates a magnetic field, which is predominantly transverse to the gap direction and therefore the arc. The effect of the magnetic field is to generate a Lorentz force, that tries to move the arc into one direction. The main mechanism of the TMF arc control is to move the arc by this with a high velocity over the surface of the electrodes, spreading the heat power over a larger area.

In order to improve the performance of such vacuum interrupters it is therefore fundamental to understand the motion of the vacuum arc. Experimental investigations are difficult due to the extreme conditions and the fast motion of the arc. Instead one would like to resort to simulations. A detailed arc model was developed in [2–5] and it was demonstrated that this model is able in principle to simulate the movement of an arc. In order to be useful for the development of new geometries, the simulations need to be fast and reliable enough. This was found to be difficult for two reasons: there are strong gradients at the edge of the vacuum arc, where the pressures of several bars decrease to values well below 1mbar in a short distance. As the temperature does not change strongly, the density follows a similar steep decrease. Standard computational fluid dynamics approaches based on the Eulerian approach were found to have difficulties in dealing with this as the ratio is too large. In addition, the arc does typically fill only a small part of the simulation domain. This means, that most of the mesh area is spent on cells having vacuum conditions. Whereas an adaptive mesh is one possible option to cope with this, we want to explore an approach, which automatically generates a fine mesh in the arc region. The Lagrangian approach has the possibility to define a mesh only in those regions, where a fluid is present. It was therefore seen as an interesting starting point.

2 Minimal arc model

In order to investigate the capability of a Lagrangian approach to vacuum arc simulations, we are defining

here a "minimal arc model". The full model is described in [2–5] and should be the ultimate aim of the simulation; but a simplified model can be of help to demonstrate the capabilities of the approach. We therefore give here a simplified model. It is the aim of it to be already very close to the real vacuum arc, that is, to capture with it realistic values as well as possible dependencies of parameters of the fluid. Still the equations should be in a form that they can be easily implemented. We have also defined a simplified 2D test geometry, which should mimic the real one.

A plasma simulation requires as input thermodynamic and transport properties and in addition suitable boundary conditions. All boundaries are defined to be outflowing apart from the region that defines the arc roots. Here the evaporation is written in the form of a Hertz-Knudsen evaporation model with the mass flux given by

$$\frac{m_{Cu}}{\sqrt{2\pi m_{Cu} k T_s}} (p^* - p)$$

as well as the momentum flux

$$\frac{1}{2} (p + p^*)$$

and the energy flux

$$\frac{2kT_s}{\sqrt{2\pi m_{Cu} k T_s}} (p^* - p)$$

where m_{Cu} is the mass of an individual copper atom and $T_s = 4000\text{K}$ and $p^* = 8.5 \times 10^5 \text{Pa}$ the surface temperature and the vapor pressure chosen in such a way to be realistic. The current density was assumed to be homogenous over the arc root and to reproduce the current density of a realistic arc.

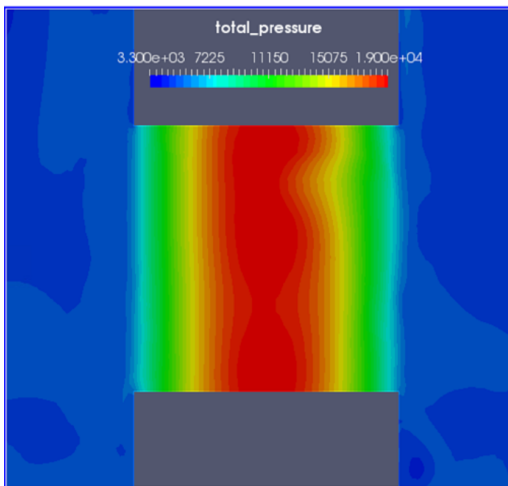


Fig. 1. Contour plot of the pressure.

3 Numerical results

The proposed numerical technique has been tested against a simplified arc problem. Figure 1 shows the contour plot of the obtained pressure field. A validation with a commercial software has also been done.

Acknowledgement. Financial support of ABB Corporate Research is gratefully acknowledged.

References

1. Slade, P. G.: The Vacuum Interrupter: Theory, Design, and Application, CRC Press, Boca Raton, London, New York (2008)
2. T. Delachaux, O. Fritz, D. Gentsch, E. Schade and D.L. Shmelev, "Numerical simulation of a moving high-current vacuum arc driven by a transverse magnetic field", IEEE Transactions on Plasma Science, vol. 35, pp. 905, 2007.
3. T. Delachaux, O. Fritz, D. Gentsch, E. Schade and D.L. Shmelev, "Simulation of a High Current Vacuum Arc in a Transverse Magnetic Field", IEEE Transactions on Plasma Science, vol. 37, pp. 1386, 2009.
4. D.L. Shmelev and T. Delachaux, "Physical Modeling and Numerical Simulation of Constricted High-Current Vacuum Arcs under the Influence of a Transverse Magnetic Field", IEEE Transactions on Plasma Science, vol. 37, pp. 1379–1385, 2009.
5. Fritz, O., Shmelev, D., Hencken, K., Delachaux, T., Gentsch, D.: Results of 3D numerical simulations of high-current constricted vacuum arcs in a strong magnetic field, in Proc. of the 24th International Symposium on Discharges and Electrical Insulation in Vacuum (IS-DEIV), 2010, p. 359–364 (2010).
6. Spitzer, L. Physics of fully ionized gases. Interscience (1965).
7. Cremonesi, M., Frangi, A. A Lagrangian Finite Element Method for 3D compressible flow applications. Computer Methods in Applied Mechanics and Engineering, **311**, 374–392 (2016)
8. Dobrev, V.A., Ellis, T.E., Kolev, T.V., Rieben, R.N.: Curvilinear finite elements for lagrangian hydrodynamics. International Journal for Numerical Methods in Fluids, **65**, 1295–1310 (2011)
9. Dobrev, V.A., Kolev, T.V., Rieben, R.N.: High-order curvilinear finite element methods for lagrangian hydrodynamics. SIAM Journal on Scientific Computing, **34**, B606–B641 (2012)

Compact Modeling for HV CMOS Technologies

Ehrenfried Seebacher

Senior Manager, Technology R&D, ams AG, Tobelbaderstraße 30, 8141 Premstätten, Austria
ehrenfried.seebacher@ams.com

Summary. Power management and sensor driver integrated circuits need technologies with high breakdown voltage (BV_{dss}) and low on-resistance (R_{dson}) [3]. HV CMOS technologies include low voltage parts for digital and analog circuits and additionally HV transistor modules. This complicated technology gives many possibilities for enhanced integrated circuits and products but is very challenging for simulation tools and the corresponding compact models. In this paper, we will discuss the main challenges in compact modeling for HV CMOS technologies including LV/HV CMOS transistor modeling [2,4], modeling of process variability [6], parasitic effects and substrate coupling [1,5].

1 Introduction

In many new applications like communication and automotive electronics, the usage of integrated high voltage MOS transistors (LDMOS and DMOS) requires highly accurate compact models. Compact models are defined as models for circuit elements, which are sufficiently simple to be incorporated in circuit simulators (SPICE) and are sufficiently accurate to make the outcome useful to circuit design. This article will inform about state of the art of HV transistor compact models and new developments like BSIM3/4, sub circuit modeling and the HV FET standard model HiSIM.HV. The requirement of a circuit design should define the needed accuracy of the used compact model, which directly defines the used model, efforts in parameter extraction, test structures and measurement, and the resulting costs for the process design kit (PDK). After a short look in the LDMOS transistor physics an overview of the main HV transistor compact models will be presented. We will discuss parasitic effects of HV transistors like parasitic diodes or bipolar transistor modeling in detail. In this paper, we will also discuss new developments for substrate coupling simulation and modeling based on the results of the EU FP7 project AUTOMICS. The design of integrated HV circuits is challenged by the activation of substrate parasitic BJTs, which can affect the whole circuit functionality. The new developed substrate current simulation environment gives excellent simulation results proven with silicon based test structures.

References

1. F. Lo Conte, J.M. Sallese, and M. Kayal. Predictive modeling of parasitic substrate currents in high-voltage Smart Power IC's. *Proceedings of the European Solid-State Device Research Conference (ESSDERC)*, 2011.
2. G. Gildeblat. *Compact Modeling, Part I, Chapter 4. High Voltage MOSFET Modeling*, ISBN 978-90-481-8613-6.
3. R. Minixhofer, N. Feilchenfeld, and M. Knaipp. A 120V 180nm High Voltage CMOS smart power technology for System-on-chip integration. *22nd International Symposium on Power Semiconductor Devices & IC's (ISPSD)*, 2010.
4. E. Seebacher, B. Senapati, K. Molnar, W. Pflanzl, W. Posch, A. Steinmair, M. Tang, and N. Mavredakis. High Voltage MOSFET Compact Modeling. *Nanotech*, 2011.
5. C. Stefanucci, P. Buccella, E. Seebacher, A. Steinmair, M. Kayal, and J.M. Sallese. Analysis of Substrate Currents Propagation in HVCMOS technology. *ESSDERC*, 2016.
6. A. Steinmair and E. Seebacher. Statistical SPICE Models for High-Voltage LDMOS Transistors based TCAD Simulation. *WCM*, 2012.

About the Author:

Ehrenfried Seebacher earned a M.Sc. in physics at Graz University of Technology in 1993. From 1994-1998 he has been working in the R&D department of austriamicrosystems, on compact modeling of CMOS, BiCMOS and HV CMOS processes. Since 1999 he is the section manager of a group responsible for compact modeling, process characterization, physical verification, and DFM. His main fields of interest are modeling of MOS, bipolar transistors and passive elements. He now is a senior manager in the Process R&D department at ams AG and a project leader of technology and PDK development projects. He published many papers in the area of compact modeling and had been working in European projects like CODESTAR, CHAMELEON-RF, MODERN, COMON, AUTOMIC and eRAMP.

Part IV

Abstracts of Contributed Talks

Sensitivity of Lumped Parameters to Geometry Changes in Finite Element Models

Sebastian A. Schuhmacher¹, Carsten Potratz², Andreas Klaedtke¹, and Herbert De Gersem³

¹ Robert Bosch GmbH - Corporate Research, Robert-Bosch-Campus, 71272 Renningen, Germany

Sebastian.Schuhmacher@de.bosch.com, Andreas.Klaedtke@de.bosch.com,

² carsten.potratz@mailbox.org,

³ TU Darmstadt, Schloßgartenstr. 8, 64289 Darmstadt, Germany degersem@temf.tu-darmstadt.de

Summary. The functional behavior of an electronic device is represented by an idealized circuit. Undesired parasitic interactions, such as electromagnetic compatibility (EMC) problems, are modeled by additional lumped elements in the circuit. Device design parameters, e.g. partial inductances, must be optimized to improve EMC. This paper presents a sensitivity analysis which relates circuit to 3D model parameter changes.

1 Introduction

The increasing integration density in modern electromechanical systems requires considering EMC issues at an early design stage in order to avoid costly changes later on. Historically, the electronic behavior of the system is modeled using a purely functional electronic circuit. Due to undesired parasitic effects, the physical realization usually behaves differently than the idealized model.

In [1] a method was proposed that automates the extraction of lumped elements between a given set of terminals from a 3D CAD model into a network model. This is comparable to the more common Model Order Reduction (MOR) [3] and Partial Element Equivalent Circuit (PEEC) [4] methods. To retain interpretability, the reduced model still embeds the functional aspects of the circuit and merely adds additional lumped elements accounting for parasitics. This enables engineers to use their intuition in designing mitigation strategies.

Once the parasitics are known, the question arises how to adapt the 3D model to improve the EMC. This is accomplished by calculating the 3D design changes related to parameters of the equivalent circuit. The sensitivity analysis for a comparably large number of model parameters is enabled by an adjoint technique. In this paper, we establish a connection between the method described in [1] and adjoint sensitivity maps. We show explicitly how those maps can be generated for the constituents of an equivalent electric circuit.

2 Equivalent Electric Circuits

Starting from the 3D CAD model with suitably defined terminals, the following sections will establish the connection to the lumped element parameters (capacitances, ohmic losses and partial inductances).

2.1 Static Capacitances

To explain the method we consider the capacitance of a two terminal system, e.g. a system comprised of two galvanically separated metallic bodies. The electrostatic problem is governed by the Laplace equation:

$$\nabla \cdot (\epsilon \nabla \phi) = 0 \quad (1)$$

where ϕ is the electric scalar potential and ϵ is the permittivity. This equation can be approximately solved for the scalar potential ϕ using the Finite Element Method (FEM). With \mathbf{A} denoting the FE-matrix and \mathbf{b} containing boundary conditions, the discretized form reads:

$$\mathbf{A}\mathbf{x} = \mathbf{b} \quad (2)$$

For a known solution \mathbf{x} , the electric field energy is:

$$W_{3D} = \frac{1}{2} \mathbf{x}^T \mathbf{A} \mathbf{x} \quad (3)$$

The energy of the capacitance C_{12} is given by:

$$W_{EEC} = \frac{1}{2} C_{12} (\phi_2 - \phi_1)^2 \quad (4)$$

with ϕ_1 and ϕ_2 denoting the imprinted potential of the respective conducting bodies. Thus the equivalent capacitance can be computed using:

$$C_{12} = \frac{\mathbf{x}^T \mathbf{A} \mathbf{x}}{(\phi_2 - \phi_1)^2} \quad (5)$$

Generalizing this approach to a multi terminal system is straight forward.

2.2 Ohmic Losses and Partial Inductances

The governing equation for the computation of ohmic losses is again the Laplace equation:

$$\nabla \cdot (\sigma \nabla \phi) = 0 \quad (6)$$

In this case the electric permittivity ϵ is replaced by the conductivity σ . Using the above approach, the resistance between terminals can be easily extracted.

The connection between the 3D model and the inductive equivalent electric circuit elements is made using the admittance matrix \mathbf{Y} . The calculation of the scalar potential ϕ using a modified formulation of the Darwin model with appropriate current sources is described in [1].

3 Adjoint Sensitivity Method

Using the example of the plate capacitor, we show how the Adjoint Sensitivity Method (ASM) can be used to map geometric or material parameter changes to modified lumped element parameters. So the question to be asked is, how do 3D model parameter variations change the capacitance. Mathematically, the change is described as:

$$\partial_p C = (\partial_x C)^T \cdot \partial_p \mathbf{x} \quad (7)$$

where \mathbf{x} is the vector of degrees of freedom from Eq. (2), representing the potential field, and p a geometry or material parameter of the 3D model.

Using (5), the expression for $\partial_x C$ is:

$$\partial_x C = \frac{2}{(\phi_1 - \phi_2)^2} \mathbf{A} \mathbf{x} \quad (8)$$

The expression $\partial_p \mathbf{x}$ can be derived from (2):

$$\partial_p \mathbf{x} = \mathbf{A}^{-1} (\partial_p \mathbf{b} - (\partial_p \mathbf{A}) \mathbf{x}) \quad (9)$$

However, every evaluation, with respect to a 3D model parameter, requires an individual solution of the above equation, which can be quite costly. A more suitable approach is the ASM. The ASM [2] allows for an efficient computation of the sensitivity, using the ansatz:

$$\partial_x C = \mathbf{A}^T \boldsymbol{\lambda} \quad (10)$$

where \mathbf{A} is the FE-matrix, $\boldsymbol{\lambda}$ is the so called adjoint solution and $\partial_x C$ is known from (8). Inserting eqns. (9) and (10) into the original problem (7) leads to the following expression:

$$\partial_p C = \boldsymbol{\lambda}^T (\partial_p \mathbf{b} - (\partial_p \mathbf{A}) \mathbf{x}) \quad (11)$$

The adjoint solution $\boldsymbol{\lambda}^T$ is independent of the parameter under consideration and thus only needs to be computed once. The changes of the excitation $\partial_p \mathbf{b}$ and

the change of the FE-matrix $\partial_p \mathbf{A}$ have to be computed for every variation, but they are usually very sparse and do not require a matrix inversion. Therefore, the method allows for the efficient computation of sensitivities with regards to a large number of model parameters.

4 Examples

We will demonstrate the methodology using various academic and industrial examples. In Fig. (1) for example, a commutation cell for a photovoltaic inverter is presented. The image shows the sensitivity of geometric changes related to a variation of the ohmic resistance between two terminals.

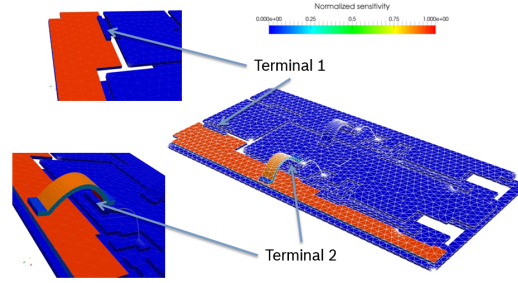


Fig. 1. Sensitivity of ohmic losses in a commutation cell

5 Conclusions

Using an adjoint sensitivity method, the sensitivity of equivalent circuit parameters to changes in the geometry, or material parameters, can be calculated efficiently.

References

1. F. Traub, Automated Construction of Equivalent Electrical Circuit Models for Electromagnetic Components and Systems, Dissertation, TU Darmstadt, 2014
2. A. Belegundu, Lagrangian Approach to Design Sensitivity Analysis, J. Eng. Mech., 111(5), 680-695, 1985
3. T. Wittig, R. Schuhmann and T. Weiland, Model order reduction for large systems in computational electromagnetics, Linear algebra and its applications, vol. 415, no. 2, pp. 499-530, 2006
4. H. Heeb and A. Ruehli, Three-dimensional interconnect analysis using partial element equivalent circuits, IEEE Transactions on Circuits and Systems I: Fundamental Theory and Applications, vol. 39, no. 11, pp. 974-982, 1992

A Trefftz Method for the time-harmonic Eddy Current Equation

Raffael Casagrande¹, Ralf Hiptmair¹, Joerg Ostrowski², and Christoph Winkelmann¹

¹ ETH Zürich casagrande@math.ethz.ch, hiptmair@sam.math.ethz.ch,
christoph.winkelmann@sam.math.ethz.ch

² ABB Switzerland Ltd., Corporate Research joerg.ostrowski@ch.abb.com

Summary. We present an extended Finite Element Method to resolve the skin effect in conductors on coarse meshes. The idea is to integrate the exponential decay into the finite element approach, which enables to resolve the skin layer independent of the size of the mesh cells. The discontinuous, Trefftz-type basis functions are coupled across the element boundaries by the Interior Penalty-/Nitsche's Method and numerical experiments affirm the effectiveness of the method for thin boundary layers.

1 Introduction

We consider the vector potential formulation of the eddy current problem in the frequency domain with temporal gauge ($\varphi = 0$),

$$\nabla \times (\mu^{-1} \nabla \times \mathbf{A}) + i\omega\sigma\mathbf{A} = \mathbf{j}^i. \quad (1)$$

Here

- $\mathbf{A}(\mathbf{x})$ is a vector potential,
- $\mathbf{B}(\mathbf{x}, t) = \exp(i\omega t)(\nabla \times \mathbf{A})(\mathbf{x})$ is the magnetic flux density,
- $\exp(i\omega t)\mathbf{j}^i(\mathbf{x})$ is the impressed electric current,
- $\omega \in \mathbb{R}$ is the angular frequency, and
- $\sigma(\mathbf{x})$ is the electric conductivity (which can be zero in parts of the domain and is assumed to be piecewise constant).

It is well known that the solution of (1) exhibits singularities in edges (and corners) of conductors [2], as well as exponential boundary layers along the surface of conductors (*skin effect*). I.e. the induced current $i\omega\sigma\mathbf{A}$ is concentrated at the surface of conductors and decays rapidly towards the interior. The thickness of the boundary layer is characterized by the skin-depth $\delta = \sqrt{\frac{2}{\mu\sigma\omega}}$.

Induction has many applications in industry. An example is inductive hardening [5], where the workpiece is heated quickly at the surface, and is then rapidly cooled down before the heat is distributed into the interior by heat conduction. In this case the skin effect plays a fundamental technical role and resolving the skin layer is essential.

For the classical Finite Element Method (FEM) this means that the boundary layers must be resolved by the underlying mesh. This can be achieved by

adapting the mesh manually or one can refine an existing mesh towards the boundary layers, which can be automated (*h-refinement*).

However, in industrial applications the skin depth δ can be orders of magnitudes smaller than the diameter of the conductor so that the mesh must be refined multiple times towards the boundary layer(s). This leads to a vast increase in the number of degrees of freedom (DOF) which may render the solution of the linear system prohibitively expensive.

Alternatively one can resolve the skin-layer by *p*-refinement, i.e. by increasing the polynomial degree in elements adjacent to the conductor surface. This avoids mesh refinement and *away from edges (and corners)* of the conductor the solution is generally smooth so one can expect exponential convergence in *p* for a fixed δ . However, we will show in the full paper that *p* must be chosen as $O(\delta^{-1/2})$ (to keep the relative L^2 -error constant) and therefore the number of DOF scales, in the best case, as $O(\delta^{-1/2})$. Asymptotically this is even worse than *h-refinement* where the number of DOF scales logarithmically in δ .

A partial remedy for this problem are Impedance Boundary Conditions (IBC) [5]: The conductor is replaced by Robin-type boundary conditions and the electro-magnetic fields are only calculated at the surface of the conductor. Since the IBC approximation assumes that the conductor surface is flat, the solution deteriorates as the radius of curvature of the conductor surface becomes comparable to the skin-depth δ . In particular the IBC solution deviates strongly from the physically correct fields at edges and corners of the conductor. Moreover, to the best of our knowledge, it is not possible to replace a conductor in which $\mathbf{j}^i \neq 0$ by IBC conditions.

In this work we propose to resolve the boundary layers directly on coarse meshes (we assume the meshsize $h \gg \delta$) by enriching the approximation space with suitable functions. More precisely, our approximation space will contain three types of (discontinuous) basis functions:

- Edge elements R_k [4],
- Exponential boundary layer functions,
- Singular functions to deal with singularities of the exact solution in edges (and corners) of the conductor [2].

We deal with the discontinuous nature of the basis functions in the framework of Discontinuous Galerkin (DG) methods and discretize (1) by the interior penalty / Nitsche's method [1]. Special care must be taken for the approximation of the volume/surface integrals appearing in the variational formulation because not all basis functions are polynomial. This will be detailed in the full paper.

2 Numerical Example

We consider the setting depicted in Fig. 1: We impose an external current, $\mathbf{j}^i = 10^4$ A in the gray conductor which induces a current in the green plate.

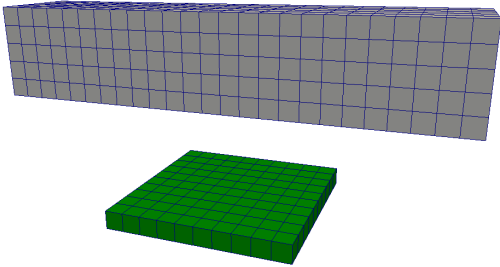


Fig. 1. 3D coarse meshes used for the simulation in Fig. 2. The exciting conductor is shown in gray, the excited conductor in green.

Figure 2 shows the distribution of $|\mathbf{A}|$ in a cross section of the green plate. The top plot shows the reference solution which was obtained on an extremely refined mesh and the skin effect is clearly visible. Here $\delta = 0.02$ m which is 10% of the thickness of the plate.

The middle plot shows the solution obtained on the coarse mesh shown in Fig. 1 using standard first order edge elements and it is apparent that the skin layer is not resolved properly. Finally, the bottom plot shows the solution of our proposed method on the same coarse mesh (not including the singular basis functions which are still ongoing research). We see that the exponential functions can capture the exponential boundary layer much better than first order edge functions alone.

3 Singularities in edges of the conductor

If we take again a close look at the bottom plot of Fig. 2 we observe that there is still considerable error in the edges of the green plate where the exponential approximation is not valid. We expect that the inclusion of singular functions, as mentioned in Sect. 1, will correct this. In fact, we have already collected

promising results for the 2D eddy current equation showing that high-order polynomials achieve exponential convergence (in p) in the vicinity of edges of the conductor if the corresponding singular functions are also included in the approximation space.

It seems that DG is a particularly well-suited framework when it comes to enriching the approximation space with singular functions: There is no need for cutoff functions (cf. [6, Chapter 8], [3]) which leads to much better approximation properties in practice. This aspect will be discussed in more detail and based on numerical evidence in the full paper.

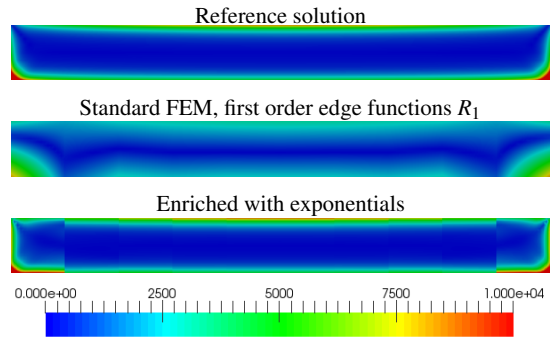


Fig. 2. Cross section through green plate (cf. Fig. 1) showing $|\mathbf{A}|$. $\omega = 400$ rad/s, $\sigma_{\text{green}} = 10^7$ S/m, $\sigma_{\text{gray}} = 10^5$ S/m, $\mu \equiv 4\pi \cdot 10^{-7}$ H/m and the dimensions of the green plate are $0.2\text{m} \times 2\text{m} \times 2\text{m}$.

Acknowledgement. This work has been funded by the Commission for Technology and Innovation (CTI), Switzerland, funding application No. 14712.1 PFIW-IW and ABB Switzerland Corporate Research.

References

1. Raffael Casagrande, Ralf Hiptmair, and Joerg Ostrowski. An a priori error estimate for interior penalty discretizations of the curl-curl operator on non-conforming meshes. *Journal of Mathematics in Industry*, 6(1):1–25, 2016.
2. Monique Dauge, Patrick Dular, Laurent Krähenbühl, Victor Péron, Ronan Perrussel, and Clair Poignard. Corner asymptotics of the magnetic potential in the eddy-current model. *Mathematical Methods in the Applied Sciences*, 37(13):1924–1955, 2014.
3. Jens Markus Melenk and Ivo Babuška. The partition of unity finite element method: basic theory and applications. *Computer methods in applied mechanics and engineering*, 139(1):289–314, 1996.
4. Peter Monk. *Finite element methods for Maxwell's equations*. Oxford University Press, 2003.
5. Jörg Ostrowski. *Boundary element methods for inductive hardening*. PhD thesis, Universität Tübingen, 2002.
6. Gilbert Strang and George J Fix. *An analysis of the finite element method*, volume 212. Prentice-Hall Englewood Cliffs, NJ, 1973.

Modelling and simulation of electrically controlled droplet dynamics

Yun Ouédraogo¹, Erion Gjonaj¹, Thomas Weiland¹, Herbert De Gersem¹, Christoph Steinhausen², Grazia Lamanna², Andreas Preusche³, and Andreas Dreizler³

¹ Technische Universität Darmstadt, Institut für Theorie Elektromagnetischer Felder,
Schloßgartenstr. 8, 64289 Darmstadt, Germany
{ouedraogo, gjonaj, thomas.weiland, degersem}@temf.tu-darmstadt.de,

² Universität Stuttgart, Institut für Thermodynamik der Luft- und Raumfahrt,
Pfaffenwaldring 31, 70569 Stuttgart, Germany
{christoph.steinhausen, grazia.lamanna}@itrl.uni-stuttgart.de,

³ Technische Universität Darmstadt, Fachgebiet für Reaktive Strömungen und Messtechnik, Center of Smart Interfaces,
Alarich-Weiss-Str. 10, 64287 Darmstadt, Germany
{preusche, dreizler}@csi.tu-darmstadt.de,

Summary. The electrohydrodynamics of millimetric droplets under the influence of slowly varying electric fields is considered. Strong electric fields applied on liquids induce forces driving fluid motion. This effect can be used, among others, in on-demand droplet generators. In this paper we discuss a convection-conduction model for the simulation of electric fields and droplet motion in an electrically driven droplet generator. The simulated dynamics for acetone droplets are compared with experiments.

1 Introduction

The application of strong electric fields on liquids is used in many engineering applications to induce liquid atomization in a controlled manner. In electro-sprays, the droplet size and the opening angle of the spray cone can be affected by charging the liquid prior to its atomization. Electric fields are also used to control droplet detachment in droplet generators. These devices are used for on-demand droplet generation in various experiments with liquid samples under different atmospheric conditions [1].

The numerical simulation of electrically driven droplet motion is a challenging problem. Due to the presence of intrinsic ionic species and dissolved impurities, liquids generally exhibit some electrical conductivity associated with charge migration [2, 3]. Free charge accumulate at the droplet interface and can result in the generation of charged droplets from initially uncharged liquid. Such a leaky dielectric behaviour requires an electroquasistatic field representation, taking into account both conduction and displacement electric currents in the liquid.

We discuss a conduction-convection model for the simulation of droplet dynamics under the influence of electric fields. The model accounts for electroquasistatic droplet charging, contact angle dynamics, and phase boundary topology changes associated with the droplet detachment process. The simulation of con-

trolled acetone droplet generation in an electrically driven droplet generator is presented.

2 Numerical model

The Volume of Fluid (VoF) approach [4] is the method of choice for the simulation of multiphase fluid problems. It allows for a numerically efficient representation of the phase boundaries, in particular when topology changes such as droplet breakup and collision are involved. In this work, the electric and hydrodynamic problems are both solved with the VoF approach using a Finite Volume discretization based on the OpenFOAM simulation framework [5].

2.1 Electric problem

The volume fraction, α , occupied by the liquid in each cell of the computational mesh defines averaged electric properties as

$$\frac{1}{\hat{\epsilon}} = \frac{\alpha}{\epsilon_{\text{liq}}} + \frac{1-\alpha}{\epsilon_{\text{gas}}}, \quad (1)$$

$$\frac{1}{\hat{\kappa}} = \frac{\alpha}{\kappa_{\text{liq}}} + \frac{1-\alpha}{\kappa_{\text{gas}}}, \quad (2)$$

where ϵ_{liq} , κ_{liq} and ϵ_{gas} , κ_{gas} are the permittivities and electric conductivities of the liquid and gas environment, respectively. Using this material averaging, the transient electroquasistatic field is governed by

$$\nabla \cdot \hat{\epsilon} \nabla \Phi = -\rho_e, \quad (3)$$

$$\frac{\partial \rho_e}{\partial t} + \nabla \cdot (\rho_e \mathbf{u}) = \nabla \cdot \hat{\kappa} \nabla \Phi. \quad (4)$$

The electric forces applied on the liquid can be calculated from the electric field $\mathbf{E} = -\nabla \Phi$, using the divergence of the Maxwell stress tensor:

$$\mathbf{f}_e = \nabla \cdot \left(\hat{\epsilon} \mathbf{E} \otimes \mathbf{E} - \frac{1}{2} \hat{\epsilon} E^2 \bar{\mathbf{I}} \right). \quad (5)$$

2.2 Fluid problem

The incompressible fluid flows considered in this work are described by the Navier-Stokes equations:

$$\frac{\partial \hat{\rho} \mathbf{u}}{\partial t} + \nabla \cdot (\hat{\rho} \mathbf{u} \mathbf{u}) - \hat{\mu} \nabla \cdot (\nabla \mathbf{u} + \nabla \mathbf{u}^T), \quad (6)$$

$$= -\nabla p + \hat{\rho} \mathbf{g} + \mathbf{f}_s + \mathbf{f}_e$$

$$\nabla \cdot \mathbf{u} = 0, \quad (7)$$

where $\hat{\rho}$, $\hat{\mu}$ are the averaged fluid density and dynamic viscosity, respectively, obtained by a similar averaging as in (1) and (2).

Surface wettability is accounted for by a contact angle model, providing a correction for the surface tension force f_s on the first boundary layer. In this work, the Kistler correlation is used, representing the dynamic contact angle θ as a function of the capillary number Ca at the contact line [6]:

$$\theta = f_H (Ca + f_H^{-1}(\theta_{adv/rec})), \quad (8)$$

$$\text{with } f_H(x) = \arccos \left(1 - 2 \tanh \left[5.16 \left(\frac{x}{1 + 1.31x^{0.99}} \right)^{0.706} \right] \right). \quad (9)$$

In (8), θ_{adv} and θ_{rec} represent, respectively, the limiting advancing and receding angles of the liquid on the given surface.

3 Application and results

The electrohydrodynamic model is applied in the simulation of the droplet generator shown in Fig. 1.

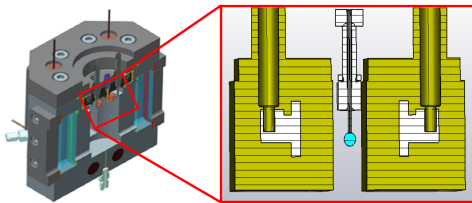


Fig. 1. Schematic of the droplet generator (cf. [1]).

A metallic capillary tube at ground voltage is placed between two electrodes in a climate chamber capable of sustaining a high-pressure, high-temperature gaseous environment. Liquid is introduced from the top of the capillary. As the droplet reaches a specified size, a short voltage pulse is applied at the electrodes. The electric forces induced on the droplet accelerate it for the duration of the pulse. The voltage is interrupted before detachment in order to allow the droplet to discharge before it breaks from the capillary and

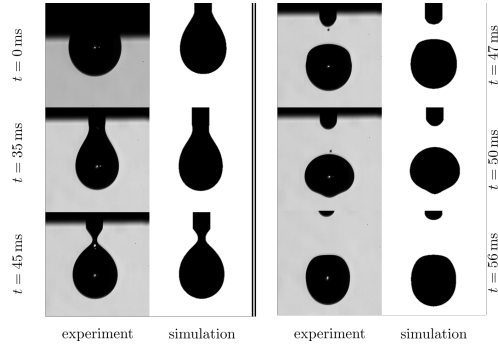


Fig. 2. Comparison between the simulated and experimentally recorded droplet dynamics in the generator during the detachment process.

falls into the pressure chamber.

In order to reduce the computational cost, the droplet generator is modelled assuming axial symmetry. The contact angle parameters on the capillary are chosen such as to properly reproduce the droplet shape shortly before the voltage pulse is applied. The simulated dynamics of detachment are compared in Fig. 2, for a 3.5 μl acetone droplet. Droplet detachment is controlled by a 2kV voltage pulse with a duration of 10ms. A very good agreement between simulation and experiment can be observed. The slight deviations in the computed droplet shapes are most probably due to uncertainties related to the determination of capillary surface wettability parameters.

Acknowledgement. This work is funded by the German Research Foundation in the framework of the Collaborative Research Center Transregio 75.

References

1. F. Weckenmann, B. Bork, E. Oldenhof, G. Lamanna, B. Weigand, B. Boehm, and A. Dreizler. Single acetone droplets at supercritical pressure: Droplet generation and characterization of PLIFP. *Zeitschrift Fur Physikalische Chemie-International Journal of Research in Physical Chemistry & Chemical Physics*, 225:1417–1431, 2011.
2. J. R. Melcher and G. I. Taylor. Electrohydrodynamics: A review of the role of interfacial shear stresses. *Annual Review of Fluid Mechanics*, 1(1):111–146, 1969.
3. D. A. Saville. Electrohydrodynamics: The Taylor-Melcher leaky dielectric model. *Annual Review of Fluid Mechanics*, 29(1):27–64, 1997.
4. C.W Hirt and B.D Nichols. Volume of fluid (VOF) method for the dynamics of free boundaries. *Journal of Computational Physics*, 39(1):201 – 225, 1981.
5. Openfoam. <http://www.openfoam.org>.
6. I.V. Roisman, L. Opfer, C. Tropea, M. Raessi, J. Mostaghimi, and S. Chandra. Drop impact onto a dry surface: Role of the dynamic contact angle. *Colloids and Surfaces A: Physicochemical and Engineering Aspects*, 322(13):183 – 191, 2008.

Survey on Semi-Explicit Time Integration of Eddy Current Problems

Jennifer Dutiné¹, Markus Clemens¹, and Sebastian Schöps²

¹ University of Wuppertal, Chair of Electromagnetic Theory, Rainer-Gruenter-Str. 21, 42119 Wuppertal, Germany
dutine@uni-wuppertal.de, clemens@uni-wuppertal.de

² Technische Universität Darmstadt, Graduate School CE, Dolivostr. 15, 64293 Darmstadt, Germany
schoeps@temf.tu-darmstadt.de

Summary. The magnetic vector potential formulation of eddy current problems is spatially discretized and a generalized Schur-complement is applied to the resulting infinitely stiff differential algebraic system of equations of index 1 to transform it into an ordinary differential equation (ODE) system of finite stiffness. This ODE can be integrated in time using the explicit Euler method. The small maximum stable time step widths require fast computations in every time step to obtain acceptable overall simulation times. Several methods for acceleration are presented.

1 Introduction

Implicit time integration methods are usually used for the time integration of eddy current problems. Here, due to the nonlinear characteristics of ferromagnetic materials, large nonlinear equation systems need to be linearized in every time step, e.g. by the Newton-Raphson method which may require several iterations per time step. Stiffness- and Jacobian matrix need to be updated in every iteration. Application of explicit time integration methods is proposed in [1,2,6,10,11]. This work is based on [2,6,10].

2 Formulation

Spatially discretizing the partial differential equation of magnetoquasistatic field problems results in an infinitely stiff differential algebraic equation system of index 1 (DAE) [9]. Separating and reordering the degrees of freedom (DoFs) depending on their allocation in nonconducting and conducting media into two vectors \mathbf{a}_n and \mathbf{a}_c yields

$$\begin{pmatrix} \mathbf{M}_{cc} & 0 \\ 0 & 0 \end{pmatrix} \frac{d}{dt} \begin{pmatrix} \mathbf{a}_c \\ \mathbf{a}_n \end{pmatrix} + \begin{pmatrix} \mathbf{K}_{cc} & \mathbf{K}_{cn} \\ \mathbf{K}_{cn}^T & \mathbf{K}_{nn} \end{pmatrix} \begin{pmatrix} \mathbf{a}_c \\ \mathbf{a}_n \end{pmatrix} = \begin{pmatrix} 0 \\ \mathbf{j}_{s,n} \end{pmatrix}, \quad (1)$$

where \mathbf{M}_{cc} is the conductivity matrix, $\mathbf{K}_{cc}(\mathbf{a}_c)$ is the nonlinear part of the stiffness matrix in conducting regions, \mathbf{K}_{nn} is the singular part of the curl-curl operator in air and $\mathbf{j}_{s,n}$ is the source current density in nonconducting regions. The matrix product

$$\mathbf{K}_S := \mathbf{K}_{cn} \mathbf{K}_{nn}^+ \mathbf{K}_{cn}^T, \quad (2)$$

is the generalized Schur-complement, where \mathbf{K}_{nn}^+ is the matrix representation of the pseudo-inverse of \mathbf{K}_{nn} . This pseudo-inverse is evaluated using the pre-conditioned conjugate gradient (PCG) method [6]. Alternatively, the singular matrix \mathbf{K}_{nn} can be regularized by a grad-div-regularization [2]. The generalized Schur-complement is applied to (1) and transforms the DAE into an ordinary equation system (ODE) of finite stiffness for the vector of degrees of freedom \mathbf{a}_c in the conducting regions [2,6,10]

$$\mathbf{M}_{cc} \frac{d}{dt} \mathbf{a}_c + (\mathbf{K}_{cc}(\mathbf{a}_c) - \mathbf{K}_S) \mathbf{a}_c = -\mathbf{K}_{cn} \mathbf{K}_{nn}^+ \mathbf{j}_{s,n}, \quad (3)$$

$$\mathbf{a}_n = \mathbf{K}_{nn}^+ \mathbf{j}_{s,n} - \mathbf{K}_{nn}^+ \mathbf{K}_{cn}^T \mathbf{a}_c. \quad (4)$$

The explicit Euler method or more sophisticated methods as Runge-Kutta-Chebyshev (RKC) can be used for time integration of (3). Here, the pseudo-inverse needs to be evaluated in every time step and this forms a multiple right-hand side problem. In [10] it was proposed to update the algebraic equation only in every n -th step. Improved start vectors for the PCG method can be computed using the cascaded subspace extrapolation (CSPE) method [3,6]. Solutions from previous time steps are orthonormalized and become the column vectors of the operator \mathbf{V} . The projected system

$$\mathbf{V}^T \mathbf{K}_{nn} \mathbf{V} \mathbf{z} = \mathbf{V}^T \mathbf{r}, \quad (5)$$

is solved for \mathbf{z} , where \mathbf{r} is the right-hand side. The improved start vector $\mathbf{x}_{0,CSPE}$ is computed as linear combination of the column vectors in \mathbf{V} weighted with the coefficients in \mathbf{z} :

$$\mathbf{x}_{0,CSPE} := \mathbf{V} \mathbf{z}. \quad (6)$$

Alternatively, improved start vectors for PCG iterations can be computed using a proper orthogonal decomposition (POD). Solutions from previous time steps are used to assemble a snapshot matrix on which a POD method is used. The number of modes of the POD can be selected adaptively [5].

The explicit Euler method is only stable for time step widths Δt smaller than the Courant-Friedrich-Levy time step width Δt_{CFL} for which holds [10]:

$$\Delta t_{\text{CFL}} \leq \frac{2}{\lambda_{\text{max}} (\mathbf{M}_{\text{cc}}^{-1} (\mathbf{K}_{\text{cc}} (\mathbf{a}_{\text{c}}) - \mathbf{K}_{\text{S}}))}. \quad (7)$$

The maximum eigenvalue λ_{max} is proportional to

$$\lambda_{\text{max}} (\mathbf{M}_{\text{cc}}^{-1} (\mathbf{K}_{\text{cc}} (\mathbf{a}_{\text{c}}) - \mathbf{K}_{\text{S}})) \propto \frac{1}{h^2 \kappa \mu}, \quad (8)$$

where κ is the electric conductivity, h is the smallest edge length in the mesh, and μ is the permeability.

Due to (8), fine spatial discretizations result in rather small time steps, possibly in the micro- to nano second range. Therefore it is proposed to bypass the matrix update of $\mathbf{K}_{\text{cc}} (\mathbf{a}_{\text{c}})$ in as many time steps as possible, as it is expected to be almost constant at successive time steps [4].

3 Numerical Validation

The ferromagnetic TEAM 10 benchmark problem is discretized in space using 1st order edge element FEM ansatz functions [7, 8]. The excitation current is described by a $(1 - \exp(-t/\tau))$ function. The first 120 ms are simulated and the explicit Euler method is used for time integration. The applied spatial discretization results in a maximum stable time step width $\Delta t_{\text{CFL}} = 1.2 \mu\text{s}$. Simulations are computed using a Dell PowerEdge workstation with Intel Xeon E5-2660 processor and an NVIDIA TESLA K80 GPU. For evaluating the pseudo-inverse, an algebraic multigrid is used as preconditioner in the PCG method, and the chosen PCG-tolerance is $\text{tol}_{\text{CG}} = 10^{-6}$. POD and CSPE reduce the average number of PCG iterations when evaluating the pseudo-inverse compared to using the solution from the previous time step as start vector, as shown in Fig. 1. The matrix $\mathbf{K}_{\text{cc}} (\mathbf{a}_{\text{c}})$ is updated only 165 times instead of 100,000 times in total, without loss of accuracy. The simulation time of the explicit time integration method using CSPE for start vector generation and bypassing the matrix update is reduced in comparison to a reference simulation using the standard formulation and using the implicit Euler method for time integration of (1), as shown in Fig. 2.

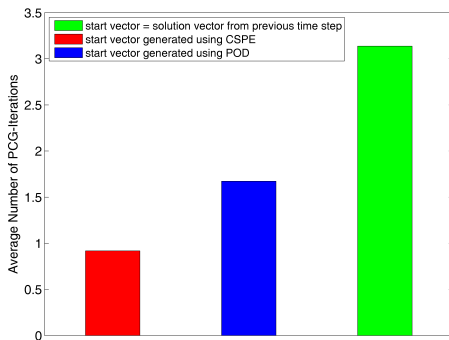


Fig. 1. Average number of PCG iterations

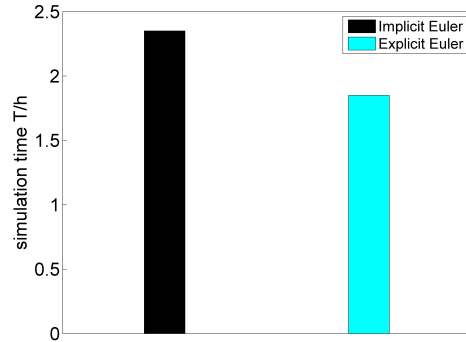


Fig. 2. Comparison simulation times

Acknowledgement. This work was supported by the German Research Foundation DFG (grant numbers CL143/11-1, SCHO1562/1-1) and by the Excellence Initiative of the German Federal and State Governments and The Graduate School of Computational Engineering at TU Darmstadt.

References

1. S. Außerhofer, O. Bíro, and K. Preis. Discontinuous galerkin finite elements in time domain eddy-current problems. *IEEE Trans. Mag.*, 45(3):1300–1303, Mar. 2009.
2. M. Clemens, S. Schöps, H. De Gersem, and A. Bartel. Decomposition and regularization of nonlinear anisotropic curl-curl daes. *Compel*, 30(6):1701–1714, Nov. 2011.
3. M. Clemens, M. Wilke, R. Schuhmann, and T. Weiland. Subspace projection extrapolation scheme for transient field simulations. *IEEE Trans. Mag.*, 40(2):934–937, Mar. 2004.
4. J. Dutié, M. Clemens, and S. Schöps. Explicit time integration of eddy current problems using a selective matrix update strategy. Submitted to IGTE 2016.
5. J. Dutié, M. Clemens, and S. Schöps. Multiple right-hand side techniques in semi-explicit time integration methods for transient eddy current problems. Submitted to CEFC 2016.
6. J. Dutié, M. Clemens, S. Schöps, and G. Wimmer. Explicit time integration of transient eddy current problems. Presented at EMF 2016.
7. A. Kameari. Calculation of transient 3d eddy current using edge-elements. *IEEE Trans. Mag.*, 26(2):466–469, Mar. 1990.
8. T. Nakata and K. Fujiwara. Results for benchmark problem 10 (steel plates around a coil). *Compel*, 9(3):181–192, 1990.
9. A. Nicolet and F. Delince. Implicit runge-kutta methods for transient magnetic field computation. *IEEE Trans. Mag.*, 32(3):1405–1408, May 1996.
10. S. Schöps, A. Bartel, and M. Clemens. Higher order half-explicit time integration of eddy current problems using domain substructuring. *IEEE Trans. Mag.*, 48(2):623–626, Feb. 2012.
11. T.V. Yioultis, K.S. Charitou, C.S. Antonopoulos, and T.D. Tsioukakis. A finite difference time domain scheme for transient eddy current problems. *IEEE Trans. Mag.*, 37(5):3145–3149, Sep. 2001.

On the spatial variations of the electric network frequency

Neil V. Budko

Numerical Analysis, DIAM, Delft University of Technology, Mekelweg 4, 2628 CD Delft, Netherlands
n.v.budko@tudelft.nl

Summary. A mathematical model is proposed explaining the spatial distribution of the dominant frequency over power networks. Although the frequency is predominantly uniform over well-connected power networks, the weak deviations from the spatial average are not purely random and reflect the sub-dominant eigenvectors of the effective connectivity matrix. Specific properties of these eigenvectors dictate that positive deviations at some locations will always be accompanied by negative deviations at other sites, which is confirmed by the European ENF data.

An electric power network can be viewed as a number of generators, transformers, switches, storage units, loads, etc., interconnected by transmission lines. The actual topology of power networks is extremely complicated, constantly changing, and is not a publicly available information. The Electric Network Frequency (ENF) is the maximum (dominant) frequency of the voltage waveform at a given location. Although the frequency at each site is very close to a certain nominal value, e.g., 50 Hz in Europe, due to the variation in power supplied to the generators and consumed by the loads, the actual ENF value fluctuates. Typically, ENF is allowed to deviate by at most 20 mHz from its nominal value. Larger deviations are mitigated by an active control mechanism, e.g., by reducing or increasing the mechanical power supplied to the generators.

The wave-like nature of large ENF deviations due to significant load/generator events is well-known and has been observed and explained by various electro-mechanical models [1]. Such models explicitly describe the changes in the angular velocity of rotors as a function of absorbed electric power and can be used, e.g., for the design of feedback mechanisms and optimal generator control.

Weaker ENF fluctuations are much less studied, and are often assumed to be random. A long-term database of ENF oscillations is maintained in Europe and can be used for forensic time stamping of audio and video recordings [2]. Careful observations show that ENF variations, while almost synchronous, are not entirely uniform in space even over well-connected networks. Potentially, this could be used for spatial localization of recordings. In fact, an attempt to recover the spatial information from ENF data over the US power network has been reported [3],

where it was shown that the correlation in oscillations at different sites decreases with distance.

The existing models of power networks and of the electromagnetic wave propagation in general say surprisingly little about the dominant frequency of the signals at a given time and location, since the main emphasis has always been on the space-time dependence of the signal amplitude. Therefore, here we develop a mathematical model specifically aimed at the spatial distribution of dominant frequencies. The present model does not concern the physical origin of variations, which are presumed to be adequately described by the aforementioned electro-mechanical models [1]. Neither are we interested in slowly propagating large-scale electro-mechanical waves. Instead, we focus on the instantaneous relation between the dominant frequencies at different locations on the network showing that they obey a simple linear-algebraic relation involving the effective connectivity matrix of the power network. The mathematical structure of this relation explains not only the prevailing uniformity of the ENF value over a well-connected network, but also predicts particular patterns in the eventual weak spatial variations of ENF. This prediction is confirmed by the experimental data provided by the FNET/GridEye Consortium [4].

We start with a simplified signal generation and propagation model. Let $u_i(t)$ be the voltage waveform measured at site $i = 1, \dots, n$ at time t . Assuming that all measurement sites correspond to the location of signal sources (power generators, nonlinear elements, impedance jumps, etc) we use the Telegrapher's equations to arrive at

$$u_i(t) = \sum_{j=1}^n r_{ij} u_j(t - \tau_{ij}) = \sum_{j=1}^n r_{ij} v_j(t), \quad (1)$$

where r_{ij} is the length dependent decay factor of the transmission line from site j to site i , and τ_{ij} is the corresponding time delay.

To derive the ENF equation we apply the short-time Fourier transform of (1), then, the Taylor expansion of the frequency-domain signal amplitudes, eventually arriving at the following linear algebraic equation describing the ENF distribution at time t_k :

$$\mathbf{f}(k) \approx A(k)\mathbf{s}(k) \quad (2)$$

where the vector $\mathbf{f}(k) \in \mathbb{R}^n$ contains the ENF values at all measurement sites, the vector $\mathbf{s}(k) \in \mathbb{R}^n$ con-

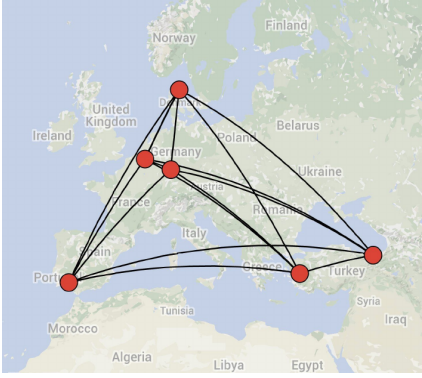


Fig. 1. Location of the available ENF measurement sites and their effective interconnects over the European power network (data provided by FNET). Turkey’s network has been synchronized with the rest of Europe in April 2015.

tains the unknown dominant frequencies of the source waveforms, and the effective connectivity matrix A is non-negative real and row-stochastic.

The fact that the matrix A in the ENF model (2) is non-negative real and row-stochastic leads to the following important conclusions concerning the possible structure of the vector $\mathbf{f}(k)$:

(1) The vector $\mathbf{e} \in \mathbb{R}^n$ filled with ones is an eigenvector of A corresponding to the eigenvalue $\lambda_1 = 1$, which, according to the Perron-Frobenius Theorem is also a largest-magnitude eigenvalue of A .

(2) If matrix A is also symmetric and irreducible (well-connected network), then $\lambda_1 = 1$ is simple and \mathbf{e} is the unique dominant eigenvector. This means that the ENF vector will be approximately uniform, i.e., $\mathbf{f}(k) \approx \alpha(k)\mathbf{e}$, where $\alpha(k)$ is some real number. The small perturbations in the overall uniform structure of $\mathbf{f}(k)$ are due to the sub-dominant eigenvectors corresponding to the next few eigenvalues.

(3) Another consequence of the Perron-Frobenius Theorem is that \mathbf{e} will be the only eigenvector of A with all positive entries. Hence, all other eigenvectors will have negative as well as positive entries. Therefore, small positive deviations of ENF from its spatial mean at some sites will always be accompanied by simultaneous negative deviations at other sites. Moreover, if $A(k) \approx A$ is time-independent, then this behavior will be consistently observed at the same sites.

The last conclusion is particularly important since it may allow approximate localization of ENF measurements within the network. To confirm this prediction experimental ENF data from six European sites shown in Fig. 1 were employed.

For $A(k) \approx A$ the structure of sub-dominant eigenvectors should be visible in the data covariance matrix. Our preliminary experimental results with the available one hour long ENF data confirm this prediction, with the typical sample covariance matrix shown in Fig. 2. Each entry C_{ij} of this matrix corresponds to

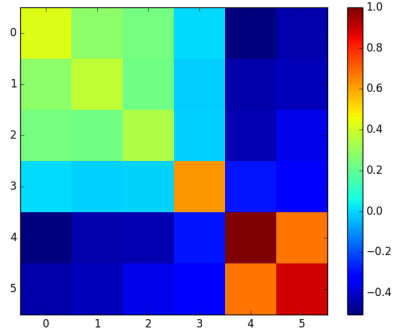


Fig. 2. Typical ENF data covariance matrix (normalized).

the sample covariance of ENF data (based on 100 consecutive data points) recorded at the sites i and j . In this matrix the indexes of the measurement sites depicted in Fig. 1 are arranged as follows: ’0’ – Aalborg, ’1’ – Heverlee, ’2’ – Darmstadt, ’3’ – Huelva, ’4’ – Manisa, ’5’ – Trabzon. As one can see, strong positive correlations in ENF oscillations are observed at the three Northern-European sites as well as at the two sites in Turkey. A weak positive correlation is seen between the Spanish Huelva and the Danish Aalborg. At the same time, strong negative correlation is observed between the Northern-European and Turkish sites, and weaker negative correlations are seen between Huelva and Darmstadt/Heverlee, and Huelva and Turkey. These negative correlations persist throughout differently chosen samples of ENF data, meaning that, on average, as ENF deviates positively (from its spatial mean) in Northern Europe, it simultaneously deviates negatively in Turkey, etc. This behavior is indicative of the sub-dominant spatial eigenvectors of a row-stochastic matrix predicted by our theory.

Acknowledgement. The author is grateful to Jiecheng (Jeff) Zhao and Prof. Yilu Liu of the University of Tennessee for providing the ENF data obtained by the FNET/GridEye Consortium [4].

References

1. L. Huang. Electromechanical wave propagation in large electric power systems. *PhD Thesis*, Virginia Polytechnic Institute and State University, 2003.
2. M. Huijbregtse and Z. Geradts. Using the ENF criterion for determining the time of recording of short digital audio recordings. *Computational Forensics*, pp. 116–124, Springer, 2009.
3. R. Garg, A. Hajj-Ahmad, and M. Wu. Geo-location estimation from electrical network frequency signals. *ICASSP*, pp. 2862–2866, 2013.
4. FNET/GridEye Consortium, University of Tennessee, <http://fnetpublic.utk.edu/index.html>

Stability Analysis of Electromagnetic Transient Simulations

Wim Schoenmaker¹, Christian Strohm², Kai Bittner³, Hans Georg Brachtendorf³, and Caren Tischendorf²

¹ MAGWEL NV, Vital Decosterstraat 44/27, B-3000 Leuven Belgium wim.schoenmaker@magwel.com,

² Humboldt University of Berlin Unter den Linden 6, D-10099 Berlin, Germany
christian.strohm@math.hu-berlin.de, caren.tischendorf@math.hu-berlin.de

³ University of Applied Sciences Upper Austria, Softwarepark 11 A-4232, Hagenberg Austria
Kai.Bittner@fh-hagenberg.at, Hans-Georg.Brachtendorf@fh-hagenberg.at

Summary. We present an analysis of the stability characteristics of the discretized Maxwell-Ampere equations that result from a finite integration of the potential formulation. We demonstrate that the derivation of the discrete versions of these equations will result into unstable formulations due to a wrong transition from a continuous expression to a discretized equivalent version. The key message of this contribution is that in the conversion from a continuous expression to a discrete expression one should be alert for the original motivation of the presence of the prior form. Moreover, we announce further conditions that must be met in the discretization procedure in order to define stable and therefore physical sensible discrete formulations of the Maxwell-Ampere equations.

1 Extended Abstract

It is a well-known fact that electrical systems containing resistors will respond to transient signals in such a way that when the stimulus stops at some time instant the electromagnetic fields will gradually decay due to two physical mechanisms. First of all the resistances convert electrical energy into heat such that the electric energy decreases. Secondly for open systems there is radiation loss which also results into the situation that the electrical energy decays when time proceeds.

When constructing a transient simulation tool of electrical systems it is required that the basic fact of above energy decay mechanism is mimiced by the simulator. For circuit simulation tools this fact is easily reproduced because the circuit equations that contain resistors are in general stable. We can identify stability as a property of the circuit equations in the following way.

Let $\mathbf{X}(t)$ be the collection of all system or circuit variables. The complete system of circuit equations is given by the state-space equations

$$E \frac{d}{dt} \mathbf{X} + \mathbf{A} \mathbf{X} = 0 \quad (1)$$

If E is a non-singular matrix we may rewrite (1) as

$$\frac{d}{dt} \mathbf{X} + \mathbf{J} \mathbf{X} = 0, \quad \mathbf{J} = E^{-1} \mathbf{A} \quad (2)$$

Stability corresponds to the property of \mathbf{J} that all its eigenvalues have real parts larger than or equal zero. If some eigenvalues have real part less than zero, the system has modes that explode when time proceeds which conflicts the energy conservation law and the system is therefore unphysical. Of course if it is impossible to create initial conditions such that when decomposed into the eigenvector base there are no components corresponding to negative real-part eigenvalues one may conclude that these modes will neither develop in the future and therefore the formulation is physical acceptable. Unfortunately this does not mean that if such a formulation of the system equations exists, e.g. \mathbf{J} has negative real-part eigenvalues but the initial condition projected onto the negative real-part eigenvectors is empty, that the simulation set up is physically save. While the transient time steps accumulate, numerical noise can mix into the transient solution and that after some time leap the solution explodes and yet becomes physically unacceptable. This was nicely demonstrated in [1].

As is seen from (2), the stability criterion could be straightforwardly connected to the formal solution

$$\mathbf{X}(t) = \mathbf{X}(0) e^{-\mathbf{J}t} \quad (3)$$

This solution is easily obtained because the system equations are *first* order in time. When the Maxwell-Ampere equations are considered we must account for the wave-like solutions and these equations are *second* order in time. The stability analysis must be revised. The Maxwell-Ampere equations in the potential formulation are given in [2]. By introducing the variable $\Pi = \partial_t \mathbf{A}$ the second-order system of equations is converted to first-order. Of course this step does not change the characteristic features of the solution, but it makes the system accessible to regular stability analysis. Of critical importance are the details of the implementation of the gauge condition. In order to make the curl-curl operator more laplacian-like we add the gauge condition to this equation ($\mu_r = 1$):

$$\begin{aligned} \nabla \times (\nabla \times \mathbf{A}) - \nabla (\nabla \cdot \mathbf{A}) &= \mu_0 \mathbf{J}_c \\ + \frac{\partial}{\partial t} (-\mu_0 \varepsilon (\nabla V + \Pi)) + \mu_0 \xi \nabla \left(\varepsilon \frac{\partial V}{\partial t} \right) & \quad (4) \end{aligned}$$

There are two terms that contain a mixture of a spatial and a time derivative, e.g.

$$-\mu_0 \frac{\partial}{\partial t} (\epsilon \nabla V) \quad \text{and} \quad \mu_0 \xi \nabla \left(\epsilon \frac{\partial V}{\partial t} \right) \quad (5)$$

It turns out that these terms need a different discretization based on the origin of appearance in the Maxwell-Ampere equation. The first term in (5) needs to be discretized as is done for the term

$$\frac{\partial}{\partial t} (-\mu_0 \epsilon \Pi) \quad (6)$$

The discretization is based on the finite-*surface* integration, whereas the second term in (5) needs to be discretized as is done for the term

$$\nabla(\nabla \cdot \mathbf{A}) \quad (7)$$

The latter is discretized using the finite-*volume* discretization. We observed that dealing with both terms using the finite-volume discretization leads to an unstable discretized formulation of the Maxwell-Ampere system. This is demonstrated in the following numerical example. In Fig. 1, a twisted metallic bar is shown and a coarse mesh is used. This allows us to do a detailed eigenvalue analysis of the discretized system. In

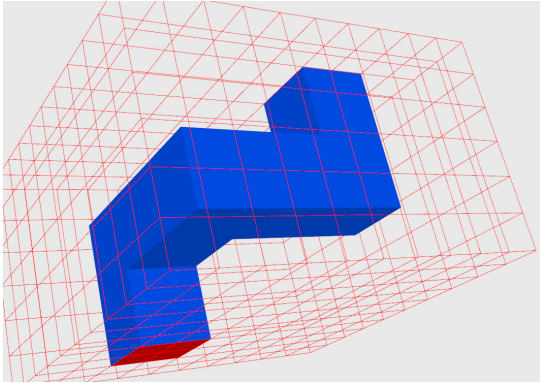


Fig. 1. Twisted bar used for computing the spectrum of the matrix that determines the system stability.

Fig. 2, the spectrum of the matrix J is shown based on a finite-volume implementation of both terms in (5). Finally, in Fig. 3, the spectrum of J is shown where J results from a discretization of (5) using the finite-*surface* integration method for the left term and keeping the discretization of the right term unaltered. With this simple example we have demonstrated that the conversion of continuous terms to discrete representative terms must account for the original motivation behind their presence. In the final submission we will also discuss the need for a strictly semi-definite discretization of the laplacian part of (4) in order to arrive at a stable system of equations.

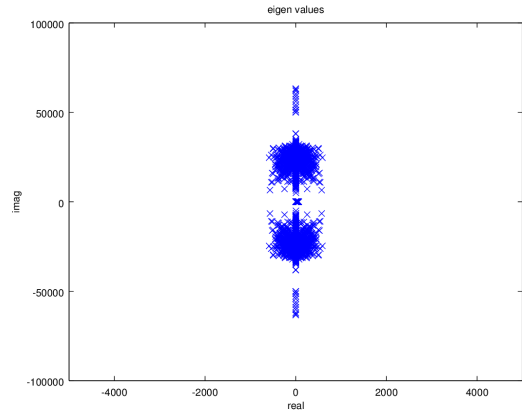


Fig. 2. Zoom -in to the eigenvalue spectrum around the real axis using exclusively finite-volume discretization for terms containing a mixed temporal and spatial differentiation.

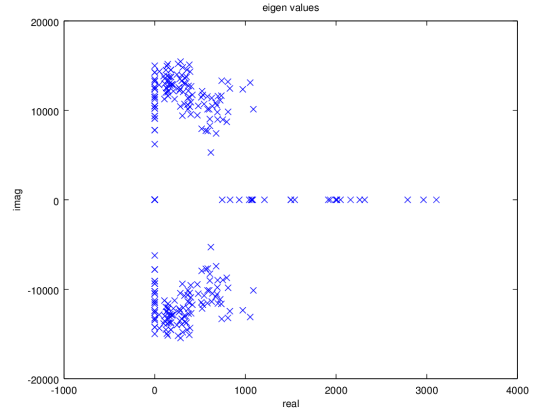


Fig. 3. Zoom -in to the eigenvalue spectrum around the real axis using finite-volume discretization and finite-surface integration for terms containing a mixed temporal and spatial differentiation.

Acknowledgement. This work is funded by the European FP7 project nanoCOPS under grant 619166.

References

1. S. Baumanns and Markus Clemens and Sebastian Schops. Structural Aspects of Regularized Full Maxwell Electrodynamic Potential Formulations Using FIT. *Proceedings of the "2013 International Symposium on Electromagnetic Theory Proc 2013 ISET, 24PM1C-01: 1007–1010, 2014*
2. W. Schoenmaker Q. Chen and P. Galy. Computation of Self-Induced Magnetic Field Effects Including the Lorentz Force for Fast-Transient Phenomena in Integrated-Circuit Devices. *IEEE Transactions on Computer-Aided Design of Integrated Circuits and Systems*, 33:893–902, 2014.

Electro-Thermal Simulations with Skin-Layers and Contacts

Jörg Ostrowski¹, Raffael Casagrande³, Ralf Hiptmair³, Philipp-Thomas Müller², Thomas Werder Schläpfer¹, and Christoph Winkelmann³

¹ ABB Switzerland Ltd., Corporate Research Joerg.Ostrowski@ch.abb.com

² RWTH Aachen

³ ETH Zürich, Seminar for Applied Mathematics

Summary. We show a coupled electro-thermal simulation of a large, complex industrial device that yields a temperature distribution with only small deviations from measurements. Firstly, the ohmic losses in the conductors are calculated by a FEM-solver of the time-harmonic Full Maxwell's equations. For this we introduce a model to account for electric contact resistances, and a gradient based error indicator for h-refinement. Secondly, convective and radiative cooling by the surrounding gas is calculated by a commercial CFD solver. An interesting finding is that computations on comparably coarse meshes which do not resolve the skin layer yield surprisingly high precision of the ohmic losses, as well as good temperature predictions.

1 Background

Industrial power devices are usually large (some meters) and geometrically complex. Examples of such devices are transformers or circuit breakers (CB). During nominal operation, the usual 50 Hz sinusoidal current produces ohmic losses that heat up the device. Losses due to contact resistances sometimes amount up to 50% of all ohmic losses. The devices are cooled by convection of the surrounding gas and by radiation. In order to prevent damage by over-heating, it is necessary to keep the temperature everywhere below device-specific limits. The experimental determination of the temperature distribution is possible but expensive. Simulations are a cheaper and enlightening alternative.

In a former research project, we developed a Full Maxwell solver in Coulomb gauge that is stable in the low frequency limit [3]. We use this existing solver for the electromagnetic part of the coupled electro-thermal simulation. We develop models for the electrical contacts and for adaptive mesh refinement. They are introduced in the next two chapters. In the last chapter we show an electro-thermal simulation of a CB and compare the results with measurements. We want to point out that for this specific example it would be sufficient to solve the eddy current equations instead of the full Maxwell equations. However, the model for the electrical contacts that we introduce here is general, i.e. also capacitive effects are included.

2 Electric Contacts

Electric contact resistances (ECR) are a consequence of the roughness of the contact surfaces [4]. Due to this roughness, the effective cross section is decreased and the resistance increases. Because this happens on a very small scale (μm), it cannot be resolved, and must be modelled macroscopically. The increase in the resistance manifests itself in a jump of the voltage. We model this jump by an additional discontinuous function s in the electric scalar potential $\varphi = \tilde{\varphi} + s$, where $\tilde{\varphi}$ is the continuous part of the potential. The normal current density in the contact can be written as $j_n = (\sigma + i\omega\epsilon)/d \cdot s$, where σ, ϵ are the material parameters inside the electrical contact with thickness d . We will show in the full paper how this expression can be included consistently in the our Full Maxwell solver. We tested the formulation with several configurations, see Fig.1.

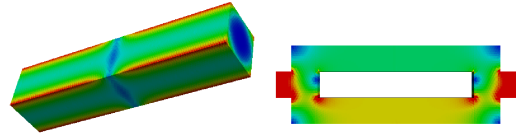


Fig. 1. Left: Current density in a bar with an ECR in the center at 50 Hz. Right: Current density in a setup with two ECRs $\frac{R_1}{R_2} = \frac{2}{1}$ in the center of the paths at 0 Hz $\Rightarrow \frac{I_1}{I_2} = \frac{1}{2}$.

3 Adaptive Refinement for Ohmic Losses

We perform adaptive h-refinement to reduce the error in the calculated ohmic losses. To this end, one could use a rigorous error estimator, e.g. as presented in [1]. Instead, we choose to develop an ad-hoc error indicator. Our error indicator η_T for cell T is defined as $\eta_T = \max\{\eta_{T,g}, \eta_{T,s}\}$. Here, the gradient indicator $\eta_{T,g} = |T| \sqrt{q_T / \sigma_T} \max_{T' \in N(T)} \|\mathbf{j}_T - \mathbf{j}_{T'}\|_2$ approximates the error in the ohmic losses using loss density q , conductivity σ , and current density \mathbf{j} on neighboring conductor cells $T' \in N(T)$. If there is only one cell across the conductor thickness, neighboring conductor cells will have very similar values, hence $\eta_{T,g}$ will be very small and wrong if the mesh does not resolve an eventual skin layer. This issue is overcome by the

skin indicator $\eta_{T,s}$ which is an approximation of the value that the gradient indicator would take if there was a neighbor cell in thickness direction.

Using the cell-wise error indicator η_T we can construct an error indicator for the total losses on some part P of the conductor as $\eta_P = (\sum_{T \in P} \eta_T^2)^{1/2}$.

We use the bar with ECR from Fig.1 (left) as a test case. Fig.2 shows the error indicator per cell for a coarse mesh. One can see that it reliably detects cells at the ECR, next to edges and to surfaces.

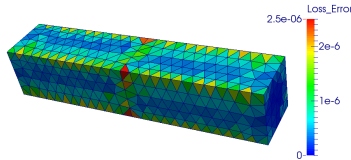


Fig. 2. Error indicator η_T / W .

We perform uniform refinement in the conductor, and plot the error indicator η_P (relative to the total losses) for the two parts on either side of the contact against the ratio of mesh size and skin depth in Fig.3 (in orange). For comparison, we also plot the error as the difference to the finest mesh (in blue). Lines are plotted for part 1 and markers for part 2. One can see that the error indicators agree quite well with the actual errors. Moreover, the total losses per part are well approximated even on meshes that do not resolve the skin layer. It is known that smooth functionals converge faster than the local solution in FEM, which explains this observation at least partly.

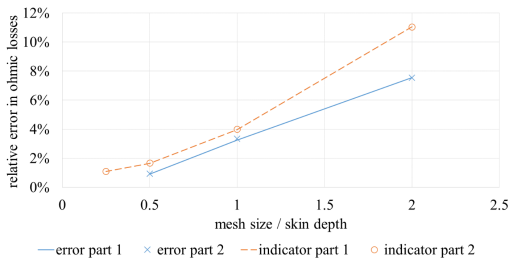


Fig. 3. Convergence of losses under refinement.

4 Thermal Simulation

We perform a simulation of convective and radiative cooling in ANSYS Fluent [2] with the ohmic losses as source terms until a steady state is reached. Electric and thermal contact resistances are included, which both have a similar significant importance. The mesh is different from the electric computation, and resolves thermal boundary layers. We use a robust, conservative procedure to map the ohmic losses from the electric to the thermal mesh.

The Wiedemann-Franz law states that good electrical conductors are also good thermal conductors.

Therefore, any uneven distribution of loss densities in a good electric conductor is strongly smoothed out in the steady state temperature profile. Consequently, the actual skin layer does not need to be resolved for this application, as long as the total losses per part are well approximated.

We simulate a 7.5 m long CB with wall thicknesses and skin depths in the order of 10 mm. The streamlines inside the CB are depicted in Fig.4. They show the natural convection.

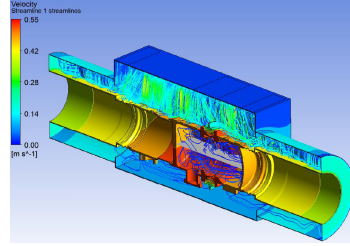


Fig. 4. Streamlines in CB.

In Fig.5 we compare the simulation with an experiment by plotting the mean temperature rise along both the inner conductor part and the enclosure. Simulation and experiment agree within 3 K.

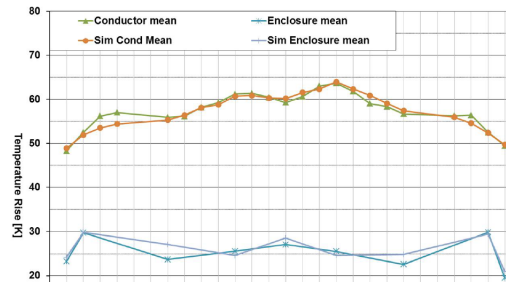


Fig. 5. Temperature rise along CB.

In the full paper, we will provide practical guidelines for balancing accuracy and computation time in electro-thermal simulations.

Acknowledgement. This work has been co-funded by the Swiss Commission for Technology and Innovation (CTI).

References

1. R. Beck, R. Hiptmair, R.H.W. Hoppe, and B. Wohlmuth. Residual based a posteriori error estimators for eddy current computation. *M2AN Mathematical Modelling and Numerical Analysis*, 34(1):159–182, 2000.
2. ANSYS Fluent. www.ansys.com/products/fluids/ansys-fluent.
3. R. Hiptmair, F. Krämer, and J. Ostrowski. A robust Maxwell formulation for all frequencies. *IEEE Transactions on Magnetics*, 44(6):682–685, 2008.
4. R. Holm. *Electric contacts handbook*. Springer, 1958.

Finite Elements for the Simulation of Coupled Acousto-Magneto-Mechanical Systems with Application to MRI Scanner Design

P.D. Ledger, S. Bagwell, and A.J. Gil

Zienkiewicz Centre for Computational Engineering, College of Engineering, Swansea University,
Bay Campus, Swansea SA1 8EN, UK
p.d.ledger@swansea.ac.uk, 638988@swansea.ac.uk, a.j.gil@swansea.ac.uk

Summary. We focus on the generation of a strongly coupled monolithic system to describe the interaction of the magnetic field, generated mechanical vibrations and corresponding acoustic behaviour active in an MRI environment. We linearise the resulting nonlinear equations and consider a frequency domain axisymmetric formulation of the full three dimensional problem using a *hp* finite element discretisation.

1 Introduction

Recently Magnetic Resonance Imaging (MRI) has become an important tool in the medical industry. The non-intrusive imaging capability and high resolution makes it desirable for identifying a range of medical ailments, such as tumours, damaged cartilage and internal bleeding. The most common type of magnet used in MRI scanners are superconducting magnets, consisting of superconducting wire cooled by liquid helium contained within a vessel known as a cryostat. Figure 1 shows a typical setup of an MRI scanner, which consists essentially of four main components. A set of main magnetic coils produce a strong uniform stationary magnetic field across the radial section of the scanner. The secondary magnetic coils are used to avoid large stray fields arising outside the scanner. The cryostat consists of a set of metallic vessels used to maintain the supercooled magnet temperatures and shield from radiation. A set of resistive coils inside the imaging volume, known as gradient coils, produce pulsed gradient magnetic fields to generate an image of the patient.

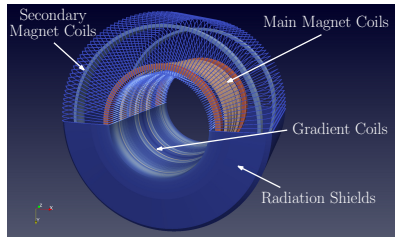


Fig. 1: Primary Components of a typical MRI scanner

The presence of eddy currents in these conducting (metallic) vessels can be caused by changing magnetic fields, such as those generated by the pulsed gradient fields. These eddy currents can cause perturbations in the magnetic field. They also give rise to Lorentz forces and exert electro-mechanical stresses in the conducting components which cause them to vibrate and deform. These deformations cause the magnetic field to further perturb thus generating more eddy currents. The vibrations also cause perturbations of the surrounding air, which in turn produces an acoustic pressure field. These phenomena can have undesired effects causing imaging artefacts (ghosting), decreased component life and uncomfortable conditions for the patient, due to the noise from mechanical vibrations.

2 Coupled System

The aim of this work is to develop a computational analysis tool to aid in the magnet design by providing a better understanding of the induced vibrations and acoustic behaviour. The coupling involves the transient eddy current equation problem

$$\nabla \times \mu^{-1} \nabla \times \mathbf{A} = \mathbf{J}^s(t) - \gamma \frac{\partial \mathbf{A}}{\partial t} + \gamma \frac{\partial \mathbf{u}}{\partial t} \times \nabla \times \mathbf{A} \quad \text{in } \mathbb{R}^3 \quad (1a)$$

$$\nabla \cdot \mathbf{A} = 0 \quad \text{in } \mathbb{R}^3 \setminus \Omega_c \quad (1b)$$

$$\mathbf{A} = O(|\mathbf{x}|^{-1}) \quad \text{as } \mathbf{x} \rightarrow \infty \quad (1c)$$

where \mathbf{A} is magnetic vector potential such that $\mathbf{B} = \mu \mathbf{H} =: \text{curl} \mathbf{A}$ is the magnetic flux density and \mathbf{H} is the magnetic field. The divergence free current source $\mathbf{J}^s(t) := \mathbf{J}_{DC}^s + \mathbf{J}_{AC}^s(t)$ has static and dynamic components with subscripts *DC* and *AC*, respectively. The conductivity γ is non-zero in conducting components Ω_c and the magnetic permeability μ reduces to that of free space in $\mathbb{R}^3 \setminus \Omega_c$. The vector potential \mathbf{A} satisfies the transmission conditions

$$[\mathbf{n} \times \mathbf{A}]_{\partial \Omega_c} = \mathbf{0} \quad [\mathbf{n} \times \mu^{-1} \nabla \times \mathbf{A}]_{\partial \Omega_c} = \mathbf{0}$$

on $\partial\Omega_c$ where $[\cdot]_{\partial\Omega_c}$ denotes the jump on this interface and \mathbf{n} is a unit outward normal vector.

The latter term in (1a) is the Lorentz currents, where \mathbf{u} denotes the mechanical displacements obtained from the solution to

$$\nabla \cdot (\boldsymbol{\sigma}^e + \boldsymbol{\sigma}^m) = \rho \frac{\partial^2 \mathbf{u}}{\partial t^2} \quad \text{in } \Omega_c \quad (2a)$$

$$\mathbf{u} = \mathbf{0} \quad \text{on } \partial\Omega_c^D \quad (2b)$$

where $\partial\Omega_c = \partial\Omega_c^D \cup \partial\Omega_c^T$, $\boldsymbol{\sigma}^m := \lambda \text{tr}(\boldsymbol{\varepsilon}(\mathbf{u}))\mathbb{I} + 2G\boldsymbol{\varepsilon}(\mathbf{u})$, is the Cauchy stress tensor, $\boldsymbol{\varepsilon} := \frac{1}{2}(\nabla\mathbf{u} + \nabla\mathbf{u}^T)$, \mathbb{I} the identity tensor, λ , G denote the Lamé parameters, ρ the mass density and

$$\begin{aligned} \boldsymbol{\sigma}^e &:= \mu \left(\mathbf{H} \otimes \mathbf{H} - \frac{1}{2} |\mathbf{H}|^2 \mathbb{I} \right) \\ &= \mu^{-1} \left(\nabla \times \mathbf{A} \otimes \nabla \times \mathbf{A} - \frac{1}{2} |\nabla \times \mathbf{A}|^2 \mathbb{I} \right) \end{aligned}$$

is the magnetic component of the Maxwell stress tensor [2].

In free space $\boldsymbol{\sigma}^m$ has only a volumetric part $\boldsymbol{\sigma}_{vol}^m = \hat{p}\mathbb{I} = \kappa \nabla \cdot \mathbf{u}\mathbb{I}$ where \hat{p} is some pressure field. This means that (2a) reduces to the scalar wave equation and the pressure field is the solution to

$$\nabla^2 \hat{p} - \frac{1}{c^2} \frac{\partial^2 \hat{p}}{\partial t^2} = \nabla \cdot (\nabla \cdot \boldsymbol{\sigma}^e) = 0 \quad \text{in } \mathbb{R}^3 \setminus \Omega_c \quad (3a)$$

$$\lim_{|\mathbf{x}| \rightarrow \infty} \left(\frac{\partial \hat{p}}{\partial |\mathbf{x}|} + \frac{\partial \hat{p}}{\partial t} \right) = O(|\mathbf{x}|^{-1}) \quad (3b)$$

$$(\boldsymbol{\sigma}^e + \boldsymbol{\sigma}^m) \mathbf{n} \Big|_{\partial\Omega_c}^- = (\hat{p}\mathbb{I} + \boldsymbol{\sigma}^e) \mathbf{n} \Big|_{\partial\Omega_c}^+ \quad (3c)$$

$$\rho \frac{\partial^2 \mathbf{u}}{\partial t^2} \cdot \mathbf{n} \Big|_{\partial\Omega_c}^- = \nabla \hat{p} \cdot \mathbf{n} \Big|_{\partial\Omega_c}^+ \quad (3d)$$

where c is the speed of sound in free space and the support of $\nabla \cdot \boldsymbol{\sigma}^e$ has been taken into account for the transmission conditions included in (3c,3d) [1]. Note that the latter condition also further reduces to

$$\nabla \hat{p} \cdot \mathbf{n} \Big|_{\partial\Omega_c^D}^+ = 0 \quad \rho \frac{\partial^2 \mathbf{u}}{\partial t^2} \cdot \mathbf{n} \Big|_{\partial\Omega_c^T}^- = \nabla \hat{p} \cdot \mathbf{n} \Big|_{\partial\Omega_c^T}^+$$

in light of the known Dirichlet displacement condition (2b) for the mechanical problem.

3 Solution Approach

In [2] we have previously proposed a fixed-point computational strategy for the computational solution of the coupled system of equations (1,2) in axisymmetric coordinates and the frequency domain. Motivated by industrial need to accurately capture the skin depth effects in conducting components and the corresponding mechanical response, we chose to discretise the problem by hp -finite elements, which permit both h

and p refinements. Although the converged results we achieved were in good agreement with an industrial benchmark, an unsatisfactory aspect was that a series of assumptions had to be made in order to arrive a *linearised system* so that the transient equations could be posed in the frequency domain. Recently, in [1], we have linearised the transient equations (1,2,3) about a static solution associated with the static component of the current source \mathbf{J}_{DC}^s , which permits us to rigorously justify the equations we proposed in [2] for the frequency domain analysis. Moreover, from this linearisation, we have obtained a monolithic system, which can be solved in a single iteration to recover the frequency domain response of the coupled acousto-magneto-mechanical problem. The presentation will explain our approach in more detail and include a series of numerical examples obtained by a hp -finite element discretisation of the equations in axisymmetric coordinates. Illustrative numerical results for the magnetic field lines associated with the static (DC) and gradient (AC) coils in a simplified model of an MRI scanner are shown in Figure 2.

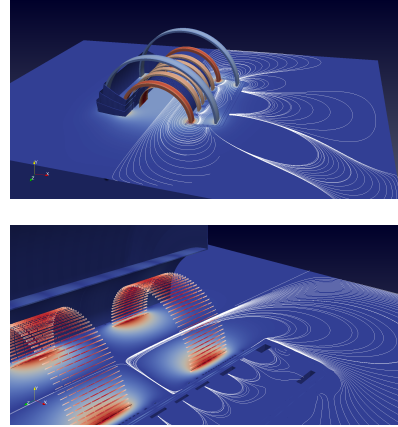


Fig. 2: Static (top) and Gradient (bottom) Magnetic fields

Acknowledgement. The authors gratefully acknowledge the support of EPSRC and Siemens Magnet Technology.

References

1. S. Bagwell, P.D. Ledger, and A.J. Gil. hp -finite element framework for acousto-magneto-mechanical coupling. 2016. In preparation.
2. P.D. Ledger, A.J. Gil, R.Poya, M. Kruip, I. Wilkinson, and S. Bagwell. Solution of an industrially relevant coupled magneto-mechanical problem set on an axisymmetric domain. *Applied Mathematical Modelling*, 40:1959–1971, 2016.

Structural and Implementational Aspects of Field/Circuit Coupling in A-V and T-Ω Based Formulations

Idoia Cortes Garcia^{1,2}, Alexander Krimm^{1,2}, Herbert De Gersem^{1,2}, and Sebastian Schöps^{1,2}

¹ Institut für Theorie Elektromagnetischer Felder, Technische Universität Darmstadt, 64289 Darmstadt, Germany

² Graduate School of Computational Engineering, Technische Universität Darmstadt, 64293 Darmstadt, Germany
schoeps@gsc.tu-darmstadt.de

Summary. This paper discusses magnetoquasistatic field and electric circuit coupling in terms of both T - Ω and A - V formulations. A flexible and efficient software implementation via TCP/IP sockets is proposed.

1 Introduction

Particularly for the design of electric energy transducers, it is common to simulate magnetoquasistatic fields together with the surrounding circuitry, e.g., the power electronics controlling a drive. In mathematical literature, mainly the magnetic vector potential based A - V -formulation coupled to a network based on nodal analysis has been analyzed, e.g. [7, 8]. However, since the surrounding circuits in power electronics are rather small, loop analysis is still very popular. Secondly, recent advances in computational cohomology [6] have led to increasing interest in the magnetic scalar potential T - Ω -formulation.

This contribution aims at discussing the structural implications of the different formulation and proposes a generic interface based on the software framework ONELAB to allow an efficient coupling of network simulator and finite element code [4].

2 Formulation

Let us consider the magnetoquasistatic approximation to Maxwell's equations excited by N_{str} stranded conductors, which are for example used for modelling coils with wire radius smaller than the skin depth. The resulting equations on a computational domain \mathcal{V} and time interval \mathcal{T} read

$$\begin{aligned} \sigma \mathbf{d}_t \mathbf{A} + \nabla \times (\mathbf{v} \nabla \times \mathbf{A}) - \chi_{\text{str}}^{(A)} \mathbf{i}_{\text{str}} &= 0 \\ \int_{\mathcal{V}} \chi_{\text{str}}^{(A)} \cdot \mathbf{d}_t \mathbf{A} \, dV + \mathbf{R}_{\text{str}} \mathbf{i}_{\text{str}} - \mathbf{v}_{\text{str}} &= 0 \end{aligned}$$

where $\mathbf{A} : \mathcal{V} \times \mathcal{T} \mapsto \mathbb{R}^3$ denotes the magnetic vector potential, \mathbf{i}_{str} and $\mathbf{v}_{\text{str}} : \mathcal{T} \mapsto \mathbb{R}^{N_{\text{str}}}$ are applied currents and voltages; σ and $\mathbf{v} : \mathcal{V} \mapsto \mathbb{R}^{3 \times 3}$ are conductivity and reluctivity tensors, $\mathbf{R}_{\text{str}} \in \mathbb{R}^{N_{\text{str}} \times N_{\text{str}}}$ the DC resistance and $\chi_{\text{str}}^{(A)} : \mathcal{V} \mapsto \mathbb{R}^{3 \times N_{\text{str}}}$ is the winding function [9] establishing the 0D-3D coupling. The problem can be equivalently stated in the T - Ω formulation

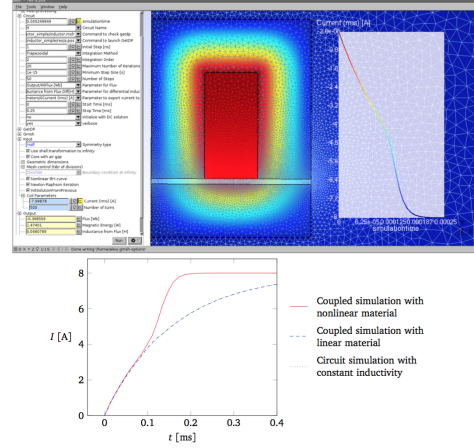


Fig. 1. The field problem in Gmsh and a plot of the current in a coupled field/circuit benchmark problem.

$$\begin{aligned} \mu \mathbf{d}_t \mathbf{T} + \nabla \times (\rho \nabla \times \mathbf{T}) - \mu \nabla \mathbf{d}_t \Omega + \mu \chi_{\text{str}}^{(T)} \mathbf{d}_t \mathbf{i}_{\text{str}} &= 0 \\ \nabla \cdot \left(\mu \frac{d}{dt} \mathbf{T} \right) - \nabla \cdot (\mu \nabla \mathbf{d}_t \Omega) + \nabla \cdot \left(\mu \chi_{\text{str}}^{(T)} \right) \mathbf{d}_t \mathbf{i}_{\text{str}} &= 0 \\ - \int_{\mathcal{V}} \chi_{\text{str}}^{(T)} \cdot (\mu \nabla \mathbf{d}_t \Omega) \, dV + \mathbf{R}_{\text{str}} \mathbf{i}_{\text{str}} + \mathbf{L}_{\text{str}} \mathbf{d}_t \mathbf{i}_{\text{str}} - \mathbf{v}_{\text{str}} &= 0 \end{aligned}$$

with electric vector potential $\mathbf{T} : \mathcal{V} \times \mathcal{T} \mapsto \mathbb{R}^3$ and magnetic scalar potential $\Omega : \mathcal{V} \times \mathcal{T} \mapsto \mathbb{R}$, the resistance $\rho = \sigma^{-1} : \mathcal{V} \mapsto \mathbb{R}^{3 \times 3}$, winding function $\nabla \times \chi_{\text{str}}^{(T)} := \chi_{\text{str}}^{(A)}$ and the self-inductance $\mathbf{L}_{\text{str}} \in \mathbb{R}^{N_{\text{str}} \times N_{\text{str}}}$ of the windings.

In both cases suitable boundary and initial conditions have to be given. Then, space discretization by finite elements or the finite integration technique with subsequent time stepping can be applied [5, 11].

Now, let us consider the case of coupling the field problem to a network given in terms of the (modified) nodal analysis [3]

$$\begin{aligned} \mathbf{A}_C \mathbf{C} \mathbf{A}_C \mathbf{d}_t \mathbf{u} + \mathbf{A}_R \mathbf{G} \mathbf{A}_R^T \mathbf{u} + \mathbf{A}_L \mathbf{i}_L + \mathbf{A}_V \mathbf{i}_V + \dots \\ \dots + \mathbf{A}_{\text{str}} \mathbf{i}_{\text{str}} + \mathbf{A}_I \mathbf{i}_s = 0 \\ \mathbf{L} \mathbf{d}_t \mathbf{i}_L - \mathbf{A}_L^T \mathbf{u} = 0 \\ \mathbf{A}_V^T \mathbf{u} = \mathbf{v}_s \end{aligned}$$

where $\mathbf{u} : \mathcal{T} \mapsto \mathbb{R}^{N_u}$ are the unknown nodal potentials, $\mathbf{i}_V : \mathcal{T} \mapsto \mathbb{R}^{N_V}$ and $\mathbf{A}_{\text{str}} \mathbf{i}_{\text{str}} : \mathcal{T} \mapsto \mathbb{R}^{N_{\text{str}}}$ are currents

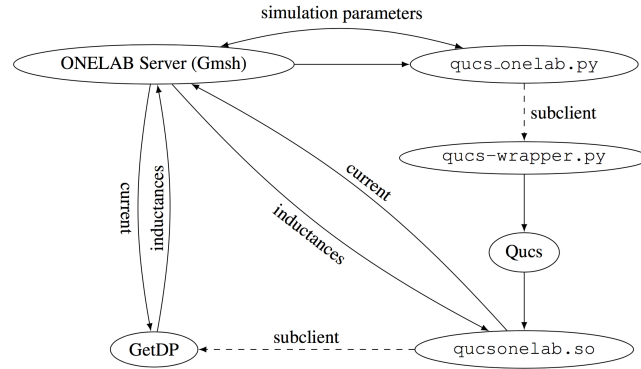


Fig. 2. Coupling Between GetDP and Quite Universal Circuit Simulator (QUCS)

through voltage sources and field devices as given above, respectively. The topology is expressed by incidence matrices $\mathbf{A}_* \in \{-1, 0, 1\}^{N_* \times N_u}$ and the capacitors, resistors, inductors, current and voltage sources are given by $\mathbf{C}, \mathbf{G}, \mathbf{L} \in \mathbb{R}^{N_* \times N_*}$, \mathbf{i}_s and $\mathbf{v}_s : \mathcal{T} \mapsto \mathbb{R}^{N_*}$, respectively. The formulation in terms of the (modified) loop analysis can be stated similarly.

It is important to note that the A - V -formulation in contrast to the T - Ω one is not formulated in terms of derivatives of the coupling quantities \mathbf{i}_{str} and \mathbf{v}_{str} . This difference will be discussed in the full paper in view of the structural properties of nodal (and loop) analysis, cf. [8].

3 Implementation

Generalizing the Schur complement idea from [7, 10], both formulations, i.e., A - V and T - Ω , allow the straightforward extraction of generalized (differential) inductances at each time step. This allows an efficient coupling where only a small amount of data is exchanged. Depending on the formulation, N_{str} perturbed curl-curl or Laplace-type problems have to be solved.

The implementation is based on a client-server model, c.f. Fig. 2, with a server-side database and local or remote clients communicating in-memory or through TCP/IP sockets. The TCP/IP-based design avoids explicit linking of software packages such that even free and non-free codes can be used. In this contribution, OCS [2] and Quite Universal Circuit Simulator (QUCS) have been coupled to GetDP, see Fig. 1, which implements both, the A - V and T - Ω formulations [1].

Acknowledgement. This work is supported by the EU within the FP7-ICT-2013 nanoCOPS project (grant no. 619166), the BMBF SIMUROM Verbundprojekt (grant no. 05M2013) and by the Excellence Initiative of the German Federal and State Governments and the Graduate School of CE at TU Darmstadt.

References

1. C. Geuzaine. GetDP: a general finite-element solver for the de Rham complex. In *PAMM Volume 7 Issue 1. Special Issue: Sixth International Congress on Industrial Applied Mathematics (ICIAM07) and GAMM Annual Meeting, Zürich 2007*, volume 7, pages 1010603–1010604. Wiley, 2008.
2. M. Günther, editor. *Coupled Multiscale Simulation and Optimization in Nanoelectronics*, volume 21 of *Mathematics in Industry*. Springer, Berlin, June 2015.
3. C.-W. Ho, A. E. Ruehli, and P. A. Brennan. The modified nodal approach to network analysis. *IEEE Trans. Circ. Syst.*, 22(6):504–509, June 1975.
4. A. Krimm. Coupling of electromagnetic fields with electric circuits using ONELAB. Bachelor’s thesis, TU Darmstadt, Darmstadt, Germany, June 2015.
5. P. Monk. *Finite Element Methods for Maxwell’s Equations*. Oxford University Press, Oxford, 2003.
6. M. Pellikka, S. Suuriniemi, L. Kettunen, and C. Geuzaine. Homology and cohomology computation in finite element modeling. *SIAM J. Sci. Comput.*, 35(5):B1195–B1214, 2013.
7. S. Schöps, A. Bartel, and H. De Gersem. Multirate time-integration of field/circuit coupled problems by Schur complements. In Bastiaan Michielsen and Jean-René Poirier, editors, *Scientific Computing in Electrical Engineering SCEE 2010*, volume 16 of *Mathematics in Industry*, pages 243–251, Berlin, January 2012. Springer.
8. S. Schöps, A. Bartel, H. De Gersem, and M. Günther. DAE-index and convergence analysis of lumped electric circuits refined by 3-D MQS conductor models. In Janne Roos and Luis R. J. Costa, editors, *Scientific Computing in Electrical Engineering SCEE 2008*, volume 14 of *Mathematics in Industry*, pages 341–350, Berlin, June 2010. Springer.
9. S. Schöps, H. De Gersem, and T. Weiland. Winding functions in transient magnetoquasistatic field-circuit coupled simulations. *COMPEL*, 32(6):2063–2083, September 2013.
10. J. Vaananen. Circuit theoretical approach to couple two-dimensional finite element with external circuit equations. *IEEE Trans. Magn.*, 32(2):400–410, 1996.
11. T. Weiland. A discretization model for the solution of Maxwell’s equations for six-component fields. *AEU*, 31:116–120, March 1977.

An Atlas Model for Simulating Deep Brain Stimulation in the Rat Model for Parkinson's Disease

Andrea Böhme¹, Christian Schmidt¹, and Ursula van Rienen¹

Institute of General Electrical Engineering, University of Rostock, Albert-Einstein-Str. 2, 18059 Rostock, Germany
 andrea.boehme@uni-rostock.de, christian.schmidt6@uni-rostock.de,
 ursula.van-rienen@uni-rostock.de

Summary. Creating realistic *in silico* models of the parkinsonian rat, forms the basis for computing the activation of periprosthetic nerve fibers. Thereby, the effect of deep brain stimulation in *in vivo* rat models can be estimated.

1 Models of Deep Brain Stimulation

Deep brain stimulation is an effective symptomatic treatment of Parkinson's Disease (PD). Although DBS is applied successfully since the late 1980s, its mechanisms of action are still to be clarified. Numerous *in vivo* animal models and *in silico* computational models exist. Most *in silico* models estimate the effect of deep brain stimulation on PD patients to predict the neuronal activation as well as the therapeutic and side effects. Yet, only few computational models exist, which study the stimulating field distribution and neural activation in rodent models. By combining finite element models (FEM) of the DBS-induced stimulating field with multicompartiment cable models of neurons the effect of DBS can be examined. This approach has been applied to create patient-specific models of DBS in PD patients with varying complexity. Thereby, the optimization of clinical DBS therapies [2] has been enabled. This approach has also been applied to subject-specific simulation of DBS in parkinsonian macaques [3]. Interrelating the *in vivo* and *in silico* models is an opportunity to optimize stimulation protocols in future studies. The PD rat model with long-term stimulation introduced in [1] can be used as reference *in vivo* model. Here, miniaturized DBS electrodes adapted for the rat brain were used to treat parkinsonian rats with DBS of the subthalamic nucleus (STN) [1]. Therefore, it is the goal of this work to create an anatomically realistic atlas model of the PD model of the rat.

2 *In silico* modeling

The coupling of neuron-models with the stimulating field distribution, computed in FEM volume conductor models (VCM), enables for the estimation of the activation of neurons of a specific type, size, and orientation [6]. Therefore, an anatomically realistic model of the DBS target region is needed.

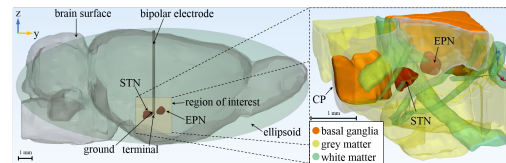


Fig. 1. Ellipsoid, aligned to the rat brain, as simulation domain including a stimulation electrode; detailed, cubic region of interest with white matter fiber tracts (e.g. the corticofugal pathway (CP)) and grey matter including the basal ganglia nuclei subthalamic nucleus (STN) as well as the entopeduncular nucleus (EPN), adapted from [5].

2.1 Volume conductor models

With the FEM software COMSOL Multiphysics® (COMSOL) the VCMs are realized. In Fig. 1 the simulation domain and a detailed cubic region of interest, including the target structures for DBS, are depicted. The rat brain surface can be idealized as an ellipsoid, because the target region for DBS is in the deep brain. Furthermore, the ellipsoids half-axes match the anatomical dimensions of the rat brain. The modeled electrodes are based on the stimulation electrodes in [1]. As described by [7], Laplace equation

$$\nabla \cdot (\boldsymbol{\sigma}(\mathbf{r})\nabla\phi(\mathbf{r})) = 0 \quad (1)$$

is solved with the electric conductivity tensor $\boldsymbol{\sigma}$ and electric potential ϕ . This is based on the quasi-static modeling approach [7]. The electrode's insulation is defined as perfect insulator, while the two electrode contacts are defined by Dirichlet boundary conditions.

Heterogeneity

It is necessary to include the heterogeneity of brain tissue in the modeling procedure, due to the differing conductivities of grey and white matter as well as the several orders of magnitude higher conductivity of cerebrospinal fluid [2, 7]. The heterogeneity can be realized either by voxelwise mapping of the tissue data based on Magnetic Resonance Imaging (MRI) data sets [2, 6, 7] or by creating three-dimensional (3D) models of the structures in the target region of DBS [4]. These are the basal ganglia nuclei STN and entopeduncular nucleus (EPN, rodent equivalent of the

globus pallidus internus) as well as the white matter fiber tracts passing the target region (see Fig. 1).

Anisotropy

It has been shown, that the anisotropy has a great influence on the stimulating field distribution [2, 6, 7]. Especially, if the electrode is placed in areas of high anisotropy, as in white matter fiber tracts. [2] discusses the impact of how the conductivity tensor σ is constructed. One of the proposed methods is scaling and mapping diffusion tensors D , derived from Diffusion Tensor Imaging (DTI) data sets, with

$$\sigma = sD. \quad (2)$$

Another option is to align the conductivity tensor σ to a vector field \mathbf{v} , which follows the anatomical structure of a white matter fiber tract. This can be achieved by creating curvilinear coordinates. By applying the *diffusion method* in COMSOL, a vector field \mathbf{v} is computed. This scalar potential method is solved by Laplace equation with

$$\Delta u = 0, \quad (3)$$

while the vector field \mathbf{v} is computed as the gradient of the solution u with

$$\mathbf{v} = -\nabla u. \quad (4)$$

2.2 Neuron-models

With cable models of myelinated axons [2] the activation of neurons by the stimulating field is computed. Therefore, the position and orientation of neuron-models is defined in the VCM. Thereby, the computed electric potential ϕ can be applied as extracellular potential on each segment of the neuron-model. By solving a set of Hodgkin-Huxley equations it can be determined, in which neuron an action potential is triggered. This depends on its orientation and distance relative to the electrode. To compute the volume of tissue activated (VTA), straight neuron-models are placed parallel and orthogonal in planes radially distributed around the electrode. To estimate the activation of fibers of passage surrounding the DBS target structures, tractography can be used to generate streamlines representing axons [2]. Another, computationally less expensive, approach is to align the neuron-models to the vector field \mathbf{v} defined by the curvilinear coordinates.

3 Comparative study

Based on the work flow described above, a comparative study is carried out. Computed are the stimulating

field distribution, VTA, and the activation of neuron-models aligned to curvilinear coordinates. On this basis, the effects of the uni- and bipolar electrodes described in [1] are compared. Furthermore, the influence of how heterogeneity and anisotropy is implemented in the atlas models, as described in Sect. 2 and depicted in Fig. 2, are evaluated.

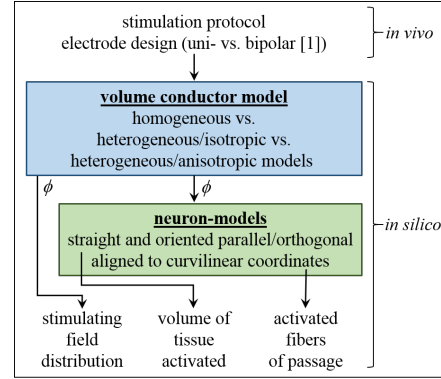


Fig. 2. Work flow of the comparative study

Acknowledgement. This work was supported by the German Science Foundation (DFG) in the scope of the Research Training Group GRK 1505 welisa.

References

1. K Badstübner, T Kröger, E Mix, U Gimsa, R Benecke, and J Gimsa. *Electrical Impedance Properties of Deep Brain Stimulation Electrodes during Long-Term In-Vivo Stimulation in the Parkinson Model of the Rat*, pages 287–297. Springer Verlag, Berlin, 2013.
2. B Howell and CC McIntyre. Analyzing the tradeoff between electrical complexity and accuracy in patient-specific computational models of deep brain stimulation. *J Neural Eng*, 13, 2016.
3. S Miocinovic, M Parent, CR Butson, PJ Hahn, GS Russo, JL Vitek, and CC McIntyre. Computational analysis of subthalamic nucleus and lenticular fasciculus activation during therapeutic deep brain stimulation. *J Neurophysiol*, 96:1569–1580, 2006.
4. A Paffi, F Camera, F Apollonio, G dInzeo, and Micaela Liberti. Numerical characterization of intraoperative and chronic electrodes in deep brain stimulation. *Front Comput Neurosci*, 9, 2015.
5. EA Papp, TB Leergaard, E Calabrese, GA Johnson, and JG Bjaalie. Waxholm space atlas of the sprague dawley rat brain. *NeuroImage*, 97:374–386, 2014.
6. M Åström, JJ Lemaire, and K Wårdell. Influence of heterogeneous and anisotropic tissue conductivity on electric field distribution in deep brain stimulation. *Med Biol Eng Comput*, 50:23–32, 2012.
7. C Schmidt and U van Rienen. Modeling the field distribution in deep brain stimulation: the influence of anisotropy of brain tissue. *IEEE Trans Biomed Eng*, 59:1583–1592, 2012.

Fast and Accurate Time-Domain Simulations of Industrial PLLs

Giovanni De Luca¹, Wil H. A. Schilders¹, Pascal Bolcato², Remi Larcheveque², and Joost Rommes²

¹ TU Eindhoven (NL) g.de.luca@tue.nl, w.h.a.schilders@tue.nl

² Mentor Graphics® (FR) pascal.bolcato@mentor.com, remi.larcheveque@mentor.com
joost.rommes@mentor.com

Summary. We present a methodology to simulate integer- N phase-locked loops (PLLs), as accurate as and faster than full transistor-level (TL) PLL’s simulation, extracting locking time, power consumption, phase noise and jitter. The speedup tends to the division ratio N for noisy simulations, drastically reducing the Time-to-Market for these circuits.

1 Introduction

Circuits with very long simulation time are phase-locked loops (PLLs). PLLs find applications in wireless systems, digital circuits and medical devices. Time-domain analyses are performed by numerically integrating the circuit’s DAEs. For PLLs, the time step during integration is related to the PLL’s output frequency f_{out} (could be GHz), thus a huge number of steps needs to be retained. Designers want to simulate PLLs for a large period of time to extract *power consumption*, *locking time*, *phase noise* and *jitter*.

In the literature, works are based on partial or full replacement of PLL’s blocks by macromodels, others on full TL simulation (e.g., see [1], [2], [3]). However, none of them estimates all the PLL’s factors of interest, equally important.

We propose a technique to accurately extract all the PLL’s characteristics while accelerating noise-free and noisy simulations, by replacing only the VCO and divider blocks with a single phase macromodel, built through steady-state (SST) analyses [4], [5], SST noise methods [6], [7] and the usage of Verilog-A, so it is not invasive for commercial simulators.

2 Methodology

We replace the VCO and divider by a phase macromodel (*VCODIV*), eliminating the fast-varying VCO’s output. The PLL adjusts the oscillator’s control voltage $v_c(t)$ to reach the locking condition ($f_{out} = N \cdot f_{ref}$, with f_{ref} the PLL’s input frequency). We can think of as the oscillator is composed by a “set of SST conditions”, and the PLL “perturbs” them by varying $v_c(t)$, mainly generating phase deviations $\Delta\theta(t)$ on the SSTs [7]. Thus, we characterize *VCODIV* by a phase equation. Since simulators use the MNA form, we specify the *VCODIV* contribution to the KCL at

each block’s pin through *equivalent, perturbed current/voltage sources*. E.g., $v_{out}(t + j(t))$ is the perturbed *VCODIV*’s output. The SST solution is related to a specific $v_c(t) = V_{c,sst}$ and computed with SST analysis, extracting the Fourier coefficients. We reconstruct the equivalent sources with

$$\begin{cases} i(t + \frac{\Delta\theta(t)}{2\pi f_{out}}) = \sum_{k=-N_h}^{N_h} I_k e^{\sqrt{-1}k \cdot \theta_{tot}(t)}, \\ \theta_{tot}(t) = 2\pi f_{out} \cdot t + \Delta\theta(t), \end{cases} \quad (1)$$

with N_h the number of harmonics. Next, we show a law for $\Delta\theta(t)$ governing the *VCODIV*.

The relation between $\Delta\theta(t)$ (or the frequency) and $v_c(t)$ characterizes the phase equation. It is the sensitivity of the oscillator with respect to variation of $v_c(t)$. E.g., for a linear VCO it is a line with constant slope. For nonlinear VCO, we compute a set of slopes $K_{macro,i}$ in the curve f_{out} vs v_c as

$$K_{macro,i} = \frac{\partial f_{out,i}}{\partial V_{c,sst,i}}.$$

The $K_{macro,i}$ is the DC component of the PPV related to the control pin, or extracted through a finite difference approach. The *VCODIV*’s phase-deviation equation due to perturbations on $v_c(t)$ reads as

$$\frac{d}{dt} \Delta\theta_c(t) = \frac{2\pi K_{macro}(V_{c,sst,i})}{N} \cdot \Delta V_c(t),$$

with $\Delta\theta_c(0) = 0$, where $K_{macro}(V_{c,sst,i}) = K_{macro,i}$ and $\Delta V_c(t) = v_c(t) - V_{c,sst,i}$ when $v_c(t) \in [V_{c,l}, V_{c,l+1}]$, with $V_{c,l}, V_{c,l+1}$ the values for which a switch happens between two consecutive SSTs. Fig. 1 shows the original curve (*data*) approximated through the piecewise curve $K_{macro}(V_{c,sst,i})$, whose $K_{macro,i}$ is valid around $V_{c,sst,i}$ for which the i th Fourier coefficients SST_i (diamond) are extracted and used within the switching points $[V_{c,l}, V_{c,l+1}]$ (circles). The SST points are selected with a greedy algorithm, by minimizing a cost-function. Besides, to avoid glitches in the reconstructed waveforms when Fourier coefficients are switched, $\theta_{tot}(t)$ in (1) is of the form

$$\theta_{tot}(t) = \frac{2\pi f_{mid}}{N} t + \int_0^t \frac{2\pi f_{diff,i}}{N} d\tau + \Delta\theta_c(t) - \theta_i, \quad (2)$$

where we remove the SST phase offsets θ_i . To approximate power consumptions, we use linear interpolation on the DC Fourier coefficients computed at the SSTs.

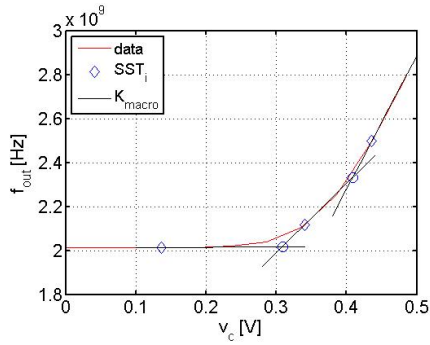


Fig. 1. Approximating f_{out} vs v_c with a combination of intersecting lines, where the i th one has slope $K_{macro,i}$.

For noise analysis, we enrich (2) with two additional terms: $\Delta\theta_{noise,vco}(t)/N$ and $\Delta\theta_{noise,div}(t)$, due to noise from VCO's and divider's device models, respectively. These are obtained by knowing the power spectral densities (PSDs) of VCO's and divider's outputs. E.g., a VCO's phase noise spectrum is approximated by

$$S_{\theta,vco}(\Delta f) = \left(\frac{c_{fl}}{\Delta f} + c_{wh} \right) \cdot \frac{1}{\Delta f^2}. \quad (3)$$

When building VCODIV, power levels c_{fl} (flicker) and c_{wh} (white) are extracted by computing and inspecting $S_{\theta,vco}(\Delta f)$, transforming it in its time-domain version $\Delta\theta_{noise,vco}(t)$ [8]; similarly for $\Delta\theta_{noise,div}(t)$. By computing $\Delta\theta_{pll}(t) = N \cdot \Delta\theta_c(t) + \Delta\theta_{noise,vco}(t)$ for each t , we extract $S_{\theta,pll}(\Delta f)$ as the PSD of $\Delta\theta_{pll}(t)$. We extract (RMS) long-term jitter $j_{lt,RMS}(k)$ of the VCO's output by reconstructing it with (1) through a parallelizable, post-simulation interpolation routine

3 Application to an integer- N PLL

Simulations ran on an Intel Xeon[®], 8 processors at 3GHz machine, on an integer-25 PLL.

To estimate the locking time t_{lk} , we let the PLL reaches the SST with $f_{ref} = 110$ MHz; at time t_1 we sweep to $f_{ref} = 115$ MHz and let the PLL locks again at t_2 : thus $t_{lk} = t_2 - t_1$ (sec). Besides, we compare average power consumption (mW) of VCO P_O and divider P_D with those from VCODIV, when the PLL is at SST and for a time equals to $1/f_{ref}$. We extract $j_{lt,RMS}(k)$ on the interpolated, reconstructed VCO's output.

In Fig. 2 we show $S_{\theta,pll}(\Delta f)$ from noisy simulation on TL and PLL with VCODIV, and SST analysis on TL: simulation results match well for $\Delta f \in [0.2, 200]$ MHz. To obtain accurate results near f_{out} , one has to increase the simulation time. In Table 1, we report accuracy results of the PLL with VCODIV's (Macro) and TL's measurements (Data). Noise-free simulation of PLL with VCODIV is 11.4x faster than TL; for noisy analysis, the speedup is 18.3x.

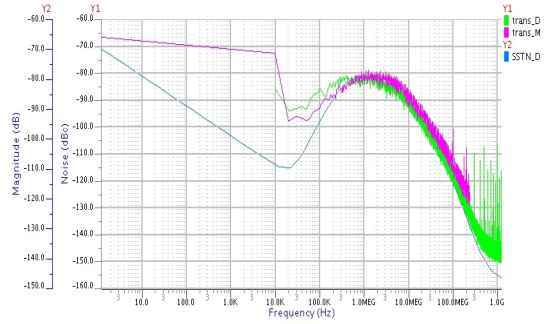


Fig. 2. $S_{\theta,vco}(\Delta f)$ from TL (*trans_D*) and PLL with VCODIV (*trans_M*) time sim, and SST noise on TL (*SSTN_D*).

Table 1. Accuracy of the factors of interest.

	t_{lk}	P_O	P_D	$S_{\theta,pll}$	$j_{lt,RMS}(k)$
Data	1.9739 μ	-5.88m	-2.35m		
Macro	1.9740 μ	-5.87m	-2.32m		
Error	$5 \cdot 10^{-5}\%$	$8 \cdot 10^{-4}\%$	1.5%	≤ 2 DB	$< 10\%$

4 Conclusion

Our method speeds up time-domain analyses of integer- N PLLs, accurately extracts all the factors of interest and is not invasive for commercial simulators.

References

- P. Maffezzoni and S. Levantino, *Analysis of VCO phase noise in charge-pump phase-locked loops*. in IEEE Trans. Circuits Syst. I: Regular Papers, vol. 59, n. 10, pp. 2165-2175, 2012.
- X. Lai and J. Roychowdhury, *TP-PPV: piecewise non-linear, time-shifted oscillator macromodel extraction for fast, accurate PLL simulation*. in ICCAD, Hassoun, Soha, 2006.
- K. Bittner and H. G. Brachtendorf, *Adaptive multi-rate wavelet method for circuit simulation*. in Radioengineering, vol. 23, pp. 300-307, 2014.
- K. S. Kundert and A. Sangiovanni-Vincentelli, *Finding the steady-state response of analog and microwave circuits*. in Proceedings of the IEEE on Custom Integrated Circuits Conference, pp. 6.1/1-6.1/7, 1988.
- R. Telichevesky, K. S. Kundert and J. K. White, *Efficient Steady-State Analysis Based on Matrix-Free Krylov-Subspace Methods*. in 32nd Design Automation Conference (DAC), pp. 480-484, 1995.
- E. Ngoya, J. Rousset and D. Argollo, *Rigorous RF and microwave oscillator phase noise calculation by envelope transient technique*. in IEEE MTT-S International Microwave Symposium Digest., vol. 1, pp. 91-94, 2000.
- A. Demir, A. Mehrotra and J. Roychowdhury, *Phase noise in oscillators: a unifying theory and numerical methods for characterization*. in IEEE Trans. Circuits Syst. I, vol. 47, pp. 655-674, 2000.
- Mentor Graphics Corp., *Eldo User Manual*. 2015.

Equivalent Netlist Extraction for Electrothermal and Electromagnetic Problems Discretized by the Finite Integration Technique

Thorben Casper^{1,2}, David Duque^{1,2}, Sebastian Schöps^{1,2}, and Herbert De Gersem¹

¹ Institut für Theorie Elektromagnetischer Felder, Technische Universität Darmstadt, 64289 Darmstadt, Germany

² Graduate School of Computational Engineering, Technische Universität Darmstadt, 64293 Darmstadt, Germany
casper@gsc.tu-darmstadt.de

Summary. We describe an approach for the synthesis of field models discretized by the Finite Integration Technique into electric networks, both describing (non-)linear electrothermal and electromagnetic problems. The result is an exact and efficient translation of the discretized partial differential equations into a circuit representation.

1 Introduction

For already more than half a century, simulation of electromagnetic devices by electric networks is a popular and important tool in computer aided design. However, classical device models have become more and more complex to account for various, in particular spatially distributed, phenomena. Their setup and validation is a tedious task. Instead, one would like to automate this by starting from the governing partial differential equations. In this work, we employ the Finite Integration Technique (FIT) [1] for the spatial discretization of the problems. However, other approaches like Finite Elements can be used similarly.

In contrast to most other approaches, we do not aim for simulator coupling but we use the resulting (possibly nonlinear) grid equations to formulate equivalent electric networks that represent the problems at hand. These networks are then straightforwardly exported as SPICE compatible netlists.

For electrothermal and electromagnetic problems, the circuit extraction is simple and consists of standard lumped elements such as resistors, capacitors, inductors, impressed voltage and current sources, as well as simple controlled sources, [2, 3], cf. Figure 1.

2 Problem Formulation

Let us consider a domain of interest \mathcal{D} discretized into a structured pair of primary and dual grids. The primary grid is composed of primary edges, primary facets and primary volumes while the dual grid is composed of dual edges, dual facets, and dual volumes.

2.1 Electrothermal Modeling

The electrothermal grid equations are given by the electroquasistatic approximation of Maxwell's equa-

tions coupled to the transient heat equation [1]. In the discrete setting, the resulting initial value problem

$$\tilde{\mathbf{M}}_{\epsilon} \tilde{\mathbf{S}}^{\top} \dot{\Phi} + \tilde{\mathbf{M}}_{\sigma}(\mathbf{T}) \tilde{\mathbf{S}}^{\top} \Phi = \mathbf{0}, \quad (1)$$

$$\mathbf{M}_{\rho c} \dot{\mathbf{T}} + \tilde{\mathbf{M}}_{\lambda}(\mathbf{T}) \tilde{\mathbf{S}}^{\top} \mathbf{T} = \mathbf{Q}_{\text{el}}(\Phi, \mathbf{T}) \quad (2)$$

is discussed. The unknowns are the electric potential Φ and the temperature \mathbf{T} . The material distribution is represented by a set of diagonal material matrices, namely the electric capacitance matrix \mathbf{M}_{ϵ} , the electric conductance matrix \mathbf{M}_{σ} , the thermal capacitance matrix $\mathbf{M}_{\rho c}$, and the thermal conductance matrix \mathbf{M}_{λ} . We assume that initial values are given and boundary conditions are considered by modification of the material matrices. The matrices $\tilde{\mathbf{S}}$ and $\tilde{\mathbf{S}}^{\top}$ denote the discrete divergence and the negative gradient operator, respectively. Ohmic losses due to Joule heating are accounted for by the thermal power \mathbf{Q}_{el} .

The modified nodal analysis [4]

$$\mathbf{A}_C \mathbf{C} \mathbf{A}_C^{\top} \dot{\mathbf{v}} + \mathbf{A}_R \mathbf{G} \mathbf{A}_R^{\top} \mathbf{v} = -\mathbf{A}_I \mathbf{I}_s(t) \quad (3)$$

describes the behavior of a circuit with capacitors, resistors and current branches in terms of nodal potentials \mathbf{v} . The topology is expressed by the incidence matrices \mathbf{A}_C , \mathbf{A}_R and \mathbf{A}_I . The values of the capacitors, resistors and current sources are stored in the circuit capacitance matrix \mathbf{C} , the circuit conductance matrix \mathbf{G} and the vector of current sources \mathbf{I}_s .

By comparison of (1)–(2) with (3), the electric (and thermal) circuit description readily follows, i.e., one constructs an electric network with the topology $\mathbf{A}_C = \mathbf{A}_R = \tilde{\mathbf{S}}$ [2].

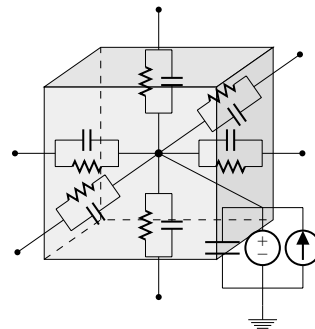


Fig. 1: Exemplary circuit elements located between primary nodes on a dual volume.

2.2 Electromagnetic Modeling

Let us now consider Maxwell's grid equations in \mathcal{D} written in terms of the auxiliary magnetic vector potential $\hat{\mathbf{a}}$ [1], viz.

$$\begin{aligned} \mathbf{C}\hat{\mathbf{e}} &= -\mathbf{C}\frac{\partial\hat{\mathbf{a}}}{\partial t}, \\ \tilde{\mathbf{C}}\mathbf{M}_\nu\mathbf{C}\hat{\mathbf{a}} &= \mathbf{M}_\varepsilon\frac{\partial\hat{\mathbf{e}}}{\partial t} + \mathbf{M}_\sigma\hat{\mathbf{e}} + \hat{\mathbf{j}}_i, \end{aligned} \quad (4)$$

with

$$\tilde{\mathbf{S}}\mathbf{D}_G\hat{\mathbf{a}} = \mathbf{F}, \quad (5)$$

where all quantities have the obvious meaning, i.e., $\hat{\mathbf{e}}$ represents the line-integrated electric field, $\hat{\mathbf{j}}_i$ is the impressed current source, $\{\mathbf{C}, \tilde{\mathbf{C}}\}$ are the primary and dual curl matrices, $\tilde{\mathbf{S}}$ is the dual divergence matrix, \mathbf{M}_ε , \mathbf{M}_ν , and \mathbf{M}_σ are the diagonal material matrices, \mathbf{D}_G is a diagonal grid geometry matrix, and \mathbf{F} is an auxiliary vector.

The system (4)–(5) can be cast as an electric network by employing a tree-cotree decomposition of $\hat{\mathbf{a}}$. In doing so, we construct a tree and cotree graph of the primary grid and proceed to split $\hat{\mathbf{a}}$ into its tree and cotree components, namely $\hat{\mathbf{a}}_t$ and $\hat{\mathbf{a}}_c$, respectively. The relation between these two components is found through (5) by imposing a gauge, e.g., *Coulomb* gauge. In this manner, the tree components $\hat{\mathbf{a}}_t$ are expressed in terms of the cotree components $\hat{\mathbf{a}}_c$. Such a decomposition enables us to regard (4) as the KVL and KCL of an electric network in which $\hat{\mathbf{e}}$ represents the voltages of primary nodes, $\hat{\mathbf{a}}_c$ represents the branch currents, and $\hat{\mathbf{a}}_t$ represents current-controlled current sources. In this network, standard lumped elements are directly obtained from the material matrices, and the electromagnetic interaction is mediated by means of voltage- and current-controlled sources.

3 Validation

We validate the method described herein by using two simple structures for which the corresponding electric circuits are generated and solved. The results are then compared with the analytic and the FIT solution.

First, the electrothermal problem is validated by using the RC-structure depicted in Figure 2. A sinusoidal excitation is applied and the charging and discharging of the capacitor is observed over time. Figure 3 shows the comparison of the SPICE and the FIT temperature solution that is quantified by a relative error of less than 0.52% only due to different time-integrators.

Secondly, the electromagnetic problem is validated by simulating a lossless rectangular resonant cavity. For this cavity, the resonance frequencies of the corresponding TM and TE modes obtained via analytic methods are compared with the resonance frequencies of the circuit representation of the cavity.

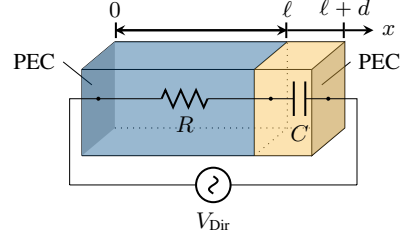


Fig. 2: Benchmark structure to validate the electrothermal setting.

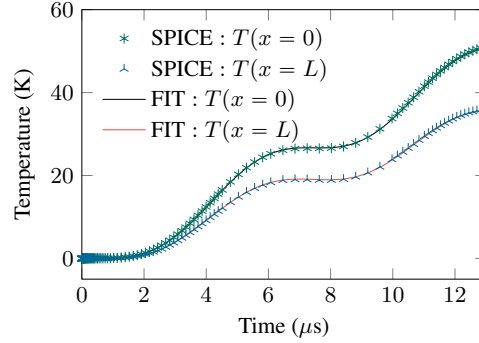


Fig. 3: Comparison of the temperature solution in the electrothermal setting.

Acknowledgement. This work is supported by the European Union within FP7-ICT-2013 in the context of the Nano-electronic COupled Solutions (nanoCOPS) project (grant no. 619166), by the Excellence Initiative of the German Federal and State Governments and the Graduate School of CE at TU Darmstadt.

References

- [1] T. Weiland. A discretization method for the solution of Maxwell's equations for six-component fields. In: *AEU* 31 (1977), pp. 116–120.
- [2] T. Casper, H. De Gersem, and S. Schöps. Automatic generation of equivalent electrothermal SPICE netlists from 3D electrothermal field models. In: *17th International Conference on Thermal, Mechanical and Multi-Physics Simulation and Experiments in Microelectronics and Microsystems (EuroSimE 2016)*. 2016.
- [3] D. Duque, S. Schöps, and H. de Gersem. An electric-circuit description of the Finite Integration Technique for electromagnetic problems. In: *19th European Conference of Mathematics for Industry (ECMI2016), Santiago de Compostela, Spain, June 2016*. 2016. In preparation.
- [4] C.-W. Ho, A. E. Ruehli, and P. A. Brennan. The modified nodal approach to network analysis. In: *IEEE Trans. Circ. Syst.* 22.6 (1975), pp. 504–509.

Multirate Partial Differential Equations for Pulsed Excitations

Andreas Pels¹, Johan Gyselinck², Ruth V. Sabariego³, and Sebastian Schöps¹

¹ TU Darmstadt, Graduate School of Computational Engineering and Institut Theorie Elektromagnetischer Felder
pels@gsc.tu-darmstadt.de, schoeps@gsc.tu-darmstadt.de

² Université libre de Bruxelles, Department of Bio, Electro And Mechanical Systems

³ KU Leuven, Department of Electrical Engineering

Summary. Multirate Partial Differential Equations have been successfully applied in radio-frequency applications. This digest extends the concept to linear low-frequency circuits excited by pulsed signals. The Multirate Partial Differential Equation is solved using a Galerkin ansatz and time integration. Two types of basis functions for the solution expansion are presented. The recently introduced PWM basis functions are firstly interpreted in the multirate context.

1 Introduction

Multirate Partial Differential Equations (MPDEs) have been successfully applied in radio-frequency applications. By using Kirchhoff's law and the device constitutive equations, electrical circuits are described by differential-algebraic equations (DAEs) [1]. Standard time discretization fastly reaches its limits when widely separated time-scales are present as very small time-steps are necessary. Reformulating the DAE into a MPDE has shown performance increase. This digest applies MPDEs on low-frequency circuits. The MPDE is solved in context of envelope modulated signals as introduced by [3]. A Galerkin ansatz and time discretization is used for solving the MPDE. The expansion of the solution uses Finite Element (FE) nodal functions and the recently introduced pulse width modulation (PWM) basis functions [2], which are interpreted in the MPDE context. An idealized buck converter is used for exemplary illustration, which is excited by a periodic pulsed signal, see Fig. 1.

2 Multirate Formulation

In this section the concept of MPDEs is presented (see [1], [3] for more details). Let the DAE describing a linear electrical circuit be given as

$$\mathbf{A} \frac{d}{dt} \mathbf{x}(t) + \mathbf{B} \mathbf{x}(t) + \mathbf{i}_s(t) = 0, \quad (1)$$

where $\mathbf{x}(t)$ is the vector of N_s unknowns (branch currents and node voltages), \mathbf{A} and \mathbf{B} are matrices containing topology information and constitutive laws and $\mathbf{i}_s(t)$ is the vector of input sources.

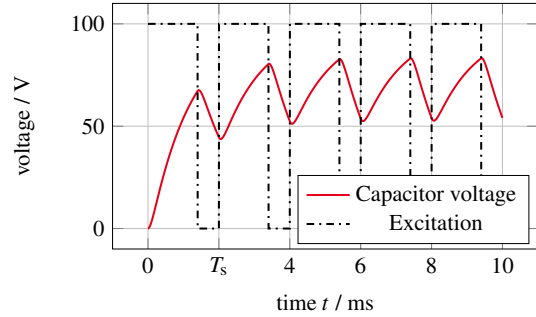


Fig. 1: Solution of the idealized buck converter. The switching cycle of the pulsed excitation is $T_s = 2$ ms.

Assuming that m different time-scales are present, the multivariate forms of $\mathbf{x}(t)$ and $\mathbf{i}_s(t)$ can be written as $\hat{\mathbf{x}}(t_1, \dots, t_m)$ and $\hat{\mathbf{i}}_s(t_1, \dots, t_m)$. The MPDE corresponding to (1) is

$$\mathbf{A} \frac{\partial}{\partial t_1} \hat{\mathbf{x}} + \dots + \mathbf{A} \frac{\partial}{\partial t_m} \hat{\mathbf{x}} + \mathbf{B} \hat{\mathbf{x}} + \hat{\mathbf{i}}_s = 0. \quad (2)$$

The solution of the MPDE is related to the solution of (1) by $\mathbf{x}(t) = \hat{\mathbf{x}}(t + c_1, \dots, t + c_m)$ and $\mathbf{i}_s(t) = \hat{\mathbf{i}}_s(t + c_1, \dots, t + c_m)$, where c_1, \dots, c_m are constants. Uniqueness and existence of a solution for quasi-periodic signals on a Fourier basis were proven in [3].

We assume in the following that the signals in the circuit can be presented by only $m = 2$ time-scales. A fast varying t_2 , which covers all periodically changing parts of the signals and a slowly varying t_1 , which captures the envelope.

3 Variational Approach

A combination of a variational approach and time integration are used to discretize the MPDE. We first apply a Galerkin ansatz to discretize the fast time-scale t_2 of the signal and then use time integration for the solution of the slow time-scale t_1 . The multirate solution $\hat{\mathbf{x}}(t_1, t_2)$ is expanded as follows

$$\hat{\mathbf{x}}_j(t_1, t_2) = \sum_{k=0}^{N_p} p_k(\tau) w_{j,k}(t_1) \quad \text{with } \tau = \frac{t_2}{T_s} \bmod 1, \quad (3)$$

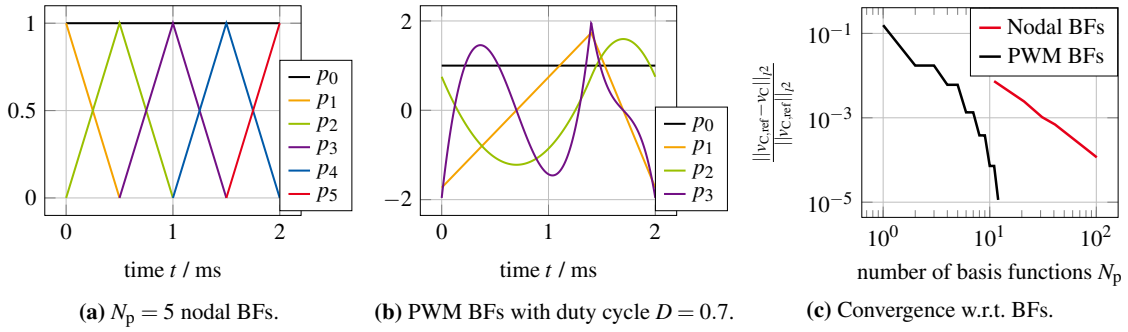


Fig. 2: Nodal and PWM basis functions (BF) and convergence.

where $\hat{x}_j(t_1, t_2)$ is the j -th component of $\hat{\mathbf{x}}(t_1, t_2)$, $p_k(\tau)$ are basis functions (BFs) and $w_{j,k}(t_1)$ are coefficients. Applying a Galerkin ansatz to the MPDE with respect to t_2 yields

$$\int_{t-T_s/2}^{t+T_s/2} \left(\mathbf{A} \frac{\partial}{\partial t_1} \hat{\mathbf{x}}(t_1, t_2) + \mathbf{A} \frac{\partial}{\partial t_2} \hat{\mathbf{x}}(t_1, t_2) + \mathbf{B} \hat{\mathbf{x}}(t_1, t_2) + \tilde{\mathbf{i}}_s(t_1, t_2) \right) p_k(\tau) dt_2 = 0 \quad \forall k \in [0, \dots, N_p]. \quad (4)$$

Using the expansion (3), integrating by parts and reorganizing leads to a system of DAEs, now only dependent on the slow time-scale t_1

$$\tilde{\mathbf{A}} \frac{d}{dt_1} \mathbf{w}(t_1) + \tilde{\mathbf{B}} \mathbf{w}(t_1) + \tilde{\mathbf{i}}_s(t_1) = 0, \quad (6)$$

where $\mathbf{w}(t_1) = [w_{1,1}, \dots, w_{1,N_p}, \dots, w_{N_s,1}, \dots, w_{N_s,N_p}]^\top$ is the vector of unknown coefficients, $\tilde{\mathbf{A}}$ and $\tilde{\mathbf{B}}$ are matrices and $\tilde{\mathbf{i}}_s(t_1)$ is the excitation term. Due to separation of scale, the DAE (6) can be solved with larger time steps compared to the original DAE (1). Despite the larger equation system a major speedup is observed on the buck converter example.

4 Numerics

Two types of basis functions (BFs) are used for the expansion (3). Nodal BFs which are a simple but universal choice and the more sophisticated PWM BFs, which were introduced in [2] and are specifically designed for use with pulsed excitations. They are depicted in Fig. 2a and Fig. 2b, respectively.

The PWM BFs are piecewise polynomial [2]. The zero-th BF is chosen as $p_0(\tau) = 1$, which enables the coefficients $w_{j,0}$ to capture envelopes of the signals. The basis is built up recursively starting from a piecewise linear function

$$p_1(\tau) = \begin{cases} \sqrt{3} \frac{2\tau-D}{D} & \text{if } 0 \leq \tau \leq D \\ \sqrt{3} \frac{1+D-2\tau}{1-D} & \text{if } D \leq \tau \leq 1 \end{cases} \quad (7)$$

The higher order BFs $p_k(\tau)$, $2 \leq k \leq N_p$ are calculated by integrating $p_{k-1}(\tau)$,

$$p_k^*(\tau) = \int_0^\tau p_{k-1}(\tau') d\tau', \quad (8)$$

which ensures C_0 continuity. The extended set is then orthonormalized by means of $k+1$ factors n_k and $o_{k,l}$:

$$p_k(\tau) = n_k p_k^*(\tau) + \sum_{l=0}^{k-1} o_{k,l} p_l(\tau). \quad (9)$$

The convergence of both types of BFs for the buck converter given in [2] is shown in Fig. 2c. As can be seen, the PWM BFs lead to much better convergence with respect to the number of BFs but may become problematic for nonlinear problems or warped MPDEs.

5 Conclusion and Outlook

The MPDE approach was applied to an example in low-frequency engineering. The MPDE was solved with a Galerkin ansatz and time integration. Nodal and PWM basis functions were presented. The PWM BFs showed a better accuracy per degree of freedom. Future research will investigate warping and nonlinear problems.

Acknowledgement. This work was supported by the ‘Excellence Initiative’ of German Federal and State Governments and the Graduate School CE at TU Darmstadt.

References

1. Hans Georg Brachtendorf, G. Welsch, R. Laur, and A. Bunse-Gerstner. Numerical steady state analysis of electronic circuits driven by multi-tone signals. *Electr. Eng.*, 79(2):103–112, 1996.
2. Johan Gyselincx, Claudia Martis, and Ruth V. Sabariego. Using dedicated time-domain basis functions for the simulation of pulse-width-modulation controlled devices – application to the steady-state regime of a buck converter. In *Electromotion 2013*, Cluj-Napoca, Romania, October 2013.
3. J. Roychowdhury. Analyzing circuits with widely separated time scales using numerical pde methods. *IEEE Trans. Circ. Syst. Fund. Theor. Appl.*, 48(5):578–594, May 2001.

Robust optimization of a RFIC isolation problem under uncertainties

Piotr Putek^{1,2}, Rick Janssen³, Jan Niehof³, E. Jan W. ter Maten^{1,4}, Roland Pulchr², and Michael Günther¹

¹Bergische Universität Wuppertal, Chair of Applied Mathematics and Numerical Analysis, Germany, {putek, termaten, guenther}@math.uni-wuppertal.de,

²Ernst-Moritz-Arndt-Universität Greifswald, Institute of Mathematics and Computer Science, Germany, pulchr@uni-greifswald.de,

³NXP Semiconductors, the Netherlands, {Rick.Janssen, Jan.Niehof}@nxp.com,

⁴Eindhoven University of Technology, Chair of Mathematics and Computer Science (CASA), the Netherlands, E.J.W.ter.Maten@tue.nl,

Summary. Modern electronics systems involved in communication and identification systems impose demanding constraints on both reliability and robustness of components. It results from the influence of manufacturing tolerances within the continuous down-scaling process into the outputs characteristics of electronics devices. Thus, constraints in terms of statistical moments have come in a natural way into optimization formulations of electronics products under uncertainties. Additionally, yield constraints require an efficient approach for the careful assessment of the propagation of uncertainties through a model of device. Therefore, we used a type of a Stochastic Collocation Method (SCM) with the Polynomial Chaos (PC). It allows for constructing a surface response model, which can be relatively easily included in a stochastic, constrained optimization problem solved for a defined random dependent functional. Finally being inspired by a real engineering problem, we have illustrated our methodology on a RFIC¹ isolation problem. Achieved results for the optimization confirmed efficiency and robustness of the used methodology.

1 Introduction

Since transistor sizes have become smaller and smaller with respect to each new technology, the impact of statistical variations in input parameters onto the outputs characteristics of electronic devices has played a crucial role in predictive and reliable simulations. On the one hand, these statistical variations, resulting from manufacturing tolerances of industrial processes, could lead to the accelerations of migrations phenomena in semiconductor devices and finally cause a thermal destruction of devices due the thermal runaway [2, 3]. On the other hand, unintended RF coupling, which can occur as a result of industrial imperfections, might additionally downgrade the quality of products and their performance or even be dangerous for safety of both environment and the end users [1].

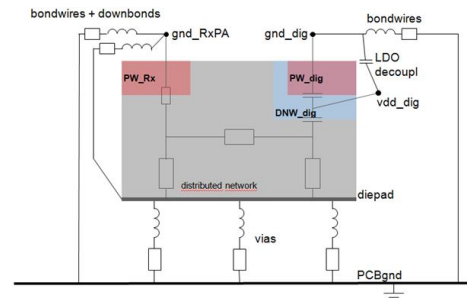


Fig. 1. Floorplan model for isolation and grounding strategies [1].

2 RFIC Design & Stochastic Modeling

In order to optimize both the electromagnetic interface and the unintended electromagnetic coupling effects in RF products, the key issue is to apply a proper floor planing with grounding strategies. More precisely, the physical design issues, shown in Fig. 1, involve on-chip coupling effects, chip-package interaction, substrate coupling, leading to the co-habitation. Thus, a stochastic coupled problem for a time-harmonic analysis is governed by

$$\begin{cases} \nabla \cdot [\varepsilon(\chi) \mathbf{E}(\chi)] = \rho(\chi), \\ \nabla \cdot \mathbf{J}(\chi) + i\omega\rho(\chi) = 0, \\ \mathbf{J}(\chi) = \sigma(\chi) \mathbf{E}(\chi), \end{cases} \quad (1)$$

equipped with suitable initial and boundary conditions, where $\chi := (\mathbf{x}, f, \boldsymbol{\xi}) \in D \times D_F \times \Xi$ with D being a bounded domain in \mathbb{R}^3 , F representing frequency spectrum $D_F \in (f_1, \dots, f_n)$ and Ξ a multidimensional domain of physical parameters. The electric conductivity σ , and the permittivity ε are independent of \mathbf{E} . ρ, \mathbf{E} are the charge density, the electric field, whereas $\mathbf{J}(\chi)$ denotes the current density.

2.1 Uncertainty Quantification

For the UQ analysis of (1), a type of the SCM in conjunction with the PC expansion has been used. Let

¹ Radio Frequency Integrated Circuit

y be a square integrable function. We assume now that ξ are random variables. Then, a response surface model of y can be obtained by a truncated series of the PC expansion, see [4],

$$y(f, \xi) \doteq \sum_{i=0}^N v_i(f) \Phi_i(\xi) \quad (2)$$

with a priori unknown coefficient functions v_i and pre-determined basis polynomials Φ_i with the orthogonality property $\mathbb{E}[\Phi_i \Phi_j] = \mathbb{E}[\Phi_i^2] \delta_{ij}$ (Kronecker delta). Therein \mathbb{E} is the expected value. Specifically, we have applied a pseudo-spectral approach with the Stroud formula of order 3 for the calculation of the unknown coefficients v_i . The basic concept of this method is first to provide the solution at each quadrature node $\xi^{(k)}$, $k = 1, \dots, K$ of the deterministic problem, defined by the system 1. Next, the multi-dimensional quadrature rule with associated weights w_k allows for computing

$$v_i(f) \doteq \sum_{k=1}^K y(f, \xi^{(k)}) \Phi_i(\xi^{(k)}) w_k, \quad (3)$$

which represents an approximation of the exact projection of y onto the basis polynomials. Finally, the moments are approximated by, cf. [4, 5],

$$\mathbb{E}[y(f, \xi)] \doteq v_0(f), \quad \text{Var}[y(f, \xi)] \doteq \sum_{i=1}^N |v_i(f)|^2$$

assuming $\Phi_0 = 1$. Furthermore, we will consider three functions y_1, y_2 and y_3 to be used in the optimization procedure. The exemplary result for the UQ analysis is depicted in Fig. 2 for $y_2 = |\text{CplRx}(f)|$, which allows for assessing the influence of the coupled impedance into a type of the transmittance function (CplRx).

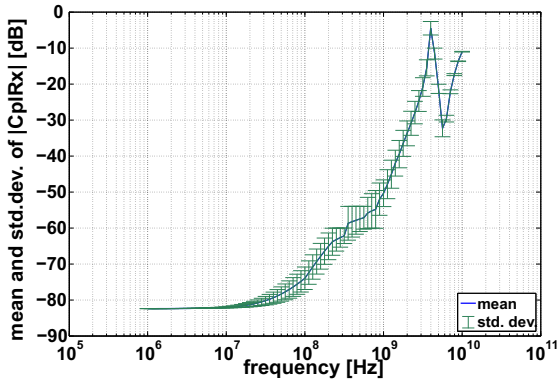


Fig. 2. Statistical moments for y_2 output function.

3 Robust optimization Problem

Finally, when considering statistical moments, an optimization problem constrained by stochastic PDEs

can be reformulated into the robust single objective optimization problem [3] as follows

$$\begin{aligned} \min_{\mathbf{p}} \quad & \mathbb{E}[F(\mathbf{p})] + \eta \sqrt{\text{Var}[F(\mathbf{p})]} \\ \text{s.t.} \quad & \mathbf{K}(\mathbf{p}^{(k)}) \mathbf{V}^{(k)} = \mathbf{f}^{(k)}, k = 1, \dots, K, \\ & p_{\max_\ell} \leq p_\ell \leq p_{\min_\ell}, \ell = 1, \dots, 6, \end{aligned} \quad (4)$$

where \mathbf{K} , \mathbf{V} and \mathbf{p} denote the mass/stiffness matrix, the electric scalar potential and a vector of optimized parameters, respectively. The random-dependent functional reads as

$$F[\mathbf{p}(\xi)] = \sum_{i=1}^n w_i \int_{\Gamma} |g_i[\mathbf{p}(\xi)]|^2 dx, \quad (5)$$

where g_i are complex-valued functions, which yield transmittance functions such as $y_1 = \text{CplADC}(f)$, $y_2 = \text{CplRx}(f)$, and $y_3 = \text{CplXolo}(f)$, respectively.

4 Conclusions

Results for the UQ analysis of a RIFC isolation problem have shown that it is possible to find a configuration with decoupled impedances, for which the influence of both noise and industrial imperfections for operational devices will be minimized in the broad frequencies spectrum. In a full paper we will present an optimized device structure.

Acknowledgement. The project nanoCOPS (Nanoelectronic COupled Problems Solutions) is supported by the European Union in the FP7-ICT-2013-11 Program under the grant agreement number 619166.

References

1. Di Bucchianico, A., ter Maten, J., Pulch, R., Janssen, R., Niehof, J., Hanssen, J., Kapora, S.: Robust and efficient uncertainty quantification and validation of RFIC isolation. *Radioengineering*, **23**, 308–318 (2014)
2. Putek, P., Meuris, P., Günther, M., ter Maten, E.J.W., Pulch, R., Wieers, A., Schoenmaker, W.: Uncertainty quantification in electro-thermal coupled problems based on a power transistor device. *IFAC-PapersOnLine*, **48**, 938–939 (2015)
3. Putek, P., Meuris, P., Pulch, R., ter Maten, E.J.W., Schoenmaker, W., Günther, M.: Uncertainty quantification for robust topology optimization of power transistor devices. *IEEE Trans. on Magn.*, **52**, 1700104 (2016)
4. Xiu, D. *Numerical methods for stochastic computations - A spectral method approach*. Princeton (NJ, USA): Princeton Univ. Press, (2010)
5. Xiu, D., Karniadakis, G.E.: Modeling uncertainty in steady state diffusion problems via generalized polynomial chaos. *Computer Methods in Applied Mechanics and Engineering*, **191**, 4927–4948 (2002)

Density Estimation in Cosimulation using Spectral- and Kernel Methods

Kai Gausling and Andreas Bartel

Bergische Universität Wuppertal, Applied Mathematics and Numerical Analysis
 gausling@math.uni-wuppertal.de, bartel@math.uni-wuppertal.de

Summary. When Co-simulation is applied to coupled differential algebraic equations (DAEs), convergence can only be guaranteed if certain properties are fulfilled. However, introducing uncertainties in the mode might have great impact into this contraction properties. Consequently, uncertainties might destroy convergence. Hence one is interested to build up the stochastic behavior of those properties. Within this paper we demonstrate two general techniques with its application in co-simulation to measure densities. Using a field/circuit coupled problem as benchmark, we clarify the benefits of both schemes.

1 Introduction

Let the i -th subsystem be given by an initial value problem of DAEs (for $i = 1, \dots, r$)

$$\begin{aligned} \dot{\mathbf{y}}_i &= \mathbf{f}_i(\mathbf{y}, \mathbf{z}), \mathbf{y}_i(0) = \mathbf{y}_{i,0}, \mathbf{y}^T = [\mathbf{y}_1^T, \dots, \mathbf{y}_r^T], \\ 0 &= \mathbf{g}_i(\mathbf{y}, \mathbf{z}), \mathbf{z}^T = [\mathbf{z}_1^T, \dots, \mathbf{z}_r^T], \end{aligned} \quad (1)$$

for the unknowns $[\mathbf{y}^T, \mathbf{z}^T]$. We assume that the Jacobian $\partial \mathbf{g}_i / \partial \mathbf{z}_i$ is not singular. Moreover also the overall system shall be of index-1, such that we have the differential part $\mathbf{f}^T = [\mathbf{f}_1^T, \dots, \mathbf{f}_r^T]$ and algebraic part $\mathbf{g}^T = [\mathbf{g}_1^T, \dots, \mathbf{g}_r^T]$. Using splitting functions \mathbf{G}, \mathbf{F} , the co-simulation scheme is encoded, see [1]. More precisely we investigate the coupled DAE system with splitting

$$\mathbf{F} := \begin{bmatrix} \mathbf{f}_1(\mathbf{y}_1, \mathbf{z}_1, 0, 0) \\ \mathbf{f}_2(0, 0, \mathbf{y}_2, \mathbf{z}_2) \end{bmatrix}, \mathbf{G} := \begin{bmatrix} \mathbf{g}_1(\mathbf{y}_1, \mathbf{z}_1, 0, \mathbf{z}_2) \\ \mathbf{g}_2(0, \mathbf{z}_1, \mathbf{y}_2, \mathbf{z}_2) \end{bmatrix}. \quad (2)$$

Hence, the ODE parts of the subsystems are isolated. Due to (2), a contraction factor $\alpha_n := \|\mathbf{G}_{\mathbf{z}^{(k)}}^{-1} \mathbf{G}_{\mathbf{z}^{(k-1)}}\|$ occurs, where convergence is only guaranteed if $\alpha_n < 1$ holds. Mainly for nonlinear models the jacobians $\mathbf{G}_{\mathbf{z}^{(k)}}^{-1}, \mathbf{G}_{\mathbf{z}^{(k-1)}}$ are hard to compute. Now, let $\mathbf{X}(t), \tilde{\mathbf{X}}(t)$ be two waveforms on the n th time window $H_n := [t_n, t_{n+1}]$. The difference after k iterations is measured by $\delta_n^{(k)} := \|\mathbf{X}_n^{(k)}(t) - \tilde{\mathbf{X}}_n^{(k)}(t)\|_{2,\infty}$. Due to algebraic coupling, see (2), one obtains the error propagation:

$$\begin{bmatrix} \delta_{\mathbf{y},n}^{(k)} \\ \delta_{\mathbf{z},n}^{(k)} \end{bmatrix} \leq \begin{bmatrix} 0 & CH_n \\ 0 & CH_n + \alpha_n \end{bmatrix}^k \begin{bmatrix} \delta_{\mathbf{y},n}^{(0)} \\ \delta_{\mathbf{z},n}^{(0)} \end{bmatrix} + \text{remainder} \quad (3)$$

Thus we found that the contraction factor is bounded from below by

$$\alpha_n \geq (\delta_{\mathbf{z},n}^{(k)} / \delta_{\mathbf{z},n}^{(0)})^{1/k} - CH_n, \quad (4)$$

which enables to estimate the contraction factor α_n during the co-simulation procedure for H_n small enough.

1.1 Richardson Extrapolation

In (4) an estimator based on a Richardson Extrapolation has been used to measure the errors. At first, one step with the macro-step size H_n is carried out which yields the numerical result $\mathbf{X}_n^{(k)}(t)$. Then, the same step is executed using two steps with the half macro-step size $H_{n/2}$ yielding the more accurate solution $\mathbf{X}_{n/2}^{(k)}(t)$. Using constant extrapolation for the initial guess, the error of $\mathbf{X}_n^{(k)}(t)$ can be estimated by

$$\delta_n^{(k)} = 2\|\mathbf{X}_n^{(k)}(t) - \mathbf{X}_{n/2}^{(k)}(t)\| + \mathcal{O}(H_n^2). \quad (5)$$

2 Density Estimation Techniques

Several well known approaches can be found for measuring the pdf of random variables. One prominent technique is the so-called Kernel Density Estimation (KDE) based on a brute-force sampling of all random variables. Another approach tries to determine the PDF analytically by covering the stochastic process using Polynomial Chaos (PC) expansion, see [2].

However, both methods are from scratch differently with its own benefits. Thus, a comparison with its application in co-simulation is of great interest.

2.1 Kernel Density Estimation Method

In contrast to determine stochastic distributions by simple histograms, KDE techniques allows to get PDFs without discontinuities and with fewer samples. Let $X = (x_1, \dots, x_n) \in \mathbb{R}$ be an independent sample drawn from some distribution with an unknown density p_X . The shape of this function can be estimated using a kernel density estimator

$$\hat{p}_X = \frac{1}{nh} \sum_{i=1}^n K\left(\frac{x - x_i}{h}\right), \quad K(x) = \frac{1}{\sqrt{2\pi}} e^{-x^2/2} \quad (6)$$

where $K(x)$ is the gaussian-kernel – a non-negative function that integrates to one and has mean zero – and smoothing operator $h > 0$. To avoid oversmoothing, KDE requires judicious choice of bandwidth h . However the choice of h can be chosen optimal in some sense. Thus this topic is not treated in this work.

2.2 Spectral Method

Suppose that the PC expansion is written as

$$f(\xi) = \sum_{\alpha} f_{\alpha} \Phi_{\alpha}(\xi) \quad (7)$$

with coefficient functions f_{α} , polynomials $\Phi_{\alpha}(\cdot)$ thus that $\langle \Phi_n(\cdot), \Phi_m(\cdot) \rangle = \delta_{nm}$, $n, m \in \mathbb{N}_0$, and random variable ξ with PDF $p_{\xi}(\cdot)$. To determine the coefficients f_{α} , we employ stochastic collocation. Now we want to write a PDF for $f(\xi)$, call it $p_{f(\xi)}(\cdot)$. Suppose we want to evaluate this PDF at some x : Then

$$p_{f(\xi)}(x) = \sum_{\xi \in R_x} \frac{p_{\xi}(\xi)}{|Df(\xi)|}, R_x = \xi : f(\xi) - x = 0. \quad (8)$$

where ξ_1, \dots, ξ_N are the N roots of $f(\xi) - x = 0$ and $Df(\xi)$ is the jacobian evaluated at ξ . In other words, many possible ξ may give use this particular x and all of them contribute to the probability density at x .

3 Numerical Test Example

A field/circuit coupled problem, see Fig. 3, serves as our test example. Field and circuit are coupled to-

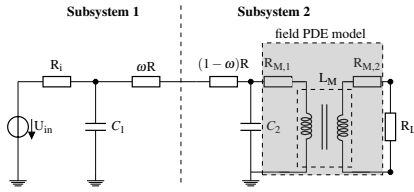


Fig. 1. Field/circuit coupling using R-coupling.

gether using the new technique of R-coupling. That is, the contraction factor is determined by the ratio of the resistances $\alpha = (\omega R) / ((1 - \omega)R)$, $\omega \in [0, 1]$. Please note that R-coupling fulfills (2). This gives the opportunity to several create cases with different stability behaviors. For simplification, we define $R_1 := \omega R$, $R_2 := (1 - \omega)R$. Now we consider R_1, R_2 to be uniformly distributed: $R_i \sim \mathcal{U}(10 \Omega - \delta R_i, 10 \Omega + \delta R_i)$ for $i = 1, 2$. We suppose an variation of about $\delta R_1 = 1 \Omega$, $\delta R_2 = 7 \Omega$. As a consequence, the contraction factor α becomes stochastic. Now, the challenge is to shape the pdf of α as good as possible from its underlying sample with as little effort as possible.

Fig. 2 shows the estimated pdf using the spectral method and the KDE approach with different number of sample. For the spectral approach, the maximum degree of polynomial that we used for the approximation by PC expansion is two. For R_1 uncertain, the spectral method becomes more powerful. That is, due to the linear mapping, the spectral method enables to approximate the stochastic process exactly. The KDE approach needs a large number of samples to draw the

uniform distribution precisely. However, for R_2 uncertain, the mapping becomes nonlinear, since R_2 is located in the denominator. Thus the spectral method fails as long as we use quadratic polynomials for its approximation. However, using polynomials of higher order allows for reducing the error. Fig. 3 compares

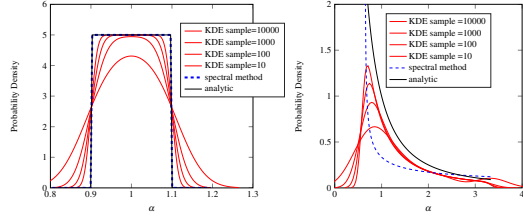


Fig. 2. pdf for uncertain R_1 (left) and uncertain R_2 (right).

the error of uniformly shaped pdf –measured in expectation value– for increasing window sizes. That is, (4) becomes less accurate for larger window sizes H_n . Furthermore, using (5) as error estimation seems to work well. Therefore, using richardson extrapolation or ref. solution yields approximately the same error.

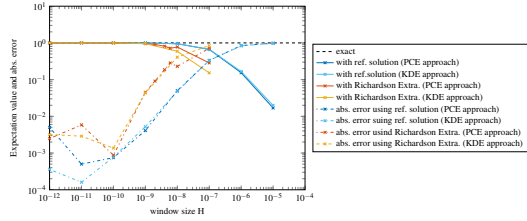


Fig. 3. Accuracy in expectation value vs. window size H .

4 Conclusions

We demonstrated that both schemes, i.e. spectral- and KDE approach, are applicable in co-simulation for estimating the distribution of the contraction factor. However, both schemes are different in nature. Hence the objective is to analyze and reduce the computational effort. Therefore, sensitivity coefficients probability helps for effective parameter space sampling.

Acknowledgement. This work is supported by the German Federal Ministry of Education and Research in the projects SIMUROM, (05M13PXB) and KoSMos, (05M13PXA).

References

1. Bartel, A., Brunk, M., Schöps, S.: *On the convergence rate of dynamic iteration for coupled problems with multiple subsystems*. J. Comput. Appl. Math., vol. 262, pp. 14–24 (2014)
2. Li J. and Marzouk Y.: *Multivariate semi-parametric density estimation using polynomial chaos expansion*. In preparation (2013)

POD-based reduced-order model of an eddy-current levitation problem

MD Rokibul Hasan and Ruth V. Sabariego

KU Leuven, Dept. Electrical Engineering (ESAT), EnergyVille, Belgium
 rokib.hasan@esat.kuleuven.be, ruth.sabariego@esat.kuleuven.be

Summary. In this paper, a proper-orthogonal-decomposition reduced-order model is applied to an eddy-current problem with movement. A classical magnetodynamic finite element formulation based on the magnetic vector potential is used as reference and as starting point to build the reduced models. The TEAM workshop problem 28 is chosen as a test case.

1 Introduction

The accurate modelling of electromagnetic devices accounting for eddy current effects, movement, nonlinearities,... is a major concern from early design stages. The finite element (FE) method is widely used and versatile for modelling these phenomena. It maybe extremely expensive in terms of computational time and memory, though. The most popular approaches for handling this issue are those based on the extraction of physical parameters (inductances, flux linkages,...) either from simulations or measurements and the construction of look-up tables covering the operating range of the device [1]. Future simulations are performed by simple interpolation, drastically reducing thus the computational cost.

Reduced order (RO) techniques with a more mathematical approach are a feasible alternative, which are gaining interest in electromagnetism [2]. Few works have addressed electromagnetic problems with movement, crucial to model of e.g. actuators, rotating electrical machines. In [3], a permanent magnet synchronous machine is studied via a POD-RO model of a magnetostatic FE formulation. The rotation is taken into account with the locked step approach, so the mesh and number of degree of freedom remain constant.

In this work, we consider a levitation problem with RO techniques, the Team Workshop problem 28 [4] (see Fig. 1). The time-varying magnetic field generated by the coils induces eddy currents in the conducting plate. The ensuing magnetic force moves the plate, which oscillates around an equilibrium levitating position. The FE mesh changes at every new position/time step. Herein a RO projection operator is developed to properly account for the different meshes with a prescribed accuracy.

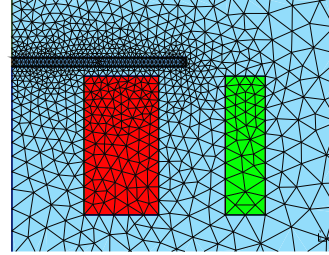


Fig. 1. Team 28 problem: 2D mesh

2 Magnetodynamic levitation model

Let us consider a bounded domain $\Omega = \Omega_c \cup \Omega_c^C \in \mathbb{R}^3$ with boundary Γ . The conducting and non-conducting parts of Ω are denoted by Ω_c and Ω_c^C , respectively. The (modified) magnetic-vector-potential (a -) magnetodynamic formulation (weak form of Ampère's law) reads: find a , such that

$$(\nu \operatorname{curl} a, \operatorname{curl} a')_{\Omega} + (\sigma \partial_t a, a')_{\Omega_c} + \langle \hat{n} \times h, a' \rangle_{\Gamma} = (j_s, a')_{\Omega_s}, \quad \forall a' \quad (1)$$

with a' test functions in a suitable function space; $b = \operatorname{curl} a$ the magnetic flux density; j_s a prescribed current density and \hat{n} the outward unit normal vector on Γ . Volume integrals in Ω and surface integrals on Γ of the scalar product of their arguments are denoted by $(\cdot, \cdot)_{\Omega}$ and $\langle \cdot, \cdot \rangle_{\Gamma}$. The derivative with respect to time is denoted by ∂_t . We further assume linear isotropic materials with reluctivity ν (magnetic field $h = \nu b$) and conductivity σ .

We adopt a weak electromechanical coupling. Once the electromagnetic problem solved, we compute the magnetic force from a by means of the Maxwell stress tensor. This force is the source of the mechanical problem to determine the plate displacement [5].

$$m \partial_t v(t) + \xi v(t) + ky(t) = F(t), \quad v(t) = \partial_t y(t) \quad (2)$$

where $y(t)$ is the position, $v(t)$ the velocity, m the mass, ξ the viscous friction coefficient, k the elastic constant and $F(t)$ the total applied force including the magnetic forces.

3 Model order reduction

The proper orthogonal decomposition (POD) is applied to reduce the matrix system resulting from the discretisation of (1):

$$A\partial_t x(t) + Bx(t) = C(t). \quad (3)$$

The solution vector x ($N \times 1$) is then approximated by a vector x^r ($M \times 1$) in a reduced basis, $M < N$,

$$x \approx \Psi x^r, \quad (4)$$

with Ψ an orthonormal projection operator generated from the time-domain full solution x via snapshot techniques [6].

Let us consider the snapshot matrix, $S = [x_1, x_2, \dots]$ from the set of solution x for the selected number of time steps. Applying the singular value decomposition (SVD) to this snapshot matrix S as,

$$S = \mathcal{U} \Sigma \mathcal{V}^T \quad (5)$$

We consider, $\Psi = \mathcal{U}^r$ corresponds to the truncation (r first columns). Therefore, the reduced-order system becomes:

$$A^r \partial_t x^r(t) + B^r x^r(t) = C^r(t). \quad (6)$$

with $A^r = \Psi^T A \Psi$, $B^r = \Psi^T B \Psi$ and $C^r = \Psi^T C$ [7]. Note that the FE mesh changes for every snapshot, what means that the projection operator Ψ must be projected to a common basis and the procedure becomes more expensive.

4 Results

We consider an electrodynamic levitation device consisting of a conducting plate over two coaxial exciting coils. At $t = 0$ the plate rests above the coils at a distance of 3.8 mm. A time-varying sinusoidal current at 50 Hz is imposed in both coils, same amplitude, opposite directions [4].

We assume a purely translational movement (rotation and tilting are neglected) and adopt a FE axisymmetric model as reference and origin of the RO models.

Reaching steady state has required time-stepping 50 periods (5000 time steps). The first 1400 time-step solutions (280 ms) are included in the snapshot matrix, as they comprise the first two peaks, see Fig. 2. We have observed that this is the optimal amount of solutions to reproduce the transient.

Three POD-based RO models are constructed with a prescribed error tolerance: RO1, RO2, RO3. The smaller the error tolerance, the bigger the RO model will be (size of $RO3 < RO2 < RO1$).

As preliminary result, the displacement and relative error of the full and RO models are shown in

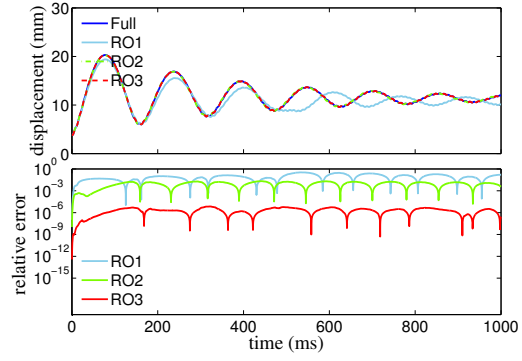


Fig. 2. Displacement (up) and relative error (down) between full and RO models

Fig. 2. With the RO approach we need 1400 time steps instead of the 5000 time steps for getting the full system behaviour. An accurate result has been achieved with the truncated basis models: RO2 and RO3. Although the RO approach is expensive for a single simulation, the gain in computational cost is clear for repetitive cases.

Details on the theory and a thorough analysis of the behaviour of the RO models with e.g. the time step size and the number of time steps for constructing the projection operator will be provided.

References

1. Z. Liu, S. Liu, O. A. Mohammed, "A Practical Method for Building the FE-Based Phase Variable Model of Single Phase Transformers for Dynamic Simulations," *IEEE Trans. Magn.*, vol. 43, no. 4, pp. 1761-1764, 2007.
2. W. Schilders, H. V. der Vorst, J. Rommes, "Model order reduction: theory, research aspects and applications," *Springer-Verlag*, 2008.
3. T. Henneron, S. Clénet, "Model order reduction applied to the numerical study of electrical motor based on POD method taking into account rotation movement," *Int. J. Numer. Model.*, vol. 27, no. 3, pp. 485-494, 2014.
4. H. Karl, J. Fetzer, S. Kurz, G. Lehner, W. M. Rucker, "Description of TEAM workshop problem 28: An electrodynamic levitation device" In Proc. of the *TEAM Workshop*, Graz, Austria, pp. 48-51, 1997.
5. F. Henrotte, K. Hameyer, "Computation of electromagnetic force densities: Maxwell stress tensor vs. virtual work principle," *J. Comput. Appl. Math.*, vol. 168, pp. 235-243, 2004.
6. Y. Sato, H. Igarashi, "Model reduction of three-dimensional eddy current problems based on the method of snapshots," *IEEE Trans. Magn.*, vol. 49, no. 5, pp. 1697-1700, 2013.
7. MD R. Hasan, R. V. Sabariego, C. Geuzaine, Y. Paquay, "Proper orthogonal decomposition versus Krylov subspace methods in reduced-order energy-converter models," In Proceedings of *ENERGYCON 2016*, April 4-8, Leuven, Belgium, 2016.

Multirate DAE/ODE-Simulation and Model Order Reduction for Coupled Circuit-Field Systems

Christoph Hachtel¹, Johanna Kerler-Back², Andreas Bartel¹, Michael Günther¹, and Tatjana Stykel²

¹ Bergische Universität Wuppertal, Chair of Applied Mathematic/Numerical Analysis, Gaußstr. 20, 42119 Wuppertal, Germany {hachtel, bartel, guenther}@math.uni-wuppertal.de

² Universität Augsburg, Institut für Mathematik, Universitätsstr. 14, 86159 Augsburg, Germany {kerler, stykel}@math.uni-augsburg.de

Summary. We simulate a coupled system consisting of a circuit subsystem and a electromagnetic field subsystem in time domain. Therefore we extend multirate time integration for systems of ODEs to coupled systems of ODEs and DAEs. For the slow changing subsystem we consider magneto-quasistatic equations and apply a model order reduction technique such that the reduced-order subsystem is a system of ODEs.

1 Introduction

We investigate electromagnetic effects in electrical circuits in time domain. Therefore we consider a coupled system of partial differential-algebraic equations (DAEs): The first subsystem describes the voltages in the circuits the other subsystem comes from a FEM semi-discretised magneto-quasistatic (MQS) equation (for the electromagnetic subsystem). By regularisation we achieve a system of ordinary differential equations (ODEs) modelling the electrical network. On the other hand, a FEM discretisation of the MQS part yields a DAE. Often the electric network and the MQS device operate on differing time scales, which will be assumed here. In our example, a low-pass filter will provide the differing scales. For coupled systems of ODEs multirate time integration schemes are a well established method to exploit this structure to gain efficiency. We introduce multirate time integration schemes for coupled ODE-DAE systems to generalize this approach to a larger type of coupled systems. In general the semi-discretised MQS equation is a high dimensional system of DAEs. We provide a model order reduction technique that reduces the large MQS DAE system to a low dimensional ODE and we end up with a small coupled system of ODEs that describe the electromagnetic effects in an electrical circuit.

2 Multirate integration for semi-explicit DAEs

Given a system of semi-explicit DAEs

$$\dot{y}_A = f_A(y_A, y_L, z_L, t) \quad (1)$$

$$\dot{y}_L = f_L(y_A, y_L, z_L, t) \quad (2)$$

$$0 = g_L(y_A, y_L, z_L, t) \quad (3)$$

of index one with constant initial values $y_{A,0}$, $y_{L,0}$, $z_{L,0}$ and a particular dynamical behaviour: y_A provides high dynamical changes while y_L and z_L are changing much slower. Multirate time integrations schemes exploit this special structure by using inherent time step-sizes subsystems: the slow changing subsystem that describes y_L and z_L is integrated with large macro-step H while the fast changing or active subsystem is integrated with smaller micro-steps h . We extend ODE multirate schemes using dynamic refinement strategies introduced in [3]. The whole system (1–3) is integrated with stepsize H by a LobattoIIIIC method, than the active subsystem (1) is integrated with micro-stepsize h while the values of y_L and z_L are interpolated.

3 Model order reduction for magneto-quasistatic equations

To study electromagnetic effects we compute the magnetic vector potential A by solving the curl-curl equation

$$\sigma \frac{\partial A}{\partial t} \nabla \times (\nu (\|\nabla \times A\|^2) \nabla \times A) = J \quad (4)$$

using a FEM discretisation. The standard Galerkin projection yields a nonlinear system of DAEs

$$\mathcal{E} \dot{x} = \mathcal{A}(x)x + \mathcal{B}u, \quad y = \mathcal{C}x \quad (5)$$

with a singular mass matrix \mathcal{E} . Under certain assumptions (see [2]) this system is of tractability index one and can be transformed into a system of ODEs

$$E \dot{x} = A(x)x + Bu, \quad y = Cx \quad (6)$$

with a nonsingular matrix E . The transformation leads, however, to a full matrix A , which is not feasible for large-scale systems. In [2], the authors present a model reduction approach to compute a reduced-order model for (6) and also for (5) which avoids the explicit construction of the ODE system (6). This is possible for a linear as well as nonlinear MQS system (4). For model reduction of the linear MQS system, they use the balanced truncation method, while the nonlinear system is reduced using the proper orthogonal decomposition technique combined with the discrete empirical interpolation method [1].

4 Simulation of coupled circuit/field systems

We consider a single phase 2D transformer with an iron core and two coils. We neglect displacement currents so that we can model the electromagnetic effects by magneto-quasistatic equations as it is described in Section 3. The transformer is coupled to a circuit via source-coupling using the well established methods from [4]. The circuit consists of a low pass filter which filters the low frequencies from a pulse width modulation voltage source to the transformer. The ODEs that describe the circuits are achieved by a modified nodal analysis. Figure 1 shows the circuit diagram of the considered system while the boxed elements represent the electromagnetic effects by their lumped devices. For the coupled system we end up with a system of ODEs (for the circuit subsystem) coupled with a system of DAEs (for the non-reduced MQS equation) or a system of ODEs (for the reduced case). For the coupled system a combination of a model order reduction for the large-scale, slow subsystem and a multirate time integration promises a gain of efficiency in time domain simulation. In this work we will use the multirate ODE/DAE-methods of section 2 for time domain simulation of the coupled system with reduced and non reduced slow subsystem (field). Detailed simulation results about error and simulation time will be presented at the conference.

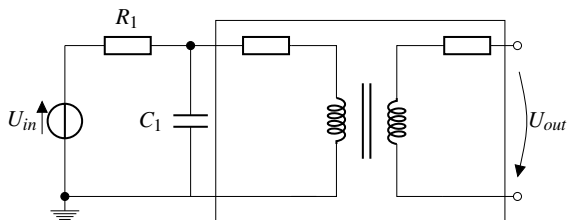


Fig. 1. Circuit diagram of the coupled systems with lumped elements for the electromagnetic effects (box).

Acknowledgement. The work of these authors was supported by the Research Network KoSMos: *Model Reduction Based Simulation of Coupled PDAE Systems* funded by the German Federal Ministry of Education and Research (BMBF), grants no. 05M13WAA and 05M13PXA. Responsibility for the contents of this publication rests with the authors.

References

1. S. Chaturantabut and D.C. Sorensen. Nonlinear model reduction via discrete empirical interpolation. *SIAM J. Sci. Comput.*, 32(5):2737–2764, 2010.
2. J. Kerler-Back and T. Stykel. Model order reduction for magneto-quasistatic equations. Preprint 14/2015, Universität Augsburg, 2015.
3. V. Savcenco, W. Hundsdorfer, and G. J. Verwer. A multirate time stepping strategy for stiff ordinary differential equations. *BIT Numerical Mathematics*, 47(1):37–155, 2007.
4. S. Schöps. *Multiscale Modeling and Multirate Time-Integration of Field/Circuit Coupled Problems*. PhD thesis, Bergische Universität Wuppertal, 2011.

Fast multigrid solvers for isogeometric discretizations

Clemens Hofreither¹ and Stefan Takacs²

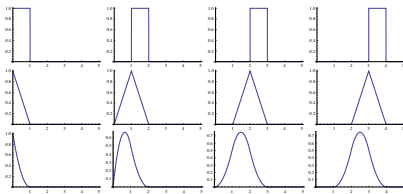
¹ Institute of Computational Mathematics, Johannes Kepler University of Linz
chofreither@numa.uni-linz.ac.at

² RICAM, Austrian Academy of Sciences
stefan.takacs@ricam.oeaw.ac.at

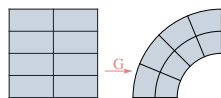
Summary. Isogeometric analysis is an approach for discretizing partial differential equations using the same function spaces which are also used for the representation of the computational domain, like B-splines. Unlike in standard high-order finite element discretizations with low continuity, where the number of degrees of freedom grows with the polynomial degree, for B-splines, the number of degrees of freedom is basically independent of the polynomial degree. This makes them very suitable for solving problems with smooth solutions. We will discuss how to construct fast multigrid solvers for such discretizations.

1 Introduction

Isogeometric Analysis (IgA), introduced by Hughes et al. [4], is an approach for the discretization of partial differential equations (PDEs) which aims to bring geometric modeling and numerical simulation closer together. The technical idea is to use spaces of B-splines or non-uniform rational B-splines (NURBS) both for the geometric description of the computational domain and as discretization spaces for the numerical solution of the PDEs. We consider the space $S_{p,h}(\Omega)$ of splines of polynomial degree p which are $p-1$ times continuously differentiable. A basis of such a space for one dimension can look as follows.



For two or more dimensions, tensor product spaces are used. Here, the domain is represented by a geometry transformation, which is – in contrast to classical finite element methods (FEM) – a global function.



More complicated domains are represented in a multi-patch fashion, where each patch has such a tensor-product structure.

As for classical FEM, we obtain large but sparse linear systems. A good approximation of the solution of the PDE requires sufficient refinement, which causes both the dimension and the condition number of the stiffness matrix to grow. At least for problems on three-dimensional domains, the use of direct solvers does not seem to be feasible. The development of efficient linear solvers or preconditioners for such linear systems is therefore essential.

2 Approximation error estimates and inverse inequality

In a recent paper [5], a robust approximation error estimate for B-splines was shown. There, some symmetry was used to show that the constructed approximation lives in a space $\tilde{S}_{p,h}(\Omega) \subset S_{p,h}(\Omega)$, which consists only of those splines whose odd derivatives (up to order $p-1$) vanish on the boundary.

Theorem 1. For all grid sizes h and all degrees $p \in \mathbb{N}$ with $h p < |\Omega| = b - a$,

$$\|(I - \Pi_{p,h})u\|_{L^2(\Omega)} \leq \sqrt{2} h |u|_{H^1(\Omega)} \quad \forall u \in H^1(\Omega)$$

is satisfied, where $\Pi_{p,h}$ is the H^1 -orthogonal projection into $\tilde{S}_{p,h}(\Omega)$.

For the space $\tilde{S}_{p,h}(\Omega)$, also an inverse inequality was provided.

Theorem 2. For all grid sizes h and all degrees $p \in \mathbb{N}$,

$$|u_{p,h}|_{H^1(\Omega)} \leq 2\sqrt{3} h^{-1} \|u_{p,h}\|_{L^2(\Omega)} \quad \forall u_{p,h} \in \tilde{S}_{p,h}(\Omega)$$

is satisfied.

This inverse inequality does not extend to the whole space $S_{p,h}(\Omega)$. Let $\Omega = (0, 1)$. The function $u_{p,h}(x) := \max\{(1-x/h), 0\}^p$ satisfies

$$\frac{|u_{p,h}|_{H^1(0,1)}}{\|u_{p,h}\|_{L^2(0,1)}} = \sqrt{\frac{2p+1}{2p-1}} p h^{-1} \not\leq c h^{-1}$$

for any fixed c . Note that (for one dimensional domains), the dimension of $S_{p,h}(\Omega)$ is $n+p$ if n is the number of subintervals. It is easy to verify that the dimension of $\tilde{S}_{p,h}(\Omega)$ is $n + (p \bmod 2)$, so its complement (the space of outliers) has a dimension of $2 \lfloor p/2 \rfloor$.

3 Robust multigrid solvers

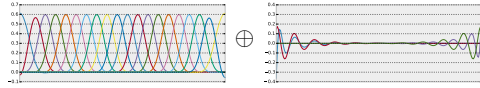
It has been shown that a standard approach for constructing geometric multigrid solvers for IgA leads to methods which are robust in the grid size, however the convergence rates deteriorate significantly when the spline degree is increased, cf. [1]. The analysis was done for the Poisson problem, which can be seen as a formulation for the potential equations or as a starting point for further research concerning other differential equations, like Maxwell's equations.

In [3], it was shown that the method can be significantly improved by using a Richardson smoother, preconditioned with the mass matrix. That method can be formulated in the function space only, so it is not affected by the bad condition number of the *bas*s. However, still the outliers mentioned in the last section play an important role, which make also that method being non-robust in the polynomial degree.

In the following, we introduce a stable subspace-splitting which is then used to construct a robust and efficient multigrid method. Any function in $u \in S_{p,h}(0,1)$ can be decomposed in a sum of a function $u_0 \in \tilde{S}_{p,h}(0,1)$ and its L^2 -orthogonal complement $u_1 \in \tilde{S}_{p,h}^\perp(0,1)$, where, of course,

$$u = u_0 + u_1, \quad \|u\|_{L^2}^2 = \|u_0\|_{L^2}^2 + \|u_1\|_{L^2}^2$$

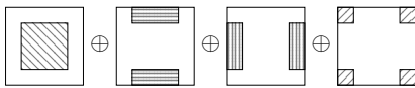
holds. A basis for these two spaces looks as follows:



Using Theorems 1 and 2, we can show that the splitting is H^1 -stable, i.e., there is a constant c such that

$$c^{-1}|u|_{H^1}^2 \leq |u_0|_{H^1}^2 + |u_1|_{H^1}^2 \leq c|u|_{H^1}^2.$$

For $d > 1$ dimensions, we use the tensor product structure of the spline space and obtain 2^d subspaces, where again a robust splitting is possible. For sake of simplicity, we restrict the discussion in the following to $d = 2$. There, the subspaces can be visualized as follows:



Based on the splitting, a p -robust h -multigrid method can be constructed as follows. As we have nested spaces, i.e., $S_{p,2h}(\Omega) \subset S_{p,h}(\Omega)$, the coarse-grid correction is completely standard. The approximation property (in the sense of Hackbusch's splitting of the analysis in approximation and smoothing property) follows then directly from Theorem 1.

The important remaining part is the construction of the smoother, which satisfies the smoothing property. Observe that the stiffness matrix \mathcal{K} is given by

$$\mathcal{K} = K \otimes M + M \otimes K,$$

where M and K are the mass matrix and the stiffness matrix in one dimension. Unlike the mass matrix $\mathcal{M} = M \otimes M$, the stiffness matrix does not have tensor product structure.

Based on the stable splitting, we obtain

$$\begin{aligned} \mathcal{K} &\approx \sum_{i=0}^1 \sum_{j=0}^1 Q_{ij} \mathcal{K}_{ij} Q_{ij}^T \\ &= \sum_{i=0}^1 \sum_{j=0}^1 Q_{ij} (K_i \otimes M_j + M_i \otimes K_j) Q_{ij}^T, \end{aligned}$$

where the (tensor-product) matrices Q_{ij} represent the embedding of the subspaces in $S_{p,h}(\Omega)$ and the matrices \mathcal{K}_{ij} , M_i and K_i represent the restriction of \mathcal{K} , M and K to the subspaces. In the interior, we use the inverse inequality in both directions and obtain $\mathcal{K}_{00} \leq 24h^{-2}M_0 \otimes M_0 =: \mathcal{L}_{00}$. On the edges, we use the inverse inequality along the edge and obtain $\mathcal{K}_{10} \leq (12h^{-2}M_1 + K_1) \otimes M_0 =: \mathcal{L}_{10}$ and the same for the other edge. Observe that \mathcal{L}_{00} , \mathcal{L}_{10} and \mathcal{L}_{01} have tensor-product structure, which is used to invert them efficiently. The $p \times p$ matrix $\mathcal{L}_{11} := \mathcal{K}_{11}$ is inverted directly. Finally, the smoother is defined by

$$u_{p,h}^{(k+1)} = u_{p,h}^{(k)} + \sum_{i=0}^1 \sum_{j=0}^1 Q_{ij} \mathcal{L}_{ij}^{-1} Q_{ij}^T (f - \mathcal{K} u_{p,h}^{(k)}).$$

It can be shown that the computational costs do not exceed $\mathcal{O}(p^d h^{-d})$, which coincides with the order of the complexity for computing the product $\mathcal{K} u_{p,h}^{(k)}$.

Based on this construction, one obtains that the multigrid solver converges with rates that are robustly bounded away from 1 for all grid sizes and all polynomial degrees. Also the numerical results indicate the same. The run times of the algorithm look promising and seem to be better than the previous results, given in [2], for every choice of the grid size and the polynomial degree. An extension to three or more dimensions is completely analogous.

References

1. K. P. S. Gahalaut, J. K. Kraus, and S. K. Tomar. Multigrid methods for isogeometric discretization. *CMAME*, 253:413–425, 2013.
2. C. Hofreither, S. Takacs, and W. Zulehner. A robust multigrid method for isogeometric analysis using boundary correction. *CMAME*, online first, 2016.
3. C. Hofreither and W. Zulehner. Mass smoothers in geometric multigrid for isogeometric analysis. In *Curves and Surfaces*, vol. 9213 of *Lecture Notes in Comp. Sci.*, 272–279. Springer, 2015.
4. T. J. R. Hughes, J. A. Cottrell, and Y. Bazilevs. Isogeometric analysis: CAD, finite elements, NURBS, exact geometry and mesh refinement. *CMAME*, 194(39-41):4135–4195, 2005.
5. S. Takacs and T. Takacs. Approximation error estimates and inverse inequalities for B-splines of maximum smoothness. *M³AS*, 26(7):1411 – 1445, 2016.

Convergence analysis of a boundary element method for Maxwell's time-harmonic interior and exterior eigenvalue problem

Gerhard Unger

Institute of Computational Mathematics, Steyrergasse 30, 8010 Graz, Austria gerhard.unger@tugraz.at

Summary. A convergence analysis of the Galerkin approximation of a boundary integral formulation of Maxwell's time-harmonic interior and exterior eigenvalue problem is presented. The analysis is based on the framework of regular approximations of eigenvalue problems for holomorphic Fredholm operator-valued functions. The derived error estimates are in consistency with numerical examples as given in [8].

1 Boundary integral formulation

We consider a boundary element approximation of the interior and the exterior time-harmonic Maxwell's eigenvalue problem for a given bounded Lipschitz domain $\Omega^i \subset \mathbb{R}^3$. The interior eigenvalue problem reads as follows: Find $\kappa \in \mathbb{R}_+$ and $\mathbf{E}^i \in \mathbf{H}(\mathbf{curl}; \Omega^i)$, $\mathbf{E}^i \neq 0$, such that:

$$\begin{aligned} \mathbf{curl} \mathbf{curl} \mathbf{E}^i - \kappa^2 \mathbf{E}^i &= 0 \quad \text{in } \Omega^i \\ \gamma_t^i \mathbf{E}^i := \mathbf{n} \times \mathbf{E}^i &= 0 \quad \text{on } \Gamma := \partial \Omega^i, \end{aligned} \quad (1)$$

where $\kappa = \sqrt{\varepsilon \mu} \omega$ is the wave number. The exterior eigenvalue problem, usually referred to as scattering-resonance problem, is formulated in $\Omega^e := \mathbb{R}^3 \setminus \overline{\Omega^i}$ and is given by: Find $\kappa \in \mathbb{C}$ and $\mathbf{E}^e \in \mathbf{H}_{\text{loc}}(\mathbf{curl}; \Omega^e)$, $\mathbf{E}^e \neq 0$, such that:

$$\begin{aligned} \mathbf{curl} \mathbf{curl} \mathbf{E}^e - \kappa^2 \mathbf{E}^e &= 0 \quad \text{in } \Omega^e, \\ \gamma_t^e \mathbf{E}^e := \mathbf{n} \times \mathbf{E}^e &= 0 \quad \text{on } \Gamma, \\ \mathbf{E}^e &\text{ is outgoing.} \end{aligned} \quad (2)$$

Any eigenpair (κ, \mathbf{E}^i) of (1) and any eigenpair (κ, \mathbf{E}^e) of (2) has a representation in terms of the single layer potential of Maxwell's equation of the form

$$\mathbf{E}^{i/e}(\mathbf{x}) = \pm \left((\Psi_{\text{SL}}(\kappa)) (\gamma_N^{i/e} \mathbf{E}^{i/e}) \right) (\mathbf{x}), \quad (3)$$

where

$$\begin{aligned} \Psi_{\text{SL}}(\kappa) \boldsymbol{\mu}(\mathbf{x}) &= \kappa \int_{\Gamma} \frac{e^{i\kappa \|\mathbf{x}-\mathbf{y}\|}}{4\pi \|\mathbf{x}-\mathbf{y}\|} \boldsymbol{\mu}(\mathbf{y}) d\mathbf{s}_y \\ &\quad + \frac{1}{\kappa} \nabla \int_{\Gamma} \frac{e^{i\kappa \|\mathbf{x}-\mathbf{y}\|}}{4\pi \|\mathbf{x}-\mathbf{y}\|} \text{div}_{\Gamma} \boldsymbol{\mu}(\mathbf{y}) d\mathbf{s}_y \end{aligned}$$

and $\gamma^{i/e} := \kappa^{-1} \gamma_t^{i/e} \circ \mathbf{curl}$ is the interior/exterior Neumann trace on Γ . The representation formula (3) shows

that any eigenfunction of (1) and (2) is determined by its Neumann trace. Let $S(\kappa) := \gamma_t^i \Psi_{\text{SL}}(\kappa)$ be the single layer boundary integral operator. It holds $S(\kappa) = \gamma_t^e \Psi_{\text{SL}}(\kappa)$ and $S(\kappa) : \mathbf{V} \rightarrow \mathbf{V}$, where \mathbf{V} is the trace space $\mathbf{V} := \gamma_t^i \mathbf{H}(\mathbf{curl}; \Omega^i) = \mathbf{H}_{\times}^{-1/2}(\text{div}_{\Gamma}, \Gamma)$, see e.g. [3]. From the representation formula (3) it follows that any eigenpair of (1) and (2) satisfies the boundary integral equation

$$(S(\kappa)) \left(\gamma_N^{i/e} \mathbf{E}^{i/e} \right) = 0 \quad \text{on } \Gamma. \quad (4)$$

As boundary integral formulation of the eigenvalue problems (1) and (2) we consider the following eigenvalue problem: Find $\kappa \in \mathbb{C} \setminus \{0\}$ and $\boldsymbol{\mu} \in \mathbf{V} \setminus \{0\}$ such that:

$$S(\kappa) \boldsymbol{\mu} = 0. \quad (5)$$

Note that this eigenvalue problem is nonlinear with respect to the eigenvalue parameter κ which appears nonlinear in the kernel of $S(\kappa)$. However, as we will show below, on the discrete level the resulting eigenvalue problem can be transferred to a linear eigenvalue problem by the so-called contour integral method. Equation (4) and the following proposition show the equivalence between the eigenvalue problems (1) and (2) with the boundary integral formulation (5).

Proposition 1. *Suppose that $(\kappa, \boldsymbol{\mu})$, $\kappa \in \mathbb{C} \setminus \{0\}$ and $\boldsymbol{\mu} \in \mathbf{V} \setminus \{0\}$, is an eigenpair of (5). If κ is real, then it is an eigenvalue of (1) and $\boldsymbol{\mu} = \gamma_N^i \mathbf{E}^i$. Otherwise, κ is an eigenvalue of (2) and $\boldsymbol{\mu} = \gamma_N^e \mathbf{E}^e$.*

Crucial for our analysis is that $S(\kappa)$ satisfies a generalized Gårding's inequality, i. e., there exists a compact operator $C(\kappa) : \mathbf{V} \rightarrow \mathbf{V}$ and a continuous and invertible operator $T : \mathbf{V} \rightarrow \mathbf{V}$ such that

$$\text{Re} \left(\langle S(\kappa) \boldsymbol{\mu}, T \bar{\boldsymbol{\mu}} \rangle + \langle C(\kappa) \boldsymbol{\mu}, \bar{\boldsymbol{\mu}} \rangle \right) \geq c \|\boldsymbol{\mu}\|_{\mathbf{V}}^2 \quad (6)$$

for all $\boldsymbol{\mu} \in \mathbf{V}$. The operator T is constructed as a projection, which is related to a suitable stable splitting of the trace space \mathbf{V} , see e.g. [3]. Inequality (6) shows that $T^* S(\kappa)$ is a Fredholm operator with index zero which implies that the eigenvalue problem (5) can be treated in framework of eigenvalue problems for Fredholm operator-valued functions [5].

2 Boundary element approximation

For the boundary element approximation of the eigenvalue problem (5) we consider a conforming Galerkin

scheme. We suppose that $\{\mathbf{V}_h\}_{h \in I}$ is a sequence of approximating subspaces of \mathbf{V} which satisfies the following two conditions:

- i) $\|\boldsymbol{\chi}_h - \boldsymbol{\chi}\|_{\mathbf{V}} \rightarrow 0$ as $h \rightarrow 0$ for all $\boldsymbol{\chi} \in \mathbf{V}$.
- ii) For \mathbb{T} as given in (6) there exists a sequence $\{\mathbb{T}_h\}_{h \in I}$, $\mathbb{T}_h : \mathbf{V}_h \rightarrow \mathbf{V}_h$ linear and continuous, such that

$$\sup_{\boldsymbol{\mu}_h \in \mathbf{V}_h \setminus \{0\}} \frac{\|(\mathbb{T} - \mathbb{T}_h)\boldsymbol{\mu}_h\|_{\mathbf{V}_h}}{\|\boldsymbol{\mu}_h\|_{\mathbf{V}_h}} \rightarrow 0 \quad \text{as } h \rightarrow 0.$$

These conditions are required in order to guarantee a regular approximation of the operator $S(\kappa)$ [4], which is crucial for the convergence of the approximation of eigenvalue problems for holomorphic Fredholm operator-valued functions [5, 6]. The Raviart-Thomas elements of degree k defined on triangulation of Γ are an example of a conforming subspace of \mathbf{V} for which above conditions i) and ii) are satisfied, where $\mathbb{T}_h = P_h \mathbb{T}$, see [2].

The Galerkin formulation of the boundary integral eigenvalue problem (5) is given as: Find κ_h and $\boldsymbol{\mu}_h \in \mathbf{V}_h \setminus \{0\}$ such that:

$$\langle S(\kappa_h)\boldsymbol{\mu}_h, \overline{\boldsymbol{\chi}_h} \rangle = 0 \quad \forall \boldsymbol{\chi}_h \in \mathbf{V}_h. \quad (7)$$

The numerical analysis of the Galerkin approximation (7) of the eigenvalue problem (5) are based on general results for the so-called regular approximation of eigenvalue problems for holomorphic Fredholm operator value functions [5, 6]. In the following theorem the derived convergence results are summarized [7].

Theorem 1. *1. (Completeness of the discrete spectrum) For every eigenvalue $\kappa \in \mathbb{C} \setminus \{0\}$ of the boundary integral eigenvalue problem (5) there exists a sequence (κ_h) of eigenvalues of the Galerkin eigenvalue problem (7) such that*

$$\kappa_h \rightarrow \kappa \quad \text{as } h \rightarrow 0.$$

2. (Non-pollution of the discrete spectrum) Let $K \subset \mathbb{C} \setminus \{0\}$ be compact such that there is no eigenvalue of the boundary integral eigenvalue problem (5) in K . Then there exists an $h_0 > 0$ such that for all $h < h_0$ the Galerkin eigenvalue problem (7) has no eigenvalues in K .

3. Let $D \subset \mathbb{C} \setminus \{0\}$ be compact. Suppose that $\kappa \in \mathring{D}$ and that there is no other eigenvalue in D . Then there exists an $h_0 > 0$ and a constant $c > 0$ such that for all $0 < h \leq h_0$ we have:

a)

$$|\kappa_h - \kappa| \leq c \delta_h(\kappa)^{2/\ell}$$

for all eigenvalues $\kappa_h \in D$ of the Galerkin eigenvalue problem (7), where $\delta_h(\kappa)$ is the gap between the generalized eigenspace corresponding to κ and \mathbf{V}_h and ℓ is maximal length of a Jordan chain corresponding to κ .

b)

$$\inf_{\boldsymbol{\mu} \in \text{GE}(\kappa)} \|\boldsymbol{\mu} - \boldsymbol{\mu}_h\|_{\mathbf{V}} \leq c (|\kappa_h - \kappa| + \delta_h(\kappa))$$

for all eigenpairs $(\kappa_h, \boldsymbol{\mu}_h)$ of (7) with $\kappa_h \in D$ and $\|\boldsymbol{\mu}_h\|_{\mathbf{V}} = 1$.

3 Numerical solution of the discretized eigenvalue problem

The Galerkin formulation of the boundary integral eigenvalue problem (7) is equivalent to a nonlinear matrix eigenvalue problem which can be solved by the so-called contour integral method [1]. The contour integral method is a reliable method for finding all eigenvalues and corresponding eigenvectors which lie inside of a given contour in the complex plane. This is achieved by reducing the nonlinear eigenvalue problem to an equivalent linear one which has the same eigenvalues as the nonlinear eigenvalue problem inside the contour. For numerical examples of the application of the contour integral method for the boundary element approximation of Maxwell's interior eigenvalue problem we refer to [8].

References

1. W.-J. Beyn. An integral method for solving nonlinear eigenvalue problems. *Linear Algebra Appl.*, 436(10):3839–3863, 2012.
2. A. Buffa and S. H. Christiansen. The electric field integral equation on Lipschitz screens: definitions and numerical approximation. *Numer. Math.*, 94(2):229–267, 2003.
3. A. Buffa and R. Hiptmair. Galerkin boundary element methods for electromagnetic scattering. In *Topics in computational wave propagation*, volume 31 of *Lect. Notes Comput. Sci. Eng.*, pages 83–124. Springer, Berlin, 2003.
4. M. Halla. Regular Galerkin approximations of holomorphic T-Gårding operator eigenvalue problems. ASC Report 4, TU Wien, 2016.
5. O. Karma. Approximation in eigenvalue problems for holomorphic Fredholm operator functions. I. *Numer. Funct. Anal. Optim.*, 17(3-4):365–387, 1996.
6. O. Karma. Approximation in eigenvalue problems for holomorphic Fredholm operator functions. II. (Convergence rate). *Numer. Funct. Anal. Optim.*, 17(3-4):389–408, 1996.
7. G. Unger. Convergence analysis of a boundary element method for Maxwell's time-harmonic eigenvalue problems. Technical report. In preparation.
8. Ch. Wieners and J. Xin. Boundary element approximation for Maxwell's eigenvalue problem. *Math. Methods Appl. Sci.*, 36(18):2524–2539, 2013.

Part V

Abstracts of Poster Session 1

A New Charge Simulation Approach for Dielectric Design of High Voltage Switchgear

Muhamet Alija¹, Markus Richter¹ and Andreas Blaszczyk²

¹ ABB GIS Research and Development 8050 Zürich-Oerlikon, Switzerland
muhamet.alija@ch.abb.com, markus.richter@ch.abb.com

² ABB Corporate Research 5405 Baden-Dättwil, Switzerland
andreas.blaszczyk@ch.abb.com

Summary. A fully automatic creation and discretization of 2D dielectric charge simulation models for high voltage switchgear components based on CAD-tool Creo is presented. The new approach enables fast and accurate computation of industrial arrangements including features like triple points, surface charge and large differences between material properties. We focus on discretization method that enables automatic and smooth distribution of surface elements along very complex geometries while ensuring a good accuracy in critical spots. The efficiency of the approach is demonstrated for selected examples of gas insulated switchgear designs.

1 Introduction

The charge simulation method (CSM) has been applied to optimize high voltage arrangements already in 1960s [1], [2], [3], long before the finite element method (FEM) has achieved maturity to handle this type of applications. In the meantime FEM has dominated the market for dielectric computation tools, but the effort required for FEM-analysis in the industrial environment is still considerable and requires maintaining specific FEM-expertise. Therefore, in 1990s we have introduced 3D boundary element method (BEM) as an industrial tool for computations of high voltage switchgear [4]. The BEM approach became very popular since it could be easily integrated into the computer-aided design (CAD) systems like ProEngineer/Creo and does not require the outer boundary box as well as the mesh outside of the solid parts. In the meantime the BEM is closely integrated into the Creo user interface and has been efficiently used by designers for automatic optimization procedures [5].

In spite of easy access to 3D computations there is still a need for a 2D analysis. One reason is the fact that parts of arrangements are partially axially symmetric. For such parts the 2D analysis is much more convenient and sufficient to design them. Another reason is that the 3D meshing is difficult for accurate evaluation of critical spots, that are typically triple points. Therefore, the switchgear designers requested to enable creation of 2D models directly from 3D by defining a cross section through a complex 3D

assembly and generate a 2D geometry. The 2D geometry inherits not only the geometrical shapes but also material properties and boundary conditions. The request of engineers for fully automated 2D computation was the main trigger for the research project presented in this paper. For realization we selected the region-oriented charge simulation method [6]. We have revised the formulation by adding a new concept for computation of triple points. Since we do not use any mesh the main effort was related to a new method of contour discretization, which significantly extended the algorithms used in the past [7].

2 Formulation

Beyond equations for surface elements [6], we introduced new equations related to explicit handling of triple points. For example, for a triple point with two dielectric media and electrode we have added two discrete charges. Each of them is assigned to the set of charges for both dielectrics. The two additional equations are expressing the known potential at triple point but are formulated separately for each dielectric region. In order to avoid numerical oscillations we added for the collocation point i at triple junction an additional flux density continuity equation expressed as follows:

$$\varepsilon_{r1} \sum_{j \in 1} \mathbf{n}_{i1} \cdot \nabla \mathbf{p}_{ij} q_{j1} + \varepsilon_{r2} \sum_{j \in 2} \mathbf{n}_{i2} \cdot \nabla \mathbf{p}_{ij} q_{j2} = \sigma_i \quad (1)$$

where ε_{rN} is relative electric permittivity of region N while \mathbf{n}_{iN} is normal vector at collocation point i assigned to region N , $\nabla \mathbf{p}_{ij}$ is a field coefficient between i and j , q_{jN} is charge value j in region N , σ_i is unknown charge density at the electrode surface.

3 Automatic Model Generation

Switchgear designers require a fully automated field computation for a cross section selected from the 3D model created in the CAD-System Creo as shown in

Fig. 1. In addition to the cross section, the engineer selects a coordinate system in order to specify the position of the rotation axis as well as the boundary condition set defined in Creo Simulate. Based on engineer's specification we extract from the Creo data base the collection of geometrical segments in form of straight lines, arcs and tessellated lines (as representation of splines). Each of the segment has a reference to the adjacent materials and the boundary conditions.

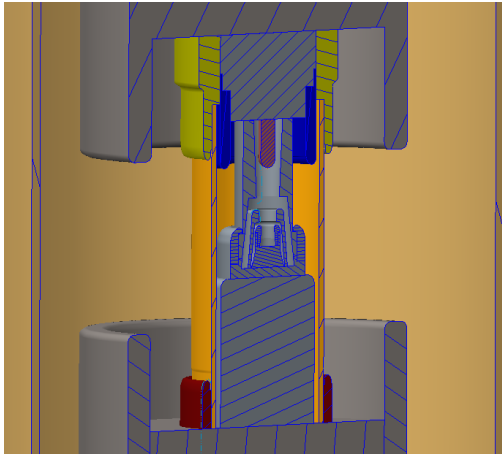


Fig. 1. Cross section created through a CAD-Creo model of an SF6 arrangement.

4 Discretization

The discretization is based on dividing the contour segments into small surface elements. In the middle of each surface element a collocation point is located. We have developed a new algorithm that ensures a smooth distribution of surface elements along very complex geometrical contours and assigns the position of the discrete charges. The distribution of charges by the new algorithm is shown in Fig. 2. A detailed description of the algorithm will be presented in the extended version of this paper.

5 Calculation Examples

The post-processing features requested by switchgear designers include color plots for selected areas and the contour graphs. We use a color plot technique based on field computation for each pixel of the computer screen. This technique allows to achieve a very high resolution and precision of result presentation. An example of a color plot is shown in Fig. 3. The fact that there are no singular points in the CSM formulation is very helpful and allows to compute with a high accuracy in the direct vicinity to boundaries.

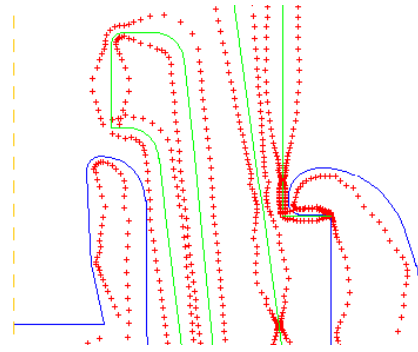


Fig. 2. Discrete charge distribution for a detail from Fig. 1

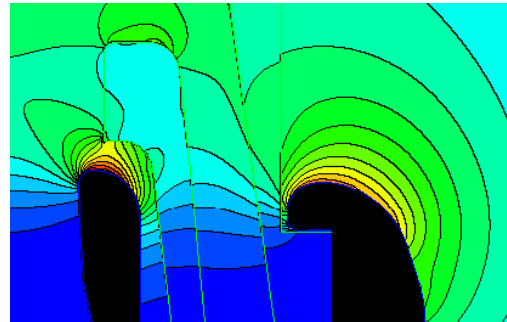


Fig. 3. Field strength distribution for the arrangement in Fig. 1

References

1. H. Steinbigler, Anfangsfeldstrken und Ausnutzungsfaktoren rotationssymmetrischer Elektrodenanordnungen in Luft. *Doctoral Thesis TH*. Munich 1969.
2. H. Singer, H. Steinbigler, P. Weiss, A Chage Simulation Method for the Calculation of High Voltage Fields. *IEEE PES Winter Meeting*, New York, January 27-February 1, 1974, pp. 1660...1668.
3. Nazar H. Malik, A Review of the Charge Simulation Method and its Applications. *IEEE Transactions on Electrical Insulation*. Vol. 24 No. 1, February 1989.
4. N. De Kock, M. Mendik, Z. Andjelic and A. Blaszczyk, Application of 3D boundary element method in the design of EHV GIS components. *IEEE Magazine on Electrical Insulation*. Vol.14, No. 3, pp. 17...22, May/June 1998.
5. B. Dobrzelecki, K. Dudek, T. Nowak, A. Blaszczyk, Integration of Dielectric Design Optimization into a Product Development Workflow. *An International Conference on Engineering and Applied Sciences Optimization*. Greece, 4-6 June 2014.
6. A. Blaszczyk and H. Steinbigler, Region-Oriented charge simulation. *IEEE Transactions on Magnetics*. Vol 30, no. 5, September 1994, pp. 2924...2927.
7. H. Nilsson, P. Wolpert, Automatic Boundary Discretization for the Region-Oriented Charge Simulation Method. *Master Thesis*. KTH Stockolm 1992, TRITANA-E9272.

Coupled circuit device simulation

Kai Bittner¹, Hans Georg Brachtendorf¹, Wim Schoenmaker², Christian Strohm³, and Caren Tischendorf³

¹ University of Applied Sciences of Upper Austria, A-4232 Hagenberg, Austria Kai.Bittner@fh-hagenberg.at, Hans-Georg.Brachtendorf@fh-hagenberg.at

² Magwel NV, Martelarenplein 13, B-3000 Leuven, Belgium Wim.Schoenmaker@magwel.com

³ Dept. of Mathematics, Humboldt-University of Berlin, D-12489 Berlin, Germany strohmch@math.hu-berlin.de, tischendorf@math.hu-berlin.de

Summary. The goal of coupled circuit simulation is to test a complex device described by a full 3D field model in the environment of a larger circuit. We present here an approach, which treats the field model as device with a large number of internal unknowns and equations.

1 Coupled simulation

The circuit is described as a network of devices, connected at nodes. We consider circuit equations in the charge/flux oriented modified nodal analysis (MNA) formulation, which yields a mathematical model in the form of a system of differential-algebraic equations (DAEs):

$$\frac{d}{dt}q(x(t)) + g(x(t)) = s(t). \quad (1)$$

The vector $x \in \mathbb{R}^n$ consists of all node potentials except ground as well as currents through inductors and voltage sources. The equations are obtained from Kirchhoff's current law for each node and additional equations for voltage sources and inductors. Kirchhoff's current law requires the sum off all currents into/from a node to be zero. These currents come from device terminals connected to the node. Except for inductors and voltage sources, where the currents are in the unknown vector, the terminal currents are functions of branch voltages (and their derivatives), which in turn are the differences of node potentials.

For coupling of electromagnetic field simulation with circuit simulation we replace lumped device models by a full 3D modell based on (discretized) Maxwell equations. The discretized field model is provided by an interface to the electro magnetic simulation tool of Magwel [2]. The circuit equations (1) are complemented by the discretized field equations (as internal device equations) of the form

$$\frac{d}{dt}a(x(t)) + f(x(t)) = 0,$$

where the vector $x(t)$ of unknowns is extended by additional variables. The new system has now the same form as the original circuit equations (1) such that solvers for circuit simulation can be applied.

For the coupling several contact surfaces are defined in the field model, which act as device terminals

in the circuit simulator as follows. The node potentials of the device terminals are used as boundary conditions for the electrical potential at the contact surface, while the terminal currents for Kirchhoff's current law are obtained as currents through the contact surfaces.

We use two kinds of interfaces to the field solver. First there is a linear interface, which can be used if the device consists only of conductors and isolators so that all field equations are linear. Then, the discretized equations can be fully described by suitable matrices. These matrices are provided by the field simulator in a pre-processing step.

If semiconductors are present in the device this approach does not work anymore since the equations become nonlinear. For this case a nonlinear interface is used (suitable for any device). Here the field solver provides for any vector of unknowns x the vectors $a(x)$ and $f(x)$ together with their Jacobian's, which are needed for Newton solvers, as part of a DAE solver used in circuit simulation.

2 Numerical results

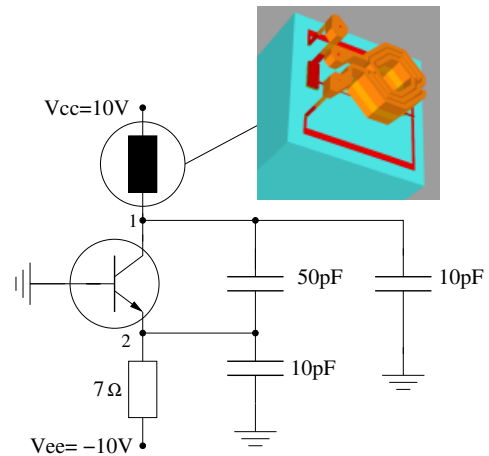


Fig. 1. Colpitts oscillator circuit with full 3D field models for inductors

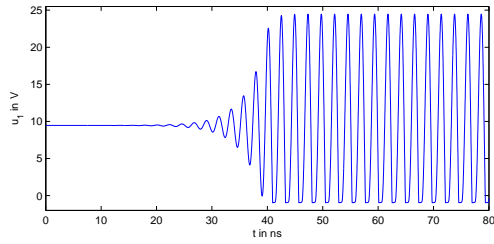


Fig. 2. Simulation result for Colpitts oscillator from Fig. 1

The coupled simulation was implemented in the in-house simulator LinzFrame (C++), where new device classes were coded for the linear and nonlinear interface. These device classes permit to use a field model in the same way as any other device in LinzFrame.

Fig. 1 depicts a Colpitts simulator where the lumped inductor is replaced by an on-chip element. The on-chip inductor is simulated by a full 3D electro magnetic field model using the linear interface. Fig. 2 shows the result of the coupled simulation.

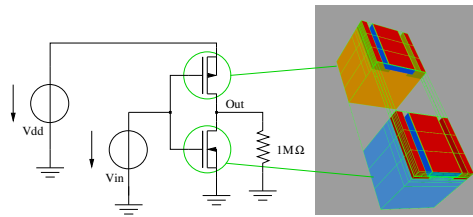


Fig. 3. CMOS inverter with full 3D field models for NMOS and PMOS

The nonlinear interface was tested on the CMOS inverter in Fig. 3, where the MOSFET's have been simulated by a 3D field model. Due to the semiconductor materials the nonlinear interface was used here.

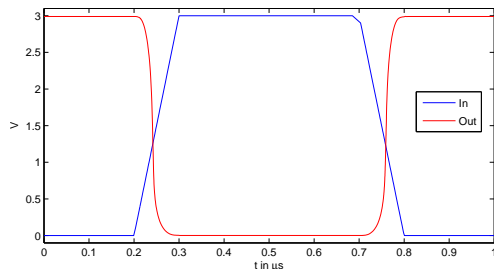


Fig. 4. Simulation result for CMOS inverter from Fig. 3

Finally we show in Fig. 6 the results of a coupled multirate simulation (see [1] for details). The simulation was performed on a differential oscillator

(Fig. 5), where again a electromagnetic field model was used for the inductors.

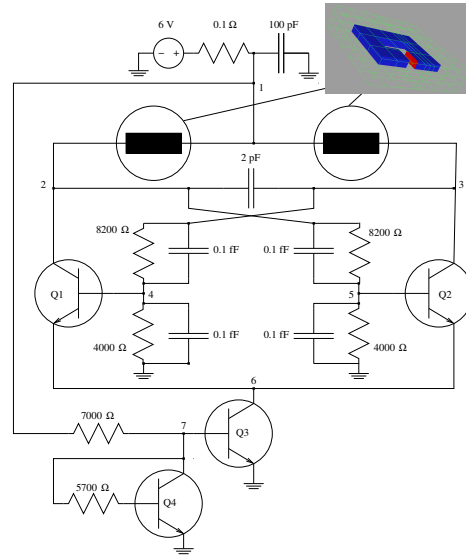


Fig. 5. Differential oscillator circuit with full 3D field models for inductors

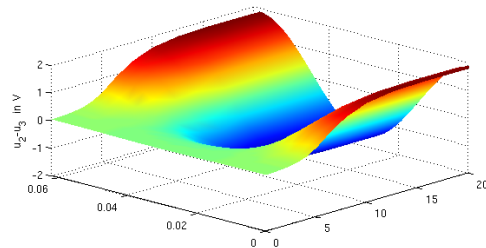


Fig. 6. Simulation result for differential oscillator from Fig. 5

Acknowledgement. This work is funded by the European fp7 project nanoCOPS under grant 619166.

References

1. K. Bittner and H.-G. Brachtendorf. Adaptive multi-rate wavelet method for circuit simulation. *Radioeng.*, 23(1):300–307, 2014.
2. Wim Schoenmaker, Quan Chen, and Philippe Galy. Computation of self-induced magnetic field effects including the lorentz force for fast-transient phenomena in integrated-circuit devices. *IEEE Transactions on Computer-Aided Design of Integrated Circuits and Systems*, 33(6):893–902, 2014.

Virtual High Voltage Lab

Andreas Blaszczyk¹, Jonas Ekeberg¹, Sergey Pancheshnyi¹, and Magne Saxegaard²

¹ ABB Corporate Research 5405 Baden-Dättwil, Switzerland Andreas.Blaszczyk@ch.abb.com,
Jonas.Ekeberg@ch.abb.com, Sergey.Pancheshnyi@ch.abb.com

² ABB AS, Skien, Norway Magne.Saxegaard@no.abb.com

Summary. A concept of simulation framework for dielectric design of high voltage devices has been explained. It is based on a simplified modeling of discharge characteristics including propagation path, withstand and inception voltages. The results of surface charging for a case study with an insulating barrier and the discharge evaluation for a complex gas insulated switchgear arrangement have been presented as application examples.

1 Introduction

During the dielectric type tests the voltage load specified in technical standards is applied to the tested device. The test is successful if either no breakdown of the device insulation occurs or, in case of lightning impulse in gases, only a limited number of breakdowns are observed. The test results are typically predicted by performing electrostatic field computations and comparing the calculated electric field strengths with the critical values specified for the relevant gases and surfaces of the geometry. This approach is very helpful, but in many cases we observe significant deviation to the results obtained in the real high voltage lab.

In this paper we present the concept of a Virtual High Voltage Lab (VHVLab), which is aimed at closing the gap between simulations and experimental results. The foreseen benefits are not only related to the accuracy of the predicted withstand voltages but also to the fact that more insight into the discharge phenomena occurring during tests is expected from simulations. For example, the knowledge of a critical discharge path in a complex geometry is of high interest to engineers.

VHVLab does not attempt to perform first principle simulations with their whole physical and numerical complexity. Instead we propose a simplified approach that evaluates different discharge stages including inception, streamer propagation, leader transition and breakdown [1] while showing in each of these stages the corresponding discharge characteristics. The first principle simulations together with dedicated experiments are used to validate the simplified models. We demonstrate that the VHVLab concept can be effectively applied to complex device geometries.

2 Basic Concept

The architecture of the software concept is shown in Fig. 1. The core, consisting of discharge modeling procedures, is connected via predefined interfaces with external components including the background field solver and the visualizer. As a first step of the analysis, engineers need to create the virtual model of the device and compute it with an electrostatic solver that implements the VHVLab interface. Within the VHVLab session, the numerical computation of discharge characteristics, such as the propagation path in different gases, is performed and presented to the user in a 3D visualizer.

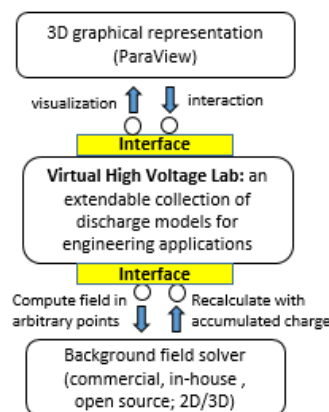


Fig. 1. Architecture of Virtual High Voltage Lab

An important feature of this architecture is the plug-in concept. VHVLab is not implemented as an add-on to any existing software system. It is a self-standing application that uses other commercial, open source and in-house components as plug-ins connected via interfaces.

3 Case Study on Surface Charging

Charging of dielectric surfaces is strongly influencing the development of the discharge process. We demonstrate it for an example of a simple arrangement including a 1.6-mm thick dielectric barrier ($\epsilon_r = 1.7$)

placed between a high voltage rod (7-mm diameter) and a grounded plane [2], see axisymmetric representation in Fig. 2a. The discharges created during a lightning impulse of 91 kV at the rod tip propagate towards the barrier and deposit positive charge on the upper surface of the barrier. Assuming that enough charge has been delivered from the rod, a state of saturation may arise. The saturation charge boundary condition can be formulated for the upper barrier surface according to the following equations:

$$E_{nBarr}\epsilon_{Barr} = \sigma_{sat}, \quad E_{nGas} = 0, \quad (1)$$

where E_{nBarr} and E_{nGas} are normal components of the field strength at the charged surface inside the barrier and in the gas respectively, ϵ_{Barr} is the permittivity of the barrier whereas σ_{sat} is the unknown saturation charge density accumulated on the barrier. The boundary condition (1) is a non-standard feature that needs to be implemented for electrostatic solvers integrated with VHVLab in order to find the unknown σ_{sat} . Once the saturation charge has been obtained, it can be applied as a load during the next stage when the potential of the rod is back to zero. The corresponding voltage distribution for this stage is shown in Fig. 2a.

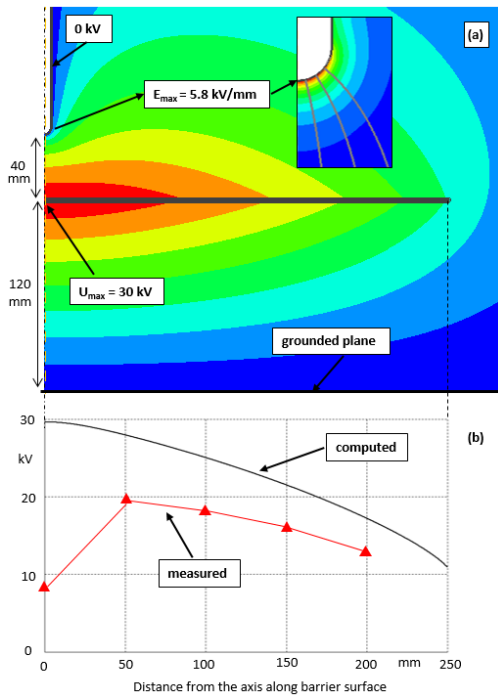


Fig. 2. Potential distribution for a barrier with accumulated saturation charge: (a) computed color plot (b) comparison with measurement

The comparison between the measured and the calculated barrier potential differs significantly within the area just below the zero-potential rod, Fig. 2b. The

difference can be explained by the fact that the computation does not include the re-strike phenomenon that may occur due to the high stress (5.8 kV/mm) at the rod tip. Analysis of inception at the rod showed that the saturation charge would be sufficient to trigger a re-strike in air for impulse voltages above 88 kV. This value is lower than the applied 91 kV and negative streamers may therefore start at the grounded tip and recombine with the positive charge accumulated on the barrier.

4 Switchgear Application

Within the VHVLab framework we can efficiently evaluate discharges for real life devices as shown in Fig. 3. The critical spots and the discharge stream lines have been evaluated for a gas mixture consisting of perfluoro-ketones and air [3]. The results have shown a good agreement with the performed dielectric type tests.

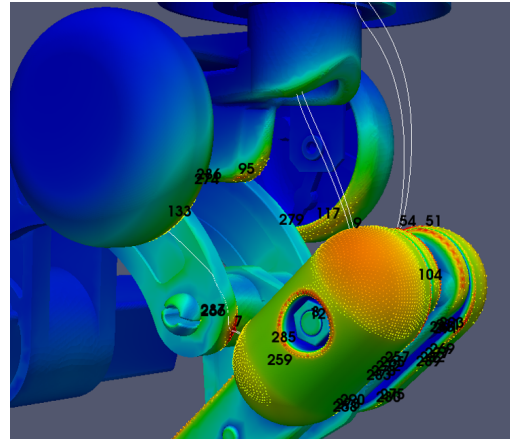


Fig. 3. Evaluation of critical spots and selected discharge stream lines in a 24 kV gas insulated ring main unit

More details on discharge evaluation procedures and their application to high voltage devices will be presented in the extended version of this paper.

References

1. A. Pedersen, T. Christen, A. Blaszczyk, H. Böhme. Streamer inception and propagation models for designing air insulated power devices. *CEIDP Conference Material*. Virginia Beach, Oct. 2009.
2. J. Ekeberg. Dielectric multi-barrier flashovers in air. ABB CH-RD 2015-61 internal report. 2015
3. M. Hyrenbach, T. Hintzen, P. Müller, J. Owens. Alternative gas insulation in medium-voltage switchgear. *23rd International Conference on Electricity Distribution*. Lyon, 15-18 June 2015.

Topology optimization of synchronous reluctance motors for achieving maximum torque capability

Gerd Bramerdorfer¹, Peter Gangl², and Armin Fohler³

¹ Johannes Kepler University Linz, Department of Electrical Drives and Power Electronics
gerd.bramerdorfer@jku.at

² Johannes Kepler University Linz, Doctoral Program “Computational Mathematics” peter.gangl@jku.at

³ Linz Center of Mechatronics armin.fohler@lcm.at

Summary. This paper covers the topology optimization of a synchronous reluctance motor (SynRM) for maximum torque capability. A typical motor design is considered and the analyses are carried out using magnetostatic nonlinear finite element calculations in two dimensions. The rotor structure is optimized by means of a level-set algorithm to provide maximum torque which is equivalent to maximum output power for given rotor speed.

1 Introduction

A typical SynRM features a slotted stator comprising a three-phase winding system and a rotor with flux barriers in order to make use of a change of the reluctance with regard to the rotor angle. Both, the stator and rotor core are usually made of laminated steel in order to minimize the respective iron losses. Recently this motor gained more attention, as companies consider it as an alternative to the widely spread induction machines. The main reasons are a better power factor and efficiency, especially at partial load. Comparing with motors equipped with permanent magnets, the synchronous reluctance motor features a worse performance. However, due to the lack of magnets, the motor design is more robust and the production costs are lower and less volatile. As the name of this motor implies, the torque is generated due to the interaction of a rotor angle dependent reluctance and properly set stator phase currents. In Fig. 1, typical transversally laminated rotor designs are presented. The ideal shape of the flux barriers, e.g., cornered or round, and the optimal number of barriers was intensively

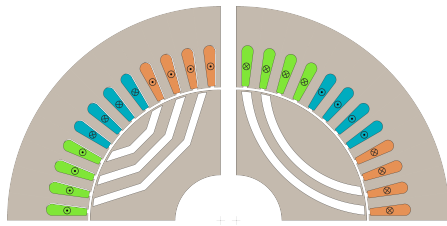


Fig. 1. Typical rotor structures with cornered (left) or round (right) flux barriers. Just a quarter of the respective motor cross sections is drawn.

investigated in the past [5, 6] and is still considered in present research [2, 4] as no superior solution was found. Most researchers deal with the optimization of a parametrized rotor with few design variables. However, this obviously limits the solution space. Thus, in this paper a topology optimization based approach is favored to derive valuable insights regarding the ideal rotor shape.

2 Optimization Scenario

In the present study, a three-phase machine is analyzed. The currents impressed to the stator coils are of sinusoidal shape and are changed according to the electric rotor angle. By introducing the current vector \mathbf{i} they can be defined by:

$$\mathbf{i}(t) = \begin{bmatrix} i_1(t) \\ i_2(t) \\ i_3(t) \end{bmatrix} = \hat{i} \begin{bmatrix} \cos(\omega_{el} t - \varphi_0) \\ \cos(\omega_{el} t - \frac{2\pi}{m} - \varphi_0) \\ \cos(\omega_{el} t - \frac{4\pi}{m} - \varphi_0) \end{bmatrix}. \quad (1)$$

\hat{i} and m denote the current magnitude and the number of phases, respectively, while φ_0 gives an initial offset. ω_{el} is specified by

$$\omega_{el} = \omega_r \frac{N_r}{2}, \quad (2)$$

where N_r gives the number of rotor poles and ω_r represents the angular speed of the rotor. The currents are changed according to the rotor position. Hence, they can alternatively be represented as functions of the rotor angle $\varphi = \omega_r t$. As the motor is assumed to be a conservative system, this also applies to all further derived machine quantities.

The motor torque t of the synchronous reluctance motor is a function of the change of the inductances and the phase currents:

$$t(\varphi) = \frac{1}{2} \mathbf{i}^T \frac{\partial \mathbf{L}}{\partial \varphi} \mathbf{i}. \quad (3)$$

\mathbf{L} denotes the matrix of inductances and is defined by:

$$\mathbf{L} = \begin{bmatrix} L_{11} & L_{12} & L_{13} \\ L_{21} & L_{22} & L_{23} \\ L_{31} & L_{32} & L_{33} \end{bmatrix}. \quad (4)$$

Matrix entries of type L_{xy} with $x = y$ are called self-inductances, while parameters L_{xy} with $x \neq y$ represent the coupling of different phases. As $L_{xy} = L_{yx}$ always holds, \mathbf{L} is symmetric. Due to the nonlinear material characteristics of the applied ferromagnetic materials, \mathbf{L} generally is a function of the stator currents and the rotor position $\mathbf{L} = f(\mathbf{i}, \varphi)$. As the current magnitude \hat{i} is kept constant throughout this analysis, \mathbf{L} can be uniquely defined by $\mathbf{L} = f(\varphi)$. From the periodicity of the stator currents and the skew symmetry of the material characteristics, it can be observed that $\mathbf{L}(\varphi) = \mathbf{L}(\varphi + \frac{2\pi}{N_r})$. In order to maximize the torque, the change of the inductances with regard to the rotor angle should be maximized. Typically, two quality measures are considered, the mean torque t_{mean}

$$t_{mean} = \frac{1}{2\pi} \int_0^{2\pi} t(\varphi) d\varphi \quad (5)$$

and the torque ripple t_{ripp} , defined as

$$t_{ripp} = \max_{0 \leq \varphi < 2\pi} t(\varphi) - \min_{0 \leq \varphi < 2\pi} t(\varphi). \quad (6)$$

While t_{mean} is related to the output power of the motor and thus should be maximized, t_{ripp} must be minimized in order to avoid vibration and acoustic noise.

Optimizing those quality measures can be achieved by modifying the rotor structure. In the present study, this is performed using topology optimization comprising a level-set algorithm, which will be explained in more detail in Section 3. The torque is calculated using magnetostatic nonlinear finite element analyses. According to (5) and (6), usually at least one full period of the torque is analyzed by considering a discrete number of rotor positions within an angular range of $\frac{2\pi}{N_r}$. By contrast, the present analysis focuses on obtaining optimal rotor structures regarding single rotor angles while maximizing the respective torque value. Thus, deep insight is provided if, besides an obvious phase shift in angular position, the impact of the current vector \mathbf{i} and the stator slotting on the optimal rotor structure is negligible or not.

3 Level-Set Algorithm

The optimization procedure is carried out by means of the level-set algorithm introduced in [1] which is based on the mathematical concept of the topological derivative, see also [3]. The topological derivative of a domain-dependent functional at a spatial point x denotes its sensitivity to a local change of the material in the neighborhood of the point x . It attains negative values in points x where a local modification of the material would decrease the functional, and positive values where a local change would increase it. The employed level-set algorithm starts out from an initial design and then subsequently uses the topological derivative information to update the materials inside the rotor to reach a design where the topological

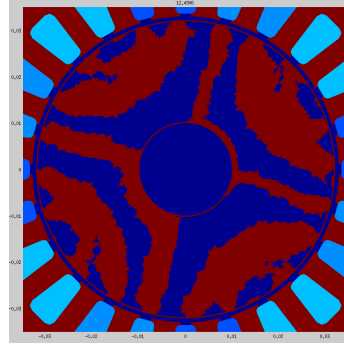


Fig. 2. Initial results of the optimized rotor structure

derivative is only positive or only negative, depending on whether the functional should be minimized or maximized, respectively.

4 Initial Results and Outlook

In our first numerical experiments, we started out with the rotor consisting of only ferromagnetic material. A first result obtained by the level set algorithm introduced in Section 3 is depicted in Figure 2. We plan to use shape optimization as a post-processing tool together with a special mesh modification method which allows for smoother representation of the sub-domain interfaces.

Acknowledgement. This work was conducted within LCM GmbH as a part of the COMET K2 program of the Austrian government. The projects are kindly supported by the Austrian and Upper Austrian government and scientific and industrial partners. The authors thank all supporters.

References

1. S. Amstutz and H. Andrä. A new algorithm for topology optimization using a level-set method. *Journal of Computational Physics*, 216(2):573 – 588, 2006.
2. F. Cupertino, G. M. Pellegrino, E. Armando, and C. Gerada. A SyR and IPM machine design methodology assisted by optimization algorithms. In *IEEE Energy Conversion Congress and Exposition (ECCE)*, Sept 2012.
3. P. Gangl, S. Amstutz, and U. Langer. Topology optimization of electric motor using topological derivative for nonlinear magnetostatics. *IEEE Transactions on Magnetics*, 52(3):1–4, March 2016.
4. J. Kolehmainen. Synchronous reluctance motor with form blocked rotor. *IEEE Transactions on Energy Conversion*, 25(2):450–456, June 2010.
5. T. Matsuo and T. A. Lipo. Rotor design optimization of synchronous reluctance machine. *IEEE Transactions on Energy Conversion*, 9(2):359–365, Jun 1994.
6. A. Vagati, M. Pastorelli, G. Francheschini, and S. C. Petracche. Design of low-torque-ripple synchronous reluctance motors. *IEEE Transactions on Industry Applications*, 34(4):758–765, Jul 1998.

Compact Reduced Order Multiphysics Models for Electrostatic Actuated MEMS Switches

Gabriela Ciuprina¹, Daniel Ioan¹, Aurel-Sorin Lup¹,
Dragos Isvoranu¹, Anton Duca¹, and Alexandra Stefanescu²

¹ Politehnica University of Bucharest, Spl. Independenței 313, 060042, Bucharest, Romania,
gabriela.ciuprina@upb.ro, daniel.ioan@upb.ro, sorin.lup@upb.ro,
dragos.isvoranu@upb.ro, anton.duca@upb.ro

² IMT-Bucharest, Str. Erou Iancu Nicolae 32B (126A), 77190, Bucharest, Romania.
alexandra.stefanescu@imt.ro

Summary. Reduced order models for the multiphysics behavior of microelectromechanical switches are obtained, starting from field simulations and analogies with mechanical systems with lumped components: masses, springs, dampers. If the degree of nonlinearity is low, even a reduced system with one mass, one spring and one damper, obtained from field simulations and time variation of the displacement of one point of interest, can be accurate enough. If the system is strongly nonlinear, the number of relevant points in which the displacement is recorded is increased. Their position is chosen in accordance with the deflection of the mobile part.

1 Introduction

The efficient design of complex systems, such as integrated systems on chips, needs accurate macromodels of their constitutive parts. In order to be useful for the designer, such a compact model has to be reduced, but accurate enough, its extraction has to be done from the physical description with a reasonable computational effort and be as automatic as possible, and its simulation must be much less than the simulation of the original, non-reduced, discretized model. Finally, it has to be described in a way which will allow its natural coupling with the other components of the system [4]. In this paper the investigated components are MEMS switches which consists of electrostatically actuated movable parts and are used to allow or block the propagation of RF signals in various applications.

There are a lot of model order reduction (MOR) algorithms available [5], the difficulty of reducing the order of RF MEMS switches discrete models coming from the non-linearity of the system to be reduced. A method based on projections have been proposed [3] and tested on a MEMS switch. A procedure to integrate several heterogeneous programs (for multiphysics evaluation with ANSYS, MOR also based on projection - Arnoldi and optimization - DOT optimizer) was described in [2] and tested for a piezoresistive cantilever beam micro accelerometer.

This paper is a continuation of [1] and investigates a data driven model reduction procedure for MEMS

switches. According to our previous experience with MOR for passive RF components, a data driven procedure might be able to obtain, for certain problems, reduced models of much lower order than the ones based on projections. Our goal is to investigate how valid is this statement for MEMS switches.

2 Method and results

In [1] we proposed a method to extract a macromodel for RF-MEMS capacitive switches that includes both the coupled multiphysics (structural-electric) behavior of the switch as well as its RF behavior. The macromodel was described as a Spice circuit model, which is controlled by the MEMS actuation voltage and is excited with the RF signal. However, the multiphysics part referred only to the static behavior, needed to extract the pull-in voltage of the switch. The extraction algorithm was inspired by the most simple model conceivable for an electrostatic switch, namely a parallel plate capacitor having one armature fixed and the other armature, of mass m suspended by a spring having the stiffness coefficient k if the elastic force is assumed to vary linearly with respect to the armature displacement z , or k_1 and k_3 if the dependence is a cubic one. The equation of motion of such a simplified model is generally

$$m \frac{d^2 z}{dt^2} + b \frac{dz}{dt} + k_1 z + k_3 z^3 = F_{ES}(u, z), \quad (1)$$

where F_{ES} is the electrostatic force, which depends on the applied voltage u and the displacement z and b is a damping coefficient. A linear elastic force corresponds to the equation with $k_1 = k$, $k_3 = 0$.

In order to extract the stiffness coefficients, k or k_1, k_3 a strongly coupled static structural-electrostatic simulation was carried out, from which the electrostatic force was fitted to a rational expression $F_{ES}(u, z) = -c_1 z / (c_1 z + c_2)^2 u^2$, where c_1 and c_2 are obtained by fitting the inverse value of the extracted capacitance to a linear dependence $c_1 z + c_2$, where z is the displacement of the point where the first contact will be made.

Then, k or the pair k_1, k_3 where obtained through first or third order least square fitting, respectively. The numerical results showed that the cubic dependence was able not only to predict accurately the pull in voltage (error less than 1%), but also the dependence of the displacement with respect to the applied voltage [1].

The effective mass m can be extracted in two ways, both relying on a time domain simulation without damping, for an excitation that is less than the pull-in voltage of the switch, such that oscillations are visible in the membrane movement. From this undamped response we can extract the fundamental frequency ω_0 and compute the mass as $m = k/\omega_0^2$, or we can extract the inertial force as $F_{in} = F_{ES}(u, z) - k_1 z - k_3 z^3$, and do a first order least square fitting of it with respect to the acceleration $a = d^2 z/dt^2$

Finally, the effective damping coefficient b is extracted from a time domain simulation with damping. The damping force is computed as $F_d = F_{ES}(u, z) - k_1 z - k_3 z^3 - m \frac{d^2 z}{dt^2}$, and fitted with a first order polynomial in dz/dt

To test the proposed algorithm, two switch configurations were considered: a cantilever (Fig. 1) and a bridge with rectangular anchors.

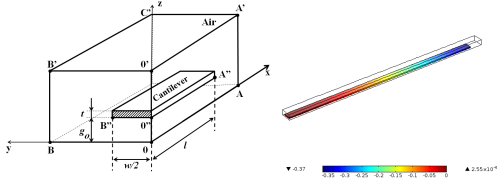


Fig. 1. Cantilever switch: left - computational domain; right - displacement just before the pull in.

The validation with damping is carried out for cantilever test, where a Rayleigh structural damping β_s is included explicitly in the FEM elastic material model. Such damping is usually expressed as $b_s = \alpha_s m + \beta_s k$, where α_s is the mass-damping coefficient and β_s is the stiffness-damping coefficient. We took $\alpha_s = 0$, imposed various values for β_s and extract the global β to be included in the macromodel.

Fig. 2 shows the comparison of dynamic responses and Table 1 holds quantitative results. Even if the relative difference between the imposed β and the extracted one is relatively high (20% in some cases), the dynamical responses are satisfactory, again better when a cubic dependence of the elastic force with respect to the displacement is considered (relative error less than 2%). It is interesting to note that the more damped is the system, the more accurate is the approximation.

For the bridge benchmark, the procedure is successful to find the stiffness coefficients, but fails in the extraction of the effective mass. This is due to the fact that the inertial force cannot be accurately fitted with

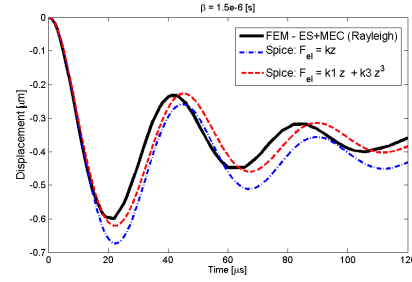


Fig. 2. Dynamic simulation for an applied step voltage of 5V applied to a model with an imposed local Rayleigh damping of $1.5e-6$ s.

Table 1. Extraction of Rayleigh Damping Parameter

Imposed β_s [s]	Extracted β [s]	Rel. diff. [%]	Computed $b = \beta * k$ [g/s]	Rel.er. [%] FEM-SPICE use k, k_1, k_3
6.0e-5	7.1e-5	19.2	1.70e-2	1.2 0.082
6.0e-6	7.3e-6	21.5	1.73e-3	2.1 0.074
1.5e-6	1.8e-6	18.7	4.23e-4	12 0.55
6.0e-7	6.8e-7	13.0	1.61e-4	26 1.4

a first order dependence with respect to the acceleration. To increase the order of the reduced system, the number of relevant points in which the displacement is recorded is increased. Their position is chosen in accordance with the deflection of the membrane.

Acknowledgement. This work was supported by the Romanian Authority for Scientific Research (project PN-II-PT-PCCA-2011-3, grant no. 5/2012).

References

1. G. Ciuprina, A.S. Lup, B. Diță, D. Ioan, D. Isvoranu, S. Sorohan, and S. Kula. Mixed-domain macro-models for rf mems capacitive switches. In G. Michael, editor, *Mathematics in Industry*. Springer, Berlin Heidelberg New York, 2016. Accepted.
2. Jeong Sam Han, Evgenii B Rudnyi, and Jan G Korvink. Efficient optimization of transient dynamic problems in mems devices using model order reduction. *J. of Micromechanics and Microengineering*, 15(4), 2005.
3. M. Rewienski and J. White. A trajectory piecewise-linear approach to model order reduction and fast simulation of nonlinear circuits and micromachined devices. *IEEE Trans. CAD of Integrated Circuits and Systems*, 22(2):155–170, 2003.
4. M.J. Rewienski. *A trajectory piecewise-linear approach to model order reduction of nonlinear dynamical systems*. PhD thesis, MIT, 2003.
5. W. H. Schilders, H.A. van der Vorst, and J. (Eds.) Rommes. *Model Order Reduction: Theory, Research Aspects and Applications*. Springer, 2008.

Solution of linear systems for electronic circuits with large numbers of parasitics capacitances

Nhung T.K Dang¹, Wil H. A Schilders¹, Joost Rommes², Pascal Bolcato², Jos Maubach¹, and Michiel Hochstenbach¹

¹ Department of Mathematics and Computer Science, Eindhoven University of Technology, 5612 AZ Eindhoven, The Netherlands t.k.n.dang@tue.nl, w.h.a.schilders@TUE.nl, J.M.L.Maubach@tue.nl, M.E.Hochstenbach@tue.nl

² Mentor Graphics, 110 Blaise Pascal, 38330 Montbonnot-Saint-Martin, Grenoble, France Joost.Rommes@mentor.com, pascal.bolcato@mentor.com

Summary. The desire of creating smaller and faster electronic devices has never ended in the electronics industry, and this leads to challenging problems in the EDA¹ industry. In order to perform more realistic simulations, it is now necessary to include a large number of additional devices in the electronic circuits describing parasitic electromagnetic effects. This leads to much larger linear systems, necessitating a closer look at the techniques to solve these. In this paper, we present a novel technique to address this problem when large numbers of parasitic capacitances are included.

1 Introduction

The demand for faster and accurate EDA tools for the simulation of AMS (analog mixed signal) circuits has been evolving with each new technology generation. In every new generation the transistors are smaller and the chip density is greater which cause parasitic electromagnetic effects in transistors and interconnects to be more pronounced. In this way, simulation time is increased with greater chip density. Advanced numerical techniques are imperative to address present-day challenges (going to 7nm!) in the electronics industry. The main aim is to speed up transient simulation of AMS circuits. For this purpose, in general, improvements in the performance of existing simulators and parallelization of simulation algorithms, with improved scalability, are targeted [?]. With regard to the first objective, due to the increasing amount of parasitics, full device-parasitic simulations are too costly. Therefore, reduced models are sought for the parasitics. Parasitic circuits are very large network models containing millions of nodes interconnected via vital circuit elements: R, RC, or RLC. Parasitic networks with millions of nodes, RC elements and thousands of terminals are often encountered in real chip designs. There are MOR² methods to deal with these large networks. However, existing MOR methods may be unsuitable for circuits with many terminals because they produce dense reduced models, yielding circuits

with fewer circuit nodes, but more circuit elements (Rs,Cs) than the original circuit [?], [?]. In addition, longer simulation times may be required than for the original one. Besides, additional elements (e.g. current/voltage controlled sources) must be introduced to reconnect reduced parasitics to other devices if the terminal connectivity is affected.

In this work, an introduction of two methods (called split-C and move-C) used to reduce the system matrices of an RC circuit is provided. Split-C grounds the coupling capacitors under a given threshold to the ground-node. Move-C consists of moving coupling capacitors between nets to another position such that the total coupling capacitance is kept constant. For some initial experiments, described below, both methods give promising results and will be investigated further.

2 Problem formulation

2.1 Split-C and move-C applied to RC networks

Consider the modified nodal analysis (MNA) [?] description of an RC circuit:

$$(G + sC)x(s) = Bu(s) \quad (1)$$

where the MNA matrices $G, C \in \mathbb{R}^{n \times n}$ are symmetric, non-negative definite and corresponding to the stamps of resistor and capacitor values, respectively. Furthermore, $x \in \mathbb{R}^n$ is the unknown vector, $u \in \mathbb{R}^m$ is the current or voltage source and $B \in \mathbb{R}^{n \times m}$. The output of the system is $y(s) = Ex(s)$ where $E \in \mathbb{R}^{p \times n}$.

For split-C methods, all coupling capacitors under a threshold will be removed (or grounded), making the modified circuit more simple than the original one. In this way, the modified matrix \tilde{C} becomes sparser than the matrix C , hence the linear system $(G + s\tilde{C})x = b$ can be solved faster. However, for large dimensional matrices there are large errors between the modified solution and the original solution. The large error is caused by removing a lot of elements which are the

¹ EDA: Electronic Design Automation

² Model Order Reduction

connections between block-diagonals.

To overcome this drawback of split-C, move-C is introduced. In circuit's view, move-C is moving coupling capacitors between nets to one or some new position(s) such that the total coupling capacitance between nets is kept. In this way, the connections between block-diagonals in the matrix can be preserved. The reason to keep investigating both split-C and move-C is that the initial goal for split-C is making split-C exploit automatically. In other words, we can predict beforehand, when given a circuit, if we accept a certain tolerance on the error, which threshold value for split-C we should take, or on the other hand, if we chose a certain threshold value for split-C, what error we will get. The goal for move-C is that we can find out the position(s) to move coupling capacitors when knowing which nets there are and how much coupling capacitors there are between nets.

3 Experiments

Three transmission lines circuit

The three transmission lines circuit used for this experiment is shown in Fig.1. The first and the third

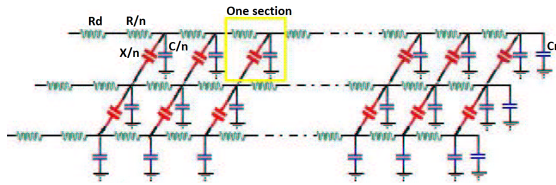


Fig. 1. Three lines model.

line carry the signal and the middle line just sits quietly. The input signal is T-sec rise-time signal, $v_o(t) = \frac{t}{T}u(t) - \frac{t-T}{T}u(t-T)$, where $u(t)$ is the unit step function:

$$u(t) = \begin{cases} 0, & t \leq 0 \\ 1, & t > 0 \end{cases}$$

The model is the same as the one presented in Li Chao's thesis [?].

The first case, the output node is the last node at the middle line (the quiet line). For this case, applying split-C for this circuit corresponds to grounding all coupling capacitors to ground node. Applying move-C for this circuit corresponds to moving all coupling capacitors to the middle section at each line. For most choices of m (the number of sections or the number of nodes in each line), the results of the three problems are as similar as shown in Fig 2. There are output signals at the middle line when applying move-C whereas there is no output signal when applying split-C. It means that with split-C, there are no crosstalks (relations) between the middle line and the other two,

whereas there are in the original problem and the move-C problem. Move-C keeps the relation between the 3 lines observed by the crosstalk, Fig 2. When the

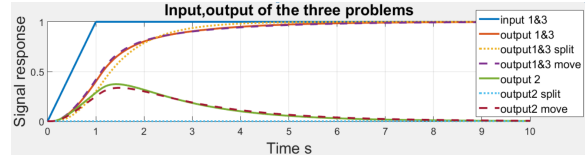


Fig. 2. Output's responses of original, split-C and move-C problem, $m = 300$ nodes in each line.

output nodes are the last nodes at the first and third lines, again move-C seems better than split-C. However, as mentioned above split-C is kept investigating.

m	$t_{original}$	$t_{split-C}$	t_{move-C}
300	131.8618	114.0398	115.9033
500	247.6781	192.1816	193.9578
1000	360.1957	300.7925	300.9557

Table 1. CPU times (sec) of the original, split-C and move-C problem.

4 Future work

In the near future we want to develop advanced split-C and move-C algorithm which are robust for large extracted netlists. Split-C can detect automatically, given an error tolerance, which value of threshold we need to chose, and in contrast, with a chosen threshold what error we will get. Furthermore, move-C also needs to be improved to deal with other large extracted netlists.

References

1. F. N. Najm. *Circuit Simulation*. ISBN 978-0-470-53871-5, Wiley, New Jersey, 2010.
2. P. Li. Foundations and Trends in Electronic Design Automation. *Parallel Circuit Simulation: A Historical Perspective and Recent Developments*. Vol.5, No.4, 2011.
3. Li Chao. *Mathematical Analysis of Crosstalk*. Ph.D.'s thesis, Eindhoven University of Technology, 2004.
4. Roxana Ionutiu. *Model Order Reduction for Multi-terminal Systems with Applications to Circuit Simulation*. Ph.D.'s thesis, Jacobs University Bremen, Germany and Eindhoven University of Technology, The Netherlands, 2011.
5. R. Ionutiu, J. Rommes, W. H. A. Schilders. SparseRC: Sparsity preserving model reduction for RC circuits with many terminals *IEEE Trans. Comput.-Aided Des.*, vol. 30, no. 12, pp. 1828-1841, Dec. 2011.

Automatic epilepsy seizure detection using wavelet transform

Gaidar V. O.¹ and Sudakov O. O.²

¹ Taras Shevchenko National University of Kyiv gaidar.viktoria@gmail.com,

² Taras Shevchenko National University of Kyiv sudakov.oleksander@gmail.com

Summary. This paper presents a mechanism by which seizures are detected using a single channel of on-scalp EEG. The proposed approach is based on Stationary Wavelet Transform (SWT) to decomposed the electrocorticography (ECoG) signal into its sub-bands to detect rhythmic discharges of specific frequencies. Afterwards, the modified post-processing procedure was applied for identification of epilepsy seizure.

1 Introduction

Epilepsy is one of the worlds most common neurological diseases, affecting more than 40 million people worldwide. Epilepsys hallmark symptom, seizures, can have a broad spectrum of debilitating medical and social consequences [1].

The problem of automated seizure detection is the first step towards tackling many related problems, such as seizure prediction, prevention, and early seizure abortion [4]. Automated seizure detection and prediction have been extensively studied in the context of human epilepsy [5]. Yet some of the more challenging problems in particular seizure abortion and prevention using neurostimulation methods, are currently being studied in animal models of epilepsy (both in-vitro and in-vivo). Thus it is important to develop solid seizure detection techniques for these animal models also.

The work described below uses data from live (*in-vivo*) rats with chronic epileptiform activity.

2 Description of the Methods

The data processing consists of three main steps: data pre-processing, stationary wavelet transform and post-processing methods.

2.1 Data pre- processing

For implementation of the seizure detection method, a general data pre- processing cycle has been implemented. This pre-processing cycle consists of three steps:

- noise cancellation;
- power line interference cancellation (at 50 Hz);
- moving average with a Gaussian window.

2.2 Stationary wavelet transform

The discrete wavelet transform (DWT) is a decomposition of the time series $x(t)$ which can be understood as a successive band-pass filtering and downsampling. Unfortunately, the DWT is not shift-invariant when applied to discrete time series $x(t)$, i.e. if the input time series $x(t)$ is shifted, the resulting coefficients may differ severely. Therefore the stationary wavelet transform [2] was invented.

After SWT for each scale a the calculated coefficients can be considered as a time series $\chi_a[n]$. Since the different scales cause a different scaling of the coefficients, the $\chi_a[n]$ need to be normalized to be compared among each other.

The mean of the $\chi_a[n]$ is calculated. A threshold ϑ_1 is calculated using standard deviation σ of the time series $\sum[n]$ and a variable parameter λ which has to be provided by the user. This threshold is then applied to $\sum[n]$, such that all values greater that ϑ_1 are labeled 1, else 0. The result is a binary time series $\beta_1[n]$.

2.3 Data post- processing

In the previous section we reviewed the single seizure detection methods generate binary time series named $\beta_1[n]$ representing the indices where a specific feature indicate the presence of a seizure. These seizures need to be classified as epileptic or non-epileptic. Therefore, the indices have to be translated into possible seizure onsets and offsets. [3].

The number of accepted seizures is given by the counter n , thus initialized with 0. Each index $i = 1 \dots$ data size is checked whether it is an epileptic seizure set or non-epileptic. A minimum ictal phase of 5 s is assumed and the minimum interictal phase of 10 s.

3 Results

In our case we had a data from live (in-vivo) rats with chronic epileptiform activity collected from one channel intracranial EEG electrode. The ECoG recording was obtained at Bogomoletz Institute of Physiology of NAS of Ukraine.

The obtained data is recorded in $x[n]$. The sampling rate of EEG dataset is 416 Hz.

Figure 1 shows one of the raw dataset.

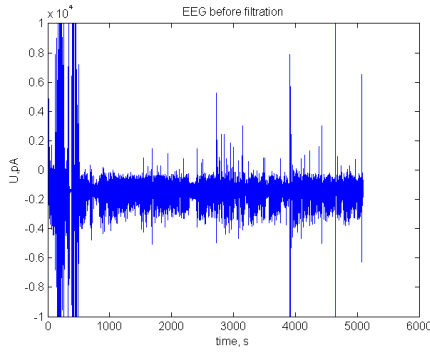


Fig. 1. The original ECoG dataset.

The first step provided by data pre-processing cycle that consists of such steps as described in data pre-processing paragraph. The raw data after pre-processing cycle is shown in Fig. 2.

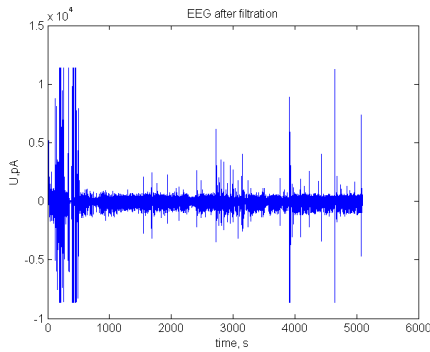


Fig. 2. The original ECoG dataset after pre-processing.

The next step is apply the seizure detection method based on stationary wavelet transform which was performed at the precious paragraph. In context of analysis we used the Daubechies 4 mother wavelet. After that, for each scale a , the calculated coefficients can be considered as a time series $\Sigma[n]$. The mean of $\Sigma[n]$ and the threshold value using are calculated (Fig. 3).

All values of $\Sigma[n]$ greater than threshold value are labeled 1, else 0. The result is a binary time series shown in Fig. 4.

After seizures detected methods we need to classify those seizures as an epileptic or no-epileptic. Thus, the last step is applying the post-processing method described in subsection 2.3. In this paper we define the minimal ictal time as 5 s and the minimal inter-ictal time as 10 s.

In Fig. 5 the as dots marked binary time series that classified as epileptic seizures, and as a 'x' seizures that are not considered as epileptic.

Acknowledgement. Financial and spiritual support is acknowledged.

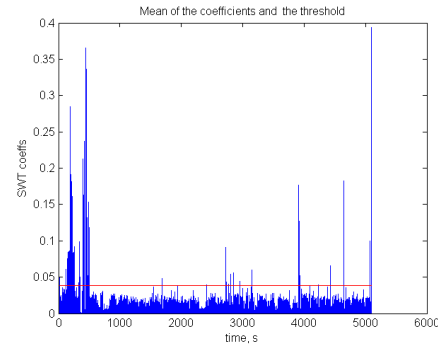


Fig. 3. The mean of SWT coefficients.

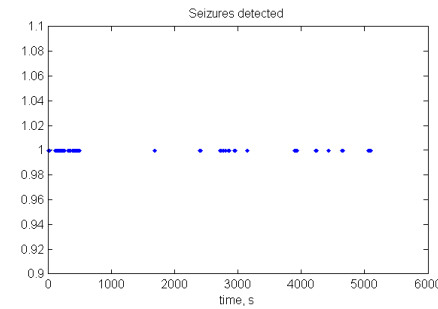


Fig. 4. The binary time series indicating where a seizures was detected.

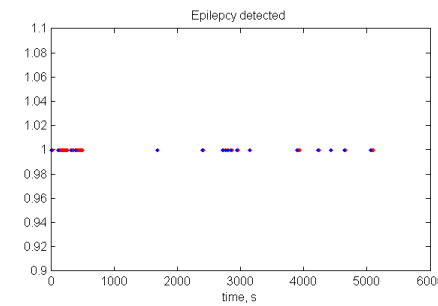


Fig. 5. The binary time series indicating where an epileptic seizures was detected.

References

1. S. Tong and N.V. Thacor *Engineering in Medicine & Biology Quantitative EEG Analysis Methods and Clinical Applications*. Artech House, Boston/London, 2009.
2. G.P. Nason, B. Silverman *The Stationary Wavelet Transform and some Statistical Applications Wavelets and Statistics: Lecture Notes in Statistics*, 103:281–299, 1995.
3. W. Christian *Automatic Seizure Detection in Rats using ECoG: A Comparison of Methods*. Lbeck, 2013.

Different DC fusing scenarios of encapsulated bonding wires

Jiri Petrzela¹, Roman Sotner¹, Tomas Gotthans³, Jiri Drinovsky¹, Tomas Kratochvil¹, Aarnout Wieers², and Renaud Gillon²

¹ Department of Radio Electronics, Faculty of Electrical Engineering and Communication, Brno University of Technology, Technicka 12, 61600 Brno, Czech Republic petrzelj@feec.vutbr.cz,

² ON Semiconductor, Westerring 15, 9700 Oudenaarde, Belgium

Summary. This contribution brings brief discussion involving measurement results of DC fusing scenarios of the bonding wires of different lengths, diameters and fabricated by using different materials. For this purpose SOIC-28 packaged test chips with six encapsulated wires have been manufactured by ON-Semiconductor Company. From the hardware point of view six-channel bond wire tester controlled by a personal computer has been designed. Software part allows to automatically and consecutively measuring six bond wires by using up to six power voltages. Measured data are both displayed as time-domain graphs as well as stored for consequential numerical analysis. This analysis covers especially calculation of change of bonding wire resistance with respect to time. Experimental observations can be provided in the form of digital oscilloscope screenshots, x-rays and graphs of maximal steady-state current vs fusing time. Obtained data will be used for developing precise mathematical model of encapsulated bonding wires. Measured results prove that fusing time does not match Preece equation which gives too pessimistic prediction of fusing current.

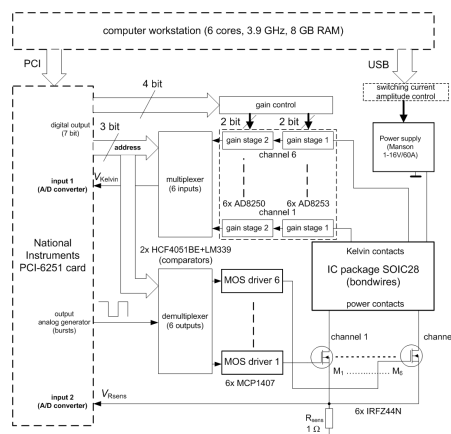


Fig. 2: Hardware part of bonding wire tester

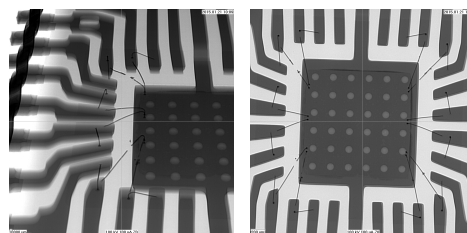


Fig. 3: Examples of x-ray, fused bonding wire

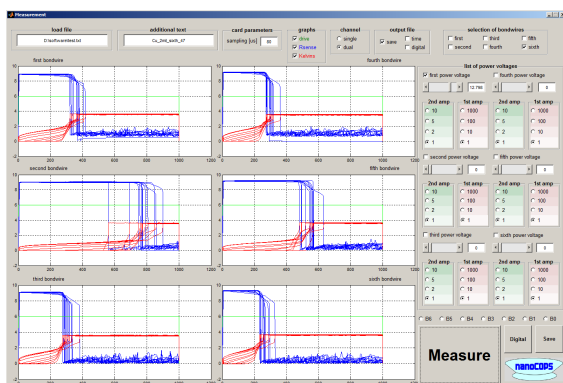


Fig. 1: Software part of bonding wire tester

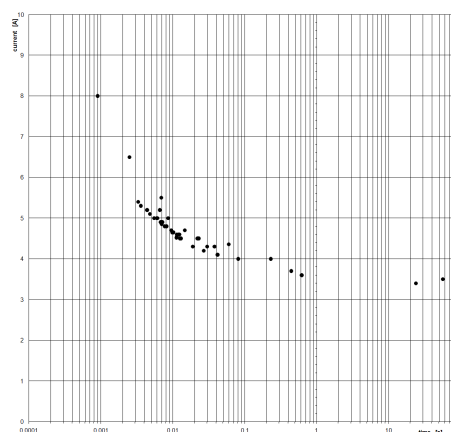


Fig. 4: Fusing current vs time for 1mil Cu bonding wire

Convergence of a Waveform Relaxation Method for Index-2 DAEs of Electromagnetic Field/Circuit Simulation

Jonas Pade¹ and Caren Tischendorf²

Humboldt University of Berlin, Unter den Linden 6, 10099 Berlin, Germany jonas.pade@math.hu-berlin.de,
tischendorf@math.hu-berlin.de

Summary. While waveform relaxation methods converge for coupled ODE systems, they may suffer from instabilities for coupled differential-algebraic equations (DAEs). Whereas several convergence criteria are known for index-1 DAEs, we present here a convergence criterion for quasilinear index-2 DAEs for the first time. It applies to systems of spatially discretized Maxwell equations for electromagnetic field approximation included into lumped circuit equations for current and voltage approximation. Such systems appear in co-simulation approaches for coupled EM/circuit simulation. The circuit topology can be exploited and makes it relatively easy to check if the convergence criterion is satisfied.

1 Introduction

The modelling of a big number of today's applications is increasingly complex and in many cases calls for a multiphysical approach resulting in coupled systems. Waveform relaxation (also: dynamic iteration) methods are well-established to solve such coupled problems. They allow for each subsystem to be solved by a dedicated numerical solver taking the different structure and time scale of the subsystems into account. Provided a sufficiently small time interval is given, waveform relaxation methods are always convergent for coupled ODEs [6]. This is not necessarily true in the case of coupled DAEs [1, 4]. Therefore, a number of studies were dedicated to finding convergence criteria for different classes of coupled DAEs, e.g. [1, 3, 4, 7, 8] to name only some of them. Here, we investigate a novel class of systems: coupled systems of implicit quasilinear DAEs of index ≤ 2 and ODEs. It is motivated by the interest in finding sufficient criteria for convergence of co-simulation approaches for coupled EM/circuit systems.

1.1 Class of Coupled Equations

We consider systems of the form

$$\begin{aligned} \dot{u} + b(t, u) &= k_1(x), & u(t_0) &= u_0 & (1) \\ E(x)\dot{x} + f(t, x) &= k_2(u), & x(t_0) &= x_0, & (2) \end{aligned}$$

where (2) forms an index-2 DAE. We assume that the initial values are consistent. The equations are coupled through the functions k_1 and k_2 . The vector field

b is assumed to be globally Lipschitz-continuous. Furthermore, we assume that $E(x)$ and $f(t, x)$ are continuous functions. The ODE system (1) can describe spatially discretized Maxwell equations, for example with finite integration technique [9]. The DAE system (2) includes circuit equations arising by the modified nodal analysis (MNA). Such systems are known to be of DAE index ≤ 2 , see [2].

1.2 Gauss-Seidel Method

We discuss the Gauss-Seidel relaxation method as one prototype example of many different waveform relaxation methods. When applying the Gauss-Seidel approach on (1)-(2), we obtain the iterative scheme

$$\begin{aligned} \dot{u}^k + b(t, u^k) &= k_1(x^{k-1}), & u^k(t_0) &= u_0 & (3) \\ E(x^k)\dot{x}^k + f(t, x^k) &= k_2(u^k), & x^k(t_0) &= x_0 & (4) \end{aligned}$$

for all iteration parameters $k \in \mathbb{N}$. The initial guess function x^0 can be found through extrapolation of the initial values.

2 Convergence Analysis

We are interested in sufficient conditions for (1)-(2) such that the sequence of solutions of (3)-(4) converges to the solution of (1)-(2). For the analysis, we do not regard possible discretization errors, i.e. we assume that the subsystems (3) and (4) are solved exactly.

We use the decoupling approach of the dissection index, introduced in [4], in order to decouple the equations (3)-(4) into an inherent ODE and algebraic constraints:

$$\dot{z}_1^k = g_1(z_1, z_1^{k-1}, z_1^{k-1}), \quad z_1(t_0) = z_{10} \quad (5)$$

$$z_2^k = g_2(z_1^k) \quad (6)$$

$$z_3^k = g_3(z_1^k, z_2^k) \quad (7)$$

with transformed coordinates $z^k := T \begin{pmatrix} u^k \\ x^k \end{pmatrix}$ with a constant matrix T . In general, one can not expect to find such a constant transformation T . However, for

circuit MNA systems, the dissection concept provides such a constant transformation T that depends only on the network topology [4].

Since g is a continuous function, uniform C^1 convergence of z_1^k would imply the uniform convergence of z^k . Thus, it is sufficient to focus the analysis onto the inherent ODE (5).

2.1 Convergence Criterion for the Iterative Solution of the Inherent Implicit ODE System

The following theorem provides a convergence criterion for (5).

Theorem 1. *Consider the sequence of initial value problems*

$$\dot{v}^k = \theta(v^k, v^{k-1}, \dot{v}^{k-1}), \quad v^k(t_0) = v_0 \quad \forall k \in \mathbb{N} \quad (8)$$

with $v^0 = s \in C^1$ and θ globally Lipschitz-continuous w.r.t. (v^k, \dot{v}^{k-1}) . Then, the sequence of solutions v^k converges on a sufficiently small time interval $[t_0, T]$ in $(C^1, \|\cdot\|_{C^1})$ to the solution of

$$\dot{v} = \theta(v, v, \dot{v}), \quad v(t_0) = t_0 \quad (9)$$

if θ is contractive w.r.t. \dot{v}^{k-1} .

Note that the Lipschitz-continuity and the contractivity of θ implies the unique solvability of (9).

2.2 Convergence Criterion for the Iterative Solution of the Coupled DAE System

The continuity conditions formulated in Theorem 1 generally hold if the (1)-(2) satisfy certain monotonicity properties, see [5]. Furthermore, it is shown in [4] that these monotonicity properties are satisfied for circuit MNA systems as soon as all non-passive devices are either time-dependent or constant but not state dependent.

From the contractivity condition of 1 and the decoupled equations (5)-(7) we may conclude the following theorem.

Theorem 2. *The Gauss-Seidel method (3)-(4) is convergent if and only if the system (1)-(2) satisfies*

$$\rho[K_1(x)A(x)K_2(u)] < 1 \quad \forall x \in \mathbb{R}^n, u \in \mathbb{R}^m, \quad (10)$$

where K_1 and K_2 are the Jacobians of the coupling functions k_1 and k_2 and

$$A(x) = P_2(Q_2F(t,x)P_2)^{-1}Q_2E(x)P_1(Q_1F(t,x)P_1)^{-1}Q_1$$

with the Jacobian $F(t,x)$ of $f(t,x)$. The matrices P_1 and P_2 represent projections extracting the index-1 and index-2 variables. The matrices Q_1 and Q_2 reflect projections extracting the index-1 and index-2 equations of (2).

Here, we mean with index-1 variables only those dynamic variables (appearing as \dot{x}) that are determined by an algebraic equation (here called index-1 equation). Index-2 variables are determined by equations (here called index-2 equations) that contain derivatives of other variables or the right hand side.

For electrical circuits, the products $Q_2F(t,x)P_2$, $Q_2E(x)P_1$ and $Q_1F(t,x)P_1$ of the matrix $A(x)$ can be described by certain subcircuits. $Q_2E(x)P_1$ comprises the dynamic part of the loop equations for all CV-loops and the cutset equations of all LI-cutsets. $Q_2F(x)P_2$ reflects the static part of the sum of the inductance equations for all inductances of each LI-cutset and the static part of the sum of all node equations for all nodes of each CV-loop. $Q_1F(t,x)P_1$ describes the static part of the sum of the voltage source equations for all voltages of each CV-loop and the static part of the sum of all node equations of each LI-cutset.

We finally notice that the static part b of the ODE (1) does not occur in the convergence criterion.

Acknowledgement. This work is supported by the German Ministry of Education and Science (BMBF) under grant 05M13KHA, project KoSMos (Model reduction based simulation of coupled PDAE systems).

References

1. M. Arnold and M. Günther. Preconditioned Dynamic Iteration for Coupled Differential-Algebraic Systems. *BIT*, 41:1–25, 2001.
2. D. Estevez Schwarz and C. Tischendorf. Structural analysis of electric circuits and consequences for MNA. *Journal of Computational and Applied Mathematics*, 25:133–151, 2006.
3. X.-G. Fan, J.-H. Zou, W. Sun. Convergence of Parallel Dynamic Iteration Methods for Nonlinear DAEs of Index-2. *Proceeding of the IEEE International Conference on Automation Science and Engineering*, 2006.
4. L. Jansen. A Dissection concept for DAEs - structural decoupling, unique solvability, convergence theory and half-explicit methods. Ph.D. Thesis, Humboldt-Universität zu Berlin, 2015.
5. L. Jansen, M. Matthes, and C. Tischendorf. Global unique solvability for memristive circuit DAEs of index 1. *Int. J. Circ. Theor. Appl.*, 43(1):73–79, 2013.
6. E. Lelarasmee. The Waveform Relaxation Method for Time Domain Analysis of Large Scale Integrated Circuits: Theory and Applications. Ph.D. Thesis, University of California, Berkeley, 1982.
7. U. Miekkala. Dynamic iteration methods applied to linear DAE systems. *International Journal of Circuit Theory and Applications*, 28:131–162, 2000.
8. S. Schöps. Multiscale Modeling and Multirate Time-Integration of Field/Circuit Coupled Problems. Ph.D. Thesis, Bergische Universität Wuppertal, 2011.
9. M. Weiland, T. Clemens. Discrete electromagnetism with the finite integration technique. *Progress In Electromagnetics Research* 32:65–87, 2001.

Simulation of the EMG for evaluation of capacitive sensors

Theresa Roland¹, Sabrina Mairhofer¹, Christian Diskus², Christoph Wolf¹, and Werner Baumgartner¹

¹ Institute for Biomedical Mechatronics, Johannes Kepler University Linz, Altenbergerstrasse 69, 4040 Linz, AUSTRIA
theresa.roland@jku.at, sabrina.mairhofer@gmail.com, christoph.wolf@jku.at,
werner.baumgartner@jku.at

² Institute for Microelectronics and Microsensors, Johannes Kepler University Linz, Altenbergerstrasse 69, 4040 Linz, AUSTRIA
c.diskus@ieee.org

Summary. This work deals with the simulation of the electric field generated by the muscle fibre action potential. The electric signal at the skin surface is used for capacitive sensing of electromyography (EMG). The prototype for capacitive sensing and the simulation in SPICE and COMSOL Multiphysics are described. These simulations are used to optimize the capacitive EMG-system.

1 Introduction

Active prostheses, controlled by EMG signal, help amputees to regain a better quality of life and a higher level of independence. In state of the art EMG measurement systems, conductive electrodes are used. This research deals with capacitive sensors to avoid the disadvantages of conductive electrodes. Such disadvantages are discomfort, malfunction or even impossibility of EMG measurement.

2 Capacitive EMG-system prototype

In this research a capacitive EMG measurement system with its sensor and electronics was developed. A photo of the sensor prototype is shown in Fig. 1. For the sensor a multi-layer construct of copper and insulation foil was used. Two sensor fields measure the differential signal, so the common mode interferences are eliminated. In the prototype the connection of the sensor to the electronics is done via miniature coaxial cables to prevent interferences. The battery powered electronics consist of the analog circuit for preamplification and filtering. Further signal processing is done in a microcontroller. In the prototype a low power AT-MEL microcontroller with a 32-bit ARM CORTEX-M0 processor is used for filtering the 50 Hz hum and its harmonics. Further, the signal is smoothed digitally to control the drive of the prosthesis.

This capacitive measurement system is to be optimized. To get a better understanding of the signals to measure, the transmission of the action potential in the muscle fibre to the surface of the skin was simulated in SPICE and in COMSOL Multiphysics. In the

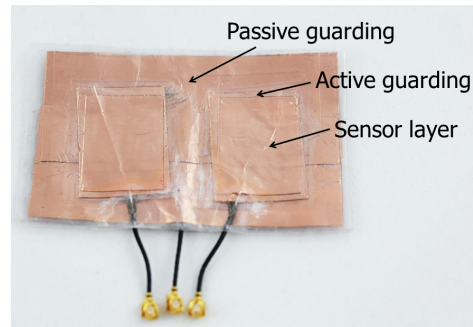


Fig. 1. Capacitive sensor prototype

human body, a motor neuron is linked via a synapsis to the motoric endplate of the muscle fibre. Starting from the endplate, the action potential is transmitted in the muscle fibre. This action potential has an amplitude of 100 mV referred to the resting potential and a width of about 2 ms [3]. The conduction velocity of the muscle signal varies between 2.6 to 5.3 m/s [4]. The sensor design is optimized according to the results of the simulation. Parameters which are optimized are the distance of the two sensor layers, as well as its size. For verification of the simulations, a physical simulator is built up. Therefore a pneumatic drive with a movement speed of 4 m/s is used as signal source. Conductive polymere layers represent the tissue layers. With this physical simulator, different electrode designs can be compared systematically. The effect of changes in the electronics on EMG measurement can also be shown.

3 Simulation of EMG

The simulation of the transmission of the action potential in the muscle fibre through the tissues is done with SPICE and COMSOL Multiphysics. The tissues parameters in Table 1 are used for both simulations.

3.1 Simulation in SPICE

The two dimensional model for the SPICE simulation is shown in Fig. 2. A thickness of 1 mm was

Table 1. Simulated tissue parameters [1]

Tissue	σ (mS/m)	ϵ_R ()
skin	1.14k	2.00
fat	457k	20.81
muscle	9329k	266.71

used for the skin and 5 mm for the fat. Simulations were done at different thicknesses of the muscle tissue, as the muscle fibres are located at different depth. The human forearm is modeled electrically as an RC-Network. One element, consisting of one horizontal and one vertical parallel RC-circuit, has a length of 2 mm, a width of 1 mm and a height of 1 mm.

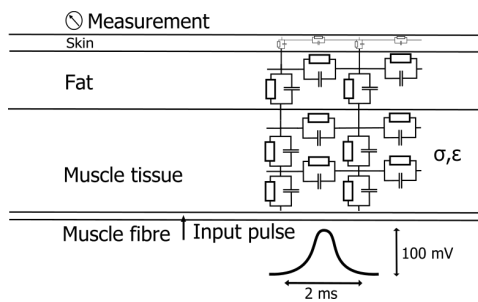
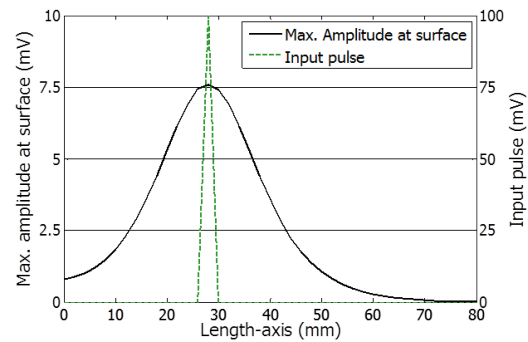
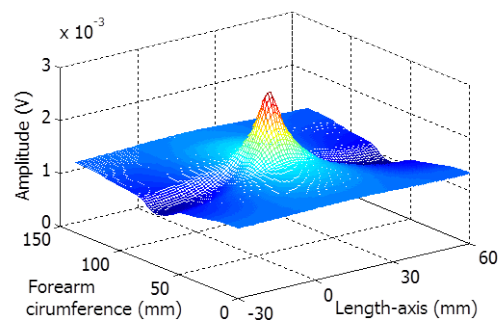
**Fig. 2.** Simulated tissue layers in human forearm

Figure 3 shows the resulting amplitude at the surface of the skin. In this result the muscle fibre is located at a depth of 10 mm in the muscle tissue. The max. amplitude at the surface shows the action potential transmitted through the tissues. The simulations were done at different depth of the muscle fibre. A muscle fibre close to the surface has the highest amplitude and a narrow signal form, as in higher depth the signal gets damped. In this work it could be shown, that the influence of the capacitive impedance can be neglected for frequencies in the range of EMG. It is sufficient to only use an R-Network.

3.2 Simulation in COMSOL Multiphysics

The COMSOL Multiphysics simulations are based on the results of Honeder's work [1]. An MRI image is segmented and used as a model for the different tissues. As a static signal source, the action potential described by Rosenfalck [2] was used. The muscle fibre was simulated at depth starting from 5 mm to 36 mm distance from the skin. The resulting electric fields of 6 muscle fibres at different depth were superpositioned in MATLAB by weighting with their circle segment area (the muscle is approximated to be circular). The resulting electric field at the surface of the skin is shown in Fig. 4.

**Fig. 3.** Input pulse and max. amplitude at skin surface (SPICE Simulation)**Fig. 4.** Electric field at skin surface determined by superposition of muscle fibres (COMSOL Multiphysics simulation)

4 Conclusion

Based on these simulations, the optimal sensor geometries can be derived. Measurements applying the sensors at physical simulator and human subjects are done to verify the simulations.

Acknowledgement. Thanks to Otto Bock Healthcare GmbH for their support with knowledge and financing. Thanks to Linz Center of Mechatronics for financing.

References

1. J. L. Honeder. A Quasi-Stationary Approach to the Approximate Solution of Finite Element Analysis applied to EMG Modeling . Master's thesis, Technikum Wien, Vienna, 2013.
2. P. Rosenfalck. Intra- and extracellular potential fields of active nerve and muscle fibres *Acta Physiol Scand Suppl.*, 321:1–168, 1969.
3. K. Golenhofen. *Physiologie heute.* URBAN&FISCHER, Muenchen, 1997.
4. S. Andreassen, L. Arendt-Nielsen. Muscle fibre conduction velocity in motor units of the human anterior tibial muscle *The Journal of Physiology*, 391:561–571, 1987.

Holistic Transient Coupled Field and Circuit Simulation

Peter Meuris¹, Wim Schoenmaker¹, Christian Strohm², and Caren Tischendorf²

¹ Magwel NV, Leuven, Belgium peter.meuris@magwel.com, wim.schoenmaker@magwel.com

² Humboldt Universität zu Berlin, Dept. of Math., Germany tischendorf@math.hu-berlin.de, strohmch@math.hu-berlin.de

Summary. We present a holistic coupled field circuit simulation and tests with a non-trivial balun device (balance-to-unbalance transformer) in a simple circuit structure. The coupled solver is based on a usual circuit net list extended by extra lines for elements modeled by full Maxwell 3D field equations whose geometry and materials are described in xml files.

1 Modeling

Circuit simulators are usually based on lumped element models described in form of net lists. In order to be able to incorporate the mutual electromagnetic influence of neighboring elements in circuits with ultra-fast transient signals (e.g. cross talking), we use refined models based on a sufficiently exact discretization of the full-wave Maxwell equations. Our simulation approach is a holistic one combining lumped circuit models with 3D electromagnetic field models for specific devices, see e.g. 3D-structure of a new balun prototype in Fig. 1. The holistic simulation is intended to be an alternative option if co-simulation approaches like dynamic iteration [5] fail.

Electromagnetic Field Modeling. All relevant electromagnetic phenomena can be described by the full-wave Maxwell's equations. Here we focus on their potential formulation, see e.g. [1],

$$\nabla \cdot (\varepsilon \nabla \varphi + \varepsilon \Pi) = -\rho \quad (1)$$

$$\nabla \times (\nu \nabla \times \mathbf{A}) + \partial_t (\varepsilon \nabla \varphi + \varepsilon \Pi) = \mathbf{J} \quad (2)$$

with the scalar potential φ and the vector potential \mathbf{A} as well as the pseudo-canonical momentum $\Pi = \partial_t \mathbf{A}$ to avoid the second-order time derivative. The material dependent parameters ε and $\mu = \nu^{-1}$ are the permittivity and the magnetic permeability. Charge ρ and current density \mathbf{J} are modeled appropriate to the underlying material. Note that the semiconductor current density model reflects the drift-diffusion model.

Lumped Circuit Modeling. Performing the modified nodal analysis, a common approach, based on Kirchhoff's laws, to simulate the electric circuits, yields the following equation system:

$$A_1 \frac{d}{dt} q(A_1^\top \mathbf{e}, t) + A_1 g(A_1^\top \mathbf{e}, t) + A_2 \mathbf{i}_2 = 0 \quad (3)$$

$$\frac{d}{dt} \phi(\mathbf{i}_2, t) + r(\mathbf{i}_2, t) - A_2^\top \mathbf{e} = 0 \quad (4)$$

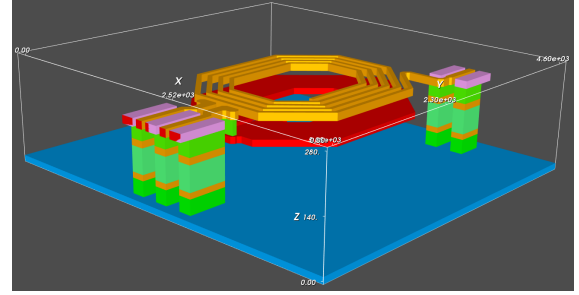


Fig. 1. Balun 3D-structure (visualization does apply stretching in the vertical direction)

having only the nodal potentials e and the currents i_2 of the voltage controlling elements as variables, see [3]. The equations (3)-(4) are generated automatically from net lists providing the node to branch element relation as well as the element related functions q , g , ϕ and r .

Coupled Modeling. In order to obtain the favored holistic coupled system, e.g. as shown in Fig. 2, we further need an additional interface model combining the electromagnetic (1)-(2) and the circuit (3)-(4) systems. Denoting Γ_k the k -th contact of the EM field element we get the current through Γ_k as

$$\mathbf{i}_k = \int_{\Gamma_k} [\mathbf{J} - \varepsilon \partial_t (\nabla \varphi + \Pi)] \cdot \mathbf{n}_\perp d\sigma. \quad (5)$$

and the potential φ as

$$\varphi(x, t) = \varphi_{bi}(x) + \varphi_c(x, t) = \begin{cases} \mathbf{v}_k & \text{if } x \in \Gamma_k \\ 0 & \text{else.} \end{cases} \quad (6)$$

Completed with the boundary conditions $(\nabla \times \mathbf{A}) \cdot \mathbf{n}_\perp = 0$ and $(\Pi + \nabla \varphi) \cdot \mathbf{n}_\parallel = 0$ and adapted gauge conditions, cf. [4], the partial differential-algebraic system (1)-(6) allows us to simulate electric circuits incorporating electromagnetic devices, such as in Fig. 2 in a holistic way.

2 Discretization

We present a holistic simulation approach with a fixed spatial discretization followed by an adaptive time scheme for the resulting differential-algebraic system.

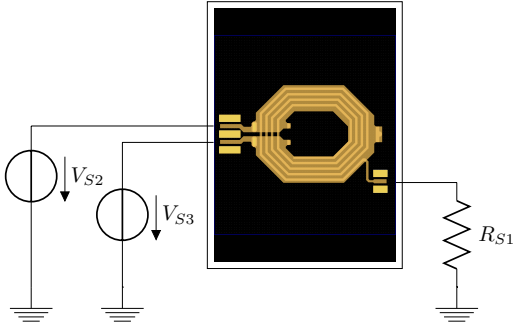


Fig. 2. Test Benchmark: Simple circuit coupled with the balun device in Fig. 1. The RF input signals V_{S2} and V_{S3} are sinusoidal ones operating with 10GHz frequency. The RF output is given as current through the resistance R_{S1} .

Spatial Discretization. Seen as a generalized finite-integration technique, (1)-(2) results in:

$$-\int \frac{\partial \Delta V_i}{\partial \Delta V_i} \varepsilon(\nabla \varphi + \Pi) \cdot d^2 \mathbf{S} = \int \frac{\Delta V_i}{\Delta V_i} \rho d^3 v \quad (7)$$

$$\oint_{\partial \Delta S_i} v \left[\frac{1}{\Delta S_i} \oint_{\partial \Delta S_i} \mathbf{A} \cdot d\mathbf{l}' \right] \cdot d\mathbf{l}_i = \int_{\Delta S_i} [\mathbf{J} - \varepsilon \partial_t (\nabla \varphi + \Pi)] \cdot d^2 \mathbf{S} \quad (8)$$

Time Discretization. The joined differential-algebraic equation system (3)-(8), rewritten as

$$\mathcal{A} \frac{d}{dt} d(x, t) + b(x, t) = 0,$$

is solved by backward differentiation methods, i.e. we solve the nonlinear systems

$$\frac{1}{h_n} \sum_{i=0}^k \alpha_{ni} \mathcal{A} d(x_{n-i}, t_{n-i}) + b(x_n, t_n) = 0$$

with BDF method coefficients α_{ni} .

3 Simulation Results

We tested the holistic transient simulation of a simple circuit coupled with a novel industrial prototype balun device, see Figure 2, yielding 133 171 equations for the coupled differential-algebraic system to solve. The particular challenge of this balun device is the open end in the middle of the device acting as an antenna. The simulated currents at contact ports $P1$, $P2$ and $P3$ of the balun can be seen in Figure 3. A detailed spatial view of the magnetic inductance at two time points is given in Fig. 4. Validating S-parameter in frequency domain, see Fig. 5, gives rise for the correctness of the transient simulation results.

Acknowledgement. This work is financially supported by the EU funded FP7 ICT project nanoCOPS GA619166. We thank Pascal Rainier from ACCO Semiconductor (France) for providing the balun structure.

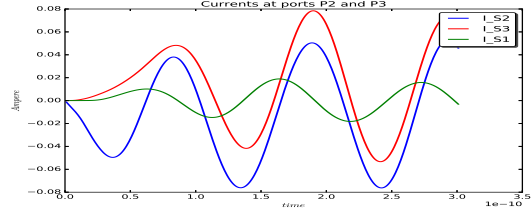


Fig. 3. Currents at ports P2 and P3 and P1.

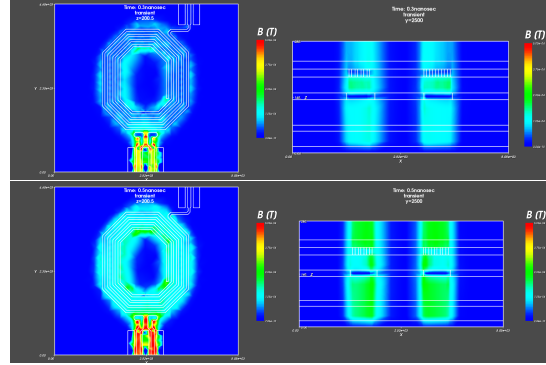


Fig. 4. Magnetic inductance in the balun at $t = 0.3, 0.5$ nanosec. Top and cross-sectional view at $y = 2500$ micron.

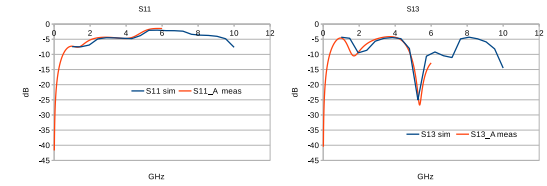


Fig. 5. Comparing measurements and simulation results of S-parameters in frequency domain.

References

1. P. Meuris, W. Schoenmaker, and W. Magnus, "Strategy for electromagnetic interconnect modeling," *Computer-Aided Design of Integrated Circuits and Systems, IEEE Transactions on*, vol. 20, no. 6, pp. 753–762, Jun 2001.
2. W. Schoenmaker, Q. Chen, and P. Galy, "Computation of self-induced magnetic field effects including the lorentz force for fast-transient phenomena in integrated-circuit devices," *Computer-Aided Design of Integrated Circuits and Systems, IEEE Transactions on*, vol. 33, no. 6, pp. 893–902, June 2014.
3. D. Estévez Schwarz and C. Tischendorf, "Structural analysis of electric circuits and consequences for mna," *Internat. J. Circ. Theor. Appl.*, vol. 28, no. 2, pp. 131–162, 2000.
4. S. Baumanns, *Coupled Electromagnetic Field/Circuit Simulation. Modeling and Numerical Analysis*. Logos Verlag, Berlin, 2012, Dissertation, Universität zu Köln.
5. S. Schöps, H. De Gerssem, and A. Bartel, "A cosimulation framework for multirate time integration of field/circuit coupled problems," *Magnetics, IEEE Transactions on*, vol. 46, no. 8, pp. 3233–3236, 2010.

The cell contractility model and the cell adhesion model: Reducing the complexity and preparing the coupling to electrical forces

Duy T. Truong¹, Christian Bahls¹, Barbara Nebe², and Ursula van Rienen¹

¹ Institute of General Electrical Engineering, University of Rostock, Albert-Einstein-Str. 2, 18059 Rostock, Germany
 duy.truong@uni-rostock.de, christian.bahls@uni-rostock.de,
 ursula.van-rienen@uni-rostock.de

² Department of Cell Biology, University Medical Center Rostock, 18057 Rostock, Germany
 barbara.nebe@med.uni-rostock.de

Summary. The bio-chemo-mechanical model for cell contractility and the bio-mechanical model for cell focal adhesion by Deshpande are described both. Applications of these models are presented and some comparative studies are made for the case of reduced order of complexity.

1 Introduction

In our DFG Research Training Group 1505, several researches are done, which focus is on the improvements of implants using wet lab experiments or experiments *in vitro* and computational methods. Since these implants are embedded in biological tissues it is important to understand the processes that take place at the interface between body cells and the surface of an implant. Especially interesting for many applications are mechanical interactions between cells and their underlying substrates [1], [5].

To examine these interactions, there have been numerous studies in terms of both experimental and mathematical modeling. The bio-chemo-mechanical model for cell contractility by Deshpande *et al.* [2] is known to be advantageous over other mathematical descriptions. When this model is combined with the bio-mechanical model for cell focal adhesion [3], a great number of situations can be studied [4], [7]. Simulations that use those two models involve solving coupled problems, whose variables characterize the deformation of the cell, the activation inside the cell and the adhesion between the cell and the substrate.

The two models are investigated to be applied in our research on the interaction between bone cells and biomaterial, in which we aim at finding beneficial surface conditions for cells to adhere to implants - both with and without electrical stimulation.

2 The models

The bio-chemo-mechanical model

The key idea of the bio-chemo-mechanical (BCM) model is the inclusion of the active stress tensor so

that the stress in the cell is given by:

$$\mathbf{S}^{\text{total}} = \mathbf{S}^{\text{active}} + \mathbf{S}^{\text{passive}}, \quad (1)$$

where $\mathbf{S}^{\text{passive}}$ is the passive elastic stress due to the cell material, which is dependent on the material properties and deformation of the cell. The active stress is resulted from tensions in stress fibres in any direction due to their activation.

The BCM model defines the contractility for a single stress fibre. The three equations for the BCM model are described in [2] which includes: (i) the level of signal given as a function of time t_i (measured from the instant of the most recent signal) as $C = \exp(-t_i/\theta)$ where θ is the decay constant, (ii) the activation level of stress fibers η described by a first order kinetic equation and (iii) the relationship between the active stresses and the strain rate represented by a simplified Hill's equation.

The model for cell focal adhesion

Focal adhesions are known as large macromolecular complexes through which mechanical force and regulatory signals are transmitted between the extracellular matrix (ECM) and an interacting cell (Fig. 1).

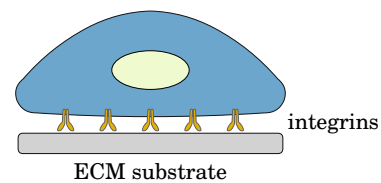


Fig. 1. Sketch of cell on substrate

The formulation for the focal adhesion model in [3] is based on the idea that there exist two states of the integrins on the cell surface: the high affinity and low affinity ones. Experiments suggest that only high affinity integrins form bonds and experience stretching. Let $\xi_0 = \xi_H + \xi_L$ be the total concentration of

integrins (unit: $1/\mu\text{m}^2$) with ξ_H, ξ_L being concentrations of high and low affinity integrins, respectively. Then, the tractions on cell surface can be obtained as $T_i = -\xi_H F_i$, where F_i is the force that the cell exerts on each bond. The equilibrium condition requires that $T_i = S_{ij} n_j$, where n_j is the surface normal and S_{ij} is a component of the stress \mathbf{S} in the cell. In 2D, the indices $i, j \in \{1, 2\}$ refer to the horizontal and vertical directions. When coupling with the BCM model, this stress becomes $\mathbf{S}^{\text{total}}$ in (1).

The focal adhesion model is completed by providing the equations for the transformation of low affinity integrins into high affinity ones when the bond stretch increases. This is described in [3].

3 Comparative Study

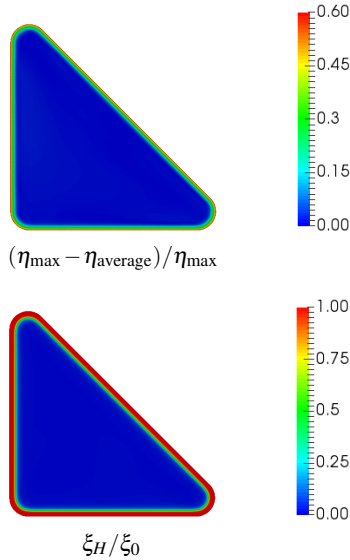


Fig. 2. Plots for predicted steady-state distributions of the stress fibre (above) and high affinity integrins (below) concentrations for a triangular cell on a ligand pattern of the same shape [6]. Our representation for the BCM model is used in combination with the focal adhesion model. Simulation is done using the open source software FEniCS. Obtained results are similar to those in [6].

The BCM model can generally be applied to simulate the contraction of the cell in 3D. Under certain assumptions, simulations in 2D are sufficient. On the other hand, we have attempted to reduce the complexity in the implementation of this model. Figure 2 shows our simulation results for a triangular cell on a ligand pattern of the same shape, which is originally done in [6], using our idea of reduction of complexity.

In this work, comparative studies will be carried out to capture the achievement in computational costs

versus the loss in accuracy of the results when applying such reduction of model.

4 Electrical stimulation

It is interesting to see how the cell contractility or the cell adhesion changes when the cell is electrically stimulated. We intend to couple electrical stimulation to the bio-chemo-mechanical model by inserting the Maxwell stress tensor (MST), which proved to be useful in examining electrical interactions in molecular level, to the total stress. Components of the MST \mathbf{S}^{el} can be written as:

$$S_{ij}^{\text{el}} = \epsilon E_i E_j - \frac{1}{2} \delta_{ij} \epsilon E_k E_k$$

where E_i is a component of the electric field, ϵ is the permittivity of the medium, which is assumed to be homogeneous and isotropic in this first simple model, and δ_{ij} is the Kronecker delta function.

Acknowledgement. This work was supported by the German Research Foundation (DFG) in the scope of the Research Training Group GRK 1505 *welisa*.

References

1. N.Q. Balaban, U.S. Schwarz, D. Riveline, P. Goichberg, G. Tzur, I. Sabanay, D. Mahalu, S. Safran, A. Bershadsky, L. Addadi, and B. Geiger. Force and focal adhesion assembly: a close relationship studied using elastic micropatterned substrates. *Nature Cell Biology*, 2001.
2. V. S. Deshpande, R. M. McMeeking, and A. G. Evans. A model for the contractility of the cytoskeleton including the effects of stress-fibre formation and dissociation. *Proc. R. Soc. A*, 463:787–815, 2007.
3. V. S. Deshpande, M. Mrksich, R. M. McMeeking, and Anthony G. Evans. A bio-mechanical model for coupling cell contractility with focal adhesion formation. *J. Mech. Phys. Solids*, 2008.
4. E.P. Dowling, W. Ronan, G. Ofek, V.S. Deshpande, R.M. McMeeking, K.A. Athanasiou, and J.P. McGarry. The effect of remodelling and contractility of the actin cytoskeleton on the shear resistance of single cells: A computational and experimental investigation. *Journal of the Royal Society Interface*, 9(77):3469–3479, 2012.
5. C. Matschegewski, S. Staehlke, R. Loeffler, R. Lange, F. Chai, D. P. Kern, U. Beck, and B. J. Nebe. Cell architecture-cell function dependencies on titanium arrays with regular geometry. *Biomaterials*, 31:5729–5740, 2010.
6. A. Pathak, V.S. Deshpande, R.M. McMeeking, and A.G. Evans. The simulation of stress fibre and focal adhesion development in cells on patterned substrates. *Journal of the Royal Society Interface*, 5(22):507–524, 2008. cited By 60.
7. W. Ronan, A. Pathak, V.S. Deshpande, R.M. McMeeking, and J.P. McGarry. Simulation of the mechanical response of cells on micropost substrates. *Journal of Biomechanical Engineering*, 135(10), 2013.

Preliminary numerical study on electrical stimulation at alloplastic reconstruction plates of the mandible

Ursula van Rienen¹, Ulf Zimmermann¹, and Peer W. Kämmerer²

¹ Institute of General Electrical Engineering, University of Rostock, Rostock, Germany

ursula.van-rienen@uni-rostock.de, ulf.zimmermann@uni-rostock.de

² Department of Oral, Maxillofacial and Plastic Surgery, University Medical Centre Rostock, Rostock, Germany

peer.kaemmerer@med.uni-rostock.de

Summary. Mechanical stress by means of electrical stimulation induces formation of endogenous electric fields and thereby influences bone remodeling. It was shown that external biophysical stimulation via application of electric currents enhances bone healing and restores its structural strength. Therefore, we conducted the first study on application of electrical stimulation for intrinsic activation of bone healing processes in defects of the facial skeleton.

1 Medical Background

Since the 1950s it is well known that the application of electromagnetic fields can enhance bone growth and bone remodelling [2]. Since the 1980s, electrical stimulation is used as an adjunct in treating complications in bony healing [6]. Recently, an electrostimulative hip revision system has been designed [7], [5] and tested in vivo [1]. This encourages incorporating electrical stimulation into the therapy of critical size defects of facial skeleton. We chose the model of mandibular defects using common alloplastic reconstruction plates [4] as well as implanted bone substitute material as scaffold for electrical stimulation devices.

2 From CT Images to a Volume Conductor Model

Basing on sectional images from computed tomography data (CT) of a patient with a critical size defect of the mandible caused by cancer, we registered and segmented the slices using Materialise Mimics[®] and thus built a CAD model for the subsequent use in an electromagnetic simulation. Figure 1 displays exemplary CT slices while fig. 2 shows the three-dimensional (3D) data after registration plus segmentation. Finally, fig. 3 shows the anatomical 3D CAD model for which the volume conductor model (VCM) is set up. This VCM serves as a representative model for our subsequent studies. Note that only the mandible bone is modelled in the VCM since the field already decays within this volume and this allows to remarkably reduce the problem size.

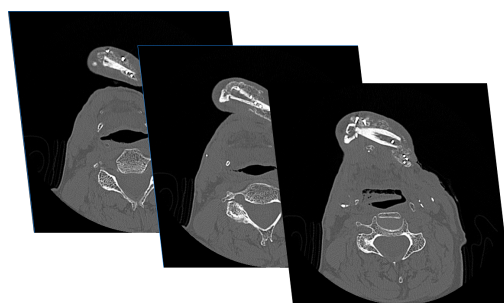


Fig. 1. Slices from computer tomography of a patient with a critical size defect of the mandible.

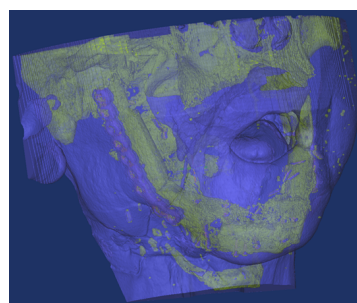


Fig. 2. 3D data after registration and segmentation. This preliminary model differentiates between highly conductive titanium (violet), conductive soft tissue (blue), and resistive bone (yellow).

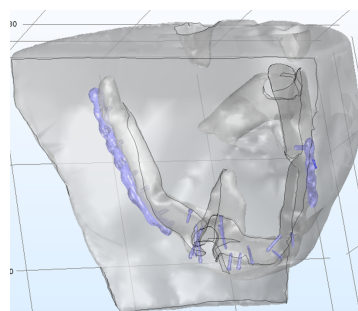


Fig. 3. CAD model. Only the relevant part of the bone is kept (the mandible) for the simulation model. The metallic implant and the fixation screws are highlighted.

We use the finite element (FEM) software COMSOL Multiphysics® (COMSOL) to set up the physical VCM from the anatomical CAD model. The electric tissue properties for the preliminary VCM are taken from [3] and amount to $7.4 \cdot 10^5$ S/m for titanium (Ti beta-21S), 0.7 S/m for soft tissue and 0.02 S/m for bone (cortical bone). We define sources using the implanted titanium prosthesis and screws. According to the method of Kraus [6] we apply an alternating voltage of 20 Hz aiming at electric fields between 5 and 70 V/m.

We compute the electric potential $\varphi(\mathbf{r})$ in the bone tissue and at the implant surface solving the Laplace equation

$$\nabla \cdot (\sigma(\mathbf{r})\nabla\varphi(\mathbf{r})) = 0 \quad (1)$$

in the computational domain. The electric tissue properties are described by the electric conductivity $\sigma(\mathbf{r})$. The boundary conditions are set to Dirichlet conditions with ± 0.2 V at the field-inducing screws, to 0.4 V at the central electrode and to ground potential at the titanium prosthesis, respectively. Neumann boundary condition has been applied for the outer shell of the soft tissue to represent the non-conductive air.

3 Comparison of Two Stimulation Sites

In this preliminary study, we compare two different stimulation sites. Firstly, we allocate the stimulation site within the screws and use a stimulation voltage of 0.4 V. Then, the highest electric field is located around the screws and a high energy consumption takes place due to direct contact to higher conductive soft tissue. Figure 4 displays a surface plot of the electric field norm on the mandible. It clearly elucidates that the desired upper limit of 70 V/m is exceeded in that case.

In a second case, instead of using the screws as stimulation site we insert a stimulation electrode into the implanted bone. Specifically, we use a cylinder with diameter of 2 mm and height of 5 mm, see fig. 5. Again we stimulate with 0.4 V. We locate ground electrodes at the larger bony implants left and right of the central mandible. Figure 6 displays again a surface plot of the electric field norm on the mandible. Now, the maximum at the surface stays below 35 V/m.

4 Conclusion

Our data reveal that the electromagnetic and electric stimulation may have a positive influence on the intrinsic activation of bone healing properties within facial skeletons defects. These results are crucial for investigations using electrostimulative implants.

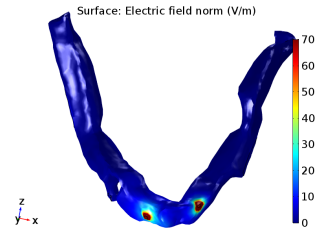


Fig. 4. Surface plot of the electric field norm on the mandible in case of screws as stimulation site.



Fig. 5. VCM with central electrode in the mandible.

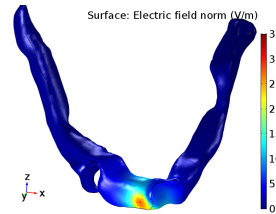


Fig. 6. Surface plot of the electric field norm on the mandible for central stimulation site.

Acknowledgement. This work was supported by the German Science Foundation (DFG) in the scope of the project DFG RI 814/24-1.

References

1. C Ebner, U Zimmermann, Y Su, U van Rienen, W Mittelmeier, and R Bader. Electrical stimulation of osseointegration of a uncemented total hip stem. *IEEE-TBME*, TrackP: S1162, 2015.
2. E Fukada and I Yasuda. On the piezoelectric effect of bone. *JPSJ*, 12:1158–1162, 1957.
3. S Gabriel, R W Lau, and C Gabriel. The dielectric properties of biological tissues: II. measurements in the frequency range 10 Hz to 20 GHz. *Physics in Medicine and Biology*, 41(11):2251–2269, 1996.
4. PW Kämmerer, MO Klein, M Moergel, M Gemmel, and GF Draenert. Local and systemic risk factors influencing the long-term success of angular stable alloplastic reconstruction plates of the mandible. *J Craniomaxillofac Surg*, 42:e271–276, 2014.
5. D Klüß, R Souffrant, H Ewald, U van Rienen, R Bader, and W Mittelmeier. Acetabuläre Hüftendoprothese mit einer Vorrichtung zur Elektrostimulation des Knochens. *Patent*, (DE202008015661 U1), 2009.
6. W Kraus. Magnetfeldtherapie und magnetisch induzierte Elektrostimulation in der Orthopädie. *Orthopädie*, 13:78–92, 1984.
7. C Potratz, D Klüß, H Ewald, and U van Rienen. Multi-objective optimisation of an electrostimulative acetabular revision system. *IEEE-TBME*, 57:460–468, 2010.

Thermal modeling of liquid-filled transformer radiators using network approach

Wei Wu¹ and Andreas Blaszczyk²

¹ ABB Transformers Technology Center North America, Raleigh, NC, United States wei.wu@us.abb.com

² ABB Corporate Research Centre, Switzerland andreas.blaszczyk@ch.abb.com

Summary. The paper presents a new thermal/pressure network model of a liquid-filled transformer radiator. The new model is based on a CFD-validated duct network component and allows to compute transformer cooling for operating points deviating from the nominal one. Results for different model configurations have been presented.

1 Introduction

An electrical transformer converts electricity from one voltage to another voltage, either of higher or lower value. Transformers are key components of electric transmission and distribution networks. The resistance to the electric current by the winding conductors of the transformer produces heat; the heat further increases the resistance to the current, and the overall efficiency of the transformer is then reduced by the added heat unless the heat is removed effectively from the transformer. Meanwhile transformer lifetime and insulation ageing are strongly dependent on the temperature rise of transformer units.

In order to guarantee the designed life of transformers, the insulation degradation has to be at a low level; as such how to design a proper cooling system to dissipate the heat becomes one of the primary tasks of a transformer manufacturer. For liquid-filled transformers radiators often play an important role for heat dissipation; for example Fig. 1 shows a transformer example with cooling radiators. Product designers and engineers have to find a reliable approach to predict radiators' cooling performance during the transformers' design stage and make sure the temperature rises can be constrained to a sufficiently low level.

Along with the computer technology developing, numerical modeling is gradually applied to predict the transformer temperature rises. The numerical approaches generally fall into two categories; either 'thermal/pressure network models' or computational fluid dynamics (CFD). CFD is a numerical method with spatial discretization including geometry details and thus will consume a lot more computational resources (CPU and memory) [1, 2]. In comparison network models abstract the fluid dynamics and thermodynamics principles into a number of interconnected



Fig. 1. A liquid-filled transformer with radiators

'lumped elements' [3–5]. Transformer network models run much faster than CFD and therefore their use for transformer cooling design is increasing [6, 7].

This paper presents a physics based radiator model which can support both natural air and forced air cooling methods and can be integrated into transformer design systems to construct a complete thermodynamic model including the core, coils and cooling systems.

2 Radiator modeling

Figure 2 shows the oil circulation between the transformer oil tank and the external radiators. In operation the transformer core and coils generate heat, which is absorbed by surrounding oil and the oil then gains in temperature. Higher temperature oil has lower density and as such by buoyancy effect, the oil flows up, from the bottom to the top, through an extensive network of crossover ducts and passages of transformer windings. The hot oil then flows from the tank into the cooling radiators from the top, where the oil dissipates heat to the ambient air, gradually loses in temperature and returns back to the oil tank from the bottom. The temperature reduction along the vertical distance from the radiator top to the bottom follows a logarithmic correlation. By this circulation the heat produced from the core and coils is transferred to the ambient environment.

The modeling of the radiator heat transfer phenomena comprises oil and air ducts and the heat exchange between them. The array of the oil ducts con-

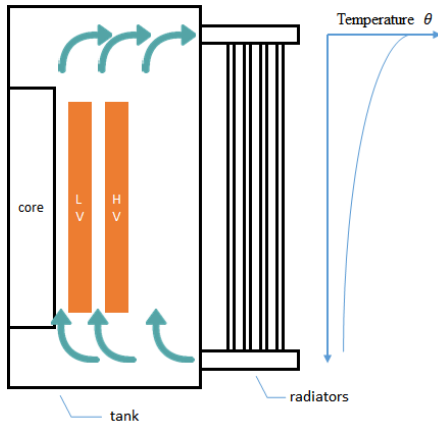


Fig. 2. The cooling oil flow circulation between oil tank and external radiators

tained in the radiator can be aggregated into a single oil duct element representation; air ducts can be managed in the same way too. This model assumption is then demonstrated in Fig. 3 (a); where oil is flowing from the top to the bottom, temperature dropping from warm to cool, and air flowing in the opposite direction, temperature picking up from cool to warm.

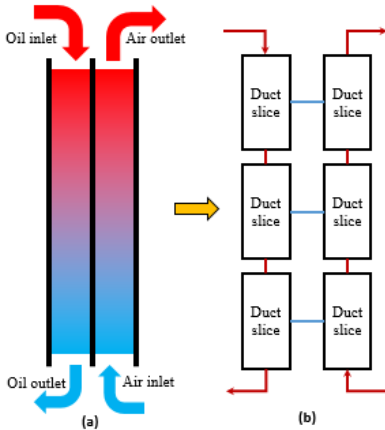


Fig. 3. Duct model (a) and its network representation (b). Blue lines between duct slices illustrate thermal network and red lines pressure network

The simplified model in Fig. 3 (a) can be represented by the network topology in Fig. 3 (b), in which oil and air ducts are both split into three vertical slices in order to simulate the logarithmic variation. Each duct slice is modeled by a network element encapsulating both the thermal and fluid dynamics principles [6]. The normal load test case in Table 1 confirms that three slices are sufficient to achieve accuracy below 1 degree (difference to 6 slices is 0.6). The three slice model works also properly for the reduced load case (which is equivalent to over-dimensioned radia-

tors), whereas the model without splitting leads to a wrong temperature that is lower than the ambient air.

Table 1. Bottom oil temperature (in °C) predicted by the sliced network model in Fig. 3 for a radiator operated under normal and reduced load (the top oil and the ambient temperatures are 65°C and 20°C respectively)

Number of vertical duct slices	Normal load $P_{\text{loss}} = 467 \text{ kW}$	Reduced load $P_{\text{loss}} = 46.7 \text{ kW}$
1	32.3	-3.6
3	34.6	20.0
6	35.2	20.1

3 Conclusions

In this work we introduced a new model of equivalent thermal and pressure networks for liquid-filled transformer cooling radiators. Comparing with heat-run test results the model shows acceptable accuracies. More details as well as the formulation of the basic equations and CFD validation will be presented in the extended version of this paper.

References

1. A. Weinlaeder, W. Wu, S. Tenbohlen, and Z. Wang. Prediction of the oil flow distribution in oil-immersed transformer windings by network modelling and computational fluid dynamics. *IET Electr. Power Appl.*, Vol. 6, No. 2, pp 82–90, 2012.
2. R.B. Fdhila, J. Kranenborg, T. Laneryd, C.-O. Olsson, and B. Samuelsson. *Thermal modeling of power transformer radiators using a porous medium based CFD approach*. THERMACOMP 2011, Dalian, China, 2011.
3. W. Wu, Z. Wang, A. Revell, H. Iacovides, and P. Jarman. Computational fluid dynamics calibration for network modelling of transformer cooling oil flows - Part I: heat transfer in oil ducts. *IET Electr. Power Appl.*, Vol. 6, No. 1, pp 19–27, 2012.
4. W. Wu, Z. Wang, A. Revell, and P. Jarman. Computational fluid dynamics calibration for network modelling of transformer cooling oil flows - Part II: pressure loss at junction nodes. *IET Electr. Power Appl.*, Vol. 6, No. 1, pp 28–34, 2012.
5. A. Blaszczyk, R. Flueckiger, T. Mueller, and C.-O. Olsson. Convergence behavior of coupled pressure and thermal networks. *Compel Journal*, Vol. 33, No. 4, pp 1233–1250, 2014.
6. E. Morelli, P. Di Barba, B. Cranganu-Cretu, and A. Blaszczyk. Network based cooling models for dry transformers. ARWtr Conference, Baiona, Spain, 2013.
7. A. Cremasco, P. D. Barba, B. Cranganu-Cretu, W. Wu, and A. Blaszczyk. Thermal simulations for optimization of dry transformers cooling system. The 10th Scientific Computing in Electrical Engineering (SCEE), Wuppertal, Germany, 2014.

Part VI

Abstracts of Poster Session 2

Modified Block-Diagonal Structured Model Order Reduction for Electro-Thermal Problems in Industrial Electronics Simulations

N. Banagaaya¹, L. Feng¹, W. Schoenmaker², P. Meuris², R. Gillon³, and P. Benner¹

¹ Max Planck Institute for Dynamics of Complex Technical Systems, Magdeburg, Germany

banagaaya@mpi-magdeburg.mpg.de, feng@mpi-magdeburg.mpg.de,
benner@mpi-magdeburg.mpg.de

² Magwel NV, Martelarenplein 13, B-3000 Leuven, Belgium wim.schoenmaker@magwel.com,

peter.meuris@magwel.com

³ ON Semiconductor Belgium, Oudenaarde, Belgium Renaud.Gillonr@onsemi.com

Summary. Recently, the block-diagonal structured model order reduction method for electro-thermal (ET) coupled problems with many inputs was proposed. After splitting, this MOR method reduces both the electrical and thermal parts separately, using the elimination and block-diagonal structured MOR (BDSM) methods, respectively. However, the reduced electrical part has very dense matrices which is still a computational burden. We propose a modified BDSM-ET method which leads to sparser reduced-order models.

1 Introduction

Spatial discretization of ET coupled problems leads to a nonlinear quadratic dynamical system of the following form,

$$\mathbf{E}\mathbf{x}' = \mathbf{A}\mathbf{x} + \mathbf{x}^T \mathbf{F}\mathbf{x} + \mathbf{B}\mathbf{u}, \mathbf{x}(0) = \mathbf{x}_0, \quad (1a)$$

$$\mathbf{y} = \mathbf{C}\mathbf{x} + \mathbf{D}\mathbf{u}, \quad (1b)$$

where $\mathbf{E} \in \mathbb{R}^{n \times n}$ is singular, indicating that the system in (1) is a system of differential-algebraic equations (DAEs), and $\mathbf{A} \in \mathbb{R}^{n \times n}$, $\mathbf{B} \in \mathbb{R}^{n \times m}$, $\mathbf{C} \in \mathbb{R}^{\ell \times n}$, $\mathbf{D} \in \mathbb{R}^{\ell \times m}$, while the tensor $\mathbf{F} = [\mathbf{F}_1^T, \dots, \mathbf{F}_n^T]^T$ is a 3-D array of n matrices $\mathbf{F}_i \in \mathbb{R}^{n \times n}$. Each element in $\mathbf{x}^T \mathbf{F}\mathbf{x} \in \mathbb{R}^n$ is a scalar $\mathbf{x}^T \mathbf{F}_i \mathbf{x} \in \mathbb{R}$, $i = 1, \dots, n$. The state vector $\mathbf{x} = (\mathbf{x}_v^T, \mathbf{x}_T^T)^T \in \mathbb{R}^n$ includes the nodal voltages $\mathbf{x}_v \in \mathbb{R}^{n_v}$, and the nodal temperatures $\mathbf{x}_T \in \mathbb{R}^{n_T}$. $\mathbf{u} = \mathbf{u}(t) \in \mathbb{R}^m$ and $\mathbf{y} = \mathbf{y}(t) \in \mathbb{R}^\ell$ are the inputs (excitations) and the desired outputs (observations), respectively. We assume system (1) to be solvable, that is, the matrix pencil $\lambda \mathbf{E} - \mathbf{A}$ is regular, $\forall \lambda \in \mathbb{C}$. For simplicity, we assume (1) to be weakly coupled, and has the following matrix structures,

$$\mathbf{E} = \begin{pmatrix} 0 & 0 \\ 0 & \mathbf{E}_T \end{pmatrix}, \mathbf{A} = \begin{pmatrix} \mathbf{A}_v & 0 \\ 0 & \mathbf{A}_T \end{pmatrix}, \mathbf{B} = \begin{pmatrix} \mathbf{B}_v & 0 \\ 0 & \mathbf{B}_T \end{pmatrix},$$

$\mathbf{C} = (\mathbf{C}_v \ \mathbf{C}_T)$, $\mathbf{D} = (\mathbf{D}_v \ \mathbf{D}_T)$, $\mathbf{u} = (\mathbf{u}_v^T \ \mathbf{u}_T^T)^T$, with $\mathbf{A}_v \in \mathbb{R}^{n_v \times n_v}$, $\mathbf{B}_v \in \mathbb{R}^{n_v \times m/2}$, $\mathbf{E}_T \in \mathbb{R}^{n_T \times n_T}$, $\mathbf{A}_T \in \mathbb{R}^{n_T \times n_T}$, $\mathbf{B}_T \in \mathbb{R}^{n_T \times m/2}$, $\mathbf{C}_v \in \mathbb{R}^{\ell \times n_v}$, $\mathbf{C}_T \in \mathbb{R}^{\ell \times n_T}$, $\mathbf{D}_v \in \mathbb{R}^{\ell \times m/2}$, $\mathbf{D}_T \in \mathbb{R}^{\ell \times m/2}$, and $\mathbf{u}_v, \mathbf{u}_T \in \mathbb{R}^{m/2}$. Then the system (1) can be written as

$$\mathbf{A}_v \mathbf{x}_v = -\mathbf{B}_v \mathbf{u}_v, \quad (2a)$$

$$\mathbf{E}_T \mathbf{x}_T' = \mathbf{A}_T \mathbf{x}_T + \mathbf{x}_v^T \mathbf{F}_T \mathbf{x}_v + \mathbf{B}_T \mathbf{u}_T, \quad (2b)$$

$$\mathbf{y} = \mathbf{C}_v \mathbf{x}_v + \mathbf{C}_T \mathbf{x}_T + \mathbf{D}_v \mathbf{u}_v + \mathbf{D}_T \mathbf{u}_T, \quad (2c)$$

with initial condition $\mathbf{x}_T(0) = \mathbf{x}_{T_0}$ and $\mathbf{F}_T \in \mathbb{R}^{n_v \times n_v \times n_T}$ being a tensor. In this work, we consider MOR of system in (2) with large ℓ and m . It is well known that, models with numerous inputs and outputs are challenging for MOR, and most MOR methods produce large, dense reduced-order models (ROMs) for such systems.

In [1], the BDSM-ET method was proposed to overcome this problem, leading to a ROM

$$\mathbf{A}_{v_r} \mathbf{x}_{v_r} = -\mathbf{B}_{v_r} \mathbf{u}_v, \quad (3a)$$

$$\mathbf{E}_{T_r} \mathbf{x}_{T_r}' = \mathbf{A}_{T_r} \mathbf{x}_{T_r} + \mathbf{x}_{v_r}^T \mathbf{F}_{T_r} \mathbf{x}_{v_r} + \mathbf{B}_{T_r} \mathbf{u}_T, \quad (3b)$$

$$\mathbf{y}_r = \mathbf{C}_{v_r} \mathbf{x}_{v_r} + \mathbf{C}_{T_r} \mathbf{x}_{T_r} + \mathbf{D}_{v_r} \mathbf{u}_v + \mathbf{D}_{T_r} \mathbf{u}_T, \quad (3c)$$

where $\mathbf{A}_{v_r} \in \mathbb{R}^{r_v \times r_v}$, $\mathbf{B}_{v_r} \in \mathbb{R}^{r_v \times m/2}$, $\mathbf{E}_{T_r} \in \mathbb{R}^{r_T \times r_T}$, $\mathbf{A}_{T_r} \in \mathbb{R}^{r_T \times r_T}$, $\mathbf{B}_{T_r} \in \mathbb{R}^{r_T \times m/2}$, $\mathbf{C}_{v_r} \in \mathbb{R}^{\ell \times r_v}$, $\mathbf{C}_{T_r} \in \mathbb{R}^{\ell \times r_T}$, $\mathbf{D}_{v_r} = \mathbf{D}_v$, $\mathbf{D}_{T_r} = \mathbf{D}_T$, $\mathbf{F}_{T_r} \in \mathbb{R}^{r_v \times r_v \times r_T}$, such that the reduced order, $r = r_v + r_T \ll n$, and the approximation error $\|\mathbf{y} - \mathbf{y}_r\|$ is small with respect to a suitable norm $\|\cdot\|$. However, matrix \mathbf{A}_{v_r} and tensor \mathbf{F}_{T_r} are dense which is still a computational burden. In the next section, we propose a modified BDSM-ET method which leads to sparser ROMs.

2 Proposed modified BDSM-ET method

We propose to first apply the superposition principle to both the electrical (2a) and thermal (2b) subsystems, respectively. Then we conduct MOR and generate a block-diagonal structured sparse ROM. Without loss of generality, assume that the input matrices \mathbf{B}_v and \mathbf{B}_T have no zero columns so that, they can be split into $\mathbf{B}_v = \sum_{i=1}^{m/2} \mathbf{B}_{v_i}$, $\mathbf{B}_T = \sum_{i=1}^{m/2} \mathbf{B}_{T_i}$ where $\mathbf{B}_{v_i} \in \mathbb{R}^{n_v \times m/2}$, $\mathbf{B}_{T_i} \in \mathbb{R}^{n_T \times m/2}$ are column rank-1 matrices

defined as $\mathbf{B}_{k_i}(:, j) = \begin{cases} \mathbf{b}_{k_i} \in \mathbb{R}^{n_k}, & \text{if } j = i, \\ 0, & \text{otherwise,} \end{cases}$

$i = 1, \dots, m/2$ and $k = v, T$. Using the above input matrix splitting, the superposition principle can be applied to both the electrical and thermal subsystems of system (2), separately as follows.

Reduction of the electrical subsystem

Using the superposition principle, the electrical subsystem in (2) can be split into $m/2$ subsystems

$$\mathbf{A}_v \mathbf{x}_{v_i} = -\mathbf{B}_{v_i} \mathbf{u}_v, \quad \mathbf{y}_{v_i} = \mathbf{C}_v \mathbf{x}_{v_i}, \quad (4)$$

$i = 1, \dots, m/2$, where $\mathbf{y}_v = \sum_{i=1}^{m/2} \mathbf{y}_{v_i}$. Let blkdiag denote the block-diagonal matrix defined by the input arguments. The next step is to reduce the dimension of each subsystem in (4). This is done by using reordering and elimination techniques for each subsystem. Reordering the entries of each subsystem in (4) such that the first $n_{v_e}^{(i)}$ rows correspond to the nonzero rows of the input matrix \mathbf{B}_{v_i} and the rest $n_{v_l}^{(i)}$ rows correspond to the internal nodes, leads to a partitioned subsystem

$$\begin{pmatrix} \mathbf{A}_{v_{11}}^{(i)} & \mathbf{A}_{v_{12}}^{(i)} \\ \mathbf{A}_{v_{12}}^{(i)T} & \mathbf{A}_{v_{22}}^{(i)} \end{pmatrix} \begin{pmatrix} \mathbf{x}_{v_e}^{(i)} \\ \mathbf{x}_{v_l}^{(i)} \end{pmatrix} = - \begin{pmatrix} \mathbf{B}_{v_e}^{(i)} \\ \mathbf{0} \end{pmatrix} \mathbf{u}_v, \quad (5)$$

$$\mathbf{y}_{v_i} = \begin{pmatrix} \mathbf{C}_{v_e}^{(i)} & \mathbf{0} \end{pmatrix} \begin{pmatrix} \mathbf{x}_{v_e}^{(i)} \\ \mathbf{x}_{v_l}^{(i)} \end{pmatrix},$$

where $\mathbf{x}_{v_e}^{(i)} \in \mathbb{R}^{n_{v_e}^{(i)}}$ and $\mathbf{x}_{v_l}^{(i)} \in \mathbb{R}^{n_{v_l}^{(i)}}$ represent the port and the internal nodal voltages, respectively, and $n_v = n_{v_e}^{(i)} + n_{v_l}^{(i)}$, $i = 1, \dots, m/2$. Eliminating all internal nodes from (5) leads to the ROM of (4) as below

$$\mathbf{A}_{v_{r_i}} \mathbf{x}_{v_{r_i}} = \mathbf{B}_{v_{r_i}} \mathbf{u}_v, \quad \mathbf{y}_{v_{r_i}} = \mathbf{C}_{v_{r_i}} \mathbf{x}_{v_{r_i}}, \quad (6)$$

where $\mathbf{x}_{v_{r_i}} = \mathbf{x}_{v_e}^{(i)} \in \mathbb{R}^{r_{v_i}}$, $\mathbf{B}_{v_{r_i}} = -\mathbf{B}_{v_e}^{(i)} \in \mathbb{R}^{r_{v_i} \times m/2}$, $\mathbf{A}_{v_{r_i}} = \mathbf{A}_{v_{11}}^{(i)} - \mathbf{A}_{v_{12}}^{(i)} \mathbf{W}_{v_i} \in \mathbb{R}^{r_{v_i} \times r_{v_i}}$, $\mathbf{C}_{v_{r_i}} = \mathbf{C}_{v_e}^{(i)} \in \mathbb{R}^{\ell \times r_{v_i}}$, $\mathbf{W}_{v_i} = \mathbf{A}_{v_{22}}^{(i)-1} \mathbf{A}_{v_{12}}^{(i)T} \in \mathbb{R}^{n_{v_l}^{(i)} \times n_{v_e}^{(i)}}$, and $r_{v_i} = n_{v_e}^{(i)} \ll n_v$. Hence, the reduced electrical subsystem can be reformulated as the parallel connection of the reduced-order subsystems in (6). Consequently, it can be equivalently transformed into a block-diagonal reduced system of dimension $r_v = \sum_{i=1}^{m/2} r_{v_i}$. Thus, the reduced-order electrical subsystem in the form of (3a), has the following matrices, $\mathbf{A}_{v_r} = \text{blkdiag}(\mathbf{A}_{v_{r_1}}, \dots, \mathbf{A}_{v_{r_{m/2}}})$, $\mathbf{C}_{v_r} = (\mathbf{C}_{v_{r_1}}, \dots, \mathbf{C}_{v_{r_{m/2}}})$, $\mathbf{B}_{v_r} = (\mathbf{B}_{v_{r_1}}^T, \dots, \mathbf{B}_{v_{r_{m/2}}}^T)^T$.

Reduction of the thermal subsystem

We observe that, splitting (2a) into $m/2$ subsystems in (4) induces the splitting of the nonlinear part in the thermal part (2b). When the approximation $\left(\sum_{i=1}^{m/2} \mathbf{x}_{v_i}^T\right) \mathbf{F}_T \left(\sum_{i=1}^{m/2} \mathbf{x}_{v_i}\right) \approx \sum_{i=1}^{m/2} \mathbf{x}_{v_i}^T \mathbf{F}_T \mathbf{x}_{v_i}$ is introduced, the thermal subsystem (2b) can be written as

$$\mathbf{E}_T \mathbf{x}_T' = \mathbf{A}_T \mathbf{x}_T + \xi_v^T \mathcal{F}_T \xi_v + \mathbf{B}_T \mathbf{u}_T, \quad (7)$$

where we have used the equality $\sum_{i=1}^{m/2} \mathbf{x}_{v_i}^T \mathbf{F}_T \mathbf{x}_{v_i} = \xi_v^T \mathcal{F}_T \xi_v$,

where $\mathcal{F}_T = \{\mathcal{F}_{T_1}, \dots, \mathcal{F}_{T_{m/2}}\} \in \mathbb{R}^{\tilde{n}_v \times \tilde{n}_v \times n_T}$, $\tilde{n}_v = mm_v/2$, being a 3D-array of n_T block-diagonal matrices $\mathcal{F}_{T_i} = \text{blkdiag}(\mathbf{F}_{T_i}, \dots, \mathbf{F}_{T_i}) \in \mathbb{R}^{\tilde{n}_v \times \tilde{n}_v}$, $\mathbf{F}_{T_i} \in \mathbb{R}^{n_v \times n_v}$ and $\xi_v = (\mathbf{x}_{v_1}^T, \dots, \mathbf{x}_{v_{m/2}}^T)^T$. We assume such an approximation to be possible. Though this seems like a strong assumption, we have observed it to be valid in some of our applications.

Also the reduction of the algebraic part induces a reduction in the differential part leading to

$$\mathbf{E}_T \mathbf{x}_T' = \mathbf{A}_T \mathbf{x}_T + \xi_{v_r}^T \mathbf{F}_{T_r} \xi_{v_r} + \mathbf{B}_T \mathbf{u}_T, \quad (8)$$

with $\mathbf{F}_{T_r} = \{\mathcal{F}_{T_{r_1}}, \dots, \mathcal{F}_{T_{r_{m/2}}}\} \in \mathbb{R}^{r_v \times r_v \times n_T}$ being a 3D-array of n_T reduced order block-diagonal matrices $\mathcal{F}_{T_{r_i}} = \text{blkdiag}(\mathbf{F}_{T_{r_i}}, \dots, \mathbf{F}_{T_{r_i}}) \in \mathbb{R}^{r_v \times r_v}$, where $\mathbf{F}_{T_{r_i}} = \mathbf{F}_{T_{11}}^{(i)} - \mathbf{W}_{v_i}^T \mathbf{F}_{T_{21}}^{(i)} - \mathbf{F}_{T_{12}}^{(i)} \mathbf{W}_{v_i} + \mathbf{W}_{v_i}^T \mathbf{F}_{T_{22}}^{(i)} \mathbf{W}_{v_i} \in \mathbb{R}^{r_{v_i} \times r_{v_i}}$. Since system (8) can also be split into $m/2$ subsystems, the thermal state \mathbf{x}_T of system (8) can be reduced using the BDSM-ET method proposed in [1]. Hence, the reduced thermal system in (3b) also has block-diagonal structured matrices given by, $\mathbf{E}_{T_r} = \mathbf{V}^T \mathcal{E}_T \mathbf{V}$, $\mathbf{A}_{T_r} = \mathbf{V}^T \mathcal{A}_T \mathbf{V}$, $\mathbf{B}_{T_r} = \mathbf{V}^T \mathcal{B}_T$, $\mathbf{C}_{T_r} = \mathcal{C}_T \mathbf{V}$, where $\mathcal{E}_T = \text{blkdiag}(\mathbf{E}_T, \dots, \mathbf{E}_T)$, $\mathcal{C}_T = (\mathbf{C}_T, \dots, \mathbf{C}_T)$, $\mathcal{A}_T = \text{blkdiag}(\mathbf{A}_T, \dots, \mathbf{A}_T)$, $\mathcal{B}_T = (\mathbf{B}_{T_1}^T, \dots, \mathbf{B}_{T_{m/2}}^T)^T$, $\mathbf{V} = \text{blkdiag}(\mathbf{V}^{(1)}, \dots, \mathbf{V}^{(m/2)})$. The projection matrices $\mathbf{V}^{(i)}$ can be constructed as in [2],

$\text{range}(\mathbf{V}^{(i)}) = \text{span}\{\mathbf{R}_i, \mathbf{M}\mathbf{R}_i, \dots, \mathbf{M}^{r_{T_i}-1} \mathbf{R}_i\}$, $r_{T_i} \ll n_T$,

where $\mathbf{M} = (s_0 \mathbf{E}_T - \mathbf{A}_T)^{-1} \mathbf{E}_T \in \mathbb{R}^{n_T \times n_T}$, and $\mathbf{R}_i = (s_0 \mathbf{E}_T - \mathbf{A}_T)^{-1} \mathbf{b}_{T_i} \in \mathbb{R}^{n_T}$, $i = 1, \dots, m/2$. Here $s_0 \in \mathbb{C}$ is chosen arbitrarily. Hence, the order of the reduced thermal subsystem (3b) is $r_T = \sum_{i=1}^{m/2} r_{T_i}$.

3 Conclusion

By construction, the modified BDSM-ET method leads to sparser ROMs than the BDSM-ET method proposed in [1] with accurate ROMs. We have compared the two methods using ET coupled problems with many inputs from industry.

References

1. N. Banagaaya, L. Feng, W. Schoenmaker, P. Meuris, A. Wieers, R. Gillon, and P. Benner. Model order reduction for nanoelectronics coupled problems with many inputs. In *Proceedings 2016 Design, Automation & Test in Europe Conference & Exhibition (DATE)*, pages 313–318, 2016.
2. U. Baur, P. Benner, and L. Feng. Model order reduction for linear and nonlinear systems: A system-theoretic perspective. *Arch. Comput. Methods Eng.*, 21(4):331–358, 2014.

Fitting Generalized Gaussian Distributions for Process Capability Index

Theo G.J. Beelen¹, Jos J. Dohmen², E. Jan W. ter Maten^{1,3}, and Bratislav Tasic²

¹ Eindhoven University of Technology, the Netherlands {T.G.J.Beelen,E.J.W.ter.Maten}@tue.nl

² NXP Semiconductors, Eindhoven, the Netherlands {Jos.J.Dohmen,Bratislav.Tasic}@nxp.com

³ Bergische Universität Wuppertal, Germany Jan.ter.Maten@math.uni-wuppertal.de

Summary. The design process of integrated circuits (IC) aims at a high yield as well as a good IC-performance. The distribution will not be standard Gaussian anymore. In fact, the corresponding probability density function has a more flat shape than in case of standard Gaussian. In order to optimize the yield one needs a statistical model for the observed distribution. One of the promising approaches is to use the so-called Generalized Gaussian distribution function and to estimate its defining parameters. We propose a numerical fast and reliable method for computing these parameters.

1 Introduction

We assume N independent samples x_i in some given interval $[U, V]$ and based on some empirical density function. To define a quality measure index we are now interested in the ‘best’ fitting function within the family of Generalized Gaussian Density (GGD) distributions as shown in Fig.1 and given by the expression

$$f(x) = \frac{\beta}{2\alpha\Gamma(1/\beta)} \exp\left(-\left(\frac{|x-\mu|}{\alpha}\right)^\beta\right), \quad (1)$$

where $\alpha, \beta > 0$, $\mu \in \mathbb{R}$ and Γ is the Gamma function. The parameters of the ‘best’ fitting distribution function can be found by maximizing the logarithm of the likelihood function $L = \ln(\mathcal{L}) = \sum_{i=1}^N \ln f(x_i)$: The necessary conditions are

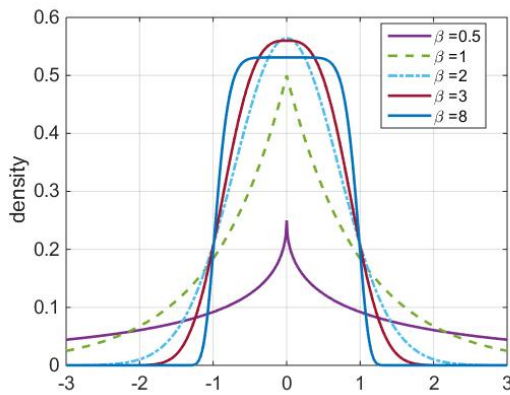


Fig. 1. Generalized Gaussian density functions with $\mu = 0$ and $\alpha = 1$.

$$\frac{\partial L}{\partial \alpha} = 0, \quad \frac{\partial L}{\partial \beta} = 0, \quad \frac{\partial L}{\partial \mu} = 0. \quad (2)$$

It appears that

$$\alpha = \left(\frac{\beta}{N} \sum_{i=1}^N |x_i - \hat{\mu}|^\beta\right)^{1/\beta}. \quad (3)$$

When we assume that $\mu = \hat{\mu}$ is known then only one additional equation remains

$$g(\beta) = g(\beta; \hat{\mu}) = 0 \quad (4)$$

in which $\mu = \hat{\mu}$ is now a given parameter. The function g involves a Ψ function and a remaining part involving x_i 's. Analytical formulae for $g(\beta)$ and $g'(\beta)$ can be found in literature [1–3]. Clearly, Eq.4 can be solved by any iterative method, for example by Newton's method. The computation of the parameters α and β of the ‘best’ fitting density function $f(x)$ can be done by the following procedure.

1. Determine the empirical pdf $\hat{f}(x)$ from the measured data.
2. Compute the cumulative density function $\hat{F}(x) = \int_{-\infty}^x \hat{f}(t) dt$.
3. Generate $\{x_i | i = 1, \dots, N\}$ using $\hat{F}(x)$.
4. Compute the zero $\hat{\beta}$ of $g(\beta) = 0$.
5. Compute $\hat{\alpha}$ from (3).

Then the GGD $f(x | \hat{\mu}, \hat{\alpha}, \hat{\beta})$ is considered as the ‘best’ fitting pdf for the density function $\hat{f}(x)$. Numerical experiments [1] show that (i) (4) has a (unique) zero as long as $\bar{x} \neq \hat{\mu}$, and no zero in case of $\bar{x} = \hat{\mu}$; (ii) $\hat{\beta}$ is very sensitive to the choice of the interval $[U, V]$ where the x_i are located. More precisely, $\hat{\beta}$ strongly depends on the difference $|\hat{\mu} - \bar{x}|$ where $\bar{x} = \text{mean}(x_i) = \sum_{i=1}^N |x_i - \hat{\mu}|$.

The first observation comes from the simplification from choosing μ , but is easy to meet. For the second observation we propose to carry out the steps 3–5 M -times within a loop, giving $\hat{\beta}_k$ and $\hat{\alpha}_k$, $k = 1, \dots, M$ and finally take $\hat{\beta} = \frac{1}{M} \sum_{k=1}^M \hat{\beta}_k$, $\hat{\alpha} = \frac{1}{M} \sum_{k=1}^M \hat{\alpha}_k$ (due to the large value of $\alpha'(\beta)$ this choice for α gives better results than by using (3)) and $\hat{\mu}$. We now consider the density function $f(x; \hat{\mu}, \hat{\alpha}, \hat{\beta})$ as best fit to the measured data [1].

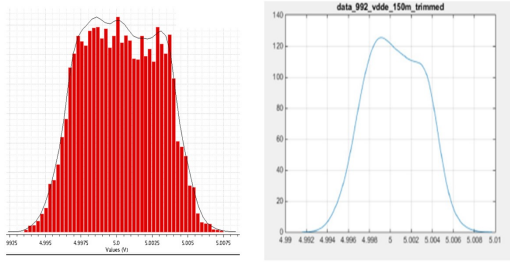


Fig. 2. Measured data (left) and empirical pdf \hat{f} (right).

2 Numerical results

We applied the modified procedure (with $M = 50$) to ‘trimmed’ data from NXP IC-measurements (Fig. 2). The computed density function f as well as the initially fitted (non-symmetrical) density function \hat{f} are given in Fig. 3. Note that even the tails are very well approximated. To get an impression of the sensitivity of the computed density w.r.t. $\hat{\alpha}$ we varied the computed value of $\hat{\alpha}$ with $\pm 10\%$, plotted the corresponding densities and computed the Mean Square Error (MSE). For further details we refer to [1].

3 A quality measure index for a Generalized Gaussian distribution

Assuming an underlying distribution being standard Gaussian, capability of a manufacturing process can be measured by using some process capability indices such as

$$C_p = \frac{U-L}{6\sigma} \text{ and } C_{pk} = \frac{\min(U-\mu, \mu-L)}{3\sigma},$$

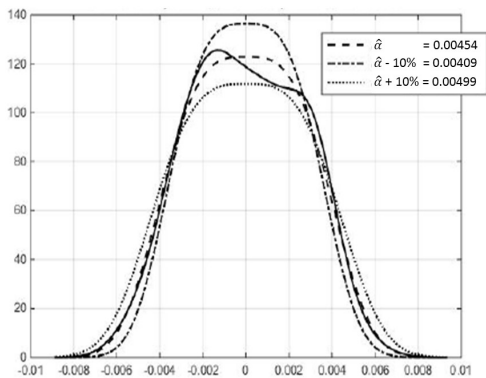


Fig. 3. Sensitivity of the density function f w.r.t. $\hat{\alpha}$. $MSE = (14.31, 56.94, 91.95)$ for $\hat{\alpha} = (454, 499, 409) * 10^{-5}$.

where $[L, U]$ is the specification interval, μ is the process mean and σ is the process standard deviation and a process is said to be capable if the process capability index exceeds a value $k \geq 1$, where usually $k = 4/3$. In case of a GGD (1) we can introduce a capability index C_{pkg} similar to the standard Gaussian case as

$$C_{pkg} = \frac{\min(U-\mu, \mu-L)}{3\sigma},$$

where $2\sigma = \alpha^\beta$. L and U are the lower and upper tolerance levels, respectively. They can be determined as described below.

Notice that if $x \leq \mu$ then the cumulative density function $F(x)$ corresponding to the GGD (1) is given by

$$\begin{aligned} F(x) &= \frac{\beta}{2\alpha\Gamma(1/\beta)} \int_{-\infty}^x \exp\left(-\left(\frac{|y-\mu|}{\alpha}\right)^\beta\right) dy \\ &= \frac{1}{2\Gamma(1/\beta)} \int_{((\mu-x)/\alpha)^\beta}^{\infty} \exp(-z) dz. \end{aligned}$$

This can be further simplified using the Upper Incomplete Gamma function [4] for which standard software is available. For $x > \mu$ a similar expression holds.

4 Conclusions

We have shown that measured IC chip production data can adequately be modelled by a Generalized Gaussian distribution (GGD). We developed a new robust numerical procedure for computing the parameters of such GGD. The GGD did fit very accurately. Using the GGD a quality measure can be defined analogously to the CPK index for standard Gaussian distributions.

Acknowledgement. The authors acknowledge support from the projects CORTIF (<http://cortif.xlim.fr/>) and nanoCOPS (<http://fp7-nanocops.eu/>).

References

1. T.G.J. Beelen, J.J. Dohmen: *Parameter estimation for a generalized Gaussian distribution*. CASA Report 15-40, TU Eindhoven, 2015. Online: <http://www.win.tue.nl/analysis/reports/rana15-40.pdf>.
2. K. Kokkinakis, A.K. Nandi: *Exponent parameter estimation for generalized Gaussian probability density functions with application to speech modeling*. Signal Processing 85:1852–1858, 2005.
3. R. Krupiński, J. Purczyński: *Approximated fast estimator for the shape parameter of generalized Gaussian distribution*. Signal processing 86:205–211, 2006.
4. Wikipedia: *Incomplete Gamma Function* https://en.wikipedia.org/wiki/Incomplete_gamma_function. 2016.

Numerical Simulation of Magnetization and Demagnetization Processes

A. Bermúdez¹, D. Gómez¹, M. Piñeiro¹, P. Salgado¹, and P. Venegas²

¹ Departamento de Matemática Aplicada, Universidade de Santiago de Compostela, Spain marta.pineiro@usc.es

² Departamento de Matemática, Universidad del Bío-Bío, Concepción, Chile

Summary. The purpose of this work is to describe a finite element method for the numerical simulation of magnetization and demagnetization processes in ferromagnetic pieces with hysteresis. In particular, the proposed methodology will be applied to compute the remanent flux density after a Magnetic Particle Inspection test on specimens with cylindrical symmetry, consisting of three stages: longitudinal magnetization, circular magnetization and demagnetization.

1 Introduction

Magnetic Particle Inspection (MPI) is a non-destructive testing method that uses magnetization to detect surface defects in ferromagnetic pieces. Taking into account that the breakings are more easily detected when they are oriented perpendicularly to the magnetic field in the specimen, two kinds of magnetic field are usually established within the material: with circular and longitudinal orientation. Furthermore, in most cases, pieces have to be demagnetized after the inspection, as residual magnetism could interfere with subsequent processing.

While magnetic hysteresis could be neglected in the simulation of the magnetization step (since the material is saturated to a great extent, see [1] and [2]), for the modelling of the demagnetization process, incorporating a hysteresis law is unavoidable. The main contribution of this work is the simulation of the complete magnetization and demagnetization process by including the hysteresis.

2 Mathematical Models of Magnetization

The electromagnetic models will be based on the eddy current model:

$$\mathbf{curl} \mathbf{H} = \mathbf{J}, \quad (1)$$

$$\frac{\partial \mathbf{B}}{\partial t} + \mathbf{curl} \mathbf{E} = \mathbf{0}, \quad (2)$$

$$\mathbf{div} \mathbf{B} = 0, \quad (3)$$

where \mathbf{H} is the magnetic field, \mathbf{J} is the current density, \mathbf{B} is the magnetic induction and \mathbf{E} is the electric field.

2.1 Circular Magnetization

To model circular magnetization, we will consider that the ferromagnetic pieces have cylindrical symmetry and that all fields are θ -independent. We will also assume that the current density traverses the piece along its axial direction and has the form $\mathbf{J}(\mathbf{x}, t) \equiv J_z(\rho, z, t) \mathbf{e}_z$. As a consequence, $\mathbf{H}(\mathbf{x}, t) \equiv H_\theta(\rho, z, t) \mathbf{e}_\theta$.

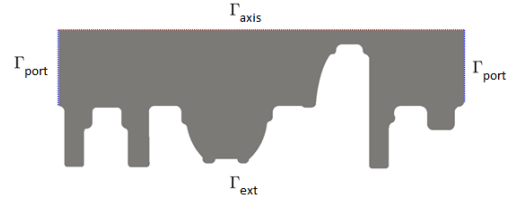


Fig. 1. Meridional section of a crankshaft. Circular magnetization.

Taking (1) and (2) into account, and using the notation appearing in Fig. 1, the problem to solve is defined only in the meridional section Ω of the piece to inspect, and reads:

$$\frac{\partial \mathcal{F}(H_\theta, \xi)}{\partial t} \mathbf{e}_\theta + \mathbf{curl} \left(\frac{1}{\sigma} \mathbf{curl}(H_\theta \mathbf{e}_\theta) \right) = \mathbf{0} \quad \text{in } \Omega, \quad (4)$$

$$H_\theta = 0 \quad \text{on } \Gamma_{axis}, \quad (5)$$

$$H_\theta = \frac{I(t)}{2\pi\rho} \quad \text{on } \Gamma_{ext}, \quad (6)$$

$$\frac{\partial H_\theta}{\partial \mathbf{n}} = 0 \quad \text{on } \Gamma_{port}, \quad (7)$$

where σ is the electric conductivity, $I(t)$ is the current crossing the domain and \mathcal{F} is the hysteresis operator (see Section 2.3).

2.2 Longitudinal Magnetization

Both in longitudinal magnetization and final demagnetization, the piece to be examined is located inside a conducting coil carrying an alternating current. In order to avoid the employment of a vector hysteresis law, we consider infinite cylindrical pieces and approximate the coil by an infinitely thin conducting surface I_S carrying a surface current density

$\mathbf{J}_S \equiv J_S(\rho, t)\mathbf{e}_\theta$ (see Fig. 2). We will denote by Ω_c the piece to be inspected, composed by a conducting ferromagnetic material with hysteresis, and by Ω_0 the air surrounding it, R_∞ being its outer radius.

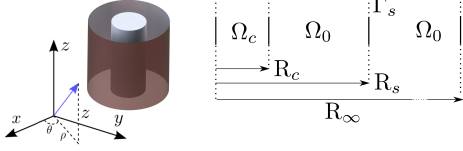


Fig. 2. Geometric domain 3D (left) and meridional section (right). Longitudinal magnetization.

The geometric considerations, along with the source direction, suggest that the fields are independent of the (θ, z) coordinates. Then, taking (1) and the source form into account, we deduce that $\mathbf{H}(\mathbf{x}, t) \equiv H_z(\rho, t)\mathbf{e}_z$. Moreover, we assume that the material has an isotropic behaviour, which implies that $\mathbf{B}(\mathbf{x}, t) \equiv B_z(\rho, t)\mathbf{e}_z$.

In the case considered, Gauss' magnetic law (3) leads to the existence of magnetic vector potential of the form $\mathbf{A}(\mathbf{x}, t) \equiv A_\theta(\rho, t)\mathbf{e}_\theta$. Then, taking (1)–(2) and Ohm's law into account, we can rewrite the problem as follows:

$$\sigma \frac{\partial A_\theta}{\partial t} - \frac{\partial}{\partial \rho} \left(\mathcal{F}^{-1} \left(\frac{1}{\rho} \frac{\partial}{\partial \rho} (\rho A_\theta), \xi \right) \right) = 0 \quad \text{for } \rho \in (0, R_c), \quad (8)$$

$$\frac{\partial}{\partial \rho} \left(\frac{1}{\mu_0} \frac{1}{\rho} \frac{\partial}{\partial \rho} (\rho A_\theta) \right) = 0 \quad \text{for } \rho \in (R_c, R_s) \cup (R_s, R_\infty), \quad (9)$$

$$\left[\frac{1}{\mu_0} \frac{1}{\rho} \frac{\partial}{\partial \rho} (\rho A_\theta) \right]_{\rho=R_s} = J_S, \quad (10)$$

$$A_\theta = 0 \quad \text{at } \rho = 0, \quad (11)$$

$$\frac{\partial A_\theta}{\partial \mathbf{n}} = 0 \quad \text{at } \rho = R_\infty, \quad (12)$$

where μ_0 is the vacuum's magnetic permeability and the source is imposed by the jump of $\mathbf{H} \times \mathbf{n}$ at $\rho = R_s$.

2.3 Magnetic Hysteresis

The behaviour of hysteretic materials is characterized by the dependence of the \mathbf{B} at each point \mathbf{x} not only on the value of \mathbf{H} at the present time but also on the so-called magnetic history. In our problems, \mathbf{H} and \mathbf{B} only have one non-null component, what allows us to use a scalar law for the nonlinear material. To simulate the magnetic hysteresis, we have chosen the well-known classical Preisach model (see [3]), which characterizes soft ferromagnetic materials by means of a hysteresis operator:

$$\begin{aligned} \mathcal{F}(H, \xi)(\mathbf{x}, t) \\ = \iint_{\alpha < \beta} \mathcal{R}_{\alpha\beta}(H(\mathbf{x}, t), \xi(\mathbf{x})) \mu(\alpha, \beta) d\alpha d\beta, \end{aligned}$$

where μ is a weight function that identifies the ferromagnetic material, ξ contains the information about the initial state of magnetization and $\mathcal{R}_{\alpha\beta}$ is the relay function. Thus, we will have that $B_z = \mathcal{F}(H_z, \xi)$ for longitudinal magnetization and $B_\theta = \mathcal{F}(H_\theta, \xi)$ for circular magnetization.

3 Numerical Results

Finally, we show the remanent flux in a cylindrical piece after some demagnetization processes with different number of cycles. These numerical results allow us to become familiar with the inspection procedure as they give useful information about which source parameters are more important for successfully demagnetize the pieces.

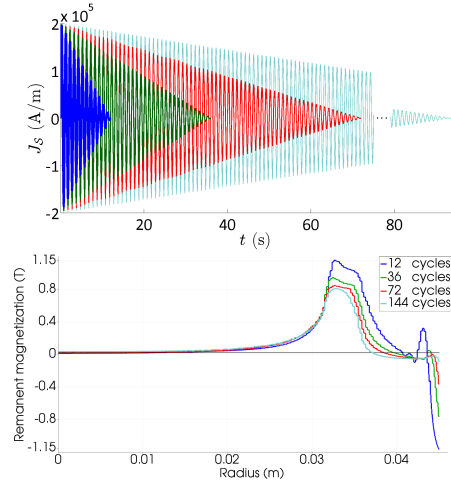


Fig. 3. Demagnetizing source (top). Remanent flux density vs. radius in the cylindrical piece (bottom).

Acknowledgement. This research was partially supported under grants FPU13/03409 and GRC2013-014, and under the research projects ENE2013-47867-C2-1-R and FOR-JACEMIC.

References

1. J. Y. Lee, S. J. Lee, D. C. Jiles, M. Garton, R. Lopez and L. Brasche. Sensitivity Analysis of Simulations for Magnetic Particle Inspection Using the Finite-Element Method. *IEEE Trans. Magn.*, 39:6, pp. 3604–3606, 2003.
2. B. S. Wong, Y. G. Low, X. Wang, J. H. Ho, C. S. Tan, J. B. Ooi. 3D Finite Element Simulation of Magnetic Particle Inspection. In *Proceedings of the 2010 IEEE Conference on Sustainable Utilization and Development in Engineering and Technology*, pp. 50-55, Nov. 2010.
3. I. D. Mayergoyz. *Mathematical Models of Hysteresis*. 1st ed. Springer, 1991.

Heat effects in graphene due to charge transport

Marco Coco¹, Giovanni Mascali², and Vittorio Romano¹

¹ Department of Mathematics and Computer Science, University of Catania, viale A. Doria 6, 95125 Catania, Italy
 mcoco@dmi.unict.it, romano@dmi.unict.it

² Dipartimento di Matematica ed Informatica, Università della Calabria and INFN-Gruppo c. Cosenza, 87036 Cosenza, Italy
 g.mascali@unical.it

Summary. The effects of crystal heating in graphene due to charge transport are investigated. The evolution of electron, hole and phonon occupation numbers is described by a system of Boltzmann equations. In view of application to electron devices, we derive also hydrodynamical models with the aid of the maximum entropy principle (MEP). The numerical solutions of the Boltzmann equations are obtained with a recent DSMC approach [1] and comparisons with the results given by the hydrodynamical models are performed.

1 The mathematical models

Electrons which mostly contribute to the charge transport in intrinsic graphene are those being in states of the conduction and valence band, close to the K and K' Dirac points. In these neighborhoods the energy dispersion relation is approximately linear [2] $\mathcal{E}_{\pm} = \pm \hbar v_F |\mathbf{k}|$, where \mathcal{E} is the electron energy, \mathbf{k} is the electron wave-vector, v_F is the Fermi velocity. The plus and minus signs refer to the electrons in the conduction and the valence band respectively. The latter are most conveniently described as holes.

We will consider the longitudinal optical (LO) phonons, the transversal optical (TO) phonons, the K-phonons, and the acoustical phonons. For LO, TO and K phonons the Einstein dispersion relation approximation is used, $\hbar\omega \approx \text{const}$, with ω the phonon frequency. While for the acoustical phonons, a linear isotropic dispersion relation is employed $\varepsilon_{ac} = \hbar\omega_{ac} = \hbar c_{ac} |\mathbf{q}|$, with ε_{ac} the phonon energy, c_{ac} the sound speed in graphene, \hbar the Planck reduced constant and \mathbf{q} the phonon wave-vector.

The semiclassical kinetic description of the charge transport in graphene can be based on two Boltzmann equations for electrons and holes

$$\frac{\partial f_{\alpha}}{\partial t} + \mathbf{v}_{\alpha} \cdot \nabla_{\mathbf{r}} f_{\alpha} + \frac{e_{\alpha}}{\hbar} \mathbf{E} \cdot \nabla_{\mathbf{k}} f_{\alpha} = \mathcal{C}_{\alpha}, \quad \alpha = e, h, \quad (1)$$

where $f_{\alpha}(\mathbf{r}, \mathbf{k}, t)$, $\alpha = e, h$, represent the occupation numbers of electrons and holes at position \mathbf{r} , time t and with wave-vector \mathbf{k} . The symbols $\nabla_{\mathbf{r}}$ and $\nabla_{\mathbf{k}}$ represent the gradients with respect to the position and the wave vector respectively, e_{α} , $\alpha = e, h$, are the particle charges (negative for electrons and positive for

holes), \mathbf{E} is the electric field and \mathbf{v} is the group velocity. The operators \mathcal{C}_{α} , $\alpha = e, h$, are the sum of the operators associated to the intra and inter-band interactions of electrons and holes with acoustic, optical and phonons (see [3] for the details).

The phonon dynamics is governed by the following Boltzmann equations

$$\frac{\partial g_{\eta}}{\partial t} + \underbrace{\mathbf{c}_{\eta} \cdot \nabla_{\mathbf{r}} g_{\eta}}_{\approx 0} = \mathcal{C}_{\eta}, \quad \eta = LO, TO, K,$$

$$\frac{\partial g_{ac}}{\partial t} + \mathbf{c}_{ac} \cdot \nabla_{\mathbf{r}} g_{ac} = \mathcal{C}_{ac},$$

with $\mathbf{c}_p = \nabla_{\mathbf{q}} \omega_p$ the phonon group velocities, $p = LO, TO, K, ac$, and $\mathbf{c}_{\eta} \approx 0$, $\eta = LO, TO, K$, as a consequence of the Einstein approximation. The collision operators are given by

$$\mathcal{C}_{\eta} = \sum_{\alpha\beta} \mathcal{C}_{\eta}^{\alpha\beta} - \frac{(g_{\eta} - g_{\eta}^{LE})}{\tau_{\eta}}, \quad \mathcal{C}_{ac} = -\frac{g_{ac} - g_{ac}^{LE}}{\tau_{ac}},$$

where the sum is for $(\alpha, \beta) \in \{(e, e), (h, h), (e, h)\}$. The τ_p 's, depending on the temperature, are the relaxation times relative to the optical phonon decay process, and the g_{η}^{LE} 's, $\eta = LO, TO, K$, g_{ac}^{LE} are the local equilibrium occupation numbers corresponding to the common temperature the phonon branches involved in the process would have if they were in local equilibrium [4].

In view of applications to electron devices, models based on integrated quantities are preferable for CAD purposes. Macroscopic quantities can be defined as moments of the occupation numbers with respect to some suitable weight functions $\psi(\mathbf{k})$. In particular for electrons and holes we propose the following set of macroscopic quantities ($\alpha = e, h$)

$$\text{density} \quad n_{\alpha} = y \int_{\mathbb{R}^2} f_{\alpha}(\mathbf{r}, \mathbf{k}, t) d\mathbf{k},$$

$$\text{velocity density} \quad n_{\alpha} \mathbf{V}_{\alpha} = y \int_{\mathbb{R}^2} f_{\alpha}(\mathbf{r}, \mathbf{k}, t) \mathbf{v} d\mathbf{k},$$

$$\text{energy density} \quad n_{\alpha} W_{\alpha} = y \int_{\mathbb{R}^2} f_{\alpha}(\mathbf{r}, \mathbf{k}, t) \mathcal{E} d\mathbf{k},$$

$$\text{energy-flux density} \quad n_{\alpha} \mathbf{S}_{\alpha} = y \int_{\mathbb{R}^2} f_{\alpha}(\mathbf{r}, \mathbf{k}, t) \mathcal{E} \mathbf{v} d\mathbf{k},$$

where y is electron density of states.

By integrating the Boltzmann equations with respect to \mathbf{k} , one obtains the following balance equations for the time evolution of the above-defined macroscopic quantities ($\alpha = e, h$)

$$\begin{aligned}\frac{\partial}{\partial t} n_\alpha + \nabla_{\mathbf{r}} \cdot (n_\alpha \mathbf{V}_\alpha) &= n_\alpha C_{n_\alpha}, \\ \frac{\partial}{\partial t} (n_\alpha \mathbf{V}_\alpha) + \nabla_{\mathbf{r}} \cdot (n_\alpha \mathbf{F}_\alpha^{(0)}) - e_\alpha n_\alpha \mathbf{G}_\alpha^{(0)} \cdot \mathbf{E} &= n_\alpha C_{V_\alpha}, \\ \frac{\partial}{\partial t} (n_\alpha W_\alpha) + \nabla_{\mathbf{r}} \cdot (n_\alpha \mathbf{S}_\alpha) - e_\alpha n_\alpha \mathbf{E} \cdot \mathbf{V}_\alpha &= n_\alpha C_{W_\alpha}, \\ \frac{\partial}{\partial t} (n_\alpha \mathbf{S}_\alpha) + \nabla_{\mathbf{r}} \cdot (n_\alpha \mathbf{F}_\alpha^{(1)}) - e_\alpha n_\alpha \mathbf{G}_\alpha^{(1)} \cdot \mathbf{E} &= n_\alpha C_{S_\alpha},\end{aligned}$$

where the rank-2 tensors \mathbf{G} 's and \mathbf{F} 's are extra-fluxes while the terms at the right hand sides are productions.

Similarly for the phonons we choose the following macroscopic variables

$$\begin{aligned}W_\eta &= y_\eta \int_{\mathcal{B}} \hbar \omega_\eta g_\eta d\mathbf{q}, & \text{energy density,} \\ \mathbf{P}_\eta &= y_\eta \int_{\mathcal{B}} \hbar \mathbf{q} g_\eta d\mathbf{q}, & \text{quasi-momentum density,} \\ \\ W_{ac} &= y_{ac} \int_{\mathbb{R}^2} \hbar \omega_{ac} g_{ac} d\mathbf{q}, & \text{energy density,} \\ \mathbf{Q}_{ac} &= y_{ac} \int_{\mathbb{R}^2} \hbar \omega_{ac} \mathbf{v}_{ac} g_{ac} d\mathbf{q}, & \text{energy-flux,}\end{aligned}$$

$y_{LO} = y_{TO} = y_K = 1/(2\pi)^2$, $y_{ac} = 3/(2\pi)^2$, being the phonon density of states. The corresponding evolution equations are

$$\frac{\partial}{\partial t} W_\eta = C_{W_\eta}, \quad \frac{\partial}{\partial t} \mathbf{P}_\eta = C_{\mathbf{P}_\eta}, \quad \eta = LO, TO, K,$$

$$\frac{\partial}{\partial t} W_{ac} + \nabla_{\mathbf{r}} \cdot \mathbf{Q}_{ac} = C_{W_{ac}}, \quad \frac{\partial}{\partial t} \mathbf{Q}_{ac} + \nabla_{\mathbf{r}} \cdot \mathbf{T}_{ac} = C_{\mathbf{Q}_{ac}}.$$

The extra fluxes and the production terms are additional unknown quantities. Following a well theoretically founded way, the desired closure relations have been obtained by resorting to MEP.

2 Numerical results

Direct simulations based on the above-written semi-classical kinetic equations have been performed by the Monte Carlo method proposed in [1], which properly takes in to account the Pauli exclusion principle.

The numerical solutions lead to the significant heating effects presented in Figs. 1 where there is plotted the evolution of the temperature starting from the room one (300 K). Instead, the thermal effects have little influence on the charge transport, as shown in Fig.2.

The results obtained with the MEP hydrodynamical models are in a good qualitative agreement.

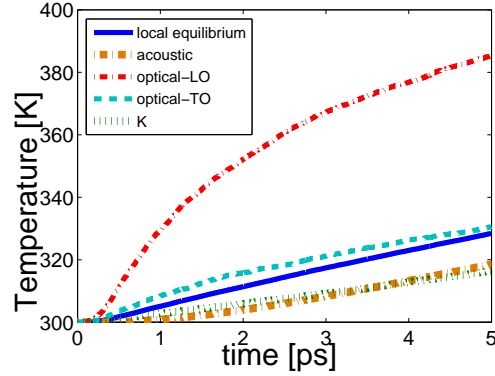


Fig. 1. Phonon temperatures and global temperature versus time in the case of a Fermi level of 0.3 eV under an electric field of strength 10 kV/cm

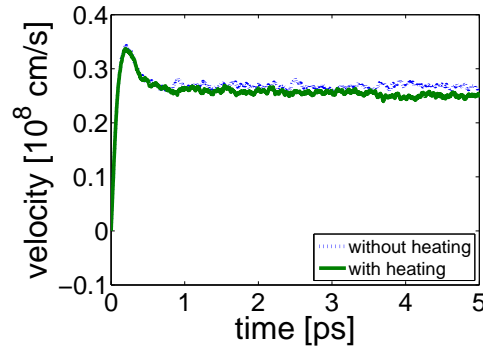


Fig. 2. Electron average velocity versus time in the case of a Fermi level of 0.6 eV under an electric field of strength 20 kV/cm

Acknowledgement. G.M. acknowledges the financial support from the P.R.A. of the University of Calabria and Progetto Giovani 2015-INDAM. M.C and V.R. acknowledge the financial support by the project FIR 2014 *Charge Transport in Graphene and Low dimensional Structures: modeling and simulation*, University of Catania, Italy.

References

1. V. Romano, A. Majorana and M. Coco. DSMC method consistent with the Pauli exclusion principle and comparison with deterministic solutions for charge transport in graphene. *J. Comp. Physics*, 302: 267–284, 2015.
2. A. H. Castro Neto, F. Guinea, N. M. R. Peres, K. S. Novoselov, and A. K. Geim. The electronic properties of graphene. *Rev. Modern Phys.*, 81: 109–162, 2009.
3. V. D. Camiola and V. Romano. Hydrodynamical model for charge transport in graphene. *Journal of Statistical Physics*, 157: 1114?1137, 2014.
4. G. Mascali. A New Formula for Thermal Conductivity Based on a Hierarchy of Hydrodynamical Models. *Journal of Statistical Physics*, 163: 1268?1284, 2016.

Computation of electric field in transformers by boundary element method and fast multipole method

Ana Drandić¹ and Bojan Trkulja¹

Department of Fundamentals of Electrical Engineering and Measurements, Faculty of Electrical Engineering and Computing, University of Zagreb, 10000 Zagreb, Croatia ana.drandic@fer.hr, bojan.trkulja@fer.hr

Summary. Accurate calculation of electric field is important to properly dimension the isolation system of a transformer. This abstract gives an overview of boundary element methods (BEM) and fast multipole methods (FMM) used to develop a solver for computation of the electric field.

1 Introduction

During its operation the transformer and consequently its' isolation system is subjected to electric stresses which may cause damage or complete breakdown of the isolation system. Isolation breakdown is one of the most common causes of transformer malfunction. Therefore, it is very important to properly dimension the insulation system during the transformers' design phase. During the dimensioning process it is important to take into account that electric field should not exceed the specified critical value. This requires use of complex analytical or numerical methods for electric field computation during the design phase while it is easy to change the isolation level. Usually, finite element methods (FEM) and boundary element methods (BEM) are used for this purpose. In this paper, BEM is used for the computation of the electric field. Since the application of BEM results in a fully, in case of using point-matching also non-symmetric, populated system matrix fast multipole method (FMM) is employed in order to reduce the CPU time and memory requirements. Results aquired by both computations are then compared with the results of a commercial software based on FEM.

2 Calculation method

Calculation of electric field is based on the approximation of charge density on the transformer winding. This can be done with constant, linear, quadratic and bicubic spline approximation [1–3]. Collocation method is used and the integration is done both analytically and numerically.

2.1 Problem formulation

Green's function of free space for 2D Laplace equation is [4]:

$$G(\mathbf{r}, \mathbf{r}') = -2\pi \ln(|\mathbf{r} - \mathbf{r}'|) \quad (1)$$

where \mathbf{r} is the vector distance of a calculation point, \mathbf{r}' is the vector distance of a referent point on a source. Therefore, electric field potential ϕ can be represented by:

$$\phi = \int \frac{1}{2\pi} \sigma \ln\left(\frac{1}{|\mathbf{r} - \mathbf{r}'|}\right) d\Omega \quad (2)$$

where σ is the distribution of surface charge density, and Ω is the surface of two-dimensional elements. By finding charge distribution σ on every boundary element, it is possible to calculate potential and electric field in space around the winding.

The surface charge is approximated by N basis functions f_i :

$$\sigma(\xi) = \sum_{i=1}^N \alpha_i f_i \quad (3)$$

where α_i are the unknown coefficients. Those coefficients are obtained from known potential using the collocation method.

Since the problem is two dimensional it is valid for $|\mathbf{r} - \mathbf{r}'|$ in (2) we use

$$|\mathbf{r} - \mathbf{r}'| = \sqrt{(x - x')^2 + (y - y')^2}. \quad (4)$$

For the problem is depicted in Fig. 1 $\sigma(x)$ and $\sigma(y)$ need to be obtained for every turn k . Since the approximation is linear the basis functions are:

$$\begin{aligned} f_{1x} &= x & f_{2x} &= 1 - x \\ f_{1y} &= y & f_{2y} &= 1 - y. \end{aligned} \quad (5)$$

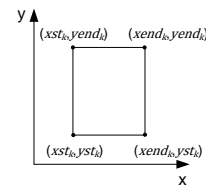


Fig. 1. Problem representation in Cartesian coordinate system

To calculate the unknown coefficients integrals (6) and (7) need to be solved. Both integrals are solved numerically and analytically.

$$\iint \ln \left[\frac{1}{\sqrt{(x-x')^2 + (y-y')^2}} \right] dx' dy' \quad (6)$$

$$\iint y' \ln \left[\frac{1}{\sqrt{(x-x')^2 + (y-y')^2}} \right] dx' dy' \quad (7)$$

After acquiring the unknown charge density the potential at any point \mathbf{r} and the electric-field strength can be determined.

2.2 Fast multipole method

Use of the FMM, first proposed by Greengard and Rokhlin [5–7], with BEM reduces the computation time and memory requirements to order $O(N)$ where N is the number of unknowns.

The main idea of the fast multipole method is interaction between cells instead of interaction between elements or nodes. This is done with expressions for expansion and translation of moments [8]. The principle of computation with the combination of BEM and FMM is based on the computation of far-field interactions between the elements with the multipole algorithm and direct integration of near-field interactions.

In the paper FMM is used to accelerate the BEM computation and the comparison of the results, computation time and memory requirements is done.

3 Numerical example

As an example we present the solution for the 2D problem shown in Fig. 2 where the potential of the elements on the positive y -axis is 1 V and on the negative y -axis -1 V. The problem was modelled with aforementioned methods and compared with the solution given by commercial FEM software ElecNet. The comparison of the results is depicted in Fig. 3 and the results are in good agreement.

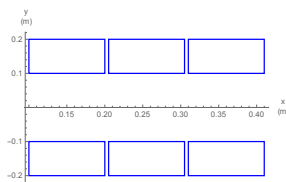


Fig. 2. Example of 2D problem

In point-by-point comparison of the results of the BEM modelled problem against the FEM results the maximum relative error is less than 10%, as shown in Fig. 4, and the biggest difference between the results occurs in the points that are on the elements.

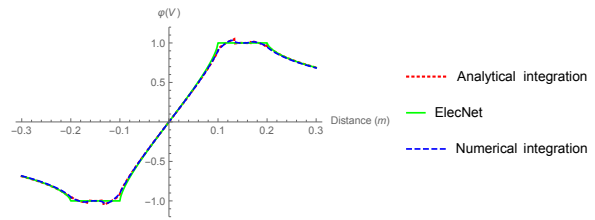


Fig. 3. Comparison of results for y in range $[-0.3, 0.3]$ and $x=0.1$

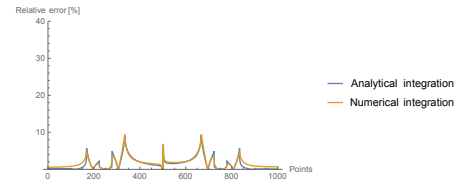


Fig. 4. Relative error when compared with FEM

4 Conclusion

Contributions of the paper include:

- application of self-developed BEM solver for the electric field calculation
- application of fast multipole method in order to increase computational efficiency
- comparison of acquired results with results given by commercial FEM software.

Acknowledgement. This work was supported in part by the Croatian Science Foundation under the project number IP-2013-1118.

References

1. S. Mukhopadhyay and N. Majumdar. Computation of 3d mems electrostatics using a nearly exact bem solver. *Engineering Analysis with Boundary Elements*, 2006.
2. E.T. Ong and K.M. Lim. Three-dimensional singular boundary elements for corner and edge singularities in potential problems. *Engineering Analysis with Boundary Elements*, 29, 2005.
3. Z. Stih and B. Trkulja. Application of bicubic splines in the boundary element method. *Engineering Analysis with Boundary Elements*, 33, 2009.
4. Z. Haznadar and Z. Stih. *Elektromagnetizam I*. Školska knjiga, 1997.
5. L.F. Greengard and V Rokhlin. A fast algorithm for particle simulations. *J. Comput. Phys.*, 1987.
6. L.F. Greengard. The rapid evaluation of potential fields in particle systems. *Cambridge: The MIT Press*, 1988.
7. V. Rokhlin. Rapid solution of integral equations of classical potential theory. *J. Comput. Phys.*, 1985.
8. Y. Liu and N. Nishimura. The fast multipole boundary element method: A tutorial. *Engineering Analysis with Boundary Elements*, 30:371–381, 2006.

Adaptive Mesh Refinement for Rotating Electrical Machines taking Boundary Approximation Errors into Account

Armin Fohler¹ and Walter Zulehner²

¹ Linz Center of Mechatronics armin.fohler@lcm.at

² Johannes Kepler University Linz, Institute of Computational Mathematics zulehner@numa.uni-linz.ac.at

Summary. We will present an error estimator for the computation of the z-component of the vector potential in the framework of rotating electrical machines. Focus of the work is on handling approximation errors of the occurring curved domain boundaries and the used domain decomposition method. Furthermore we want to end up with a mesh that is optimal for all rotor positions of one simulation period.

1 Electrical Machines

The following work focuses on the analysis of permanent magnet synchronous machines, consisting of two parts: a fixed exterior part – the stator; and a rotating interior part – the rotor. We only have to simulate one

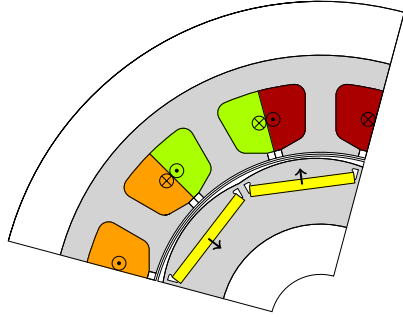


Fig. 1. Example: PMSM

quarter of the whole motor due to symmetry of the geometry and the winding.

Depicted in yellow we have the permanent magnets with a parallel magnetization direction indicated by the arrows. The machine has 12 slots with 4 pole-pairs – the double layer winding is defined according to the scheme in figure 1. Gray area symbolizes iron material, whose non-linear material property is described via a parameter $v(\nabla u)$.

2 Model Problem

We use the magnetostatic case of Maxwell's equations in 2 dimensions to model our problem. This sim-

plification is reasonable since most of the flux is in the x-y plane. Furthermore we are dealing with slowly varying magnetic fields.

Due to the fact, that we are looking at rotating electrical machines it is convenient to work with a domain decomposition approach with non-matching meshes for rotor and stator. For the coupling of the domains we use an idea of Nitsche for incorporating Dirichlet boundary conditions into the variational formulation [2, 3]. In this approach an artificial interface Γ_{ij} is introduced between the domains Ω_i and Ω_j we want to separate – in our case the rotor and the stator. The jump of the solution over this interface is then penalized. With the notation $u_i := u|_{\Omega_i}$ the resulting variational formulation of the multi-domain approach reads:

Find $u : \bar{\Omega} \rightarrow \mathbb{R}$, $\lambda_{ij} : \Gamma_{ij} \rightarrow \mathbb{R}$ such that

$$\begin{aligned} & \sum_i \left(\int_{\Omega_i} (v(|\nabla u_i|) \nabla u_i - M_{\perp}) \cdot \nabla v_i dx \right. \\ & \quad - \int_{\Gamma_{ij}} (v(|\nabla u_i|) \nabla u_i \cdot n_i) (v_i - \psi_{ij}) dS \\ & \quad + \beta \int_{\Gamma_{ij}} (v(|\nabla u_i|) \nabla v_i \cdot n_i) (u_i - \lambda_{ij}) dS \\ & \quad \left. + \frac{\alpha}{|\Gamma_{ij}|} \int_{\Gamma_{ij}} v(|\nabla u_i|) (u_i - \lambda_{ij}) (v_i - \psi_{ij}) dS \right) \\ & = \sum_i \left(\int_{\Omega_i} J_3 v_i dx - \int_{\Gamma_{ij}} M_{\perp} \cdot n_i (v_i - \psi_{ij}) dS \right) \quad (1) \end{aligned}$$

$\forall v : \bar{\Omega} \rightarrow \mathbb{R}, v|_{\partial\Omega} = 0$ and $\forall \psi_{ij} : \Gamma_{ij} \rightarrow \mathbb{R}$

The variable λ represents the solution on the new interface Γ ; the functions ψ are the test-functions there. J_3 is a load term coming from the current feed in the coils, the magnetization is taken into account via M_{\perp} .

3 Adaptive Mesh Refinement

For the optimization of an electrical machine many motor geometries have to be simulated to find a suitable topology. Thus the speed of the used solver is

crucial. To enhance the simulation time while retaining full quality of the simulation result we want to use mesh adaptivity. First step is the construction of a reliable a posteriori error estimator for the non-linear problem in the energy norm.

The energy norm for our problem is given by:

$$\|(u_i, \lambda_{ij})\|_{NC}^2 = \sum_i \int_{\Omega_i} |\nabla u_i|^2 + \sum_i \frac{\alpha}{|\Gamma_{ij}|} \int_{\Gamma_{ij}} |u_i - \lambda_{ij}|^2$$

For the estimator we can make a similar approach as in the case of a discontinuous Galerkin scheme [4].

3.1 Error Analysis

The difficulties arise from the structure of the variational formulation due to the used domain decomposition method as well as from the boundary approximation error.

As a guideline to deal with the approximation error of a curvilinear bounded domain by a polygonal one, we used the publication by W. Dörfler and M. Rumpf [1]. The basic strategy presented there can also be applied to our problem.

Additional challenges come from the discretization of the two considered domains near the interface Γ .

3.2 Domain Discretization

Due to the chosen domain decomposition method the discretization on the interface has to be considered with special care. Since the rotor and the stator are meshed independently we have to deal with non-matching meshes at Γ . This leads to regions where

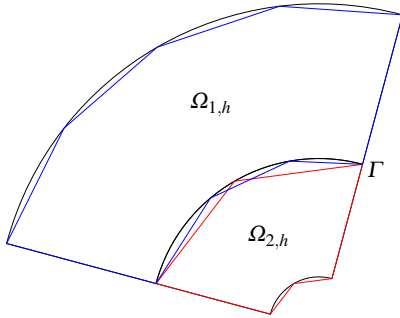


Fig. 2. Non-matching Rotor and Stator Meshes

we observe an overlap in the mesh as well as regions where we have gaps in the mesh.

3.3 Error Estimator

The estimator we obtain can be split into the different influences on the error $\tilde{e}_h := (\tilde{u}, \tilde{\lambda}) - (\tilde{u}_h, \tilde{\lambda}_h)$.

$$\|\tilde{e}_h\|_{NC}^2 \leq \sum_i C_i \left(\sum_{T \in \Omega_{i,h}} (\eta^2 + \mathcal{O}_\eta(f_h, u_h)) + \sum_{e \in \Gamma_{ij}} \gamma^2 + \sum_{e \in \Gamma_{h,ij}} \gamma_h^2 + \sum_{E \in \Omega_{i,h} \setminus \Omega_i} (\theta^2 + \mathcal{O}_\theta(f_h, u_h)) + \sum_{D \in \Omega_i \setminus \Omega_{i,h}} (\kappa^2 + \mathcal{O}_\kappa(f_h, u_h)) \right)$$

Here $\Omega_{i,h}$ denotes the discretization of the curvilinear bounded domain Ω_i . \mathcal{O}_* are the data-oscillation terms. The η -terms contain terms we expect for every residual based a posteriori error estimator [5], namely the residual itself and the jumps of the normal derivative over the edges of the triangles; γ_h and γ denote the terms coming from the (discretized) interface of he used domain decomposition method and therefore the resulting energy norm. θ - and κ -terms are related to the approximation error of the computational domain by the mesh.

Using this estimator we get an adaptive refinement of the mesh for one rotor position. We are interested in the construction of an optimal mesh for all considered rotor-positions during a simulation period, therefore will study the dependency of the problem on the rotation angle φ .

Acknowledgement. This work has been supported by the Austrian COMET-K2 programme of the Linz Center of Mechatronics (LCM), and was funded by the Austrian federal government and the federal state of Upper Austria.

References

1. Willy Dörfler and Martin Rumpf. An adaptive strategy for elliptic problems including a posteriori controlled boundary approximation. *Mathematics of Computation*, 67(224):1361–1382, 1998.
2. Herbert Egger. A class of hybrid mortar finite element methods for interface problems with non-matching meshes. *preprint AICES-2009-2, Jan, 2009*.
3. Karl Hollaus, Daniel Feldengut, Joachim Schöberl, Markus Wabro, and Dzevat Omeragic. Nitsche-type Mortaring for Maxwell’s Equations. *Progress In Electromagnetics Research Symposium Proceedings*.
4. Paul Houston, Endre Süli, and Thomas P Wihler. A posteriori error analysis of hp-version discontinuous galerkin finite-element methods for second-order quasi-linear elliptic pdes. *IMA journal of numerical analysis*, 28(2):245–273, 2008.
5. Rüdiger Verfürth. *A review of a posteriori error estimation and adaptive mesh-refinement techniques*. Advances in numerical mathematics. Wiley-Teubner, 1996.

An Efficient Optimization Tool for the Design of Electric Motors

Peter Gangl^{1,2} and Ulrich Langer³

¹ Doctoral Program “Computational Mathematics, Johannes Kepler University Linz, Austria
peter.gangl@dk-compmath.jku.at

² Linz Center of Mechatronics GmbH, Linz, Austria

³ Johann Radon Institute for Computational and Applied Mathematics (RICAM), Linz, Austria
ulrich.langer@ricam.oeaw.ac.at

Summary. We present an efficient optimization tool for the design of rotating electrical machines by combining topology optimization shape optimization. In the first stage, we determine the optimal topology of the material in the design areas of the motor. In the second stage, we perform shape optimization as a post-processing and enforce manufacturability by penalizing geometrically complex designs. In both stages, we employ a local mesh modification strategy that allows for an accurate resolution of the interface between the different materials.

1 Model Problem

As a model problem, we consider an Interior Permanent Magnet (IPM) electric motor as depicted in Figure 1, which consists of a fixed outer part, called the stator, and a rotating inner component, the rotor. They are separated by a thin air gap. The stator contains coils where electric current is induced, whereas the rotor holds permanent magnets. Both the rotor and the stator have an iron core, denoted by Ω_f where the magnetic reluctivity is a nonlinear function of the magnetic flux density. Our goal is to find the optimal distribution of ferromagnetic material in a design sub-region of the rotor such that a given objective function is minimized. We are facing the optimization problem

$$\min_{\Omega_f} \mathcal{J}(u(\Omega_f)) \quad (1)$$

$$\begin{aligned} \text{s.t. } -\operatorname{div}(v_{\Omega_f}(|\nabla u|)\nabla u) &= F && \text{in } \Omega \\ u &= 0 && \text{on } \partial\Omega, \end{aligned} \quad (2)$$

with the right hand side F comprising the impressed current in the coils and the permanent magnetization in the magnets, and with the magnetic reluctivity

$$v_{\Omega_f}(|\nabla u|) = \chi_{\Omega_f} \hat{v}(|\nabla u|) + \chi_{\Omega \setminus \Omega_f} v_0,$$

which is a nonlinear function \hat{v} in the ferromagnetic subdomains and a constant v_0 elsewhere.

2 Topology Optimization

In the topology optimization stage, we employ a level set algorithm [1] that is based on the topological

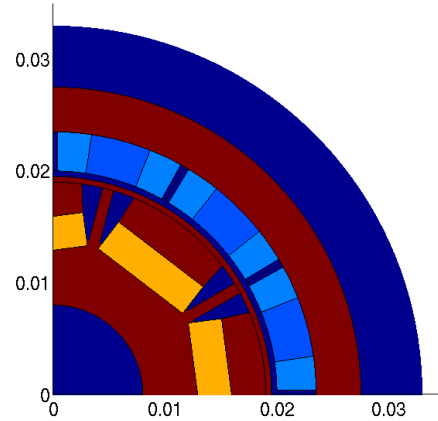


Fig. 1. Geometry of electric motor with different subdomains

derivative of the optimization problem. The algorithm is capable of performing large topological changes. The topological derivative of a domain-dependent functional $\mathcal{J} = \mathcal{J}(\Omega)$ describes its sensitivity with respect to a local perturbation of the domain Ω by the introduction of a hole or inclusion of a different material. See also [3] for the application of this algorithm to the design optimization of electrical machines.

3 Shape Optimization

Results obtained by topology optimization are often geometrically complex and hard to manufacture. Therefore, we apply shape optimization in a second stage of the optimization procedure. In shape optimization, it is also possible to penalize high geometric complexity of the arising structure by including a perimeter term into the optimization problem, i.e., by replacing the objective function $\mathcal{J}(u(\Omega_f))$ in (1) by the function

$$\tilde{\mathcal{J}}(u(\Omega_f)) = \mathcal{J}(u(\Omega_f)) + \gamma \operatorname{Per}(\Omega_f).$$

Here, $\operatorname{Per}(\Omega_f)$ denotes the perimeter of Ω_f , i.e., the sum of lengths of the interfaces between Ω_f and $\Omega \setminus \Omega_f$, and $\gamma > 0$ is a weighting parameter which

allows to manually control the allowed geometrical complexity. Note that proceeding like this is not possible in the topology optimization stage since it is not possible to compute the topological derivative of $\text{Per}(\Omega_f)$, but it is possible to compute its shape derivative.

In order to allow merging of components of the topology optimization result, we represent the geometry in an implicit way by means of a level set function ψ also in the shape optimization stage. The evolution of the design is then given as the solution of the Hamilton-Jacobi equation

$$\frac{\partial \psi}{\partial t} + V \cdot \nabla \psi = 0,$$

where V is a vector field that yields a descent of the shape function \mathcal{J} when perturbing Ω_f along V . We obtain this vector field $V \in H_0^1(\Omega)$ as the solution of an auxiliary boundary value problem of the form

$$b(V, W) = -d \mathcal{J}(\Omega_f, W) \quad \forall W \in H_0^1(\Omega),$$

where $b(\cdot, \cdot)$ is an arbitrary positive bilinear form and $d \mathcal{J}(\Omega_f, W)$ denotes the shape derivative of the shape function $\mathcal{J}(\Omega_f)$ in direction W , see [4].

4 Interface Handling

In both the topology and the shape optimization stage, we are faced with an interface between the ferromagnetic subdomain and the air region that is evolving in the course of the optimization process. In order to evaluate the topological derivative or the shape derivative in each iteration of the optimization algorithms, the state equation (2) and the adjoint equation of optimization problem (1)–(2) have to be solved, which is done by a finite element method on a triangular grid.

We present a mesh adaptation strategy that modifies the triangular finite element mesh only locally around the interface and allows to accurately resolve the interface. The method is based on the idea of [2] where the authors deal with quadrilateral meshes, but we adapt the strategy to the more involved case of triangular elements. The mesh modification strategy is based on the assumption of a hierarchical structure of the mesh where always 10 elements form one larger makro element, see Fig 2. The idea of the method is to leave the vertices of the makro elements unchanged and only adapt the points P_4, \dots, P_9 . This should be done in such a way that, on the one hand, the interface is resolved accurately by the adapted mesh, and on the other hand, each of the interior angles is bounded away from 180° . See Fig. 2 for an illustration of the method in the case of a circular interface. The latter property is important for convergence results.

We show that, independently of the location of the interface relative to the mesh, all angles in the mesh

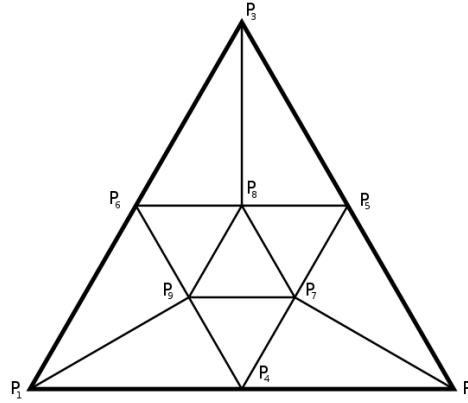


Fig. 2. Makro element consisting of 10 smaller triangles

are bounded away from 180° , which yields optimal order of convergence as the mesh size h approaches 0.

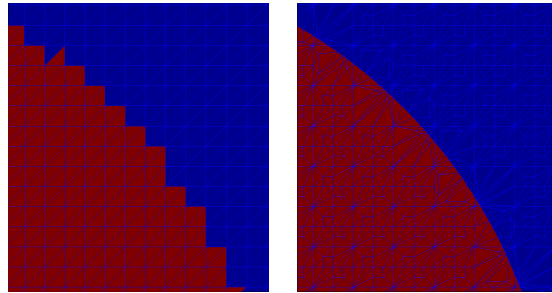


Fig. 3. Circular interface without special interface treatment (left) and with proposed local mesh modification (right)

Acknowledgement. This work was supported by the Austrian Science Fund through the Doctoral Program DK W1214 (project DK4) and by the Linz Center of Mechatronics, through the COMET K2 program of the Austrian Government.

References

1. S. Amstutz and H. Andrä. A new algorithm for topology optimization using a level-set method. *J. Comp. Phys.*, 216(2):573–588, 2006.
2. S. Frei and T. Richter. A locally modified parametric finite element method for interface problems. *SIAM J. Numer. Anal.*, 52(5):2315–2334, 2014.
3. P. Gangl, S. Amstutz, and U. Langer. Topology optimization of electric motor using topological derivative for nonlinear magnetostatics. *IEEE Trans. Mag.*, 52(3):1–4, March 2016.
4. P. Gangl, U. Langer, A. Laurain, H. Meftahi, and K. Sturm. Shape optimization of an electric motor subject to nonlinear magnetostatics. *SIAM J. Sci. Comp.*, 37(6):B1002–B1025, 2015.

Numerical methods for derivative based global sensitivity measures in high dimensions

Qingzhe Liu and Roland Pulch

Institut für Mathematik und Informatik, Ernst-Moritz-Arndt-Universität 17487 Greifswald, Germany
liuq,pulchr@uni-greifswald.de

Summary. For dynamical systems involving random parameters the output vector can be generally viewed as a function defined in the associated random domain. Without loss of generality, a function defined on the unit hypercube is considered of which a major issue is sensitivity analysis. If the function is differentiable, the derivative based sensitivity measures have received much attention. We design numerical algorithms using quasi Monte Carlo and cubature methods for computing these indices, afterwards determine their performances on electric network to compare these two numerical methods.

1 Introduction

In many applications sensitivity analysis becomes an important concept to address the uncertainty quantification in the output of a physical or mathematical model to different sources of uncertainty in its input. With the help of sensitivity analysis one can especially identify model parameters that cause significant uncertainty and the ones leading tiny impacts in the response. The less important parameters can be then replaced by constants to reduce the dimensionality of the problem without a significant loss of accuracy.

In order to quantify these impacts of uncertainties two categories are often taken into account: variance and derivative based global sensitivity indices, see e.g. [1, 2]. The variance based global sensitivities have been subject to intensive research by the authors in [7]. Alternatively, if the function in consideration is differentiable, the derivative based sensitivity measures have also received much attention.

Concerning numerical issues we focus on quasi Monte Carlo (QMC) as well as cubature methods, see [4]. QMC methods are straightforward, however, have a relatively slow convergence rate, hence looses efficiency. In contrast, cubature methods may have high efficiency compared to sampling methods since their degrees of freedom (DOF) are predetermined depending on the dimension of the random parameters. The accuracy, however, cannot be updated any further.

2 The stochastic model

We consider linear single-input-single-output (SISO) dynamical systems of the form

$$\begin{aligned} \mathbf{E}(\mathbf{x})\dot{\mathbf{y}}(t, \mathbf{x}) &= \mathbf{A}(\mathbf{x})\mathbf{y}(t, \mathbf{x}) + \mathbf{B}(\mathbf{x})u(t) \\ z(t, \mathbf{x}) &= \mathbf{C}(\mathbf{x})\mathbf{y}(t, \mathbf{x}) \end{aligned} \quad (1)$$

including physical parameters $\mathbf{x} = (x_1, \dots, x_n)^T$ being independently uniformly distributed in the domain $\prod_{i=1}^n [a_i, b_i]$. The output of (1) can be standardized to a function $f(\mathbf{x})$ defined in the unit hypercube \mathcal{H}^n at each evolutionary point in time as well as frequency domain. Assuming f is differentiable, functionals depending on $\frac{\partial f}{\partial x_i}$ are suggested as estimators for the sensitivity with respect to x_i . The modified Morris measure [3] based on absolute values reads as

$$\mu_i = \int_{\mathcal{H}^n} \left| \frac{\partial f}{\partial x_i} \right| d\mathbf{x} \quad \text{for } i = 1, \dots, n. \quad (2)$$

In contrast to the variance based sensitivities the measures μ_i may become arbitrarily large.

3 Numerical approaches

The partial derivative of the i th parameter is approximated using a finite difference

$$\frac{\partial f}{\partial x_i} \approx D_i f := \frac{1}{2h_i} \left(f(x^{h_i^+}) - f(x^{h_i^-}) \right)$$

with $x^{h_i^+} = (x_1, \dots, x_{i-1}, x_i + h_i, x_{i+1}, \dots, x_n)$, $x^{h_i^-} = (x_1, \dots, x_{i-1}, x_i - h_i, x_{i+1}, \dots, x_n)$. Typically, a small stepsize $h_i > 0$ is chosen depending on machine precision. A general discretization of measure (2) has the form

$$\tilde{\mu}_i := \sum_{j=1}^N \frac{w_j}{2h_i} \left| f(x^{h_i^+}) - f(x^{h_i^-}) \right| \quad (3)$$

for $i = 1, \dots, n$ with weights $w_j \in \mathbb{R}$. The computational cost of (3) is reflected in $2Nn$ function evaluations of f . Here a quasi Monte Carlo method is involved as a special case with $w_j = \frac{1}{N}$ for all j and the nodes from a sequence of low discrepancy. Concerning cubature points we propose the Stroud-3 approach (see [4, 6]) which generates nodes

$$\begin{aligned} x_{l,2k-1} &= \sqrt{\frac{2}{3}} \cos\left(\frac{(2k-1)l\pi}{n}\right) \\ x_{l,2k} &= \sqrt{\frac{2}{3}} \sin\left(\frac{(2k-1)l\pi}{n}\right) \end{aligned}$$

in $[-1, 1]^n$ for the components $k = 1, 2, \dots, \lfloor \frac{n}{2} \rfloor$ and if n is odd $x_{l,n} = \frac{(-1)^l}{\sqrt{3}}$ for $l = 1, \dots, 2n$. The number of nodes is just $N = 2n$. A linear transformation is necessary to map the nodes from $[-1, 1]^n$ onto \mathcal{H}^n , then the weights of the cubature all become $\omega_j = \frac{1}{2n}$.

4 Application example

In order to illustrate the approaches presented above we consider a linear RLC circuit system appearing in modelling of interconnects and pin packages within an electric circuit which was introduced in [5].

Figure 1 depicts this RLC circuit consisting of a chain of K cells which then obviously implicate K capacitances, $K - 1$ inductances and $K + 2$ conductances (reciprocal resistances). A voltage source U_{in}

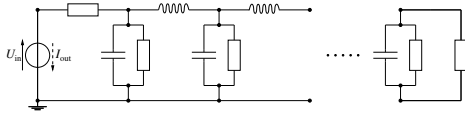


Fig. 1. Linear RLC circuit.

is stimulated as input from which the branch current I_{out} through this source is defined as output. Modified nodal analysis yields a dynamical system described by differential algebraic equations (DAEs). The set of random parameters are all capacitances, all inductances, and the conductances except for the two conductances at the boundaries. The dimension of the random space results to $n = 3K - 1$. We assume uniform distributions with ranges varying 10% around their mean values.

The expected value and the total variance of the transfer function of (1) computed by Stroud-3 and QMC are presented in Fig. 2.

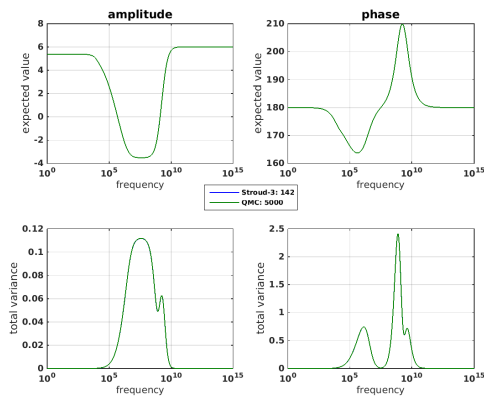


Fig. 2. Expected value and total variance of amplitude and phase in a Bode diagram ($K = 24$).

In Fig. 3 and Fig. 4 the approximated total sensitivity coefficients (2) for all inductances are traced out. We observe a good agreement between Stroud-3 and QMC methods while Stroud-3 requires less computational effort.

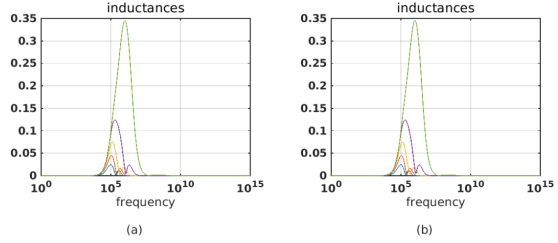


Fig. 3. Derivative based sensitivities of amplitude ($K = 24$) computed by (a) Stroud-3; (b) QMC with DOF 500.

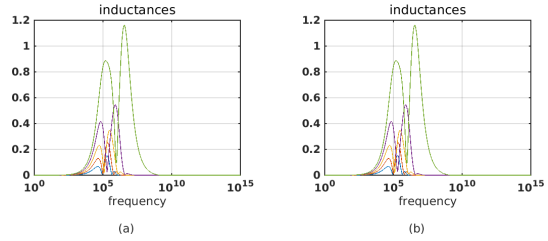


Fig. 4. Derivative based sensitivities of phase ($K = 24$) computed by (a) Stroud-3; (b) QMC with DOF 500.

References

1. B. Sudret. *Global sensitivity analysis using polynomial chaos expansions*. Reliability Engineering & System Safety 93 (2008), 964-979.
2. I.M. Sobol, S. Kucherenko. *Derivative based global sensitivity measures and their link with global sensitivity indices*. Math. Comput. Simulat. 79 (2009), 3009-3017.
3. M.D. Morris. *Factorial sampling plans for preliminary computational experiments*. Technometrics 33 (1991) 161-174.
4. D. Xiu, J.S. Hesthaven. *High order collocation methods for differential equations with random inputs*. SIAM J. Sci. Comput. 27 (2005) 3, 1118-1139.
5. M. Saadvandi. *Passivity Preserving Model Reduction and Selection of Spectral Zeros*. Master thesis, KTH, Stockholm, 2008.
6. A. Stroud. *Remarks on the disposition of points in numerical integration formulas*. Math. Comput. 11 (1957), 257-261.
7. Q. Liu, R. Pulch. *A comparison of global sensitivity analysis methods for linear dynamical systems*. In preparation, Ernst-Moritz-Arndt-Universität Greifswald, 2016

Fill-reducing reordering of saddle-point matrices for block $LD^{-1}L^T$ factorization

S. Lungten¹, W. H. A. Schilders¹, and J. M. L. Maubach¹

Eindhoven University of Technology, the Netherlands. s.lungten@tue.nl, w.h.a.schilders@TUE.nl, J.M.L.Maubach@tue.nl

Summary. This paper focuses on solving large and sparse indefinite systems of linear equations in saddle-point form. A saddle-point matrix is transformed and partitioned into a block structure constituting ‘a priori’ block pivots of order 1 and 2. A compressed graph of this partitioned matrix is determined by treating each nonzero block as a single entity. Using a fill-reducing reordering of this compressed graph, the partitioned matrix is permuted at the block level. Based on the reordered ‘a priori’ pivots, a block $LD^{-1}L^T$ factorization is computed in a straightforward manner.

1 Introduction

We focus on large and sparse symmetric indefinite systems of linear equations in saddle-point form:

$$\mathbf{M}\mathbf{u} = \mathbf{b}, \quad (1)$$

with $\mathbf{M} = \begin{bmatrix} \mathbf{A} & \mathbf{B}^T \\ \mathbf{B} & -\mathbf{C} \end{bmatrix}$, $\mathbf{u} = \begin{bmatrix} \mathbf{x} \\ \mathbf{y} \end{bmatrix}$, $\mathbf{b} = \begin{bmatrix} \mathbf{f} \\ \mathbf{g} \end{bmatrix}$,

where the (1,1) block \mathbf{A} is an $n \times n$ symmetric positive definite matrix, the (2,1) block \mathbf{B} is an $m \times n$ matrix of full rank with $m < n$, the (2,2) block \mathbf{C} is an $m \times m$ symmetric positive semidefinite matrix (including $\mathbf{C} = \mathbf{0}$), \mathbf{u} is the solution vector, and \mathbf{b} is a given vector.

The systems of the form (1) originate for instance from discretization of Maxwell’s equations [2, 3] and Stokes equations using mixed finite element methods, constrained optimization problems, and network analysis in electronic circuits [7] and water distribution systems. A significant portion of the computational time in numerical simulations is spent in solving these large linear systems. Numerical linear algebra algorithms for solving these systems more efficiently in terms of robustness, computer memory requirements and computational complexity are of great demand for software development. Designing such algorithms is intimately connected with an understanding of the structure of the resulting block matrix system and relies heavily on exploiting this structure.

Aim of the paper

In [5, 6], structured block $LD^{-1}L^T$ factorizations with blocks of order 1 and 2 are proposed based on the transformation of \mathbf{M} by transforming \mathbf{B} for the case

(2,2) block zero or diagonal. These methods retain some of the blocks of the transformed \mathbf{M} without having to update during the factorization. Although such factorizations are special, more fill-in is created in the updated blocks. To address this issue, we describe a fill-reducing reordering technique based on the graph of a compressed matrix. A saddle-point matrix is transformed and partitioned into a block $n \times n$ structure with blocks of order 1 and 2 as in [5] or [6, 8]. Each block of this structured saddle-point matrix is treated as a single entity forming a compressed matrix of order n . Using a fill-reducing reordering of the graph of the compressed matrix, the block partitioned saddle-point matrix is reordered at the block level. Using the reordered a priori pivots, a sparse factorization is computed in a straightforward manner.

2 Factorization

The factorization method entails the following steps. Steps 1 and 2 are as in [6, 8].

1. Transform \mathbf{M} by transforming \mathbf{B} to a trapezoidal form

$$\mathbf{B} = [\mathbf{B}_1 \ \mathbf{B}_2], \quad (2)$$

where \mathbf{B}_1 is an $m \times m$ nonsingular upper triangular matrix and \mathbf{B}_2 is an $m \times (n - m)$ matrix. The transformed \mathbf{M} is split into a block 3×3 structure:

$$\begin{bmatrix} \mathbf{A}_{11} & \mathbf{A}_{12} & \mathbf{B}_1^T \\ \mathbf{A}_{21} & \mathbf{A}_{22} & \mathbf{B}_2^T \\ \mathbf{B}_1 & \mathbf{B}_2 & -\mathbf{C} \end{bmatrix},$$

where \mathbf{A}_{ij} , $i, j = 1, 2$, are the blocks that partition the permuted \mathbf{A} due to (2). See [6, 8] for the details. The transformation (2) can be obtained via row and column permutations for node-arc incidence matrices \mathbf{B} , which appear in resistor network modeling. For such algorithm, see [4].

2. Define a permutation matrix Π of order $n + m$ as in [8]. Applying Π to the transformed \mathbf{M} partitions into a block $n \times n$ structure:

$$\mathbf{M}_\Pi = \Pi^T \mathbf{M} \Pi, \quad (3)$$

constituting 1×2 , 2×1 , 2×2 , and 1×1 blocks forming a priori pivots.

- Determine the adjacency graph G_Ψ of the compressed matrix of order n defined by

$$\Psi = \left[\begin{array}{c|c} |A_{11}| + |B_1| + |B_1^T| + |-C| & |A_{12}| + |B_2| \\ \hline |A_{21}| + |B_2^T| & A_{22} \end{array} \right], \quad (4)$$

where $|H| = [|h_{ij}|]$ represents a matrix whose elements are the absolute values. The matrix Ψ gives the nonzero pattern of M_Π at the block level by treating each block as a single entity.

- Permute the block columns and rows of M_Π using the fill-reducing reordering of G_Ψ . Let this permuted matrix be \widetilde{M}_Π .
- Compute the block $LD^{-1}L^T$ factorization

$$\widetilde{M}_\Pi = LD^{-1}L^T, \quad (5)$$

where L is a block lower triangular matrix with blocks of order 1 and 2, and $D = \text{diag}(L)$ is the block diagonal part.

The existence of factorization (5) is based on the following theorem.

Theorem 1. Let $M \in \mathbb{R}^{(n+m) \times (n+m)}$ be the transformed saddle-point matrix

$$M = \begin{bmatrix} A_{11} & A_{12} & B_1^T \\ A_{21} & A_{22} & B_2^T \\ B_1 & B_2 & -C \end{bmatrix}, \quad (6)$$

where $B = [B_1 \ B_2] \in \mathbb{R}^{m \times n}$ is of full rank with $B_1 \in \mathbb{R}^{m \times m}$ a nonsingular triangular matrix, $B_2 \in \mathbb{R}^{m \times (n-m)}$, $A \in \mathbb{R}^{n \times n}$ a symmetric positive definite matrix with blocks A_{ij} , $i, j = 1, 2$, partitioned accordingly and $C \in \mathbb{R}^{m \times m}$ a symmetric positive semidefinite matrix including $C = 0$. Suppose the last two block rows and columns are permuted such that

$$\widetilde{M} = \begin{bmatrix} A_{11} & B_1^T & A_{12} \\ B_1 & -C & B_2 \\ A_{21} & B_2^T & A_{22} \end{bmatrix}. \quad (7)$$

Then the Schur complements of the symmetric indefinite matrix $\begin{bmatrix} A_{11} & B_1^T \\ B_1 & -C \end{bmatrix}$ and symmetric positive definite matrix A_{22} are nonsingular.

3 Numerical results

The sparsity of $LD^{-1}L^T$ factorization described in steps 1 to 5 is compared with the sparsity of factorization described in [6]. The approximate minimum degree (AMD) algorithm [1] is used for reordering the compressed graph G_Ψ . We refer to (5) as the block AMD (BAMD) factorization in the numerical results.

Whereas the factorization in [6] is referred to as structured block $LD^{-1}L^T$ factorization (SBFACT). The test problems are the saddle-point matrices from resistor network modeling in [7]. Define the fill-ratio

$$\text{fill}(\mathbf{L}) = \frac{\text{nnz}(\mathbf{L})}{\text{nnz}(\text{btril}(\mathbf{M}_\Pi))}, \quad (8)$$

where $\text{nnz}()$ is the number of nonzero entries and $\text{btril}(\mathbf{M}_\Pi)$ is the block lower triangular part of \mathbf{M}_Π .

Table 1. Comparison of BAMD with SBFACT for the saddle-point matrices from resistor network modeling. $\text{nnz}()$ is the number of nonzero entries, and $\text{fill}(\mathbf{L})$ is the fill-ratio defined in (8).

Matrix	nnz(M)	nnz(L)		fill(L)	
		SBFACT	BAMD	SBFACT	BAMD
RNA3	12,374	408,102	24,781	45.52	3.34
RNB3	17,619	1,534,494	28,238	119.30	2.67
RNB6	106,034	31,185,501	145,646	406.10	2.29
RNB8	28,869	1,896,218	42,543	90.96	2.46
RNC3	61,104	11,458,224	94,235	258.70	2.57
RNC4	37,289	2,951,023	60,200	109.20	2.69
RNC5	82,749	8,541,178	214,091	141.40	4.31

References

- P. R. Amestoy, T. A. Davis, and I. S. Duff, An approximate minimum degree ordering algorithm. *SIAM J. Matrix Anal. Appl.*, 17:886–905, 1996.
- C. Grief and D. Schötzau, Preconditioners for the discretized time-harmonic Maxwell equations in mixed form. *Numer. Linear Algebra Appl.*, 14:281–297, 2007.
- P. Houston, I. Perugia, A. Schneebeli, and D. Schötzau, Mixed discontinuous Galerkin approximation of the Maxwell operator: The indefinite case. *ESAIM Math. Model. Numer. Anal.*, 39:727–753, 2005.
- S. Lungten, W. H. A. Schilders, and J. M. L. Maubach, Sparse inverse incidence matrices for Schilders’ factorization applied to resistor network modeling. *Numer. Algebra Control Optim.*, 4:227–239, 2014.
- S. Lungten, W. H. A. Schilders, and J. M. L. Maubach, Sparse block factorization of saddle point matrices. *Linear Algebra Appl.*, 502:214–242, 2015.
- S. Lungten, W. H. A. Schilders, and J. M. L. Maubach, Incomplete block $LD^{-1}L^T$ factorization constraint preconditioners. *Technical Report, Centre for Analysis Scientific Computing and Applications, Eindhoven University of Technology, CASA-Report*, 15–22, 2015. Revised version submitted to SIMAX journal, Feb., 2016.
- J. Rommes and W.H.A. Schilders, Efficient methods for large resistor networks. *IEEE Transactions on Computer-Aided Design of Integrated Circuits and Systems*, 29:28–39, 2010.
- W.H.A. Schilders, Solution of indefinite linear systems using an LQ decomposition for the linear constraints. *Linear Algebra Appl.*, 431:381–395, 2009.

The dynamical impact of structural perturbations in electrical circuits

Jan Philipp Pade¹ and Caren Tischendorf¹

Humboldt Universität zu Berlin, Dept. of Mathematics, Unter den Linden 6, 10099 Berlin
pade@math.hu-berlin.de, tischendorf@math.hu-berlin.de

Summary. The function of many electrical circuits is defined through the stability of a fixed point. Assume that due to damage or other external influences the value of a circuit's element is perturbed. Although the circuit's fixed point remains stable, the transient behaviour might change. Even the simplest example shows that determining whether such a perturbation has a stabilizing or a destabilizing effect in terms of the circuit's topology is very hard. Here, we present first results for the case of circuits with two different types of elements.

1 Introduction

In many applications, the function of an electrical circuit is defined through the stability of certain states such as fixed points. However, due to faulty elements, damage or other external influences the stability can change. Also, one might be able to increase the stability and hence improve the function by just changing the value of a few elements. This raises the question of how the stability is connected to the circuit's topology and more generally to the values of elements in the circuit. In the context of ODEs this question was addressed to some extent [1–3]. However, important models of electrical circuits are given by differential-algebraic equations. For this class of equations almost no answers aiming at this type of question are known. Using perturbation theory of generalized eigenvalues we present first results here. We also mention that the results can be transferred to certain power-grid models.

1.1 A simple example

In this subsection we illustrate the complex relation between the site of the perturbed link in the circuit and the effect of the perturbation.

In Fig. 1 we illustrate the dynamical impact of perturbations on two edges of the circuit's graph. More precisely, we vary the values of the conductance $\frac{1}{R_2}$ and the inductance C resp. The color in inset a) codes the distance to instability in terms of the real part of the system's spectral gap. Depending on the conductance and inductance values, increasing either one of them can have a stabilizing or a destabilizing effect.

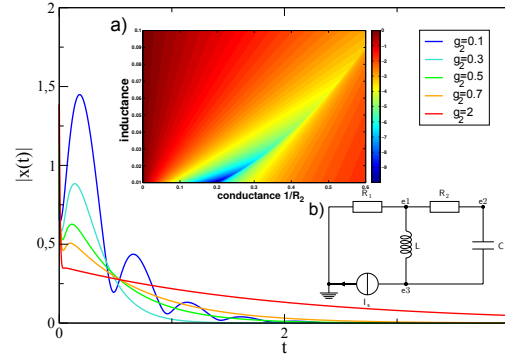


Fig. 1. The effect of perturbations in circuit b). Color in inlet a) codes the spectral gap for different values of conductance g_2 and inductance L for $C = 1$. The main plot shows time traces for different values of g_2 and $L = 0.02$.

2 Linear stability in circuits

In order to investigate the linear stability of a circuit's fixed point we consider the MNA model equations

$$\begin{pmatrix} M_C & 0 \\ 0 & L \end{pmatrix} \frac{d}{dt} \begin{pmatrix} e \\ i_L \end{pmatrix} + \begin{pmatrix} M_R & A_L \\ -A_L^T & 0 \end{pmatrix} \begin{pmatrix} e \\ i_L \end{pmatrix} = \begin{pmatrix} -A_I I_S \\ 0 \end{pmatrix} \quad (1)$$

where we only take into account current sources. Here, the node potentials e_i and the currents over the inductivities $(i_L)_i$ are the unknown variables. $M_R = A_R G A_R^T$, $M_C = A_C C A_C^T$, A_C, A_R, A_L and A_I are the incidence matrices corresponding to capacities, conductances, inductivities and current sources and C, G and L are diagonal matrices with the values of capacities, conductances and inductivities resp. on their diagonals. The governing equations (1) are differential algebraic equations (DAE). The linear stability of fixed points in a linear DAE of the form $E\dot{z} + Az = I$ was shown to be determined by the eigenvalues of the matrix pencil (E, A) , that is the $\lambda \in \mathbb{C}$ such that $\lambda E x + A x = 0$ for an eigenvector $x \in \mathbb{C}^n$ [4]. More precisely, a fixed point is stable if all eigenvalues λ fulfill $\Re(\lambda) < 0$. In [5] it was shown, that the eigenvalues in (1) always fulfill $\Re(\lambda) \leq 0$. Hence, the system never becomes unstable. However, depending on the distance of the spectral gap (i.e. the eigenvalue with largest real part) to the imaginary axis, the relaxation time towards the fixed point can become arbitrarily large.

In order to track the motion of the spectral gap under perturbations, we show the following

Lemma 1. *Let $E, A, \tilde{E}, \tilde{A} \in \mathbb{R}^{n \times n}$ with E, A symmetric and $\lambda_0 \in \mathbb{C}$ be a finite eigenvalue of the pencil (E, A) . Then for $\varepsilon > 0$ small enough there exists a smooth family of solutions $\lambda(\varepsilon)$ with $\lambda(0) = \lambda_0$ of the perturbed pencil $\lambda(E + \varepsilon\tilde{E})x + (A + \varepsilon\tilde{A})x = 0$ with appropriate $x = x(\varepsilon)$. Furthermore, the first order term of $\lambda(\varepsilon)$ is given by*

$$\lambda'(0) = -\frac{x^*(\lambda(0)\tilde{E} + \tilde{A})x}{x^*Ex}. \quad (2)$$

The pencil corresponding to (1) can be reformulated as the second order matrix polynomial

$$P(\lambda) = \lambda^2 M_C + \lambda M_R + M_{L^{-1}}. \quad (3)$$

Using algebraic properties of this polynomial together with the above Lemma, we can show

Theorem 1. *Assume the circuit from (1) does not have any inductions and I-cutsets. Then*

1. *increasing the value of a resistor does not decrease the stability*
2. *increasing the value of a capacity does not increase the stability.*

In other words, resistors and capacities act as counter-players. We can prove an analogous result for a circuit without capacities

Theorem 2. *Assume the circuit from (1) does not have any capacities and I-cutsets. Then*

1. *increasing the value of a resistor does not increase the stability*
2. *increasing the value of an induction does not increase the stability.*

So remarkably, increasing the weight of any of the elements in this last case will either leave the stability invariant or destabilize the system. The only way to stabilize the system is to decrease the value of certain elements.

In the case of a circuit without resistors, all eigenvalues lie on the imaginary axis [6]. In order to determine the type of stability one would have to take into account higher order terms. However, it is known that these are oscillatory systems and referring to the eigenfrequencies of the system we have

Theorem 3. *Assume, the circuit from (1) does not have any resistors and I-cutsets. Then*

1. *increasing the value of a capacity does not increase the eigenfrequencies*
2. *increasing the value of an induction does not decrease the eigenfrequencies.*

3 Discussion

We have presented a first step in the study of the dynamical impact of structural perturbations in electrical circuits. More precisely, we studied the effect of changing the weight of a circuit's element on the stability of a fixed point. The obtained results apply to the case of circuits with only two different types of elements. In this case another natural question arises: for which perturbation can we achieve the maximal change of stability? In the light of Lemma 1 this calls for a more detailed study of the eigenvectors of matrix pencils. More precisely, the relation between a pencil's eigenvector and the circuit's coupling topology. As mentioned in the introduction and seen in the example, the situation for the general case of an RLC circuit is much more involved. We remark that the matrices M_X in (3) are so-called (singular) grounded Laplacians and thus have a very special structure [7, 8]. It is desirable to develop a spectral theory for matrix polynomials with such structure, building up on previous work on matrix polynomials [9] in order to obtain results for the general case of an RLC circuit.

Acknowledgement. Supported by Einstein Stiftung Berlin through the Research Center Matheon Mathematics for key technologies in Berlin and the European FP7 project nanoCOPS under grant 619166.

References

1. M. Jalili. Enhancing synchronizability of diffusively coupled dynamical networks: a survey. *IEEE TNNLS*, 24:1009–1022, 2013.
2. A. E. Motter, C. Zhou and J. Kurths. Network synchronization, diffusion and the paradox of heterogeneity. *Phys. Rev. E*, 71:016116, 2005.
3. J.P. Pade and T. Pereira. Improving the Network Structure can lead to Functional Failures. *Nature Scientific Reports*, 5:09968, 2015.
4. R. März. On quasilinear index 2 differential-algebraic equations. *Seminarberichte HU Berlin*, 1992.
5. R. Riaza and C. Tischendorf. Qualitative features of matrix pencils and DAEs arising in circuit dynamics. *Dynamical Syst.*, 22(2):107–131, 2007.
6. R. Riaza and C. Tischendorf. Structural characterization of classical and memristive circuits with purely imaginary eigenvalues. *Int. J. Circ. Theor. Appl.*, 41:273–294, 2013.
7. M. Pirani and S. Sundaram. On the Smallest Eigenvalue of Grounded Laplacian Matrices. *IEEE Trans. Autom. Cont.*, 61(2):509–514, 2016
8. U. Miekkala. Graph properties for splitting with grounded Laplacian matrices. *BIT*, 33:485–495, 1993.
9. I. Gohberg, P. Lancaster and L. Rodman. *Matrix Polynomials*. Academic Press, New York, 1982.

Deterministic and stochastic solutions of the Boltzmann equation for charge transport in graphene on substrates

Marco Coco¹, Armando Majorana¹, and Vittorio Romano¹

Department of Mathematics and Computer Science, University of Catania, viale A. Doria 6, 95125 Catania, Italy
 mcoco@dmi.unict.it, majorana@dmi.unict.it, romano@dmi.unict.it

Summary. The effects of the substrate on the characteristic curves in graphene on a oxide are investigated. The transport equations for charge carriers are solved by both a DSMC method and a Discontinuous Galerkin scheme.

The results, as expected, show a degradation of the electron mobility due to the additional scattering with the remote impurities of the substrate.

1 The mathematical models

A physically accurate model for charge transport in graphene is given by a semiclassical Boltzmann equation whose scattering terms have been deeply analyzed in the last decade. Due to the computational difficulties, the most part of the available solutions have been obtained with direct Monte Carlo simulations. The aim of this work is to simulate a monolayer graphene on a substrate, as, for instance, considered in [1].

In a semiclassical kinetic setting, the charge transport in graphene is described by four Boltzmann equations, one for electrons in the valence (π) band and one for electrons in the conduction (π^*) band, that in turn can belong to the K or K' valley,

$$\begin{aligned} \frac{\partial f_{\ell,s}(t, \mathbf{x}, \mathbf{k})}{\partial t} + \mathbf{v}_{\ell,s} \cdot \nabla_{\mathbf{x}} f_{\ell,s}(t, \mathbf{x}, \mathbf{k}) - \frac{e}{\hbar} \mathbf{E} \cdot \nabla_{\mathbf{k}} f_{\ell,s}(t, \mathbf{x}, \mathbf{k}) \\ = \left. \frac{df_{\ell,s}}{dt}(t, \mathbf{x}, \mathbf{k}) \right|_{e-ph}, \end{aligned}$$

where $f_{\ell,s}(t, \mathbf{x}, \mathbf{k})$ represents the distribution function of charge carriers in the valley ℓ (K or K'), band π or π^* ($s = -1$ or $s = 1$) at position \mathbf{x} , time t and wave-vector \mathbf{k} . We denote by $\nabla_{\mathbf{x}}$ and $\nabla_{\mathbf{k}}$ the gradients with respect to the position and wave-vector, respectively. The microscopic velocity $\mathbf{v}_{\ell,s}$ is related to the energy band $\varepsilon_{\ell,s}$ by

$$\mathbf{v}_{\ell,s} = \frac{1}{\hbar} \nabla_{\mathbf{k}} \varepsilon_{\ell,s}.$$

With a very good approximation [2] a linear dispersion relation holds for the energy bands $\varepsilon_{\ell,s}$ around the equivalent Dirac points; so that $\varepsilon_{\ell,s} = s \hbar v_F |\mathbf{k} - \mathbf{k}_{\ell}|$, where v_F is the (constant) Fermi velocity, \hbar is the Planck constant divided by 2π , and \mathbf{k}_{ℓ} is the position of the Dirac point ℓ . The elementary (positive) charge is denoted by e , and \mathbf{E} is the electric field. The

right hand side of the Boltzmann equation is the collision term representing the interaction of electrons with impurities and phonons, the latter due to both the graphene crystal and substrate [2]. We assume that phonons are at thermal equilibrium.

The main differences between graphene on a substrate and the suspended case are due the presence of an additional scattering between the electrons in the graphene sheet and the remote phonons of the substrate. This usually leads to a reduction of the electron velocity with a degradation of the electron mobility.

2 Numerical results

We use a numerical scheme based on the discontinuous Galerkin method for finding deterministic (non stochastic) solutions of the electron Boltzmann equation in graphene (see [4] for more details). The results are compared with those obtained with a recent DSMC approach that properly takes into account the Pauli exclusion principle [3]. From the comparison we have got a cross-validation of both the approaches. The remarkable agreement between the deterministic and the stochastic solutions give a strong numerical indication of the robustness and accuracy of both DG and DSMC simulators.

In order to analyze the influence of the substrate on the average electron velocity, and therefore on the charge mobility, we have considered different values of the distance d between the graphene layer and the impurities of a SiO_2 substrate, by assuming that they are placed in a plane parallel to the graphene.

The results are plotted in Fig. 1. It is evident the decrease of the velocity for low values of d with a resulting degradation of the mobilities. This fact can play a crucial role in the design of electron devices that make use of graphene because the presence of a substrate can produce a sizable reduction of the current and an relevant modification of the characteristic curves.

Acknowledgement. The authors acknowledge the financial support by the project FIR 2014 *Charge Transport in Graphene and Low dimensional Structures: modeling and simulation*, University of Catania, Italy.

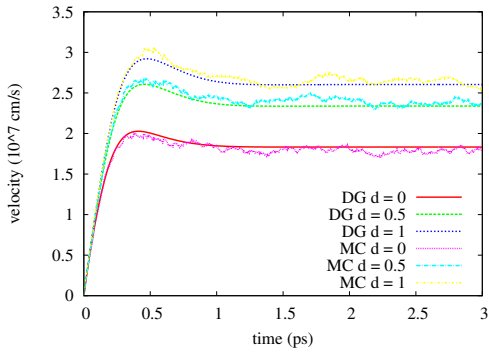


Fig. 1. Electron average velocity versus time in the case of Fermi level 0.4 eV under an electric field of strength 10 kV/cm for $d = 0, 0.5, 1$ nm.

References

1. H. Hirai, H. Tsuchiya, Y. Kamakura, N. Mori, M. Ogawa, Electron mobility calculation for graphene on substrates. *J. Appl. Phys.*, 116:083703, 2014.
2. A. H. Castro Neto, F. Guinea, N. M. R. Peres, K. S. Novoselov, and A. K. Geim. The electronic properties of graphene. *Rev. Modern Phys.*, 81: 109–162, 2009.
3. V. Romano, A. Majorana and M. Coco. DSMC method consistent with the Pauli exclusion principle and comparison with deterministic solutions for charge transport in graphene. *J. Comp. Physics*, 302: 267–284, 2015.
4. M. Coco, A. Majorana and V. Romano. Cross validation of discontinuous Galerkin method and Monte Carlo simulations of charge transport in graphene on substrate. *Ricerche di Matematica*, to appear (DOI 10.1007/s11587-016-0298-4).

Time-domain reduced-order modelling of linear finite-element eddy-current problems via RL-ladder circuits

Ruth V. Sabariego¹ and Johan Gyselinck²

¹ KU Leuven, Dept. Electrical Engineering, EnergyVille, Belgium ruth.sabariego@kuleuven.be

² Université Libre de Bruxelles, BEAMS Dept., Belgium johan.gyselinck@ulb.ac.be

Summary. This paper deals with the lumped-parameter modelling of magnetically linear eddy-current devices which have one terminal voltage and current. The device is first characterised by means of frequency-domain finite-element (FE) computations considering the relevant frequency band, for subsequently fitting constant-coefficient RL ladder circuits of various extent (i.e. number of branches). The accuracy of the ladder-circuit model is assessed in both frequency and time domain. This is successfully applied to the axisymmetric magnetic levitation device of TEAM Workshop problem 28.

1 Introduction

The time-stepping FE simulation of an electromagnetic device may be the suitable approach for studying (and possibly improving) its performance in simple steady-state electrical and mechanical conditions. If the next stage in the analysis/design is about more realistic transient operation, possibly with (closed-loop) control and integration in a wider system, the FE model may become prohibitively expensive. A computationally cheaper model, generically referred to as reduced-order model (ROM), should be derived, inevitably at the expense of a certain loss of accuracy.

Purely mathematical ROMs in various engineering disciplines are based on concepts such as singular value decomposition and snapshot selection [1], and mostly involve little or no physical insight of the device or problem at hand.

Alternatively, ROMs can also be based on the identification of the device via a series of simple static or dynamic FE computations [2], rather than on a manipulation of the FE matrices. Such an approach is more or less straightforward and feasible depending on the characteristics of the electromagnetic device: the number of independent currents (or voltages) n_i , the absence/presence of saturable magnetic materials and induced currents, and the number (0, 1 or more) of position degrees of freedom n_p . Different particular cases can be distinguished. If the system is magnetically linear without eddy currents, the current-independent $n_i \times n_i$ inductance matrix can be straightforwardly obtained by n_i magnetostatic computations. Through tabulation and interpolation of the inductance values, a minimum-cost model of the device is easily achieved. The situation changes dras-

tically in presence of saturable material and/or eddy currents.

In this paper we consider the levitation device of TEAM Workshop problem 28 (TWP28) [3], a relatively simple, though far from trivial case. It consists of a magnetically linear device with one terminal current ($n_i = 1$).

2 Frequency-domain identification

The axisymmetric device of TWP28 comprises two anti-series-connected coils and an aluminium circular disk at height z_{pl} above the coils. Part of the cross-section can be seen in Fig. 1. The well-known magnetic vector potential formulation, in terms of its tangential component a_ϕ , is adopted, either in the time or frequency domain. Phasors are denoted by underlined symbols; f and $\omega = 2\pi f$ are the frequency and the pulsation, and j is the imaginary unit.

The instantaneous terminal voltage $v(t)$, current $i(t)$ and associated flux-linkage $\psi(t)$ are linked as:

$$v(t) = R_0 i(t) + \frac{d\psi}{dt}, \quad (1)$$

where $R_0 = 6.73 \Omega$ is the DC resistance. In absence of eddy currents in the plate, in the low-frequency limit $f \rightarrow 0$, we have $\psi = L_0 i$, where $L_0 = 73.2$ mH is the (z_{pl} -independent) DC inductance.

In the frequency domain, in presence of eddy currents in the plate, (1) becomes $\underline{V} = \underline{Z} \underline{I}$, where the complex terminal impedance $\underline{Z} = R + j\omega L$ depends on both frequency f and position z_{pl} . The AC resistance $R(f, z_{pl})$ and inductance $L(f, z_{pl})$ can be obtained from the FE model via: 1) terminal \underline{V} and \underline{I} ; 2) the flux-linkage, $\underline{\Psi}/\underline{I} = L + j(R - R_0)/\omega$; or 3) the integral of the magnetic energy and Joule loss density.

The relative change in resistance and inductance, i.e. $\Delta R/R_0$ and $\Delta L/L_0$, with $\Delta R = R - R_0$ and $\Delta L = L - L_0$, is shown in Fig. 3, with a suitable double logarithmic scale, in the 10 to 1000 Hz band, and for three positions, viz $z_{pl} = 3, 10$ and 17 mm.

3 Ladder-circuit approximation

The frequency-dependent resistance and inductance can be approximately effected with a ladder circuit as

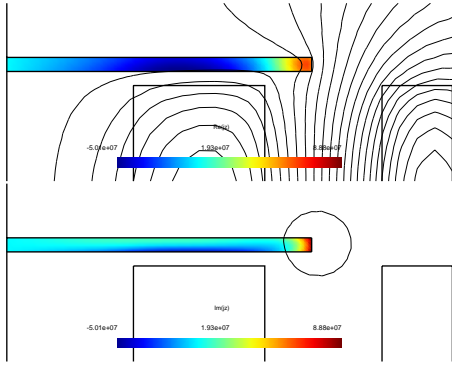


Fig. 1. Flux lines and induced current density in the plate at $f = 1$ kHz and $z_{p1} = 3$ mm, in phase (up) and quadrature (down) with imposed $20 A_{\text{peak}}$ current

in Fig. 2, with e.g. two additional loops ($n_b = 2$) and two auxiliary (loop) currents i_1 and i_2 besides the terminal current $i(t)$. The $n_b + 1$ circuit equations can be written in matrix notation in terms of the column vector $[I(t)]^T = [i(t) \ i_1(t) \ i_2(t) \ \dots]^T$ and corresponding voltage vector $[V(t)]^T = [v(t) \ 0 \ 0 \ \dots]^T$:

$$[V(t)] = [R][I(t)] + [L] \frac{d}{dt}[I], \quad (2)$$

where $[R]$ is diagonal and $[L]$ tri-diagonal. With $n_b = 2$: $[R] = \text{diag}(R_0, R_1, R_2)$ and

$$[L] = \begin{bmatrix} L_0 & -L_0 & 0 \\ -L_0 & L_0 + L_1 & -L_1 \\ 0 & -L_1 & L_1 + L_2 \end{bmatrix}. \quad (3)$$

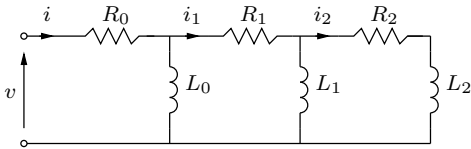


Fig. 2. Ladder circuit with two auxiliary loops ($n_b = 2$)

For a given n_b and position, the parameters $R_k(z_{p1})$ and $L_k(z_{p1})$ are determined by fitting the ensuing impedance $Z_{n_b}(f, z_{p1})$ to the reference FE impedance $Z_{\text{FE}}(f, z_{p1})$ in the relevant frequency band, e.g. by means of the Nelder-Mead simplex method (nonlinear minimization). Some results are depicted in Fig. 3 with $n_b = 1$ and $n_b = 3$. One observes an excellent agreement with the FE results for $n_b = 3$.

Next a time-domain computation with imposed $f = 1$ kHz, $500 V_{\text{peak}}$ voltage, with $z_{p1} = 10$ mm, is carried out. The Joule losses in the plate follow from the ladder-circuit model by summing $R_k i_k^2(t)$ in all resistances but the DC one ($1 \leq k \leq n_b$). Excellent

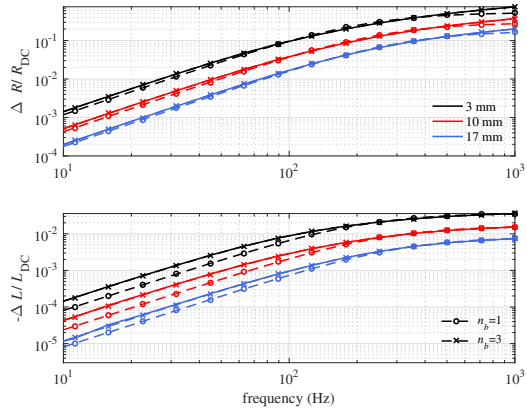


Fig. 3. Relative increase/decrease of AC resistance and inductance with frequency (for 3 different positions), obtained with FE model (full lines) and ladder circuit (markers, $n_b = 1$ and $n_b = 3$)

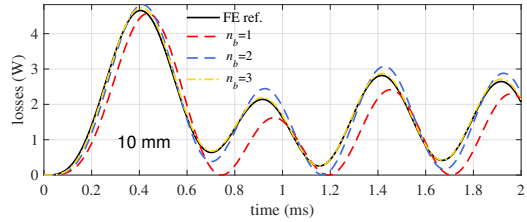


Fig. 4. Losses in the plate versus time ($z_{p1} = 10$ mm; 1 kHz voltage supply), computed with FE and LR-ladder circuits (n_b equal to 1, 2 and 3)

convergence towards the FE results is observed with increasing n_b .

Further details on the implementation and more results will be given in the full paper. Particular attention will be paid to the coefficient behaviour in terms of the position, what matters for further consideration of the mechanical equation.

Acknowledgement. Work supported in part by the Walloon Region of Belgium (WBGreen FEDO, grant RW-1217703) and the Belgian Science Policy (IAP P7/02).

References

1. W. Schilders, H. V. der Vorst, J. Rommes, Model order reduction: theory, research aspects and applications, Springer-Verlag, 2008.
2. Z. Liu, S. Liu, O. A. Mohammed, A Practical Method for Building the FE-Based Phase Variable Model of Single Phase Transformers for Dynamic Simulations, *IEEE Trans. Magn.*, vol. 43, no. 4, pp. 1761–1764, 2007.
3. H. Karl, J. Fetzer, S. Kurz, G. Lehner, W. M. Rucker, Description of TEAM workshop problem 28: An electrodynamic levitation device, In Proc. of the TEAM Workshop, Graz, Austria, pp. 41–42, 1997.

Error Estimation for MSFEM for elliptic problems in 2D

Markus Schöbinger¹, Karl Hollaus¹, and Joachim Schöberl¹

Technische Universität Wien, Wiedner Hauptstrae 8-10, A-1040 Vienna markus.schoebinger@tuwien.ac.at, karl.hollaus@tuwien.ac.at, joachim.schoeberl@tuwien.ac.at

Summary. We follow multi-scale techniques for layered medium as described in [1]. The goal is to find error estimates for the homogenized solution using modifications of flux reconstruction techniques described in [2]. Since these estimators require integration over the layered domain, efficient integration techniques will be demonstrated.

1 Problem Setting

Consider a domain $\Omega \in \mathbb{R}^2$ which is composed of an outer domain Ω_0 and a layered inner domain Ω_m as demonstrated in Fig. 1. In our examples we take Ω_0 to be the surrounding air domain and Ω_m to consist of parallel rectangular iron layers of width d_1 separated by air gaps of width d_2 . The unit cell width $d := d_1 + d_2$ is defined as the width of one iron layer including half of each surrounding gap. In the studied applications, usually $d_1 = 0.9d$.

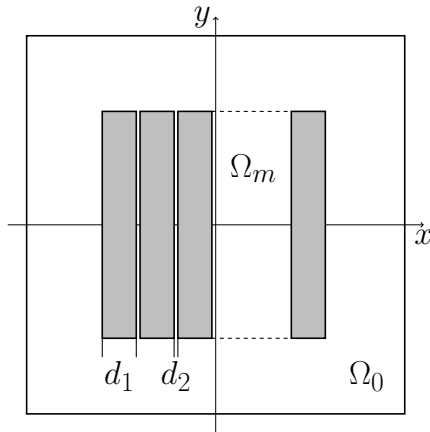


Fig. 1. The layered domain Ω

Two simplifications of Maxwell's equations are taken into consideration. Equation (1) shows the simplest setting where the real valued function u corresponds to the electric scalar potential and λ to the electric permittivity. In the numerical examples $\lambda = 1000$ in iron and $\lambda = 1$ in air. This setting will mainly be used to fix ideas and to develop the main tools which will later be modified to fit into the extended, complex valued setting (2).

$$\nabla \cdot (\lambda \nabla) u = f \quad (1)$$

$$\nabla \cdot (\rho \nabla u) + i\omega \mu u = f \quad (2)$$

In the second equation ρ corresponds to the electric resistivity.

In the following we will outline the main ideas for the setting (1), since the details for (2) become rather technical.

1.1 Multi-Scale Ansatz

Studying the behaviour of the solution of (1), one observes that in Ω_m u can be split into a “mean function” and a periodic perturbation. These observations suggest the ansatz

$$u = u_0 + \phi u_1, \quad (3)$$

where $u_0 \in H^1(\Omega)$, $u_1 \in H^1(\Omega_m)$ and ϕ chosen as a linear zigzag function with a period of d . The main idea is to calculate u_0 and u_1 on a coarser mesh which does not incorporate each layer. Equation (1) becomes in weak form

$$\int_{\Omega} \bar{\lambda} \nabla u_0 \nabla v_0 + \bar{\lambda} \phi_x (u_{0,x} v_1 + v_{0,x} u_1) + \bar{\lambda} \phi_x^2 u_1 v_1 + \bar{\lambda} \phi^2 \nabla u_1 \nabla v_1 \, d\Omega = 0. \quad (4)$$

where an index x means the partial derivative with respect to the x coordinate and the bars indicate arithmetic means over one unit cell width.

2 Error Estimation

The base for a posteriori error estimation is the theorem of Prager and Synge [2].

Theorem 1. *Let u be the solution of (1), $\sigma \in H(\text{div})$, $\sigma \cdot n = 0$ on Γ_N and $v \in H^1$ with $v = 0$ on Γ_D , then*

$$\|\nabla u - \nabla v\|^2 + \|\nabla u - \sigma\|^2 = \|\nabla v - \sigma\|^2. \quad (5)$$

In application v is taken as the FEM-solution and σ as a cheaply calculated approximate flux, so the left hand sides becomes the energy error plus a small

positive perturbation while the right hand side can be computed directly.

Efficient construction of such a σ is described in [2]. The idea is to use this technique to first reconstruct a “mean flux” depending only on u_0 and then adding further correctors of curl-type which incorporate the oscillations without changing the divergence. According to classical homogenization results, as found for example in [4], the natural mean flux has the form

$$\left(\bar{\lambda}^h \frac{\partial u_0}{\partial x}, \bar{\lambda} \frac{\partial u_0}{\partial y} \right)^T \quad (6)$$

with the arithmetic mean $\bar{\lambda}$ and the harmonic mean $\bar{\lambda}^h$ of λ over one unit cell. Defining σ_0 as the reconstructed mean flux, we set $\sigma := \sigma_0 + \text{curl}(\phi w)$ with an unknown function w so that the energy norm $\|\sigma\|_{\lambda^{-1}}^2$ becomes optimal. A good candidate for w can be found analytically without requiring further numerical calculations.

3 Highly Oscillatory Integrals

Calculating the estimation given by (5) requires integration over products of highly oscillating functions with functions defined on the course mesh. Such integrals have been extensively analyzed for example in [3]. However, the methods presented in the literature require the oscillator to be smooth. Since ϕ is only continuous, they cannot be applied directly.

3.1 Method

Let φ be a highly oscillating, not necessarily differentiable function and f be smooth. We propose the asymptotic expansion

$$\int_a^b \varphi(x) f(x) dx = \sum_{n=0}^{\infty} \int_a^b \bar{\varphi}_n f^{(n)}(x) dx. \quad (7)$$

The constants $\bar{\varphi}_n$ are calculated a priori such that (7) is exact for polynomials up to order n . Note that only the first integral in the expansion has to be calculated numerically. The others are given by evaluating $f^{(n-1)}$ at a and b .

This one dimensional setup can be applied to the two dimensional case via

$$\begin{aligned} \int_{\Omega} \varphi(x) f(x, y) d\Omega &= \int_a^b \varphi(x) \int_{c(x)}^{d(x)} f(x, y) dy dx \\ &=: \int_a^b \varphi(x) \tilde{f}(x) dx \end{aligned} \quad (8)$$

where $c(x)$ and $d(x)$ are parametrizations of the boundaries of the integration domain. Using additional information about the domain (i.e. that it is decomposed into triangles) it is possible to significantly reduce the number of evaluations of f .

While in the FEM setting \tilde{f} is a polynomial and therefore (7) could be used to compute the exact integral, \tilde{f} is of order $2n + 1$ with n being the order of f in both coordinates, which would lead to an impractical number of evaluations of derivatives as we do not assume to have direct control over the shape functions. However, Fig. 2 shows that a few terms in the expansion (7) are enough to obtain satisfying results even for greater cell widths d , with each expansion term netting an additional order in d . Here $f = x^3 y$, $\varphi = \lambda(\phi^2 + \phi) + 1$ with ϕ and the integration domain Ω given in section 1.

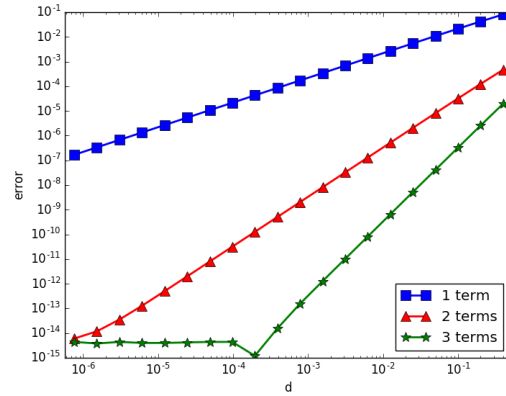


Fig. 2. Absolute error of $\int \varphi f$ for decreasing unit cell width

Acknowledgement. This work was supported by the Austrian Science Fund (FWF) under Project P 27028-N15.

References

1. K. Hollaus and J. Schöberl. Homogenization of the Eddy Current Problem in 2D. *Proceedings of the 14th International IGTE Symposium on Numerical Field Calculation in Electrical Engineering*, 154-159, 2010.
2. D. Braess and J. Schöberl. Equilibrated residual error estimator for edge elements. *Math. Comp.* 77, 651672, 2008.
3. A. Iserles and S.P. Nørsett. Quadrature Methods for Multivariate Highly Oscillatory Integrals Using Derivatives *Math. Comp.* 75, 1233-1258, 2006.
4. A. Bensoussan, J.L. Lions, G. Papanicolaou *Asymptotic Analysis for Periodic Structures*. AMS Chelsea Publishing, 1978.

Part VII

List of Participants

Achar Ramachandra
Carleton University
CANADA
achar@doe.carleton.ca

Alija Muhamet
ABB Corporate Research
SWITZERLAND
muhamet.aliya@ch.abb.com

Amrhein Wolfgang
Johannes Kepler University Linz
AUSTRIA
wolfgang.amrhein@jku.at

Arenas Manuel
TU Berlin
GERMANY
arenas@wias-berlin.de

Bagwell Scott
Swansea University
UNITED KINGDOM
638988@swansea.ac.uk

Banagaaya Nicodemus
Max Planck Institute for Dynamics of
Complex Technical Systems
GERMANY
banagaaya@mpi-magdeburg.mpg.de

Benner Peter
Max Planck Institute for Dynamics of
Complex Technical Systems
GERMANY
benner@mpi-magdeburg.mpg.de

Bittner Kai
University of Applied Sciences Upper
Austria
AUSTRIA
kai.bittner@fh-hagenberg.at

Blaszczyk Andreas
ABB Corporate Research
SWITZERLAND
Andreas.Blaszczyk@ch.abb.com

Böhme Andrea
University of Rostock
GERMANY
andrea.boehme@uni-rostock.de

Brachtendorf Hans Georg
University of Applied Sciences Upper
Austria
AUSTRIA
brachtd@fh-hagenberg.at

Bramerdorfer Gerd
Johannes Kepler University Linz
AUSTRIA
gerd.bramerdorfer@jku.at

Budko Neil
TU Delft
NETHERLANDS
n.v.budko@tudelft.nl

Capone Luigino
TU Berlin
GERMANY
luigino.capone@wias-berlin.de

Casagrande Raffael
ETH Zürich
SWITZERLAND
raffael.casagrande@sam.math.ethz.ch

Casper Thorben
TU Darmstadt
GERMANY
casper@gsc.tu-darmstadt.de

Chen Ye
TU Darmstadt
GERMANY
chen@temf.tu-darmstadt.de

Ciuprina Gabriela
Politehnica University of Bucharest
ROMANIA
gabriela@lmn.pub.ro

Cortes Garcia Idoia
TU Darmstadt
GERMANY
cortes@gsc.tu-darmstadt.de

Cremonesi Massimiliano
Politecnico di Milano
ITALY
massimiliano.cremonesi@polimi.it

Dang Nhung
TU Eindhoven
NETHERLANDS
t.k.n.dang@tue.nl

Das Prerana
TU Berlin
GERMANY
pda@no.efdgroup.net

Dautbegovic Emira
Infineon Technologies AG
GERMANY
emira.dautbegovic@infineon.com

de Falco Carlo
Politecnico di Milano
ITALY
carlo.defalco@polimi.it

De Gersem Herbert
TU Darmstadt
GERMANY
degersem@temf.tu-darmstadt.de

De Luca Giovanni
TU Eindhoven
NETHERLANDS
g.de.luca@tue.nl

Denk Georg
Infineon Technologies AG
GERMANY
georg.denk@infineon.com

Dolean Victorita
University of Strathclyde
UNITED KINGDOM
Victorita.Dolean@strath.ac.uk

Drandić Ana
University of Zagreb
CROATIA
ana.drantic@fer.hr

Duque David
TU Darmstadt
GERMANY
duque@gsc.tu-darmstadt.de

Dutin Jennifer
University of Wuppertal
GERMANY
dutine@uni-wuppertal.de

Feng Lihong
Max Planck Institute for Dynamics of
Complex Technical Systems
GERMANY
feng@mpi-magdeburg.mpg.de

Fohler Armin
Johannes Kepler University Linz
AUSTRIA
armin.fohler@lcm.at

Gaidar Viktoria
Taras Shevchenko National University of
Kyiv
UKRAINE
gaidar.viktoria@gmail.com

Gangl Peter
Johannes Kepler University Linz
AUSTRIA
peter.gangl@dk-compmath.jku.at

Gausling Kai
University of Wuppertal
GERMANY
gausling@math.uni-wuppertal.de

Gonzalez-Peñas David
University of Santiago de Compostela
SPAIN
david.gonzalez.penas@usc.es

Gotthans Tomas
Brno University of Technology
CZECH REPUBLIC
gotthans@feec.vutbr.cz

Günther Michael
University of Wuppertal
GERMANY
guenther@math.uni-wuppertal.de

Hachtel Christoph
University of Wuppertal
GERMANY
hachtel@uni-wuppertal.de

Hasan Rokibul
KU Leuven
BELGIUM
rokib.hasan@esat.kuleuven.be

Hofer Christoph
Johannes Kepler University Linz
AUSTRIA
christoph.hofer@jku.at

Janssen Rick
NXP Semiconductors
NETHERLANDS
rick.janssen@nxp.com

Keiter Eric
Sandia National Laboratories
UNITED STATES
erkeite@sandia.gov

Kielhorn Lars
TailSit GmbH
AUSTRIA
lars.kielhorn@tailsit.com

Kumar Vikas
D.A.V. College, Pundri, Haryana
INDIA
vikasmath81@gmail.com

Langer Ulrich
Johann Radon Institute for
Computational and Applied Mathematics
(RICAM)
AUSTRIA
ulrich.langer@ricam.oeaw.ac.at

Lindner Ewald
Johannes Kepler University Linz
AUSTRIA
ewald.lindner@jku.at

Liu Qingzhe
Ernst-Moritz-Arndt-Universität Greifswald
GERMANY
liuq@uni-greifswald.de

Lungten Sangye
TU Eindhoven
NETHERLANDS
s.lungten@tue.nl

Matculevich Svetlana
Johann Radon Institute for
Computational and Applied Mathematics
(RICAM)
AUSTRIA
svetlana.matculevich@ricam.oeaw.ac.at

Neumüller Martin
Johannes Kepler University Linz
AUSTRIA
neumueller@numa.uni-linz.ac.at

Ostrowski Jörg
ABB Corporate Research
SWITZERLAND
joerg.ostrowski@ch.abb.com

Ouedraogo Yun
TU Darmstadt
GERMANY
ouedraogo@temf.tu-darmstadt.de

Pade Jonas
Humboldt University of Berlin
GERMANY
jonas.pade@math.hu-berlin.de

Pade Jan Philipp
Humboldt University of Berlin
GERMANY
pade@math.hu-berlin.de

Pels Andreas
TU Darmstadt
GERMANY
pels@gsc.tu-darmstadt.de

Piñeiro Marta
University of Santiago de Compostela
SPAIN
marta.pineiro@usc.es

Pulch Roland
Ernst-Moritz-Arndt-Universität Greifswald
GERMANY
pulchr@uni-greifswald.de

Putek Piotr
University of Wuppertal
GERMANY
putek@math.uni-wuppertal.de

Reitzinger Stefan
CST AG
GERMANY
stefan.reitzinger@cst.com

Roland Theresa
Johannes Kepler University Linz
AUSTRIA
theresa.roland@jku.at

Romano Vittorio
University of Catania
ITALY
romano@dmi.unict.it

Sabariego Ruth
KU Leuven
BELGIUM
ruth.sabariego@kuleuven.be

Schilders Wil
TU Eindhoven
NETHERLANDS
w.h.a.schilders@tue.nl

Schöberl Joachim
TU Wien
AUSTRIA
joachim.schoeberl@tuwien.ac.at

Schöbinger Markus
TU Wien
AUSTRIA
markus.schoebinger@tuwien.ac.at

Schoenmaker Wim
MAGWEL NV
BELGIUM
wim@magwel.com

Schuhmacher Sebastian A.
TU Darmstadt
GERMANY
Sebastian.Schuhmacher@de.bosch.com

Seebacher Ehrenfried
ams AG
AUSTRIA
ehrenfried.seebacher@ams.com

Silber Siegfried
Linz Center of Mechatronics GmbH
AUSTRIA
siegfried.silber@lcm.at

Strohm Christian
Humboldt University of Berlin
GERMANY
strohmch@math.hu-berlin.de

Takacs Stefan
Johann Radon Institute for
Computational and Applied Mathematics
(RICAM)
AUSTRIA
stefan.takacs@ricam.oeaw.ac.at

ter Maten E. Jan W.
University of Wuppertal
GERMANY
Jan.ter.Maten@math.uni-wuppertal.de

Tischendorf Caren
Humboldt University of Berlin
GERMANY
caren.tischendorf@gmail.com

Toulopoulos Ioannis
Johann Radon Institute for
Computational and Applied Mathematics
(RICAM)
AUSTRIA
ioannis.toulopoulos@oeaw.ac.at

Truong Duy
University of Rostock
GERMANY
duy.truong@uni-rostock.de

Unger Gerhard
TU Graz
AUSTRIA
gerhard.unger@tugraz.at

van Rienen Ursula
University of Rostock
GERMANY
ursula.van-rienen@uni-rostock.de

Winkelmann Christoph
ETH Zürich
SWITZERLAND
christoph.winkelmann@sam.math.ethz.ch

Zulehner Walter
Johannes Kepler University Linz
AUSTRIA
zulehner@numa.uni-linz.ac.at